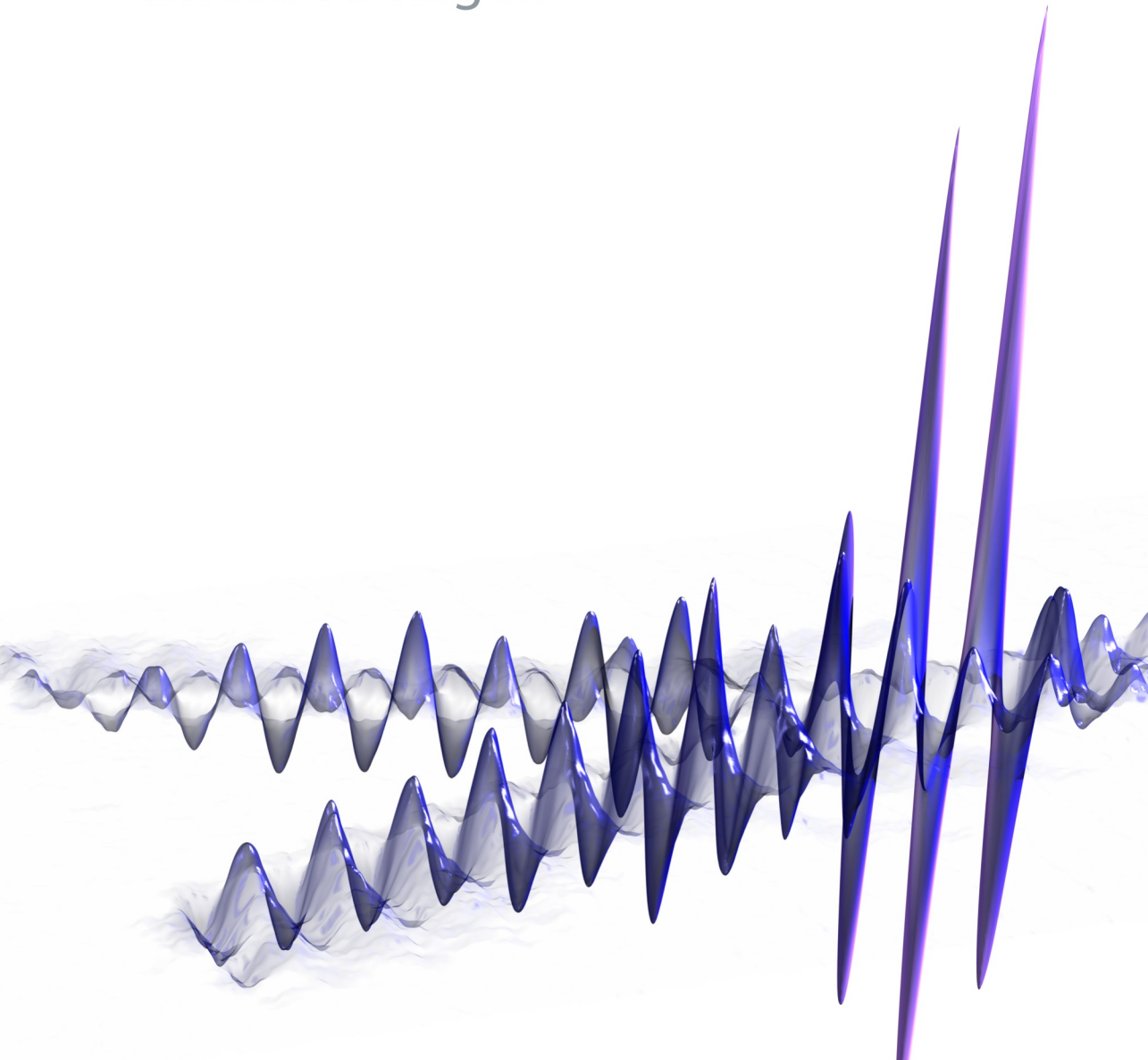


# Subwavelength light confinement with surface plasmon polaritons

Ewold Verhagen





**SUBWAVELENGTH LIGHT CONFINEMENT  
WITH SURFACE PLASMON POLARITONS**

Ph.D. Thesis Utrecht University, December 2009  
*Subwavelength light confinement with surface plasmon polaritons*  
Ewold Verhagen

ISBN 978-90-77209-37-0

A digital version of this thesis can be downloaded from <http://www.amolf.nl>.

# SUBWAVELENGTH LIGHT CONFINEMENT WITH SURFACE PLASMON POLARITONS

Opsluiting van licht op een schaal kleiner dan de golflengte  
met behulp van oppervlakteplasmonpolaritonen

(met een samenvatting in het Nederlands)

Proefschrift

ter verkrijging van de graad van doctor aan de Universiteit Utrecht  
op gezag van de rector magnificus, prof. dr. J. C. Stoof,  
ingevolge het besluit van het college voor promoties  
in het openbaar te verdedigen  
op woensdag 16 december 2009 des middags te 12.45 uur

door

**Ewold Verhagen**

geboren op 28 oktober 1980 te Leiderdorp

Promotoren: Prof. dr. A. Polman  
Prof. dr. L. Kuipers

The work described in this thesis was part of the Joint Solar Programme (JSP) of the 'Stichting voor Fundamenteel Onderzoek der Materie' (FOM), which is financially supported by the 'Nederlandse organisatie voor Wetenschappelijk Onderzoek' (NWO). The JSP is co-financed by gebied Chemische Wetenschappen of NWO and Stichting Shell Research.

---

# Contents

<b>1</b>	<b>General introduction</b>	<b>11</b>
1.1	The diffraction limit and surface plasmon polaritons	12
1.1.1	Evanescent waves	12
1.1.2	Surface plasmon polaritons	13
1.1.3	Field confinement	16
1.2	Surface plasmon polariton modes in planar multilayer waveguides	17
1.2.1	Theoretical formalism	17
1.2.2	MIM and IMI geometries	20
1.2.3	Trade-off between confinement and loss	23
1.3	Concentrating light with surface plasmon polaritons	25
1.3.1	Localized resonances in annular apertures	26
1.4	Probing the near field	28
1.5	Outline of this thesis	29
<b>2</b>	<b>Near-field probing of SPPs in metal-insulator-metal waveguides</b>	<b>31</b>
2.1	Introduction	31
2.2	Methods	32
2.2.1	Sample fabrication	32
2.2.2	Near-field experiments	33
2.2.3	Polarization dependence of probe emission	34
2.3	Single output slit: Interference of different SPP modes	35
2.3.1	One-dimensional interference model	36
2.3.2	Excitation asymmetry	36
2.3.3	Two-dimensional interference model	37

2.4	Double output slits: interference of MIM-SPPs	38
2.4.1	MIM-SPP dispersion relation	38
2.5	Conclusions	40
<b>3</b>	<b>Negative index of refraction in surface plasmon polariton waveguides</b>	<b>41</b>
3.1	Introduction	41
3.1.1	Surface plasmon waveguide-based metamaterials	42
3.2	Theoretical formalism	43
3.3	Lossy dispersion and the necessary condition for negative indices	46
3.3.1	The MIM waveguide as a negative index material	47
3.3.2	IIM and IMI waveguides as multimode metamaterials	49
3.4	Mapping plasmonic material indices and absorption	51
3.4.1	Ag/GaP and Ag/Si <sub>3</sub> N <sub>4</sub> MIM metamaterials	52
3.4.2	Ag/GaP-based IIM and IMI waveguides	54
3.5	Conclusions	57
<b>4</b>	<b>Enhanced upconversion of infrared light with a tapered plasmonic waveguide</b>	<b>59</b>
4.1	Introduction	59
4.2	Methods	60
4.2.1	Er upconversion luminescence	60
4.2.2	Fabrication of Ag microstructures	62
4.2.3	Optical measurements	63
4.3	Results and discussion	63
4.4	Conclusions	66
<b>5</b>	<b>Nanofocusing in laterally tapered plasmonic waveguides</b>	<b>67</b>
5.1	Introduction	67
5.2	Methods	69
5.2.1	Sample fabrication	69
5.2.2	Optical measurements	70
5.3	Results and discussion	71
5.3.1	Power dependence	72
5.3.2	Absence of cutoff	74
5.4	Modeling	76
5.4.1	Simulation methods	76
5.4.2	Simulation results: Three-dimensional nanofocusing	78
5.4.3	Comparison between excitation in substrate or in air	80
5.5	Conclusions	81
<b>6</b>	<b>Nanowire plasmon excitation by adiabatic mode transformation</b>	<b>83</b>
6.1	Introduction	83
6.2	Surface plasmon polariton mode transformation	84
6.2.1	Surface plasmon polaritons on a metal cylinder	84
6.2.2	Computation method for complex waveguiding geometries	85



---

6.2.3	Stripe waveguides in a homogeneous dielectric environment	86
6.2.4	SPP modes in stripe waveguides on a dielectric substrate	87
6.2.5	The symmetry of the dielectric surrounding	88
6.3	Methods	90
6.3.1	Phase- and polarization-sensitive near-field microscopy	90
6.4	Results and discussion	92
6.4.1	Coupling to nanowire SPPs	92
6.4.2	Polarization nature of the nanowire mode	93
6.4.3	Wavevector of SPPs on nanowires	95
6.4.4	Coupling efficiency	96
6.4.5	Calculated efficiency: comparison to conical geometry	97
6.4.6	Exciting SPPs at the air side of the Au film	98
6.5	Conclusions	98
<b>7</b>	<b>Plasmonic nanofocusing in a dielectric wedge</b>	<b>101</b>
7.1	Introduction	101
7.2	SPPs on a metal surface covered with a thin dielectric film	102
7.3	The geometrical optics approximation	105
7.4	Comparing the geometrical optics approximation to FDTD	107
7.4.1	Subwavelength confinement	109
7.5	Conclusions	110
<b>8</b>	<b>Field enhancement in metallic subwavelength aperture arrays</b>	<b>111</b>
8.1	Introduction	111
8.2	Methods	113
8.3	Field enhancement in hole arrays	115
8.3.1	Quantifying field enhancement	117
8.3.2	Dependence of enhancement on structural parameters	118
8.4	The Fano model: far field transmission and near field enhancement	119
8.5	Field enhancement in arrays of annular apertures	122
8.5.1	Angle dependence of field enhancement in annular apertures	123
8.6	Conclusions	124
<b>9</b>	<b>Enhanced spontaneous emission rate in annular plasmonic nanocavities</b>	<b>127</b>
9.1	Introduction	127
9.2	Methods	128
9.2.1	Sample fabrication	128
9.2.2	Optical measurements	129
9.2.3	Tuning the localized resonance	130
9.3	Results	130
9.4	Discussion	133
9.5	Conclusions	134

<b>10 Applications and outlook</b>	<b>135</b>
10.1 Integrated photonics	135
10.1.1 Coupling light to the nanoscale	135
10.1.2 Nanowire directional couplers	137
10.2 Photovoltaics	141
10.2.1 Light absorption in plasmonic solar cells	141
10.2.2 Adiabatic concentration of light from free-space	143
10.2.3 Upconversion for photovoltaics	146
10.3 Sensing and spectroscopy	147
10.3.1 Localized surface plasmon resonance sensing	147
10.3.2 Enhanced spectroscopy	148
10.4 Towards a three-dimensional left-handed material	150
<b>Appendix A Waveguide modes in multilayer geometries: TE polarization</b>	<b>155</b>
<b>References</b>	<b>157</b>
<b>Summary</b>	<b>171</b>
<b>Samenvatting</b>	<b>175</b>
<b>List of publications</b>	<b>179</b>
<b>Dankwoord</b>	<b>181</b>
<b>About the author</b>	<b>183</b>





# 1

---

## General introduction

Light is crucial to human perception. Since the advent of modern science, we have sought to manipulate the flow of light to extend the range of our optical perception. Exploiting light-matter interaction with dielectric lenses and metallic mirrors has enabled us to directly visualize a vast variety of phenomena in nature, from the division of cells to the birth of stars.

In modern technology, the manipulation of light serves many more purposes than imaging alone. A multitude of applications make use of light that is confined to small length scales. All of these would benefit from a further increase of the optical confinement. The majority of telecommunication signals travel in the form of light through optical fibers, which offer an enormous bandwidth and have a low power dissipation compared to electronic connections [1]. When photonics is brought to the level of computer chips in the form of optical interconnects or active photonic circuitry, the same advantages can result in increased computation power. Efficient integration of photonics with electronic functionality should benefit from a scaling down of optical components to the nanoscale size of electronic components [2, 3].

In photovoltaic energy conversion, a more efficient capturing of light in solar cells would reduce the volume of active material needed to absorb all incident light. This reduction could decrease material cost, offer higher efficiencies by increasing the open circuit voltage, and would possibly allow for solar cell designs based on unconventional materials, in which charge extraction is otherwise limiting performance [4]. In a similar fashion, light concentration could increase the sensitivity and speed of biological and optical sensors [5–7], and enhance the strength of non-linear interactions [8–11].

An emitter placed in a structure that exhibits strong optical field enhancement can radiate more efficiently than an emitter in free space, due to the large photonic mode density associated with highly confined light waves [12, 13]. This can enhance the efficiency of light-emitting diodes and lasers. It is also important in quantum information technology, in which single emitters need to be efficiently interfaced to photonic circuits [14, 15].

## 1.1 The diffraction limit and surface plasmon polaritons

The smallest size to which light can be concentrated with standard optical elements such as lenses and mirrors is limited by the wavelength of light. This limit arises from diffraction of light by the aperture of the optical device that is used to focus light. Even if that aperture is very large, a minimum distance exists between the position where the diffracted light waves interfere constructively (the focus) and a position where they interfere destructively. It can be seen from the Fourier transform that the smallest size  $\Delta x$  to which a plane light wave can be focused in one dimension is of the order of

$$\Delta x \approx \frac{2\pi}{\Delta k_x} = \frac{\lambda_0}{2}, \quad (1.1)$$

where  $\Delta k_x = 4\pi/\lambda_0$  is the maximum possible spread of the wavevector component  $k_x$  along the  $x$  direction, and  $\lambda_0$  is the wavelength in vacuum. Conversely, this length scale also governs the smallest distance between two objects for which the objects can be individually resolved in a microscope.

Light can be confined to length scales beyond the reach of conventional lenses or dielectric photonic structures by making use of light-matter interactions at a metal surface. An interface between a metal and a dielectric supports surface plasmon polaritons, which are evanescent electromagnetic waves bound to the interface that are strongly coupled to coherent oscillations of free charges at the metal surface. They allow control over the flow of optical energy at small dimensions. In recent years, the study of surface plasmon photonics or ‘plasmonics’ has attracted much attention [3, 16, 17], spurred by the possible applications of strongly confined optical fields [3, 18, 19] and enabled by advances in nanofabrication technology.

### 1.1.1 Evanescent waves

A proper derivation of the diffraction limit was first formulated by Ernst Abbe in 1873 [20]. It can be explained by expanding the electromagnetic field in a homogeneous medium with dielectric constant  $\varepsilon$  in plane waves  $e^{i\mathbf{k}\cdot\mathbf{x}}$  with wavevector  $\mathbf{k}$  satisfying

$$\varepsilon k_0^2 = k_x^2 + k_y^2 + k_z^2, \quad (1.2)$$

where  $k_0 = \omega/c$  is the wavevector in free space. In the focus of a conventional lens only propagating plane waves with real wavevector components contribute

to the field. All wavevector components  $k_i$  of one of the plane waves constituting the field are therefore smaller than  $k_0$ , and the high spatial frequencies needed for subwavelength concentration are lacking.

The diffracted field close to a dielectric object can however vary on a subwavelength scale. That field is described in terms of evanescent waves. Because for such waves the projection of the wavevector in at least one direction is imaginary, the wavevector component in another direction will be larger than  $k_0$ , while (1.2) is still satisfied. Provided that the proper evanescent waves are excited with large enough amplitude in the direct vicinity of a dielectric object, light can thus be localized to dimensions smaller than the diffraction limit. Large evanescent fields can be reached most easily if the evanescent fields are associated with a (quasi-)eigenmode\* of the system with a finite linewidth, which can be resonantly excited with large amplitude.

### 1.1.2 Surface plasmon polaritons

The eigenmodes of an interface between a dielectric and a metal are surface plasmon polaritons (SPPs). We refer to them as eigenmodes in the sense that they are solutions of Maxwell's equations that can be formulated in the absence of an incident field [23]. On a flat interface between dielectric and metal half-spaces with dielectric constants  $\epsilon_d$  and  $\epsilon_m$ , respectively, SPPs are transverse magnetic (TM) plane waves propagating along the interface. Assuming the interface is normal to  $\hat{z}$  and the SPPs propagate along the  $x$  direction (i.e.,  $k_y = 0$ ), the SPP wavevector  $k_x$  is related to the optical frequency  $\omega$  through the dispersion relation [24]

$$k_x = k_0 \sqrt{\frac{\epsilon_d \epsilon_m}{\epsilon_d + \epsilon_m}}. \quad (1.3)$$

We take  $\omega$  to be real and allow  $k_x$  to be complex, since our main interest is in stationary monochromatic SPP fields in a finite area [25].

The optical response of metals is often described by the Drude model for a free-electron gas [27],

$$\epsilon_{\text{Drude}}(\omega) = 1 - \frac{\omega_p^2}{\omega^2 + i\Gamma\omega}, \quad (1.4)$$

in which  $\omega_p$  is the plasma frequency and  $\Gamma$  a damping rate due to electron-electron and electron-phonon scattering. Figure 1.1(a) shows the dispersion curve (1.3) for an interface between a Drude metal and air in the absence of losses ( $\Gamma = 0$ ). When  $\epsilon_m < -\epsilon_d$ , i.e., for frequencies below the surface plasmon resonance frequency  $\omega_{\text{sp}} = \omega_p / \sqrt{1 + \epsilon_d}$ , the SPP wavevector is larger than  $k_0$  and the dispersion curve thus lies to the right of the light line. As a result, the field decays evanescently in the

---

\*Because all systems considered in this thesis exhibit Ohmic losses and the modes of interest are often coupled to a radiation continuum, they are in general not proper eigenmodes of the system. We will however drop the prefix 'quasi' when describing eigenmodes from here on. For a discussion on mode orthogonality and normalization, we refer to references [21, 22].

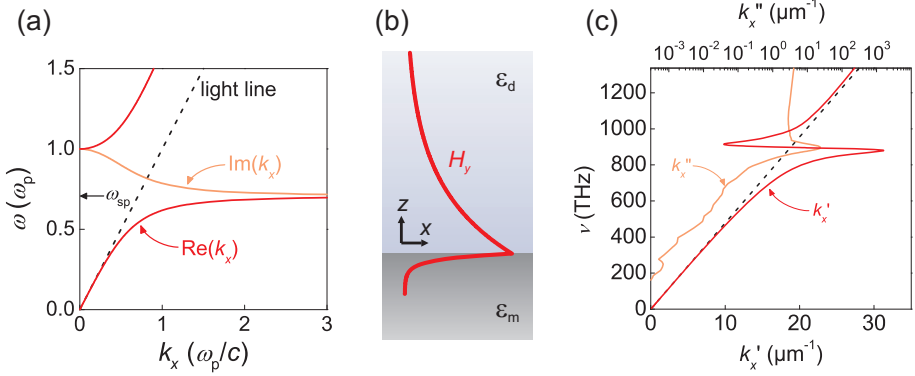


**Figure 1.1:** (a) Dispersion of SPPs at the interface of a lossless Drude metal with air. (b) Transverse dependence of the  $H_y$  field of SPPs at a Ag/air interface. (c) Dispersion of SPPs at the interface of Ag with air. The optical constants are measured on a Ag film [26]. Both the real ( $k'_x$ ) and imaginary ( $k''_x$ ) parts of the wavevector  $k_x$  are plotted. The dashed line denotes the light line,  $\omega = \sqrt{\epsilon_d} c k_x$ .

direction normal to the interface, since  $k_z$  is connected to  $k_x$  through (1.2). A large real part of the wavevector  $k_x$  is therefore directly related to a large transverse (vertical) confinement determined by the imaginary part of  $k_z$ . A typical  $z$ -dependence of the SPP  $H_y$  field is depicted in Fig. 1.1(b).

In the absence of losses,  $k_x$  is purely imaginary for  $\omega_{sp} < \omega < \omega_p$ , meaning that the wave does not propagate along the interface. Above  $\omega_p$  the metal is transparent, and the solution to (1.3) corresponds to the condition of illumination of the interface at the Brewster angle. The branch observed for high frequencies in Fig. 1.1(a) is as such not a proper guided eigenmode of the system.

As can be seen in Fig. 1.1(a), the wavevector diverges at  $\omega_{sp}$  for a lossless Drude metal. In reality, the maximum possible wavevector is limited by absorption in the metal, causing the dispersion curve to bend back close to  $\omega_{sp}$  to result in the typical s-shaped curve characteristic of polaritons [28]. At high frequencies the Drude model (1.4) represents the response of most metals less accurately due to the presence of interband transitions [29]. Although the Drude model is useful for understanding the basic behavior of SPPs, it can therefore not be used to make quantitative predictions of SPP properties on metals throughout the entire optical frequency regime.

In the presence of loss, the wavevector  $k_x = k'_x + i k''_x$  is in general a complex number for all  $\omega$ . Figure 1.1(c) shows the dispersion curve of SPPs at a Ag/air interface using the experimentally determined optical constants reported in ref. [26]. Also plotted is the imaginary part of the wavevector ( $k''_x$ ) which denotes the magnitude of the loss along the direction of propagation. Ohmic dissipation causes the SPPs to decay with a characteristic propagation length  $L_{SPP}$  (defined as the distance



in which the SPP intensity decays to  $1/e$  of its original value) given by

$$L_{\text{SPP}} \equiv \frac{1}{2k_x''} \quad (1.5)$$

As Fig. 1.1(c) shows, the loss grows rapidly as the frequency increases towards  $\omega_{\text{sp}}$ . In general, the loss increases when the transverse confinement of a SPP mode increases, as a larger fraction of the modal field is located inside the metal. Thus, dissipation limits the efficiency with which light can be concentrated to nanoscale volumes using SPPs. For many practical applications of plasmonics, the trade-off between the advantageous attributes of SPPs and Ohmic losses is of pivotal importance. The metal that exhibits the smallest absorption while having a large and negative real part of  $\epsilon_m$  throughout the visible and near-infrared frequency regimes is Ag. In the near-infrared, Au is a good alternative.

The fact that the SPP dispersion curve lies to the right of the light line ( $\omega = ck_x/\sqrt{\epsilon_d}$ ) in Figs. 1.1(a) and (c) for all frequencies smaller than  $\omega_{\text{sp}}$  means that SPPs cannot directly couple to radiation modes in the bounding dielectric, whose dispersion is located to the left of the light line. The wavevector mismatch between SPPs and radiation modes needs to be overcome in order to excite or detect SPPs. This can be achieved by multiple methods [24]. In the Otto configuration, light in a prism that is brought in close vicinity to a metal surface can excite SPPs through tunneling of the evanescent field. Because the light in the prism has a larger wavevector than that in air, it can be phase-matched to the SPPs. In the related Kretschmann-Raether geometry, tunneling to SPPs occurs through a metal film that is deposited on a prism. Grating diffraction can also provide the necessary momentum to excite SPPs on a periodically corrugated metal surface. In general, any surface corrugation can scatter light to SPPs without relying on a precise momentum matching. Finally, dipole emitters located in close vicinity to a metal surface can radiate energy into SPP modes.

So far, we have only considered SPPs on an infinitely extended metal surface that acts as a SPP waveguide. If the surface is not translationally invariant, the wavevector  $k_x$  is not conserved and coupling between SPPs and free-space radiation will occur. In a finite-sized system, surface plasmon resonances are localized. They can be labeled by complex eigenfrequencies denoting the center frequencies and linewidths of the resonances. The quintessential localized plasmon resonance is the dipole mode of a metal nanoparticle, which has been widely studied and exploited in many applications ranging from stained glass windows to molecular sensing [17, 30].

It can be instructive to consider even finite sized plasmonic systems in terms of waveguide modes, as we will see throughout this thesis. By treating such systems as truncated or gradually changing waveguides, the effect of size, shape, and symmetry on the mode properties can often be readily understood in terms of the fields and the dispersion of waveguide modes in infinitely long waveguides.

### 1.1.3 Field confinement

On a single metal/dielectric interface, the transverse confinement of SPPs depends strongly on the frequency. The  $1/e$  intensity decay length  $L_{z,j}$  into medium  $\epsilon_j$  is obtained from (1.3) and (1.2):

$$L_{z,j} = k_0 \frac{\epsilon_j}{\sqrt{\epsilon_d + \epsilon_m}}. \quad (1.6)$$

For SPPs on a Ag/air interface at a free-space wavelength of 633 nm,  $L_{z,d}$  is 210 nm in the air, and  $L_{z,m}$  is 11 nm in the metal. At 1550 nm, the decay length in air is 1400 nm, and that into the metal is again 11 nm. The confinement is thus comparable to or somewhat smaller than the free-space wavelength. It can be significantly increased by raising the permittivity of the dielectric, since  $k_z$  in the dielectric scales linearly with  $\epsilon_d$  for small frequencies, and with an even higher power of  $\epsilon_d$  close to  $\omega_{sp}$ . The increase in confinement occurs in conjunction with an increase of the losses, as  $k_x'' \propto \epsilon_d^{3/2}$ .

For a single flat metal/dielectric interface, strong confinement is limited to high-index dielectrics and frequencies close to  $\omega_{sp}$ . Confinement to arbitrarily small scales can be achieved at any frequency and without having to increase the dielectric constant by changing the waveguide geometry. In the search for such geometries that allow subwavelength confinement, it is instructive to consider the zero-frequency limit of electrostatics, in which any design that allows fields to be localized in a finite volume offers subwavelength confinement by definition.

Two conducting geometries that are well-known for their ability to store charges and therefore exhibit high electric fields are depicted in Fig. 1.2. Firstly, the energy stored in a parallel-plate capacitor when a potential difference is applied to the plates is inversely proportional to the plate separation. The surface charges on the two plates that give rise to the electric field between them have opposite sign. Secondly, charges tend to localize at sharp features on a charged conductor, such

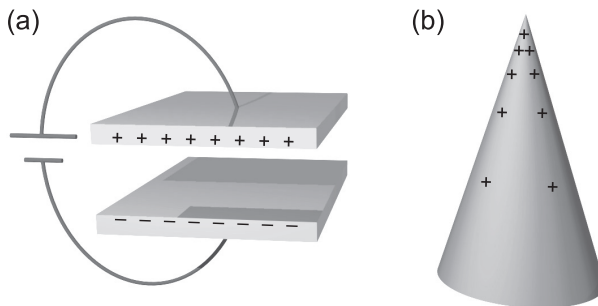


**Figure 1.2:** Two structures that exhibit localized electric fields at zero frequency: a parallel plate capacitor (a) and a sharp conducting protrusion, such as the tip of a lightning rod (b).

as the tip of a metallic cone. This is the reason why in a thunderstorm electrical breakdown occurs first at the tip of a lightning rod. Similar fields are localized at the edge of a thin conducting sheet. The energy density on the surface of a sheet with a smoothly rounded edge is known to be inversely proportional to the sheet thickness. In these cases, the charges on opposing sides of the cone or the sheet have equal sign.

The above examples show that (static) electric fields can be confined in small insulating gaps between oppositely charged conducting interfaces and close to metal protrusions carrying charge of one particular sign, surrounded by insulating material. It comes therefore natural to search for highly confined waveguided SPP modes at optical frequencies in two similar geometries; a dielectric slab between two metal halfspaces in analogy with a parallel plate capacitor, and a metal slab between two dielectric halfspaces, which is related to a metal protrusion surrounded by dielectric, such as a conducting sheet with a rounded edge or the cone depicted in Fig. 1.2(b). Before we consider the modes in those geometries, we will first provide the theoretical framework for calculating eigenmodes in multilayer slab waveguides.

## 1.2 Surface plasmon polariton modes in planar multilayer waveguides

### 1.2.1 Theoretical formalism

We consider a multilayer stack of  $n$  dielectric slabs, as depicted in Fig. 1.3. The dielectric constant of layer  $j$  is  $\epsilon_j$ , and its thickness is  $d_j$ . The outer media  $\epsilon_1$  and  $\epsilon_n$  extend to  $z = -\infty$  and  $z = \infty$ , respectively.

To find the waveguided eigenmodes in the multilayer geometry we need to search for solutions to the wave equation

$$\nabla \times \nabla \times \mathbf{H} - \epsilon k_0^2 \mathbf{H} = 0, \quad (1.7)$$

in the absence of waves that are incident from  $z = -\infty$  or  $z = \infty$ . Since  $\epsilon(\mathbf{x})$  is piecewise homogeneous, we can solve (1.7) separately in the different media, and connect the solutions using the boundary conditions for the fields at the interfaces. Since we are interested in SPPs, we only consider TM-polarized eigenmodes here. For completeness, we provide the solution for TE polarization in Appendix A.

Because of translational invariance in  $x$  and  $y$ , the magnetic field of TM-polarized solutions to the wave equation in layer  $j$  can be written as

$$\mathbf{H}_j(x, z, t) = H_{yj}(z) e^{ik_x x - i\omega t} \hat{\mathbf{y}}, \quad (1.8)$$

where we have chosen  $k_y = 0$  by convention;  $\hat{\mathbf{y}}$  denotes a unit vector in the  $y$  direction. The solutions are waves that propagate in the  $x$  direction with characteristic

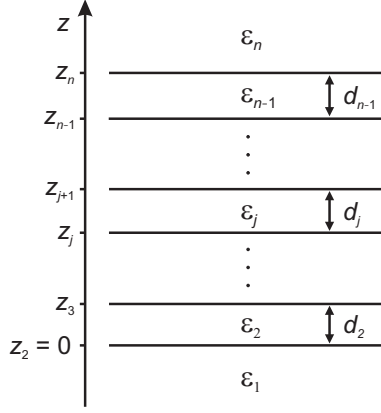


**Figure 1.3:** The multilayer slab geometry.

wavevector  $k_x$ . The wave equation in layer  $j$  then reduces to

$$\frac{d^2}{dz^2} H_{yj}(z) + (\varepsilon_j k_0^2 - k_x^2) H_{yj}(z) = 0. \quad (1.9)$$

The general solution for the  $z$  dependence of the field is therefore

$$H_{yj}(z) = A_j \sin(k_{zj}(z - z_j)) + B_j \cos(k_{zj}(z - z_j)), \quad (1.10)$$

where we have defined the transverse wavevector component  $k_{zj}$  as

$$k_{zj} = \sqrt{\varepsilon_j k_0^2 - k_x^2}. \quad (1.11)$$

In the outer media, we need to fulfill the condition that there are no waves incident from outside the structure. Therefore, we write the field in those media as

$$H_{y1}(z) = C_0 e^{-ik_{z1}z} \quad (1.12)$$

$$H_{yn}(z) = C_n e^{ik_{zn}(z-z_n)}, \quad (1.13)$$

and we have to make sure that the signs of  $k_{z1}$  and  $k_{zn}$  are chosen such that the above condition is fulfilled. This could mean that both  $\text{Im}\{k_{z1}\}$  and  $\text{Im}\{k_{zn}\}$  are positive, i.e., the solution decays to zero far away from the waveguide, in which case the waveguided mode is purely bound. But leaky waves, which radiate power to the far field in one or both of the outer media, can also be eigenmodes. The field of such waves grows with increasing distance from the waveguide, which is a direct consequence of the fact that these waves are damped in the  $x$  direction [31, 32]. Of course we must always ensure that when the signs of  $k_{z1}$  and  $k_{zn}$  are chosen

such that the fields grow with increasing  $|z|$ , power flow is directed away from the waveguide before a solution is accepted as a (leaky) eigenmode.

The coefficients  $A_j$ ,  $B_j$ ,  $C_0$ , and  $C_n$  need to be determined. One of these can be chosen at will to normalize the mode. We choose  $C_0 = H_{y0}$  for that purpose. To determine the other coefficients in (1.10) and (1.13), the fields in adjacent media have to be matched at the interfaces through the boundary conditions. Inside layer  $j$ , the magnetic field  $H_{yj}(z)$  and its first derivative can be expressed in terms of the field at the bottom interface of that layer (at  $z = z_j$ ) using (1.10):

$$\begin{bmatrix} H_{yj}(z) \\ \frac{d}{dz}H_{yj}(z) \end{bmatrix} = \begin{bmatrix} \cos(k_{zj}(z - z_j)) & \frac{1}{k_{zj}} \sin(k_{zj}(z - z_j)) \\ -k_{zj} \sin(k_{zj}(z - z_j)) & \cos(k_{zj}(z - z_j)) \end{bmatrix} \begin{bmatrix} H_{yj}(z_j) \\ \frac{d}{dz}H_{yj}(z_j) \end{bmatrix}. \quad (1.14)$$

The electric field can be found with the Ampère-Maxwell law:

$$\mathbf{E}_j(x, z, t) = \left( -\frac{i}{\varepsilon_j \varepsilon_0 \omega} \frac{d}{dz} H_{yj}(z) \hat{\mathbf{x}} - \frac{k_x}{\varepsilon_j \varepsilon_0 \omega} H_{yj}(z) \hat{\mathbf{z}} \right) e^{ik_x x - i\omega t}. \quad (1.15)$$

By applying the boundary conditions of tangential  $\mathbf{E}$  and  $\mathbf{H}$  at  $z = z_j$ , we find a relation between the fields in adjacent layers at  $z = z_j$ :

$$\begin{bmatrix} H_{yj}(z_j) \\ \frac{d}{dz}H_{yj}(z_j) \end{bmatrix} = \mathbf{T}_j \begin{bmatrix} H_{yj-1}(z_j) \\ \frac{d}{dz}H_{yj-1}(z_j) \end{bmatrix}, \quad (1.16)$$

$$\mathbf{T}_j = \begin{bmatrix} 1 & 0 \\ 0 & \frac{\varepsilon_j}{\varepsilon_{j-1}} \end{bmatrix}. \quad (1.17)$$

Together with (1.14), this relates the fields at  $z = z_j$  and  $z = z_{j+1}$  in adjacent media as

$$\begin{bmatrix} H_{yj}(z_{j+1}) \\ \frac{d}{dz}H_{yj}(z_{j+1}) \end{bmatrix} = \mathbf{M}_j \begin{bmatrix} H_{yj-1}(z_j) \\ \frac{d}{dz}H_{yj-1}(z_j) \end{bmatrix}, \quad (1.18)$$

with

$$\mathbf{M}_j = \begin{bmatrix} \cos(k_{zj}d_j) & \frac{\varepsilon_j}{k_{zj}\varepsilon_{j-1}} \sin(k_{zj}d_j) \\ -k_{zj} \sin(k_{zj}d_j) & \frac{\varepsilon_j}{\varepsilon_{j-1}} \cos(k_{zj}d_j) \end{bmatrix}. \quad (1.19)$$

Now we can express  $H_{yj}(z)$  and its first derivative in terms of the field at  $z = 0$ , to which we had assigned a value of  $H_{y0}$ :

$$\begin{bmatrix} H_{yj}(z_j) \\ \frac{d}{dz}H_{yj}(z_j) \end{bmatrix} = \mathbf{Q}_j \begin{bmatrix} H_{y0} \\ -ik_{z1}H_{y0} \end{bmatrix}, \quad (1.20)$$

with

$$\mathbf{Q}_j = \mathbf{T}_j \mathbf{M}_{j-1} \mathbf{M}_{j-2} \cdots \mathbf{M}_2. \quad (1.21)$$

We finally arrive at a relation between the magnetic fields in the outer media 1 and  $n$  at  $z = 0$  and  $z = z_n$ :

$$\begin{bmatrix} H_{y0n} \\ ik_{zn}H_{y0n} \end{bmatrix} = \mathbf{Q}_n \begin{bmatrix} H_{y0} \\ -ik_{z1}H_{y0} \end{bmatrix}, \quad (1.22)$$

which has a nontrivial solution when

$$Q_{n,11} - ik_{z1}Q_{n,12} + \frac{i}{k_{zn}}Q_{n,21} + \frac{k_{z1}}{k_{zn}}Q_{n,22} = 0, \quad (1.23)$$

where  $Q_{n,ij}$  denotes the (i,j)th matrix element of  $\mathbf{Q}_n$ .

Equation (1.23) is the dispersion relation for TM modes in the multilayer slab waveguide. Its solutions are complex eigenvalues  $k_x$ . If  $n = 2$ , (1.23) can be readily inverted to yield (1.3). For more than two layers, it can be solved using a minimization algorithm or by applying the Argument principle in the complex  $k_x$  plane [33].

The corresponding  $\mathbf{H}$  field of the modes is given by (1.8) with

$$H_{yj}(z) = \begin{cases} H_{y0}e^{-ik_{z1}z}, & j = 1, \\ (Q_{j,11} - ik_{z1}Q_{j,12})H_{y0}\cos(k_{zj}(z - z_j)) \\ \quad + (Q_{j,21} - ik_{z1}Q_{j,22})\frac{H_{y0}}{k_{zj}}\sin(k_{zj}(z - z_j)), & 1 < j < n, \\ (Q_{n,11} - ik_{z1}Q_{n,12})H_{y0}e^{ik_{zn}(z - z_n)}, & j = n. \end{cases} \quad (1.24)$$

The electric field is determined by (1.15).

## 1.2.2 Metal-insulator-metal and insulator-metal-insulator geometries

In this section, we will focus our attention on two types of slab waveguides that both support modes that become highly confined as the slab thickness is reduced. In analogy with the electrostatic devices introduced in section 1.1.3, the first is a so-called metal-insulator-metal (MIM) waveguide, consisting of a thin dielectric slab between two metals [34–36]. The second is the inverted geometry, i.e., an insulator-metal-insulator (IMI) waveguide [31, 34, 37].

The eigenmodes of MIM or IMI waveguides arise from evanescent coupling between the SPPs supported by the individual metal/dielectric surfaces. The coupling results in symmetric and antisymmetric eigenmodes of the coupled system with different eigenvalues  $k_x$ . By convention, we will use the term ‘symmetric’ to describe modes that have a symmetric distribution of  $H_y$  and  $E_z$  across the waveguide, and therefore an antisymmetric distribution of  $E_x$  and of the induced surface charge. Conversely, ‘antisymmetric’ modes have an antisymmetric distribution of  $H_y$  and  $E_z$  and a symmetric distribution of  $E_x$  and of the induced surface charge.

In a MIM waveguide with core dielectric constant  $\epsilon_d$ , the antisymmetric mode exhibits cutoff when the waveguide size is approximately  $(\pi c / (\sqrt{\epsilon_d}\omega))$  [36]. Below that thickness, only the lowest order symmetric TM-polarized mode can propagate. Its dispersion in a Ag/air/Ag geometry is plotted in Fig. 1.4(a) for core thicknesses  $d$  of 5, 10, 20 and 50 nm. The dispersion for a single-interface Ag/air geometry is also plotted. As can be seen, the wavevector increases for all frequencies below  $\omega_{\text{sp}}$  when  $d$  is reduced. The corresponding propagation length  $L_{\text{SPP}}$  is plotted in Fig. 1.4(a) as well.

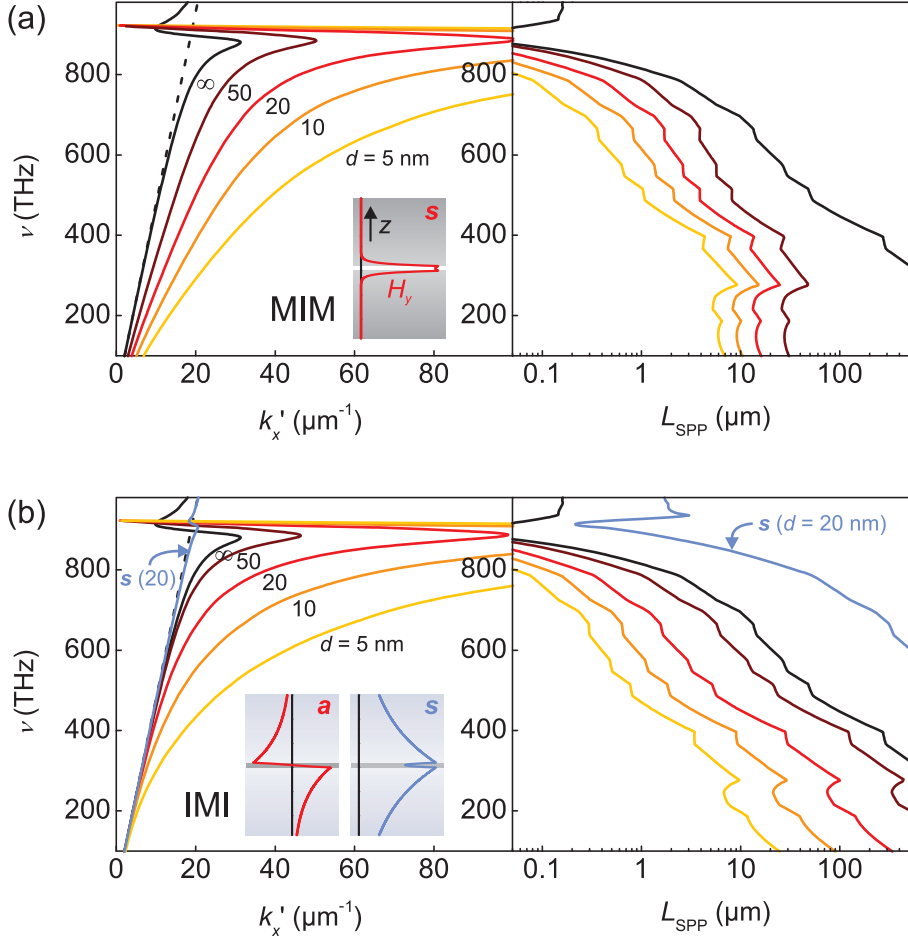


**Figure 1.4:** Dispersion of SPPs in MIM and IMI geometries consisting of Ag and air. (a) Real part of the wavevector  $k'_x$  and propagation length  $L_{\text{SPP}}$  in a MIM geometry, for different core thicknesses. The inset shows the  $H_y$  field profile for a 50 nm thick air layer. (b) Real part of the wavevector  $k'_x$  and propagation length  $L_{\text{SPP}}$  of the antisymmetric mode in a IMI geometry, for the same range of core thicknesses as in (a). The blue curves shows the dispersion of the symmetric mode for a Ag thickness of 20 nm. The insets show the field profiles of the antisymmetric and symmetric modes for a thickness of 50 nm.

The inset of Fig. 1.4(a) depicts the  $z$  dependence of the  $H_y$  field for an air thickness of 50 nm at a free-space wavelength of 633 nm. It shows that the field is largely confined within the dielectric slab. The extent of the field into the metal cladding is comparable to the skin depth, which does not vary much throughout the visible and near-infrared. The transverse confinement of the mode is therefore rather independent of frequency [36]. As a result, the propagation length below  $\sim 400$  THz does not change as rapidly with frequency as that of SPPs at a single Ag/air interface.

The situation is different in an IMI geometry. There, both the lowest-order symmetric and antisymmetric modes can be guided on arbitrarily thin metal films. The wavevector of the symmetric mode tends to the light line as the thickness is reduced, and its decay length  $L_{z,d}$  into the dielectric surrounding becomes large. The dispersion of the symmetric SPP mode on a 20 nm thick Ag film surrounded by air is plotted as the blue curve in Fig. 1.4(b). It lies very close to the light line. Because the relative fraction of energy located in the metal is small for this mode, its propagation length can be of the order of millimeters to centimeters [38]. This mode is therefore often called a long-range SPP. Because of its weak transverse confinement, it is however of limited interest for nanophotonic applications.

In stark contrast, the antisymmetric mode can acquire a large wavevector and strong confinement on a thin metal film. Its dispersion is depicted in Fig. 1.4(b) for the same range of core thicknesses as for the MIM geometry. For large frequencies, the achievable wavevectors are comparable to those in the MIM geometry. For small frequencies, the dispersion curves are however closer to the light line than those in MIM waveguides of similar thickness. This difference between IMI and MIM waveguides is related to the fact that in an IMI waveguide the extent of the field into the dielectric cladding increases when the frequency is reduced.

If the dielectric environment of a metal film is not symmetric, the eigenmodes are not purely symmetric or antisymmetric. Nonetheless, we will retain the words ‘symmetric’ and ‘antisymmetric’ to denote the different eigenmodes in an asymmetric environment. We base the labeling of those modes on the symmetry of the modes in a symmetric environment from which the modes in an asymmetric environment evolve when the environment is continuously changed from symmetric to not symmetric. For example, when the permittivity of one of the media in an IMI geometry is raised, the symmetric mode has a larger fraction of its energy propagating in the low-index dielectric, and the antisymmetric mode is mostly localized in the high-index dielectric. When the difference between the permittivities is larger than typically  $\sim 1\%$ , the symmetric mode becomes leaky into the high-index medium, as its wavevector is then smaller than the wavevector of light in the high-index medium [39]. Because of the associated radiation losses, the symmetric mode therefore loses its long-range character. It will become more lossy when the metal thickness is reduced [31]. The antisymmetric mode, however, retains its interesting property of increasing confinement with decreasing metal thickness.



### 1.2.3 Trade-off between confinement and loss

To achieve large wavevectors, a strong light-matter interaction is needed. Highly confined SPP modes are therefore necessarily lossy. To quantify the trade-off between confinement and loss, one needs to determine which quantitative properties of the modes define the merits of SPP confinement best. To define these properly, one needs to have a specific application in mind. Nonetheless, we would like to compare the trade-off between confinement and loss for the two geometries discussed before without losing too much generality.

For this purpose, we will consider the propagation length  $L_{\text{SPP}}$  normalized to the SPP wavelength  $\lambda_{\text{SPP}} = 2\pi/\text{Re}\{k_x\}$  as a measure of the effect of losses on the SPP propagation. This normalized quantity bears strong resemblance to the quality factor of a resonator, as it specifies the number of optical cycles in which the intensity of the wave has decayed to  $1/e$  of its original value. It therefore defines an upper limit to the quality factor of a resonator based on a truncated waveguide. It will influence the sensitivity of sensors involving SPP waveguides, and will be related to the number of operations that can be performed in a plasmonic circuit before the signal needs to be regenerated.

To evaluate the transverse confinement, we consider a confinement factor  $\lambda_0/(\sqrt{\epsilon_d}\delta_z)$ , where  $\delta_z$  is the transverse size of the mode, which is compared to the wavelength in the dielectric ( $\lambda_0/\sqrt{\epsilon_d}$ ). We use an empirical definition of  $\delta_z$  as the difference between the values of  $z$  at which  $|\mathbf{H}|^2$  decays to  $1/e$  times its maximum value on either side of the waveguide.<sup>†</sup> For the symmetric MIM and IMI geometries,  $\delta_z$  is given by

$$\delta_z = d + 1/\text{Im}\{k_{z1}\}. \quad (1.25)$$

In Fig. 1.5(a) the relation between transverse confinement and normalized propagation length is shown for the symmetric mode in a Ag/air/Ag waveguide (full curves) and the antisymmetric mode in a air/Ag/air waveguide (dashed curves), for three different free-space wavelengths. Along each curve, the core thickness  $d$  is varied from 200 nm (large propagation length but small confinement) to 2 nm (strong confinement but short propagation length). The symbols denote the position of four specific thicknesses along the curves, to indicate the physical thickness  $d$  needed to obtain the plotted values of confinement and propagation length.

Figure 1.5(a) shows that a MIM geometry offers stronger normalized transverse confinement at larger normalized propagation lengths than an IMI geometry. The difference is largest for long wavelengths, as expected since the skin depth is rather constant with changing frequency. In a 2 nm thin air gap surrounded by Ag, the  $\mathbf{H}$  field intensity of 1550 nm light can be confined in a size more than 70 times smaller than the free-space wavelength, while it can still propagate 10 optical cycles before it decays. Similar relative confinement in an IMI slab can occur for comparable thicknesses of Ag at shorter wavelengths, but  $L_{\text{SPP}}$  then starts to approach  $\lambda_{\text{SPP}}$ .

<sup>†</sup>We do not define the transverse mode size in terms of the electromagnetic energy density, since a proper general definition of that quantity in dispersive media with high loss is lacking [40]

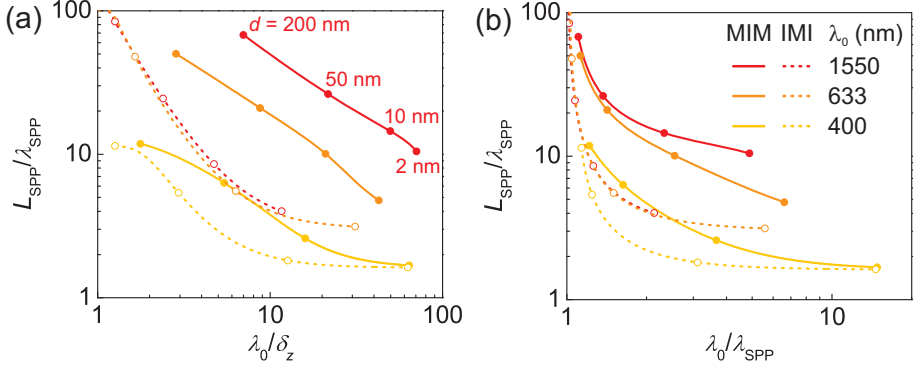


**Figure 1.5:** Trade-off between localization and loss in MIM (solid curves) and IMI (dashed curves) waveguides, for three different free-space wavelengths (1550, 633, and 400 nm) and core thicknesses varied from 200 nm down to 2 nm. (a) The relative SPP propagation length plotted against the transverse confinement factor for both types of geometries. For reference, the four symbols along each curve denote the results obtained for the core thicknesses of 200, 50, 10, and 2 nm. (b) Relative propagation length plotted against the longitudinal confinement factor for the same parameters as in (a). The curves for wavelengths of 400 and 633 nm overlap partially.

The possibility of confining the SPPs in the longitudinal  $x$  direction — by placing a waveguide of length  $\lambda_{\text{SPP}}/2$  between two mirrors, for example — is related to the magnitude of  $\text{Re}\{k_x\}$ . We therefore compare the normalized propagation length to the longitudinal confinement factor defined as  $\lambda_0/(\sqrt{\epsilon_d}\lambda_{\text{SPP}})$  in Fig. 1.5(b), for the same waveguide geometries as those depicted in Fig. 1.5(a).

Similar to transverse confinement, MIM waveguides offer stronger longitudinal confinement at longer propagation lengths, especially for large free-space wavelengths. The magnitude of  $\lambda_0/\lambda_{\text{SPP}}$  is significantly smaller than that of  $\lambda_0/\delta_z$  for the same waveguides. Unlike transverse confinement, the longitudinal confinement in MIM geometries is always larger for larger frequencies at a given waveguide thickness.

We note that for more complex waveguide geometries, that are not infinite in the  $y$  direction, the trade-off can be markedly different. As we will see in Chapter 6, a metal cylinder supports an antisymmetric mode that can become strongly confined for small cylinder radii. The responsible coupling mechanism is similar to that for the antisymmetric mode in IMI waveguides. The charges across the cylinder couple however more strongly than those on opposite sides of a metal slab, enabling significant confinement in all dimensions. In contrast, all propagating modes in the inverse geometry, i.e., a dielectric cylinder surrounded by metal, exhibit cutoff at a finite cylinder radius. For a further discussion on the trade-off between localization and loss in plasmonic waveguides, we refer to references [35, 41, 42].

### 1.3 Concentrating light with surface plasmon polaritons

The previous section has shown that certain plasmonic waveguide geometries can exhibit subwavelength transverse confinement of SPP modes while significantly shrinking the SPP wavelength with respect to the free-space wavelength. There are several strategies that incorporate such waveguide designs in three-dimensional structures to achieve three-dimensional nanoconcentration of light. Three of those concepts are schematically depicted in Fig. 1.6.

Firstly, one can gradually vary the size or shape of a waveguide along the direction of propagation, forming for example a laterally tapered metal waveguide on a dielectric substrate as sketched in Fig. 1.6(a). If the variation of the waveguide geometry is chosen properly, SPPs propagating along the waveguide can gradually transform to become more strongly confined as they approach the end of the taper. As a result, the field will be concentrated in a small volume at the taper apex [43].

Secondly, subwavelength concentration of light can be achieved in a slab of negative index material, depicted in Fig. 1.6(b). If a material has both negative permittivity and negative permeability, it must necessarily exhibit a negative refractive index [44]. A slab of such negative index material will work as a lens, concentrating the rays from an object on one side of the lens to a focus on the other side, as sketched in Fig. 1.6(b). Pendry realized in 2000 that such a lens would amplify the evanescent field of an object, reconstructing also the subwavelength details of the object field in the image plane, provided that the lens material has no absorption [45].

No materials in nature exhibit negative permeability at optical frequencies. The desired magnetic response can be obtained in metamaterials consisting of metal-

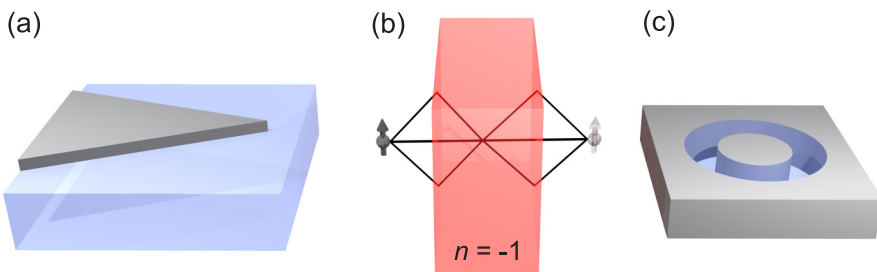


**Figure 1.6:** Three concepts to achieve subwavelength concentration of light using SPPs. (a) A tapered metal waveguide can squeeze SPPs into a subwavelength volume at the taper tip. (b) A slab of negative index material can serve as a perfect lens, focusing the field of a point source to a subwavelength spot on the other side of the slab. (c) A subwavelength annular aperture serves as a truncated SPP waveguide, exhibiting a localized resonance with the associated fields confined within the aperture.

lodielectric elements much smaller than the wavelength, which exhibit a magnetic resonance [46, 47]. With such designs, it has however proven challenging to obtain a negative index with low loss at high frequencies [48, 49]. Alternative two-dimensional designs are based on SPP waveguides that exhibit an effective refractive index  $n_{\text{eff}} = k_{\text{SPP}}/k_0$  that can be negative for some carefully chosen waveguide designs [50–54]. For a slab waveguide, those SPP modes enable negative refraction in the plane of the slab [51, 55]. In this way the two-dimensional analogue of the lens depicted in Fig. 1.6(b) can be made. By using coupling between waveguides in a stacked geometry, three-dimensional negative refraction at optical frequencies could be within reach.

Thirdly, truncated waveguides can act as resonators if a waveguided mode reflects at both ends of the waveguide. Resonant modes occur when

$$k_x L + \varphi_r = n\pi, \quad (1.26)$$

where  $L$  is the length of the waveguide and  $\varphi_r$  the phase change upon reflection at one of the waveguide terminations. This intuitive picture can explain the existence of Fabry-Pérot-type modes in a wide variety of plasmonic structures, including nanoantennas [56–58], narrow slits in a metal film [59–61], subwavelength apertures [62], metal strips [63] and MIM waveguides [64, 65].

A special case is encountered when  $k_x = 0$ , since (1.26) is then satisfied with  $n = 0$  for any length  $L$  (provided that  $\varphi_r$  is 0 or  $\pi$ ). Subwavelength apertures in a metal film can be interpreted as waveguides in the direction normal to the film surfaces. In that picture, the film surfaces act as the terminations of the truncated waveguide. Localized resonances occur at the cutoff frequency of a mode that propagates inside the apertures, since the wavevector of a mode approaches zero at the cutoff condition of the mode. These resonances assist large transmission of light through arrays of apertures in an otherwise opaque metal film. The cutoff-related transmission resonances occur in circular and rectangular apertures [66–70], and in annular apertures such as that depicted in Fig. 1.6(c) [71–75]. Because of the relevance of the latter geometry for Chapters 8 and 9, we will discuss the resonances in annular apertures in more detail.

### 1.3.1 Localized resonances in annular apertures

An annular aperture can be described as a finite-length coaxial waveguide with metal core and cladding. With the fields confined to the dielectric gap between the inner metal surface with radius  $R_i$  and the outer surface with radius  $R_o$ , this geometry bears strong resemblance to a MIM waveguide of thickness  $(R_o - R_i)$ . Because of the cylindrical symmetry, the waveguide modes will obey a  $e^{im\varphi}$  dependence on azimuth angle  $\varphi$ . Interpreting the waveguide as a ‘rolled’ MIM slab waveguide, the lowest order  $m = 1$  mode (i.e., the  $\text{TE}_{11}$  mode) will exhibit cutoff when the circumference  $2\pi \frac{1}{2}(R_o + R_i)$  is approximately equal to  $\lambda_{\text{SPP}}$ , where  $\lambda_{\text{SPP}}$  is the SPP wavelength in the MIM slab.

Under those conditions, the  $TE_{11}$  mode reflected back and forth between the top and bottom of the aperture will cause resonant constructive interference inside the aperture because the wavelength at cutoff is much longer than the length of the waveguide. The field associated with this resonance is localized within the subwavelength volume of the aperture. Because of its dipolar character, the  $m = 0$  mode will couple strongly to an incident plane wave. The localized resonance can thus cause field enhancement and subwavelength concentration of incident light inside the aperture.

This is illustrated in Fig. 1.7, which shows the results of a full-vectorial finite-difference time-domain (FDTD) calculation of the fields in coaxial apertures in a 100 nm thick Au film, illuminated with a plane wave under normal incidence from the air above the film [76]. The apertures, with  $R_i = 140$  nm and  $R_o = 245$  nm, are arranged in a hexagonal array with a periodicity of 903 nm. The substrate is  $SiO_2$ , and the apertures are also filled with  $SiO_2$  (see Chapter 9). The optical constants of Au are modeled by a Lorentz-Drude model that is fitted to the optical constants reported in ref. [26].

In Fig. 1.7(a), the transmittance through the array is seen to exhibit a pronounced maximum, accompanied by a minimum in reflection. The apparent resonance occurs as expected at a wavelength close to the predicted cutoff wavelength of 1900 nm, which we obtain by assuming that  $\lambda_{SPP} = \lambda_0 \sqrt{\epsilon_d}$ , as is

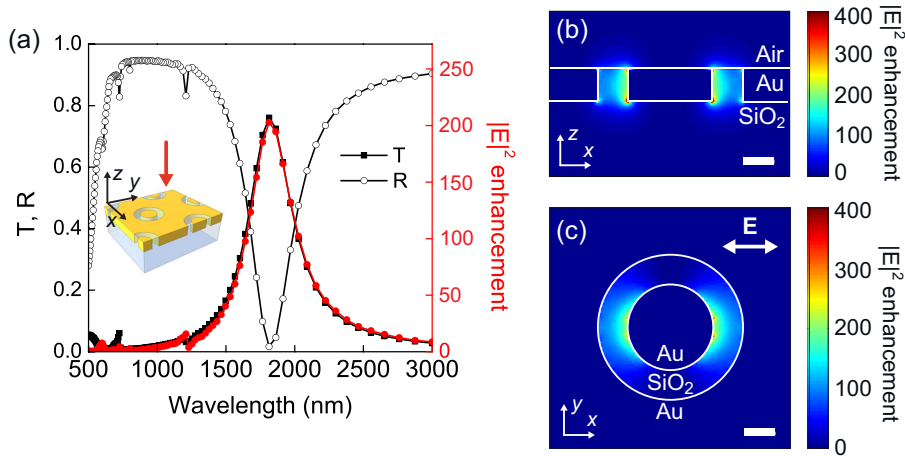


**Figure 1.7:** (a) Calculated transmittance (closed squares) and reflectance (open circles) of a hexagonal array of annular apertures in a Au film on  $SiO_2$ . Also plotted is the electric field intensity enhancement (red circles) in the  $SiO_2$  inside the aperture, at the inner Au surface at a depth of 50 nm below the top film surface. (b) Vertical crosscut of the intensity enhancement at the resonance wavelength, showing that the enhanced field is confined to the aperture. (c) Horizontal crosscut of the intensity enhancement, in a plane through the middle of the Au film. The incident beam is polarized along the  $x$  direction. The scale bars are 100 nm.

the case in a MIM waveguide with perfectly conducting metal. The red curve shows the enhancement of the electric field intensity with respect to that of the incident plane wave at a position inside the aperture on the inner metal surface in the SiO<sub>2</sub> halfway between the top and bottom surfaces. The electric field inside the aperture is enhanced by a factor 200 at resonance, and the spectral shape of the enhancement resembles that of the far-field transmission.

The distribution of the field intensity enhancement in the aperture is depicted in Figs. 1.7(b) and (c), plotted in horizontal and vertical planes intersecting a single aperture in the array. It is clear that the field is mostly confined within the aperture, which has a subwavelength physical volume of  $0.002 \times \lambda_0^3$ . The field exhibits a  $e^{i\varphi}$  dependence, as expected for the TE<sub>11</sub> mode. Close examination of the fields shows that no nodes are found in the vertical direction along the annular waveguide, in agreement with the fact that the SPP wavelength at cutoff is much larger than the aperture.

### 1.4 Probing the near field

Two factors make the experimental investigation of plasmonic field concentration at subwavelength scales a challenging task. First, because of the wavevector difference between SPPs on a metal surface and light in the bounding dielectric, SPP modes often do not radiate directly to the far field. Second, to demonstrate subwavelength concentration and to unravel the physics associated with it the system must be studied with subwavelength resolution, which is not achievable with a conventional far-field microscope.

Therefore, small probes need to be introduced in the near field of the metal surfaces, that convert the evanescent fields of SPPs to radiation that can be detected in the far field. Two approaches are used in this thesis. On the one hand, a metal-coated near-field microscope probe with a subwavelength aperture at its end can be brought in close proximity to a sample surface. It can scatter SPP fields to radiation inside the probe, which can be detected in the far field [77]. Conversely, it can be used as a subwavelength source of SPPs [78].

On the other hand, fluorescent emitters such as molecules, quantum dots, or rare earth ions can be placed in a dielectric host close to metal surfaces supporting SPPs. The emitters can absorb a small fraction of the SPP field and emit radiation to the far field. This can be collected in a microscope to serve as a measure of the local SPP intensity that is responsible for exciting the emitters [79, 80]. Although this method does not in principle yield subwavelength resolution, the imaging resolution can be improved by making use of anti-Stokes processes in the emitters, such as cooperative upconversion in erbium ions. In that way the SPP fields can be probed using emission at a wavelength that is shorter than that with which the SPPs are excited, yielding a resolution better than the diffraction limit at the excitation wavelength.

## 1.5 Outline of this thesis

This thesis describes experiments and calculations that aim to demonstrate and understand the nanoconcentration of light using surface plasmon polaritons in a variety of nanostructures, employing the concepts outlined in the preceding sections.

In Chapter 2 we probe highly confined SPPs in a MIM waveguide with a 50 nm thin dielectric core, exciting them with the fields from a near-field aperture that tunnel through a thinned metal cladding. By using SPP interference, the MIM dispersion curve is mapped.

Chapter 3 provides a theoretical study of plasmon modes in different slab waveguides; MIM and IMI geometries as well as a thin dielectric film on metal, i.e., an insulator-insulator-metal (IIM) geometry. Above the surface plasmon resonance frequency, such waveguides support modes that can be described by an effective negative refractive index. We discuss their basic properties and possible figures of merit, and show in a simulation that they can enable negative refraction of light into such a waveguide.

Chapter 4 demonstrates the enhancement of upconversion of infrared to visible radiation in erbium ions due to SPP concentration in a tapered Ag waveguide. It introduces the concept of upconversion luminescence imaging to probe infrared SPP fields at high resolution.

In Chapter 5, the focusing of near-infrared SPPs in laterally tapered Au stripe waveguides is studied. Upconversion luminescence imaging reveals that SPPs concentrate at the taper tip without a sign of waveguide cutoff. Full-field simulations support the conclusion that these structures can achieve subwavelength nanofocusing, and show the importance of the symmetry of the dielectric surrounding.

Chapter 6 presents near-field experiments that demonstrate the adiabatic conversion of a SPP mode with a broad ‘macroscopic’ mode profile to a highly confined nanowire mode in a tapered waveguide. The modes in the waveguide are identified and related to those in cylindrical waveguides. Phase- and polarization-resolved microscopy reveals the nature of the mode that propagates along nanowires with diameters as small as 60 nm. The efficiency of the transformation process is measured to be of the order of 50%.

Chapter 7 introduces a new design that allows nanofocusing of SPPs. It is theoretically shown that SPPs propagating on a dielectric wedge on a Ag substrate are brought to a subwavelength focus at a particular thickness of the wedge. An analytical adiabatic model that explains the focusing mechanism is compared to full-field simulations.

In Chapter 8, Er upconversion luminescence is used to probe the plasmonic field enhancement in arrays of subwavelength apertures. The conversion of 1.5  $\mu\text{m}$  light to 980 nm upconversion emission is shown to be up to 450 times enhanced on arrays of square apertures. The relation between near-field enhancement and far-field optical transmission is explained by a Fano model. The field enhancement due to the localized resonance in annular apertures is shown to be independent of

the incident angle.

Chapter 9 demonstrates the modification of the emission rate of Er ions selectively placed inside annular apertures. When the resonance frequency of the annular apertures is tuned to the Er transition wavelength at  $1.54 \mu\text{m}$ , both the photoluminescence intensity and decay rate are enhanced.

Finally, Chapter 10 discusses several possible applications of the work described in this thesis, in integrated optics, photovoltaics, sensing, and metamaterials.



# 2

---

## Near-field probing of surface plasmon polaritons in metal-insulator-metal waveguides

*A nanoscale gap between two metal surfaces can confine propagating surface plasmon polaritons (SPPs) to very small dimensions, but this geometry makes it inherently difficult to image SPP propagation at high resolution. We demonstrate the near-field probing of these SPPs, propagating within a 50 nm thick  $\text{Si}_3\text{N}_4$  waveguide with Ag cladding layers for frequencies ranging from the blue to the near-infrared. Using near-field SPP interferometry, we determine the wavevector, showing that the wavelength is shortened to values as small as 156 nm for a free-space wavelength of 532 nm.*

### 2.1 Introduction

In dielectric media, the diffraction limit sets a lower bound to the size within which guided waves can be confined. This limit can be significantly reduced using surface plasmon polaritons. The SPP wavelength is shorter than that of light, and modal fields are confined close to the metal surface. These effects are particularly strong for SPPs guided in a nanosized dielectric gap between two metals [34–36]. Such a metal-insulator-metal (MIM) geometry serves as a plasmonic slot waveguide, ‘squeezing’ the SPP field into the dielectric core. As a result, the wavelength along the direction of propagation is shortened significantly. MIM-SPPs can therefore be guided in waveguides with very small transverse dimensions [65, 81] and

allow the realization of nanocavities with extremely small mode volumes [64, 82]. In comparison to other SPP guiding geometries, the cost of extra losses that are linked to the increase in confinement is relatively low [35, 36, 41]. MIM-SPPs are responsible for the resonances in slits in metal films that lead to large field enhancements and large resonant transmission [59] and are closely related to SPPs guided along grooves and slits in metal films [83, 84].

In order to develop new nanostructured components that control the propagation of these waves, it is crucial to image their fields at the highest possible resolution and to study their propagation properties. It is therefore important to gain direct access to the near field of these modes. However, such imaging is inherently difficult because of the presence of the metal cladding. So far, experiments have been limited to spectral analysis of the far-field reflection and transmission of finite length waveguides and cavities [64, 65].

In this chapter, we present the near-field imaging and quantitative analysis of MIM-SPPs. By reducing the thickness of one of the metallic cladding layers of the slot waveguide, tunneling of light from a near-field probe to the highly confined SPP mode is demonstrated without negatively affecting the interesting properties associated with these waves. With the light scattered from subwavelength slits, interferometric measurements are performed that provide accurate in situ determination of the wavevector of SPP modes guided either in the MIM slot or in the air outside the sample. Excellent correspondence with calculated dispersion is obtained for frequencies ranging from the blue to the near-infrared. The smallest observed MIM-SPP wavelength is 156 nm, measured at a free-space wavelength of 532 nm.

## 2.2 Methods

### 2.2.1 Sample fabrication

The sample consists of a 50 nm thick suspended  $\text{Si}_3\text{N}_4$  membrane, coated on both sides with Ag by thermal evaporation. This design results in small interface roughness determined by the smoothness of the  $\text{Si}_3\text{N}_4$ , which limits scattering losses. The Ag thickness on the front side of the sample is only 35 nm to allow for sufficient near-field coupling of a probe outside the sample to the dielectric core of the waveguide. The Ag film on the back of the membrane is 310 nm thick. Slits with widths smaller than 100 nm and lengths of 5  $\mu\text{m}$  are made in the back Ag film by focused ion beam milling. Care is taken to stop the milling once the  $\text{Si}_3\text{N}_4$  layer was exposed. Both single slits and pairs of parallel slits with various separations are fabricated. Figure 2.1 shows scanning electron microscopy (SEM) images of a typical structure with two slits spaced 1  $\mu\text{m}$  apart, viewed in cross section (a) and from the back side (b).

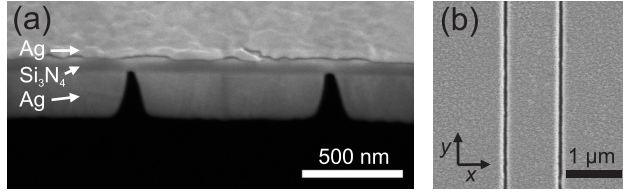


**Figure 2.1:** SEM micrographs of the fabricated waveguide, shown in cross-section (a) and as viewed from the bottom (b). The waveguide consists of 50 nm of  $\text{Si}_3\text{N}_4$  clad with 35 nm Ag on the top and 310 nm Ag on the bottom.

### 2.2.2 Near-field experiments

A sketch of the experimental geometry is shown in Figure 2.2(a). The near-field probe is a hollow Al pyramid on a Si cantilever, with a probe aperture that has a diameter smaller than 100 nm (WITec GmbH). The thickness of the Al sidewalls of the probe is  $\sim 250$  nm. Light from various laser sources is coupled in through the probe, which is brought into contact with the sample. The probe acts as a local SPP excitation source. The slits serve to scatter SPPs to the far field at the back side of the sample. The scattered radiation is collected by a  $50\times$  microscope objective (NA = 0.7) and focused on a  $100\ \mu\text{m}$  core diameter multimode optical fiber that is led to an APD detector. Two-dimensional near-field images are obtained by scanning the probe with respect to the sample while monitoring the output from one or two fixed exit slits.

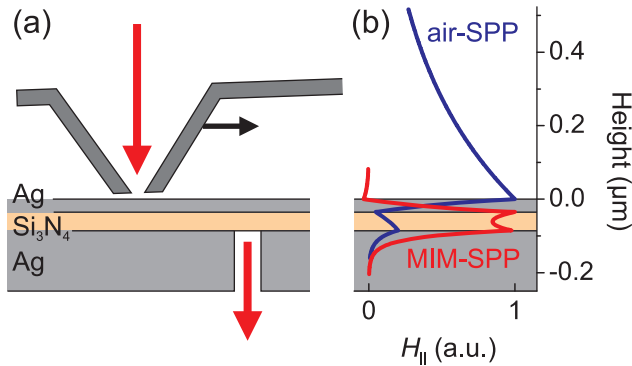


**Figure 2.2:** (a) Schematic depiction of the measurement geometry. Laser light is incident through the aperture of an Al near-field probe, which is scanned with respect to the sample. Light transported through the MIM waveguide is collected after scattering from subwavelength slits in the back Ag film. (b)  $H$  field mode profiles of the two waveguided SPP modes supported by the multilayer stack.

### 2.2.3 Polarization dependence of probe emission

In general the light emitted by the probe has a high degree of polarization due to its geometry, the incident polarization, or a combination of both [78, 85]. In Fig. 2.3(a), the polarization dependence of light emitted by a typical probe into the far-field is depicted. The polarized character of the far-field emission, evident from the two lobes in Fig. 2.3(a), is consistent with the near-field image obtained with the same probe shown in Fig. 2.3(b). This image was obtained by scanning the probe over a circular slit with a width of 100 nm in a 200 nm thick Ag film on a glass substrate, while collecting the light through the substrate (see Fig. 2.3(c)). Since a subwavelength slit can only transmit TM-polarized waves efficiently, it effectively acts as an analyzer in the near field of the probe. A strong polarization dependence is observed in Fig. 2.3, with a polarization direction that is in agreement with the far-field polarization of this particular probe shown in Fig. 2.3(a). This dependence is attributed to the polarization of the incident light in combination with a slight ellipticity of the probe aperture. The incident polarization was rotated such that the transmittance through the probe is maximal. The polarized nature of the probe emission in the near field means that it acts as a directional source of SPPs [78]. Throughout the measurements, the sample orientation is kept such that the slits are oriented normal to the dominant direction of SPP excitation.

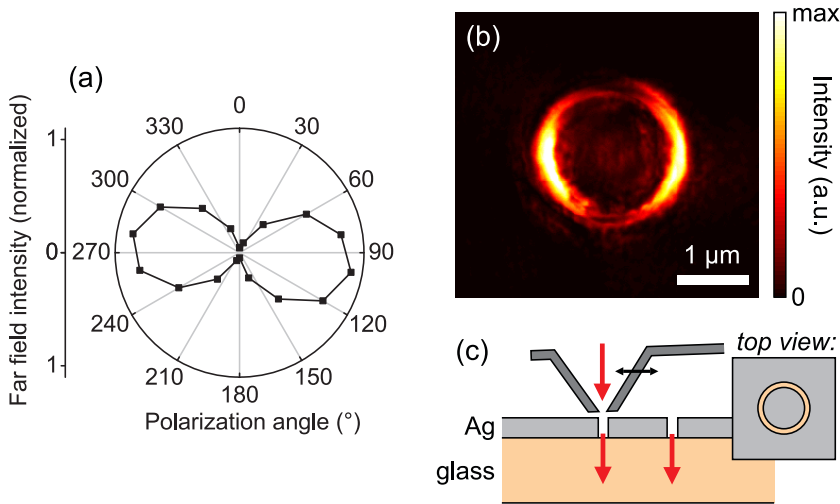


**Figure 2.3:** (a) Typical polarization dependence of the far-field emission of a probe that is illuminated with 640 nm light. (b) Near-field image obtained by scanning the same probe on a circular slit in a 200 nm thick Ag film on a glass substrate. Light ( $\lambda = 640$  nm) transmitted through the slit is collected through the substrate. (c) Schematic depiction of the measurement geometry used to obtain image (b).

## 2.3 Single output slit: Interference of different SPP modes

Figure 2.4(a) shows a near-field intensity image taken with 638 nm excitation light with a single output slit. The slit is located in the middle of the scan area and oriented in the vertical direction. Three observations can be readily made. First, the signal is highly modulated. The period of the modulation is determined to be 300 nm. In similar measurements on metal films without a MIM structure such modulations were not observed [86, 87]. Second, the signal decays as the excitation source is moved away from the output slit. Third, the image is clearly asymmetric with respect to the slit, which at first sight appears surprising given the symmetry of the measurement geometry. As we will show, this asymmetry can be ascribed to a small asymmetry in the shape of the near-field probe.

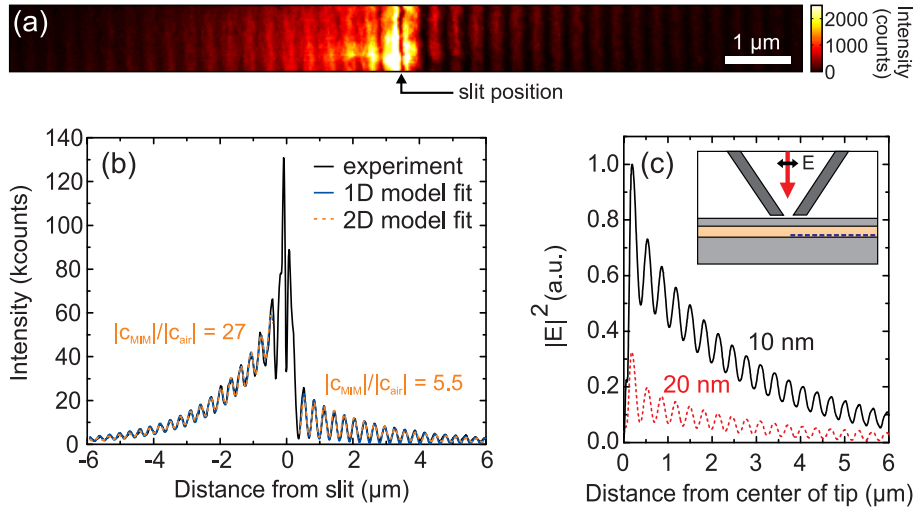


**Figure 2.4:** (a) Near-field image obtained by scanning the excitation probe position over the sample containing a single output slit. The excitation wavelength is 638 nm. (b) Collected intensity in Fig. 2.4(a) as a function of probe-slit distance (black curve), and a fit to the data of the one- and two-dimensional models described in the text (blue and orange curves, respectively). The ratio of the amplitudes of both modes in the 2D model is indicated. (c) Simulated electric field intensity in the  $\text{Si}_3\text{N}_4$  film as a function of distance from the center of the probe. The inset shows a schematic of the simulated two-dimensional geometry. The dashed blue line indicates the position at which the calculated intensity is plotted. The probe-sample separation is 10 nm (black) or 20 nm (red).

### 2.3.1 One-dimensional interference model

To explain the signal modulation and decay, we develop the following model. In the sample geometry that includes the thinned Ag cladding layer, two waveguided SPP modes can propagate. These modes arise from the coupling of SPPs on the three metal/dielectric interfaces: the MIM-SPP mode localized predominantly in the  $\text{Si}_3\text{N}_4$  layer, and a mode that resides mostly in the air outside the sample (termed “air-SPP” from here on). Figure 2.2(b) shows the  $H$  field profiles of both modes at a free-space wavelength of 638 nm, calculated with the method described in section 1.2.1. The optical constants of Ag are taken from ref. [26]. Judging from the mode profiles, both modes can be excited by the near-field probe, albeit with different excitation probabilities. Both modes also have a fraction of their energy inside the  $\text{Si}_3\text{N}_4$  layer, so that they can be scattered by the subwavelength slit to the detector. Because the two modes have a clearly different wavevector, their interference at the output slit will produce the oscillating pattern with varying probe-slit distance that is seen in Fig. 2.4(a). As a first approximation, the field at the slit as a function of probe distance  $x$  can be described in a one-dimensional scalar model as  $E(x) = c_{\text{air}} e^{i k_{\text{air}} x} + c_{\text{MIM}} e^{i k_{\text{MIM}} x}$ , where  $k_{\text{air}}$  and  $k_{\text{MIM}}$  are the complex wavevectors  $k = k' + i k''$  of the air-SPP and MIM-SPP modes, respectively. The complex coefficients  $c_{\text{air}}$  and  $c_{\text{MIM}}$  include the amplitude and phase with which each mode is excited. They represent the mode amplitude and phase at the depth of the output slit that scatters the light to the detector. The intensity at the slit then becomes

$$I(x) = |c_{\text{air}}|^2 e^{-2k''_{\text{air}} x} + |c_{\text{MIM}}|^2 e^{-2k''_{\text{MIM}} x} + 2|c_{\text{air}}||c_{\text{MIM}}| e^{-(k''_{\text{air}} + k''_{\text{MIM}})x} \cos[(k'_{\text{MIM}} - k'_{\text{air}})x + \Delta\varphi], \quad (2.1)$$

where  $\Delta\varphi = \arg(c_{\text{MIM}} c_{\text{air}}^*)$  is the phase difference with which the two modes are excited by the probe.

Figure 2.4(b) shows the intensity as a function of distance from the slit, obtained by integrating the intensity in Fig. 2.4(a) along the vertical direction. The blue curve is a least-squares fit of (2.1) to the data, where the coefficients  $|c_{\text{air}}|$  and  $|c_{\text{MIM}}|$  and the phase difference  $\Delta\varphi$  were allowed to differ on either side of the slit. The data within a distance of 250 nm from the slit were not fit, since directly under the probe the field can obviously not be described sufficiently in terms of two waveguided SPP modes only. Figure 2.4(b) shows that the model fits the data well. The oscillatory behavior is reproduced very well, and the decay with distance is identical on each side.

### 2.3.2 Excitation asymmetry

The asymmetry in the magnitude of the signal on either side of the slit is the result of a difference between the amplitude coefficients at either side of the slit. To understand how the excitability of the modes at opposite sides of the slits can be so different, we perform finite-difference time-domain (FDTD) simulations of the

experimental geometry [76]. The geometry of the calculation is sketched in the inset of Fig. 2.4(c). The structure is modeled to be invariant in one dimension. The mesh size is 1 nm in the vicinity of the sample and 3 nm further away from it. A p-polarized Gaussian beam with a free-space wavelength of 638 nm is incident through the probe. The output slit is absent in the simulations. The calculated electric field intensity at the bottom side of the Si<sub>3</sub>N<sub>4</sub> layer is plotted in Fig. 2.4(c) for two different separation heights between the probe and the sample. Assuming that the slit acts as a point scatterer, the intensity in this plane can be directly related to the measured signal collected through the slit.

The calculations reveal interference patterns with a period and decay similar to the experiment in Fig. 2.4(b). For the 10 nm probe-to-sample separation, the overall intensity is larger and the visibility of the fringes is smaller than those for the 20 nm probe-to-sample separation. For small separations, the Al sidewalls hinder the excitation of the air-SPP [78]. On the other hand, more power is coupled into the MIM-SPP when the distance between probe and sample is reduced. Although during the experiment the probe is in contact with the sample surface, small imperfections in the probe can easily result in different local separations between probe and sample at different sides of the probe. As a result, the asymmetries observed in Fig. 2.4(b) for the interference pattern on either side of the slit can be ascribed to a small asymmetry in the probe shape. Indeed, when experiments are performed with different probes on the same sample, different asymmetries are observed that can be explained by changed coefficients  $c_{\text{MIM}}$  and  $c_{\text{air}}$  at both sides of the slit.

By fitting (2.1) to the data, the difference of the real part of the wavevectors of the two SPP modes is obtained. From the fit we find  $\Delta k' = (k'_{\text{MIM}} - k'_{\text{air}}) = 20.69 \mu\text{m}^{-1}$ .

### 2.3.3 Two-dimensional interference model

This simple one-dimensional model ignores the fact that SPP waves excited by the near-field probe will diverge on the two-dimensional sample surface and that SPPs emitted in different directions travel different distances to the output slit. For this reason, it may be important to consider the resultant field distribution along the length of the slit and the way this distribution is imaged on the detector. To account for the SPP divergence, we construct a two-dimensional model that assumes the probe acts as a polarized point source of SPPs as mentioned above, emitting a field

$$E(r, \theta) = \left( c_{\text{air}} e^{ik_{\text{air}}r} + c_{\text{MIM}} e^{ik_{\text{MIM}}r} \right) \frac{\cos \theta}{r^{1/2}} \quad (2.2)$$

where  $r$  is the distance to the probe and  $\theta$  is the angle with respect to the normal of the output slit. To predict the detected intensity as a function of the distance  $x$  between probe and slit, the field distribution along the slit is obtained from (2.2). A scalar amplitude point spread function is subsequently used to calculate the field in the image plane of the microscope, and the intensity in this plane is integrated over the area of the fiber core. A resulting fit of this two-dimensional model to the data is shown in Fig. 2.4(b) as an orange dashed curve. This model also fits the

data well, yielding  $\Delta k' = 20.43 \mu\text{m}^{-1}$ . The fitted propagation length  $L = 1/(2k'')$  of the MIM-SPP mode is  $1.4 \mu\text{m}$ , which is smaller than the value of  $2.6 \mu\text{m}$  obtained from the mode calculation. We ascribe this discrepancy to a deviation of the actual optical constants to those used in the calculation and additional scattering losses. The fact that the obtained value of  $\Delta k'$  for the one-dimensional model is so close to that obtained with the two-dimensional model shows that a fit of the simple one-dimensional model to the data already yields accurate estimations of the real part of the wavevector. Nevertheless, in the remainder of the analysis, the more accurate two-dimensional model is used.

## 2.4 Double output slits: interference of MIM-SPPs

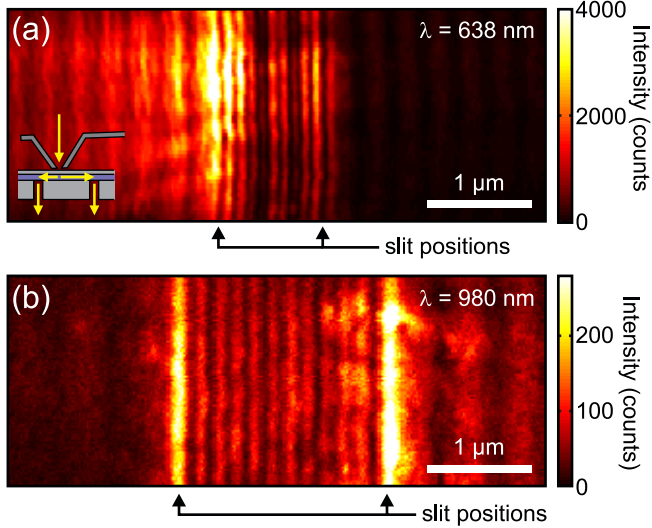
To determine absolute values of the wavelengths of both SPP modes in addition to the differential wavevector magnitude  $\Delta k'$ , we performed experiments on pairs of aligned slits separated by micrometer-scale distances. The collection objective is positioned such that light from both slits is collected simultaneously. When the probe is scanned outside both slits, a similar interference pattern is expected as for the single slit. However, for a probe position between the two slits, a different interference mechanism is expected to come into play, depicted in the inset of Fig. 2.5(a). Because the light originating from the two slits will interfere on the detection fiber, a change of the relative phase of the field at the two slits will alter the detected intensity. MIM-SPP waves excited between the slits in opposite directions will arrive at the two slits with a relative phase difference that depends on the position of the excitation source. Because the difference between the two path lengths scales linearly with twice the distance to one of the slits, an interference pattern with a period of half the MIM-SPP wavelength should appear as the probe scans between the slits. The double-slit geometry also produces a pattern with a period of half the air-SPP wavelength. The single slit experiments showed that the contribution of MIM-SPPs to the output signal is larger than that of air-SPPs. Accordingly, the pattern due to MIM-SPP interference can be discerned with respect to the air-SPP pattern, provided that the slit separation is not much larger than the MIM-SPP propagation length.

Figure 2.5(a) shows the measured near-field image for 638 nm excitation wavelength and a slit separation of  $1 \mu\text{m}$ . Between the slits an oscillatory pattern with a period of 102 nm is observed. This interference pattern is superimposed on the pattern that was also observed for the single slit and that is also present outside the pair of slits.

### 2.4.1 MIM-SPP dispersion relation

Experiments for single slits and pairs of slits are repeated for various excitation wavelengths between 458 and 980 nm. Figure 2.5(b) shows an image taken with a pair of slits with a separation of  $2 \mu\text{m}$  taken at 980 nm. Clearly an interference





**Figure 2.5:** (a) Near-field image obtained by scanning the excitation probe position over the sample containing a pair of output slits separated by  $1 \mu\text{m}$ . Excitation wavelength is  $638$  nm. The inset shows the interference mechanism leading to the fast spatial intensity oscillations between the slit. (b) Near-field image as in (a), but for an excitation wavelength of  $980$  nm and a slit separation of  $2 \mu\text{m}$ .

pattern is again observed between the slits, with a larger period than that shown in Fig. 2.5(a). Because the interference patterns for single slit and double slit experiments provide independent measurements of  $k'_{\text{MIM}}$  and  $\Delta k'$  at each frequency, we can construct dispersion curves for both the MIM-SPP and the air-SPP modes. The results are plotted in Fig. 2.6. The dispersion of light in air and in  $\text{Si}_3\text{N}_4$  is plotted for reference (dashed lines). For an excitation wavelength of  $532$  nm, the measured MIM-SPP wavelength is  $156$  nm, corresponding to a wavevector that is  $1.7$  times larger than that of light in  $\text{Si}_3\text{N}_4$ . In stark contrast, the dispersion of the air-SPP mode follows the light line in air closely.

The solid curves are the calculated dispersion curves for both modes in the multilayer waveguide geometry. The experimentally determined wavevectors show excellent agreement with these calculations. For wavelengths shorter than  $532$  nm, it was not possible to accurately determine the value of  $k'_{\text{MIM}}$  independently, because of limited spatial resolution. For these excitation wavelengths, bars are plotted that show the measured magnitude of  $\Delta k'$ , which corresponds well with calculations up to the shortest wavelength of  $456$  nm used in the experiment. These measurements show that the MIM-SPP mode can be probed with the near-field method throughout the visible and near-infrared frequency regimes. The propagation lengths are of the order of micrometers — long enough to perform interferometric measurements of wavevector differences.

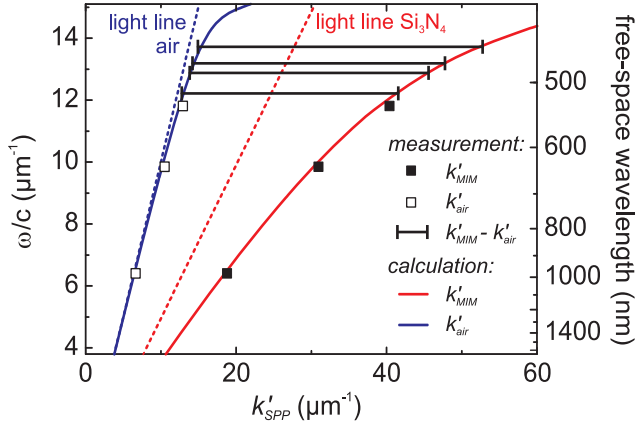


**Figure 2.6:** Dispersion relations of the two SPP modes that are supported by the system. Closed and open symbols indicate the measured values of  $k'_{MIM}$  and  $k'_{air}$ , respectively. The length of the horizontal bars at high frequencies is equal to the experimentally-determined values of  $\Delta k'$ . The solid blue and red lines are the calculated dispersion curves for the air- and MIM-SPP modes, respectively.

## 2.5 Conclusions

In conclusion, we have demonstrated the direct imaging of MIM-SPPs with sub-wavelength resolution using a near-field probe, despite the buried nature of these highly confined waves. Interference of MIM-SPPs with air-SPP modes allows the determination of the local wavevector and provides insight into the relative excitation efficiency of both modes. Accurate knowledge of MIM-SPP wavevectors and dispersion is essential for the development of subwavelength components and devices based on MIM geometries. The work presented in this chapter provides the means to investigate such nanostructures in detail.

# 3

---

## Negative index of refraction in surface plasmon polariton waveguides

*We present a theoretical analysis of planar plasmonic waveguides that support propagation of positive and negative index modes. Particular attention is given to the modes sustained by metal-insulator-metal (MIM), insulator-metal-insulator (IMI), and insulator-insulator-metal (IIM) geometries at visible and near-infrared frequencies. All three plasmonic structures are characterized by negative indices over a finite range of visible frequencies, with figures of merit approaching 20. Using finite-difference time-domain simulations, we demonstrate that visible-wavelength light propagating from free space into these waveguides can exhibit negative refraction. Refractive index, figure-of-merit and propagation length calculations are presented for Ag/GaP- and Ag/Si<sub>3</sub>N<sub>4</sub>-based structures with waveguide core dimensions ranging from 5 to 50 nm and excitation wavelengths ranging from 350 nm to 850 nm.*

### 3.1 Introduction

The interaction of light with matter is almost exclusively determined by the electric permittivity  $\epsilon$  and magnetic permeability  $\mu$ , two intrinsic material properties that describe the response of charges and currents to an applied electromagnetic field. At optical frequencies, both the permittivity and the permeability of all transparent

natural materials are positive, leading to a positive index of refraction. However, if the sign and magnitude of the index could be tuned at will, the flow of light could be controlled in unprecedented ways [88, 89]. Among the many unusual applications of index tunability are sub-diffraction-limited superlenses [45, 90–92], optical nanocircuits [93], and cloaks to render objects invisible [94, 95].

In recent years, metamaterials have received considerable attention for their ability to precisely control the dispersion and propagation of light. These engineered materials are generally composed of subwavelength resonators — such as metallic coils or rods — that serve as ‘artificial’ atoms of the material [47, 50, 96]. Considered as a bulk material, these metamaterials will exhibit properties altogether distinct from their constituent resonator elements. Through variation of the resonator materials or dimensions, metamaterials allow for refractive index tunability that can span positive, negative, and near-zero indices. Resonator-based metamaterials have been shown to effectively cloak two-dimensional objects at microwave frequencies [94], and have exhibited negative refraction at infrared frequencies [97].

#### 3.1.1 Surface plasmon waveguide-based metamaterials

Apart from resonator-based metamaterials, surface-plasmon-based geometries have also been shown to exhibit broad index tunability (see Chapter 2 and ref. [64]). Unlike traditional metamaterials, these geometries consist of planar waveguides with alternating layers of metals and dielectrics. Light propagates through the structure via one or more surface plasmon waves, which are characterized by group and phase velocities distinct from the incident light. If the waveguide is characterized by only a single propagating mode, light will emerge from the structure as if it had passed through a material with an index equal to the mode index. Such plasmon-based geometries have the potential to exhibit the same response as resonator-based metamaterials [50–54], without the necessity of patterning discrete resonator elements. Of course, single slab waveguides will exhibit an anisotropic response, restricting guided wave propagation to two dimensions. This characteristic renders planar waveguides particularly useful for on-chip applications, where optical components are interconnected in-plane. However, plasmonic waveguides can also potentially serve as basic elements of fully three-dimensional metamaterials, when arranged in stacked geometries [52, 98].

Experimentally, negative refraction at visible frequencies has been directly observed in metal-insulator-metal (MIM) surface plasmon waveguides [99]. In addition, superlensing has been reported for plasmonic waveguides coated with a thin insulating layer (an insulator-insulator-metal, or IIM geometry) [100]. Still, debate remains as to whether these structures exhibit the requisite condition of negative index materials: namely, light propagation characterized by oppositely-oriented phase and energy velocities. Moreover, the attainable mode indices and propagation lengths, as well as constraints on geometrical parameters, remain largely

unexplored.

In this chapter, we theoretically investigate the range of negative and positive indices accessible in these surface plasmon waveguides, including calculations of dispersion and absorption. Attention is given to the modes of MIM, IIM, and insulator-metal-insulator (IMI) waveguides. Our analysis considers both Ag/Si<sub>3</sub>N<sub>4</sub>- and Ag/GaP-based geometries, to compare the effect of different insulator permittivities. By carefully exploring the magnitude and sign of complex wavevectors accessible in these structures, we explicitly determine their utility as negative index materials. Our analytic results are confirmed with finite difference time domain simulations that directly demonstrate the refraction of free-space waves into these plasmonic materials. In addition, our analysis provides detailed maps of plasmonic indices, figures of merit and propagation lengths as a function of wavelength and geometry. Such maps serve as a “guide to the experimentalist” in designing future plasmon-based negative index materials and transformation-based (i.e., index-tuned) optical elements.

### 3.2 Theoretical formalism

In conventional materials, the complex refractive index can be derived from knowledge of the wavelength and absorption of light in the material. Surface-plasmon-based geometries are no exception. The plasmon wavevector  $k_x$  can be used to uniquely determine the complex refractive index of waves traveling along a direction  $x$  parallel to a metallodielectric interface. A dispersion relation relates the wavevector  $k_x$  and frequency  $\omega$ , which are both in general complex quantities [101]. However, in the context of monochromatic excitation of a waveguided mode, it is sensible to impose the frequency to be real [25]. The complex wavevector then describes spatial propagation and decay of the surface plasmon wave along the waveguide. This mode's wavelength  $\lambda_{\text{SPP}}$  and index  $n$  are related to the magnitude of the real component of  $k_x$  via

$$\lambda_{\text{SPP}} = \frac{2\pi}{|\text{Re}\{k_x\}|}, \quad (3.1)$$

$$n = \frac{c\text{Re}\{k_x\}}{\omega}. \quad (3.2)$$

The extinction of the wave can be extracted from the magnitude of the imaginary component of  $k_x$ , with mode propagation lengths  $L_{\text{SPP}}$  given by

$$L_{\text{SPP}} = \frac{1}{2\text{Im}\{k_x\}}. \quad (3.3)$$

Solving Maxwell's equations subject to continuity of the tangential electric and magnetic fields yields the wavevector, as described in section 1.2.1.

It is well known that light propagation in isotropic negative index materials is characterized by antiparallel phase and energy flow [44]. For all propagating

plane waves (with  $\text{Re}\{k_x\} \neq 0$ ), the phase velocity is defined by  $v_p = \omega/\text{Re}\{k_x\}$ . In the absence of losses and high dispersion, the energy velocity  $v_E$  is equal to the group velocity  $v_g = d\omega/dk_x$ . Therefore, for lossless materials, negative indices will manifest themselves by a region of negative slope on a plot of  $\omega$  versus  $|k_x|$ .

Figure 3.1 plots the dispersion relationships  $\omega$  versus  $|\text{Re}\{k_x\}|$  for lossless MIM, IIM, and IMI geometries with Ag as the metallic layer and GaP as the dielectric. Here, the Ag is described by a lossless Drude model with a bulk plasma frequency  $\hbar\omega = 9.01$  eV. The index of GaP is taken as 3.31. For reference, the surface plasmon resonance frequency is shown as a dotted line. In Fig. 3.1(a), 50 nm of GaP is surrounded by two semi-infinite layers of Ag. As seen, the dispersion curve of this MIM geometry is characterized by three distinct bands, including a region of negative slope between the bulk and surface plasmon frequencies and regions of positive slope below the surface plasmon resonance and above the bulk plasma resonance. Note that these three bands correspond to two different modes with varying magnetic field distributions across the waveguide. Below the surface plasmon resonance,  $H_y = B_y/\mu$  is symmetric across the waveguide (light gray branch). The wavevectors of this mode are purely real below the surface plasmon resonance, but become purely imaginary for frequencies between the bulk and surface plasmon resonance frequencies. In contrast,  $H_y$  is antisymmetric throughout the regime of negative slope (dark gray branch). Interestingly, the wavevectors of this antisymmetric mode become purely imaginary for frequencies below the surface plasmon resonance. Thus, the MIM mode allowed to propagate in the traditional surface plasmon bandgap (between the bulk and surface plasmon resonant frequencies) has a field distribution altogether distinct from the propagating plasmon mode below resonance.

As seen in Fig. 3.1(a), each input frequency is assigned to a unique MIM wavevector throughout the entire  $k$ -space domain. Therefore, for a given excitation wavelength, this lossless MIM geometry will be characterized by a single propagating mode. Provided excitation wavelengths are between the bulk and surface plasmon resonance frequencies, the plasmon mode will exhibit a negative index, rendering the entire MIM composite an effective negative index material. Note that as the thickness of the dielectric is increased, the cutoff frequency of the  $H_y$  field antisymmetric mode (i.e., the frequency for which  $k_x = 0$ ) shifts to lower frequencies. Above a critical thickness this cutoff frequency becomes smaller than the surface plasmon resonance frequency and the band acquires a positive energy velocity, since it will still asymptotically approach the surface plasmon resonance frequency for large values of  $k_x$ . Therefore, propagating modes with a negative index only exist in MIM waveguides with a core thickness smaller than the critical thickness.

Like the lossless MIM geometry, IIM and IMI waveguides can also be characterized by regions of negative slope, and hence negative indices. For example, Fig. 3.1(b) plots the dispersion relationship for the bound modes of a semi-infinite layer of Ag coated with a thin, 20 nm thick layer of GaP. As seen, this geometry is characterized by a single continuous bound mode that exists for frequencies both

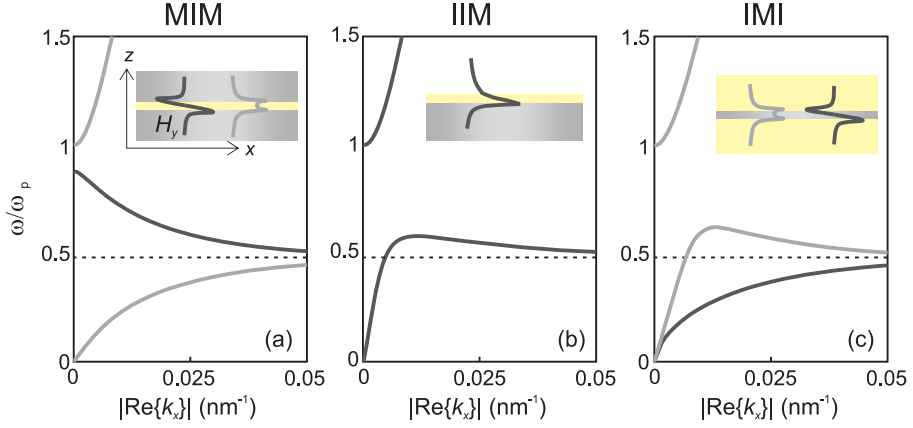


**Figure 3.1:** Lossless dispersion for three plasmon geometries: (a) a MIM waveguide composed of 50 nm GaP clad by Ag; (b) an IIM waveguide composed of a semi-infinite Ag film coated with 20 nm GaP; and (c) an IMI waveguide composed of 50 nm Ag clad by GaP. The dotted line indicates  $\omega_{SP}$ . Insets show the waveguide geometry and the associated  $H_y$  mode profiles for both the symmetric mode (light gray) and the antisymmetric mode (dark gray). Notice that all three geometries are characterized by regions of negative slope and hence negative indices. However, this negative index frequency regime is single valued in  $k_x$  for the MIM geometry only.

below and above the surface plasmon resonance. Its dispersion follows that of surface plasmons at a single Ag/air interface for low frequencies and wavevectors, but as a larger fraction of the field is contained in the GaP for higher frequencies, the wavevector diverges at the Ag/GaP surface plasmon resonance. For frequencies above the surface plasmon resonance, this mode can exhibit negative slope, corresponding to oppositely-oriented group and phase velocities. Note, however, that this geometry is not characterized by a unique wavevector assignment at each frequency. Above the surface plasmon resonance, for example, this lossless IIM geometry is characterized by two wavevectors, and hence two propagating waves of different wavelength. Since each excitable wavevector resides in regimes of opposite slope, these two waves will be characterized by counter-propagating phase. Note, however, that a frequency regime with double wavevector solutions again exists only for insulator thicknesses smaller than a critical cutoff thickness [102].

Similar features can be observed for the bound modes of the IMI geometry, plotted in Fig. 3.1(c). Here, 50 nm of Ag is clad by two semi-infinite regions of GaP. Like the MIM geometry, this structure is characterized by both a  $H_y$  field antisymmetric mode (light gray curve, located exclusively below the surface plasmon resonance) and a  $H_y$ -symmetric mode (dark gray, located both above and below the surface plasmon resonance). The symmetric mode exhibits a regime of negative slope for certain frequencies above the plasmon resonance frequency. However, as

with the IIM geometry, this negative index regime is accompanied by wavevectors that exhibit positive slope — and hence a positive index — throughout the same frequency range.

As Fig. 3.1 reveals, in the absence of losses all three plasmonic geometries appear to support propagation of negative index modes over a finite frequency range. The MIM geometry is the only structure that can be characterized by a single propagating negative index mode — and hence a unique negative index — for these frequencies. Of course, the many enabling and exotic applications of plasmonic systems, including negative indices, do not come without an expense: namely, the cost of losses. Metals are characteristically lossy, particularly near their resonant frequencies, and Ag is no exception. While this section outlined the potential for plasmon waveguides to support propagation of negative index waves, the next section explores the extent to which these results are altered when losses are included.

### 3.3 Lossy dispersion and the necessary condition for negative indices

The equivalence between the energy velocity  $v_E$  and the group velocity  $v_g$  described above provides a simple way of identifying negative index regimes directly from a dispersion diagram. However, this equivalence only holds for non-absorbing media. For absorbing (i.e., lossy) materials, the more general expression of the energy velocity must be used:

$$v_E = \frac{\bar{S}}{\bar{W}}, \quad (3.4)$$

where  $\bar{S}$  is the average power flow in the waveguide and  $\bar{W}$  is the time-averaged energy density [103]. The average power flow can be derived from the integrated Poynting flux, and always points in the direction of wave propagation. Therefore, the direction of power flow will be collinear with the direction of wave decay for lossy materials:

$$\text{sign}(v_E) = \text{sign}(\text{Im}\{k_x\}). \quad (3.5)$$

In contrast to power flow, phase can flow in either direction, either parallel or opposite to the direction of wave decay. For plane waves, including plasmons, phase flow is described by the ratio of the excitation frequency to the mode wavevector via  $v_p = \omega/\text{Re}\{k_x\}$  and so:

$$\text{sign}(v_p) = \text{sign}(\text{Re}\{k_x\}). \quad (3.6)$$

Therefore, to achieve the antiparallel energy and phase velocities associated with negative indices, the plasmon wavevector must satisfy the criterion:

$$\text{sign}(\text{Re}\{k_x\}) \neq \text{sign}(\text{Im}\{k_x\}) \quad (3.7)$$

assuming the electromagnetic fields take the form  $e^{i(k_x x - \omega t)}$ . Note that this condition on the sign of the real and imaginary components of  $k$  is both a necessary and



sufficient condition for achieving negative indices in absorbing media, including plasmon-based geometries [53].

Because of point symmetry in the complex  $k_x$  plane with respect to the origin, we can impose  $\text{sign}(\text{Im}\{k_x\}) > 0$ . This choice restricts the direction of net energy flow to the positive  $x$  direction. Then, negative index plasmonic geometries will necessarily be characterized by a negative real component of the plasmon wavevector. Assuring consistency with Fig. 3.1, we note that the choice of  $\text{sign}(\text{Im}\{k_x\}) > 0$  also affects the sign of  $\text{Re}\{k_x\}$  obtained in the lossless dispersion curves. Notably, the branches plotted in Fig. 3.1 are accompanied by counterpropagating modes that have  $k_x < 0$ . Imposing a constraint on the energy flow direction allows only curves with positive slope in the lossless case. The branches with negative slope in Fig. 3.1 (which were recognized as exhibiting a negative index) are then omitted. Instead, their counterparts with  $k_x < 0$  remain, reflecting the connection between the signs of  $k_x$  and  $n$  when imposing this restriction on the direction of energy flow. As we will see, these dispersion curves can still be recognized when realistic material parameters, including absorption losses, are used.

### 3.3.1 The metal-insulator-metal waveguide as a negative index material

Figure 3.2 plots the real and imaginary components of the plasmon wavevector  $k_x$  versus energy for MIM geometries. Here, the metallic layer is Ag, described by the empirically-determined optical constants reported by Johnson and Christy [26]. The insulating layer is again taken to be GaP, with absorption both above and below the bandgap included [104]. GaP core thicknesses of 10 nm, 17 nm, and 25 nm are considered. For reference, the surface plasmon resonance is shown as a dotted horizontal line. As noted in Fig. 3.1(a), MIM geometries are characterized by both a  $H_y$  field symmetric mode and a  $H_y$  field antisymmetric mode. Both modes are also found in this lossy geometry, with the  $H_y$ -symmetric mode (with  $\text{Re}\{k_x\} > 0$ ) shown in blue and the  $H_y$ -antisymmetric mode (with  $\text{Re}\{k_x\} < 0$ ) plotted in red. Schematics of these mode profiles are also plotted in Fig. 3.2.

As seen in Fig. 3.2, the losses of the  $H_y$ -symmetric mode are quite low below the surface plasmon resonance frequency. Recall that between the surface plasmon and bulk plasma frequencies, this mode exhibited a bandgap in the lossless case, where  $k_x$  was purely imaginary. The introduction of loss now causes the real component to be non-zero in this frequency regime as well. However, since  $\text{Im}\{k_x\} \gg \text{Re}\{k_x\}$  above the surface plasmon resonance, the mode is in essence still a nonpropagating evanescent wave. Importantly, although this mode exhibits a regime of negative slope in the plot of  $\text{Re}\{k_x\}$ , its real wavevector component, and hence the phase velocity, remains exclusively positive. Since  $\text{Im}\{k_x\} > 0$ , both energy velocity and phase velocity of the mode are always positive. Accordingly, these  $H_y$ -symmetric modes will be characterized by refractive indices that are exclusively positive for all frequencies.

While the  $H_y$ -symmetric modes do not exhibit negative indices, MIM wave-

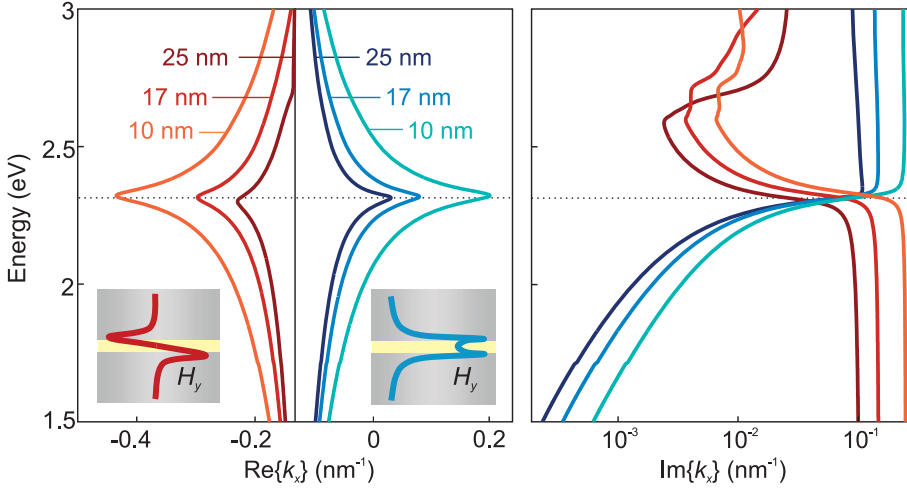


**Figure 3.2:** Lossy dispersion for MIM waveguides consisting of GaP clad by Ag. Three GaP thicknesses are included ( $d=25$  nm, 17 nm, and 10 nm), and dispersion relations for both  $H_y$  field symmetric (blue hues) and antisymmetric (red hues) modes are shown. Including losses, the necessary condition for negative index modes is:  $\text{sign}(\text{Re}\{k_x\}) \neq \text{sign}(\text{Im}\{k_x\})$ . This condition is clearly satisfied for the  $H_y$  field antisymmetric mode, which can exhibit negative indices with low loss above the surface plasmon resonance (shown as a dotted line).

guides can also support  $H_y$ -antisymmetric modes. The real and imaginary wavevector components of these modes are shown in Fig. 3.2 in red. As seen, the sign of  $\text{Re}\{k_x\}$  is negative throughout the entire frequency domain, corresponding to a negative phase velocity. In contrast, the sign of  $\text{Im}\{k_x\}$  is positive. Therefore, these antisymmetric modes will exhibit oppositely-oriented energy and phase velocities, and hence negative indices. Note that  $\text{Im}\{k_x\} \gg \text{Re}\{k_x\}$  for frequencies below the surface plasmon resonance, indicating that these modes are essentially non-propagating below resonance. Such results are consistent with the lossless dispersion curves of Fig. 3.1(a), where the wavevector of the antisymmetric mode was purely imaginary below the surface plasmon resonance. However, above resonance, the losses of this  $H_y$ -antisymmetric mode become remarkably low — so low, in fact, that losses begin rival the low  $\text{Im}\{k_x\}$  components seen for the propagating positive index mode. The low losses reflect the allowed band of propagation for this mode seen in Fig. 3.1(a). Therefore, between the bulk and surface plasmon resonant frequencies, the  $H_y$ -antisymmetric mode will be the only propagating mode. As this mode exhibits opposite phase and energy velocities, MIM geometries will indeed be characterized by negative indices in this frequency range. The range of achievable refractive indices and losses will be discussed in detail in section 3.4.

### 3.3.2 Insulator-insulator-metal and insulator-metal-insulator waveguides as multimode metamaterials

Figure 3.3 plots the dispersion relation for the bound modes of an IIM waveguide, considering both the sign and magnitude of  $\text{Re}\{k_x\}$  and  $\text{Im}\{k_x\}$ . A thin layer of GaP ( $d = 10$  nm, 17 nm, and 25 nm) is embedded between Ag and air half-spaces. The dielectric functions of Ag and GaP are adopted from empirically-determined optical constants, and thus include realistic losses for all plotted frequencies. As with the MIM waveguides, this geometry exhibits real wavevector components that are both positive and negative, corresponding to positive and negative indices, respectively. Below resonance, only the positive index mode exhibits long-range propagation. Above resonance, the losses of this positive index mode increase, while the losses of the negative index mode are reduced. Note however that unlike the MIM geometry, the losses of the IIM negative index mode are generally comparable with those of the positive index mode at a given frequency. For example, GaP thicknesses of 10 nm and 17 nm exhibit negative-index  $\text{Im}\{k_x\}$  components that are higher than for the positive index mode. As the thickness of GaP is increased to 25 nm, the losses of both modes increase dramatically. This increased loss reflects the presence of the critical thickness for the negative index mode. For thicker dielectrics both modes exhibit very short propagation lengths above the surface plasmon resonance frequency that are comparable to or smaller than the mode wavelength.

Similar features are observed for the  $H_y$ -symmetric mode of an IMI waveguide,

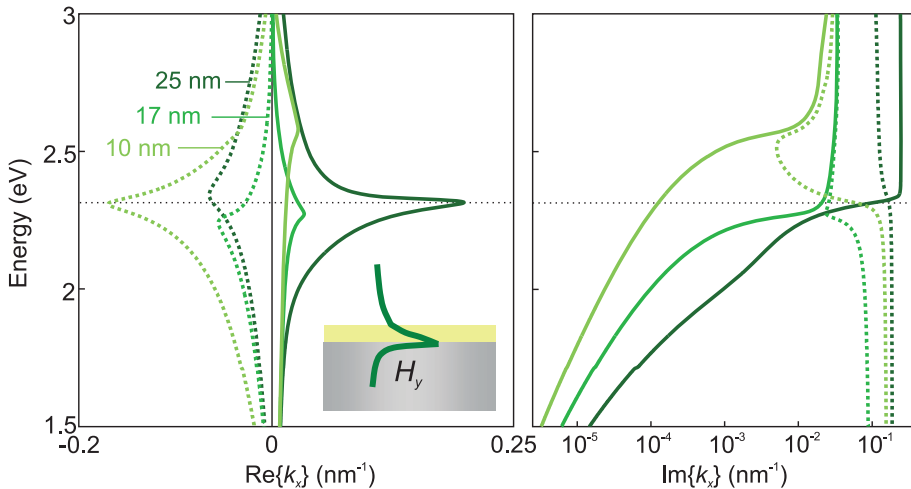


**Figure 3.3:** Lossy dispersion for insulator-insulator-metal waveguides composed of a semi-infinite Ag film coated with a thin layer of GaP and embedded in air. Three GaP thicknesses are included ( $d = 25$  nm, 17 nm, and 10 nm), and dispersion relations for both positive index (solid) and negative index (dotted) branches are shown.

shown in Fig. 3.4. Recall that this mode exhibited simultaneously positive and negative indices above the surface plasmon resonance for the lossless geometry (Fig. 3.1(c)). Here, a thin Ag slab is embedded in GaP. Ag thicknesses of  $d = 10$  nm, 17 nm, and 25 nm are considered. Note that the wavevectors of the  $H_y$ -antisymmetric mode are not shown, since this mode is characterized by exclusively positive wavevectors with  $\text{Im}\{k_x\}$  components that generally exceed those of the symmetric mode. As with the MIM and IIM geometries, losses for the positive index IMI modes are low below resonance, but increase strongly in the bandgap region. In contrast, losses for the negative index mode are high below resonance, and can be substantially reduced above resonance. However, the losses for these negative index modes are generally never lower than the losses for the positive index modes.

As Figs. 3.3 and 3.4 reveal, both IIM and IMI geometries can support negative index modes. However, these negative index modes are generally found in a frequency regime where additional positive index modes also exist. Such characteristics prohibit assignment of a single, unique index to the IIM and IMI geometries above the plasmon resonance, even including realistic material losses. Therefore, unlike the MIM geometry, planar IIM and IMI waveguides may not be regarded as single-mode, negative index materials. One could propose to excite only one of the two modes preferentially by matching the symmetry of an incident wave to the

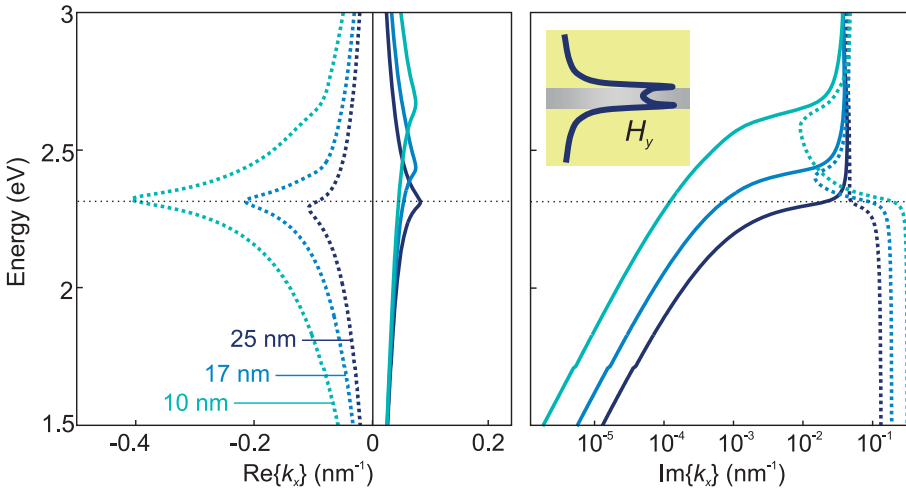


**Figure 3.4:** Lossy dispersion for insulator-metal-insulator waveguides composed of a thin Ag film clad with GaP. Three Ag thicknesses are included ( $d = 25$  nm, 17 nm, and 10 nm), and dispersion relations for the positive and negative index branches of the  $H_y$  field symmetric mode are shown. While solutions satisfying  $\text{sign}(\text{Re}\{k_x\}) \neq \text{sign}(\text{Im}\{k_x\})$  may be again found, the losses of this branch always exceed those of the positive index mode.

mode profile. This is however not possible in this case, since both modes originate from the same dispersion branch (see Figs. 3.1(b,c)) and therefore obey the same field symmetry. Nevertheless, the existence of multiple modes propagating with opposite phase and comparable absorption may be interesting for a variety of on-chip photonic applications. Moreover, their symmetric mode profiles may render these waves more easily excitable than the asymmetric negative index modes of MIM geometries.

### 3.4 Mapping plasmonic material indices and absorption: A guide to the experimentalist

Design of practical metamaterials requires precise knowledge of the index and absorption. For metamaterials based on plasmonic resonances or waveguides, such parameters depend strongly on the constituent materials, the structure dimensions, and the excitation wavelength. The preceding sections outlined the potential for index tunability in plasmonic waveguides: while MIM geometries can achieve low-loss, single-mode negative indices above the plasmon resonance, IIM and IMI geometries can sustain simultaneous propagation of waves with positive and negative phase velocity. In addition, the magnitude of the wavevectors (and hence the effective mode indices) can span from near-zero to both large positive or negative values. In this section, we explore the range of achievable indices and absorption in plasmonic waveguides. We focus our attention to the negative index modes.

In comparing the merits of different metamaterial designs, one has to consider the intended application of the metamaterial. Usually, the figure of merit (FOM) is defined as the magnitude of the ratio of  $\text{Re}\{n\}$  to  $\text{Im}\{n\}$ , as a measure of the number of optical cycles in which a wave decays to a certain fraction of its original strength ( $\text{FOM} = \text{Re}\{n\}/\text{Im}\{n\} = 4\pi L_{\text{SPP}}/\lambda_{\text{SPP}}$ ). However, if the intent is to use the metamaterial in an effort to construct a ‘perfect lens’, for example, one will in practice want to satisfy the condition that the impedance of the waveguide is matched to that of the medium outside the lens. This means that the FOM should be optimized under the restriction that the impedance-matching condition is satisfied.\* Moreover, the resolution of the lens will be degraded severely if the ratio of  $L_{\text{SPP}}$  to the lens thickness is small [105]. Even if one has the freedom to choose the medium outside the lens at will, the absolute propagation length rather than the FOM should be optimized to achieve the best image transfer over some specified distance. Therefore, we present both the FOM and the propagation length  $L_{\text{SPP}}$  for various geometries, and display them alongside the effective mode index. The associated plots are intended as a guide to the experimentalist in designing plasmonic

---

\*When both the lens and its surrounding are homogenous media, impedance is matched when the magnitude of the negative refractive index of the lens material is equal to that of the positive index of the surrounding [45], but in a slab waveguide the condition is not necessarily fulfilled when mode indices have equal magnitude.

materials for a variety of metamaterial and transformation-based applications.

### 3.4.1 Ag/GaP and Ag/Si<sub>3</sub>N<sub>4</sub> MIM metamaterials: Negative indices and negative refraction

Figure 3.5(a) plots the refractive indices achievable with the  $H_y$ -antisymmetric (negative index) mode in a MIM geometry, using GaP as the core and Ag as the cladding material. GaP core thicknesses are varied from 5 nm to 50 nm in 1 nm increments, and excitation wavelengths are varied from the near-infrared to the ultraviolet (energies of 1.5–3.5 eV). Note that each vertical cut through the chart depicts one dispersion diagram, with the index plotted on the color scale. The associated FOM is displayed in Fig. 3.5(b), and the propagation length  $L_{\text{SPP}}$  is shown in Fig. 3.5(c). For comparison, dashed lines are indicated in all panels to indicate the parameters for which  $n = -1$ ,  $-3.5$ , and  $-10$ .

As seen in the figure, the achievable refractive index magnitude spans from  $n \approx 0$  to  $n < -60$  as the core GaP thickness is reduced. As expected, figures of merit for the negative index mode are near zero for frequencies below the surface plasmon resonance and for thicknesses larger than the critical thickness of  $\sim 40$  nm, but approach 20 for thinner waveguides excited above resonance. The FOM for the negative index modes actually increases with decreasing core thickness along with the bandwidth of negative indices. For example at a wavelength of  $\sim 480$  nm (2.57 eV), a negative index of  $n = -23$  can be achieved with a figure of merit equal to 20, using a 5 nm thick GaP core. In contrast, the FOM for the positive index mode

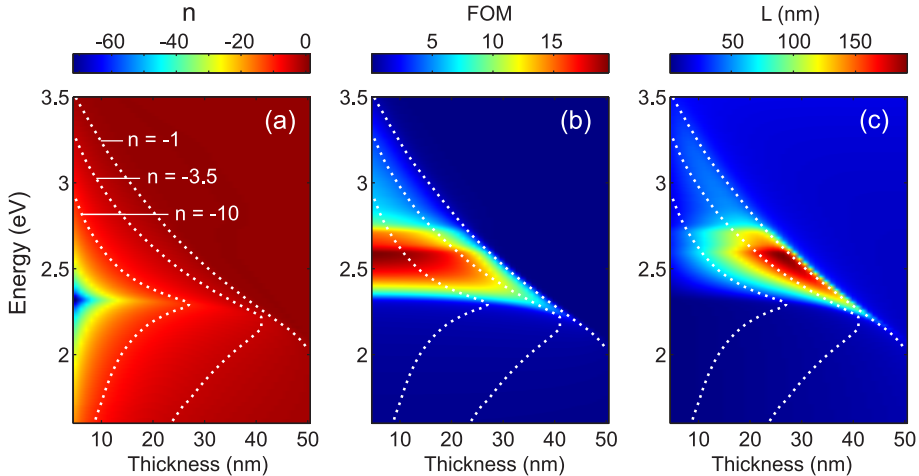


**Figure 3.5:** Refractive index (a), FOM (b), and propagation length (c) of the negative index mode in a Ag/GaP/Ag MIM waveguide, for varying GaP thickness and photon energy.

at the same wavelength is smaller than 0.5 (not shown). The increasing FOM with decreasing core thickness does not necessarily imply an increase of the propagation length, as can be seen from Fig. 3.5(c). Below a thickness of 25 nm,  $L_{\text{SPP}}$  becomes smaller when the thickness is reduced. Instead, the FOM slightly increases when the thickness is decreased due to the fact that the decrease of the propagation length is compensated by the increase of the effective mode index. Figure 3.5(c) shows that the optimum propagation length is found to approach 200 nm, for indices between  $n = -1$  and  $n = -2$ . The FOM for those conditions is of the order of 5–10, which is comparable to the calculated FOM achievable using resonator-based metamaterials at smaller frequencies [97, 106]. Note that for photon energies larger than  $\sim 2.6$  eV, absorption in the GaP starts to limit both the FOM and  $L_{\text{SPP}}$ .

To investigate the refraction of light into a typical negative index MIM waveguide, we performed a three-dimensional finite-difference time-domain simulation [76] of the structure depicted in Fig. 3.6(a). A 488-nm plane wave of infinite extent is incident from free space on a 30-nm-thick GaP slot clad with 400 nm Ag. At this wavelength, this geometry has a negative index of  $n = -2.86$  with a figure of merit equal to 10. The negative index mode in the waveguide cannot be excited at normal incidence due to its antisymmetric character. In order to allow excitation, the plane wave is polarized in the  $z$  direction and incident at a slightly oblique angle ( $10^\circ$ ) to the  $xy$  plane. Bloch boundary conditions are used to simulate an incident plane wave that is infinite in extent.

Figure 3.6(b) shows the simulated  $H_y$  field in a plane through the waveguide core at a distance of 5 nm from the top Ag/GaP interface. The field is not evaluated in the middle of the waveguide, since the  $H_y$  component of the antisymmetric mode is zero there. To the left, the incident wave makes an angle of  $30^\circ$  with respect to the  $xz$  plane, as shown by the arrow indicating the calculated Poynting vector. Inside the MIM waveguide, a wave can be seen to propagate over a distance of the order of a micron. The wavefront angle is consistent with refraction into a material with a negative index of  $n = -2.86$ , as predicted. Additionally, in the first 100 nm from the edge of the waveguide, the quickly decaying evanescent  $H_y$ -symmetric mode makes a contribution to the field as well. The Poynting vector is calculated in the waveguide beyond the first 100 nm and shown as an arrow in Fig. 3.6(b). The power is seen to flow away from the normal in the direction associated with negative refraction. This result proves that the negative index mode can indeed enable negative refraction of light.

Replacing the GaP with  $\text{Si}_3\text{N}_4$  ( $n \approx 2.02$ ) shifts the surface plasmon resonance to higher energies. Figure 3.7 shows index and FOM maps for Ag/ $\text{Si}_3\text{N}_4$ /Ag MIM geometries, again with core thicknesses spanning 5 nm to 50 nm. As seen, the region of high figure of merit for negative index modes has increased in energy to 3.1 eV. While the refractive indices achievable in this geometry range are comparable with the GaP-based geometry, the maximum figure of merit has been reduced to 10. This can be heuristically explained: Reducing the dielectric index shifts the surface plasmon resonance to higher frequencies, where Ag is inherently more absorbing. Nevertheless, the range of index tunability is significant. Figures 3.5 and

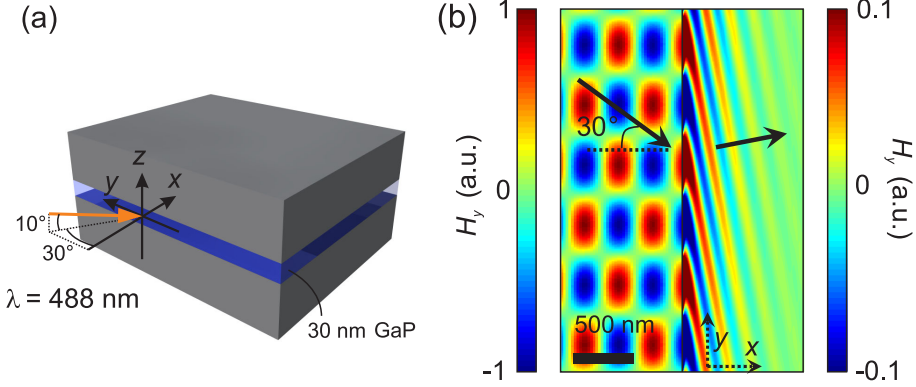


**Figure 3.6:** Finite difference time domain simulation of negative refraction of a 488-nm plane wave into a MIM waveguide. (a) Schematic of the simulation geometry. The plane wave is incident at an angle of  $30^\circ$  with respect to the  $xz$  plane and  $10^\circ$  with respect to the  $xy$  plane. (b)  $H_y$  field component snapshot in a plane through the waveguide core. Bloch boundary conditions are used to simulate an incident plane wave that is infinite in extent. For clarity, the color scale in the waveguide to the right differs from that in the air region to the left. The arrows depict the calculated Poynting vector directions of the incident and refracted waves.

3.7 show that MIM-based geometries exhibit broadband negative-index operation. High FOM negative indices for this Ag/Si<sub>3</sub>N<sub>4</sub>/Ag MIM geometry span wavelengths from 354 nm – 397 nm; in this wavelength range, FOMs range from 7–10. Likewise, high figure-of-merit negative indices for the Ag/GaP/Ag MIM geometry span wavelengths of 456 – 524 nm (energies of 2.37 – 2.72 eV) — a wavelength range of nearly 75 nm, where FOMs range from 12–20. Note that for higher energies, figures of merit for this GaP waveguide are predominately limited by increased absorption in the GaP.

### 3.4.2 Ag/GaP-based IIM and IMI waveguides

Figure 3.8 plots the index, FOM, and  $L_{\text{SPP}}$  maps for the negative index mode of an IIM waveguide, considering a thin layer of GaP between air and Ag half-spaces. As before, the thicknesses of GaP is varied from 5 nm to 50 nm in 1 nm increments. Similar to the results shown in Fig. 3.3, Fig. 3.8 reveals the existence of high FOM negative index modes below a critical GaP thickness. For thin insulating layers ( $d < 10$  nm), the figure of merit for these modes can approach 16. However, we know from Fig. 3.3 that at frequencies for which the negative-index mode has small extinction, a low-loss positive index mode also exists. Therefore, IIM geometries cannot be characterized as negative index materials identifiable with a unique index at a given wavelength, as the field in the waveguide is in general a superposition of both positive and negative index modes. Interestingly, Fig. 3.8 shows that the largest



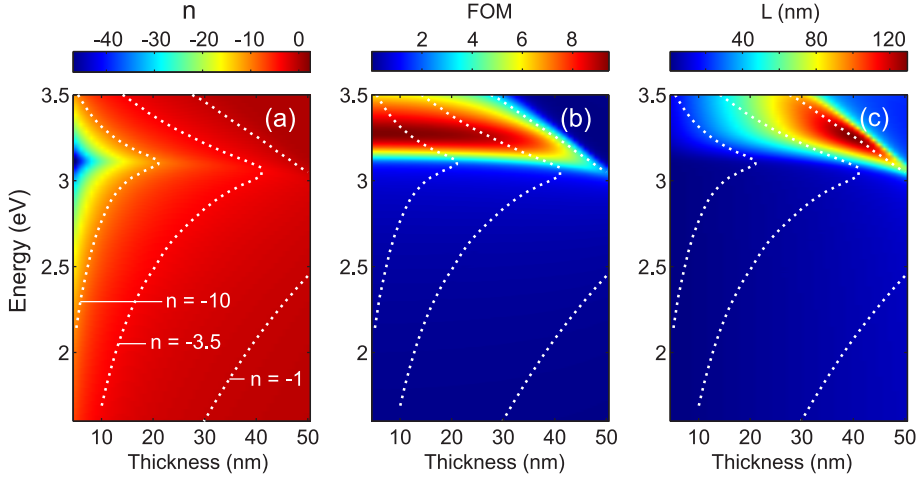


**Figure 3.7:** Refractive index (a), FOM (b), and propagation length (c) of the negative index mode in a Ag/Si<sub>3</sub>N<sub>4</sub>/Ag MIM waveguide, for varying Si<sub>3</sub>N<sub>4</sub> thickness and photon energy.

propagation lengths of the negative index mode ( $L_{SPP} \approx 100$  nm) are now achieved for an index of  $-3.5$ , which is higher than for the MIM geometry. The reason that propagating negative index modes with indices of smaller magnitude do not exist can already be seen in the lossless case. In Fig. 3.1, the lowest-energy dispersion branch exhibits two different wavevector regimes: Below a specific wavevector, the branch has a positive slope and hence a positive effective index. Only for wavevectors larger than that specific wavevector, the branch acquires a negative slope. This means that unlike the MIM geometry, the IIM geometry is not suitable to achieve negative indices with small magnitudes.

Similar results are observed for IMI-based geometries, shown in Fig. 3.9 for GaP-clad Ag slabs, respectively. Figures-of-merit comparable to those for MIM waveguides can be reached, but now only for  $n < -10$ . The maximal propagation length is  $\sim 50$  nm, which is smaller than for the other geometries. We note that the FOM for the negative index mode never exceeds the FOM for the accompanying positive index mode (data not shown). Indeed, as the Ag thickness is decreased, the electromagnetic field of this  $H_y$ -symmetric positive index mode penetrates farther into the surrounding dielectric, eventually approximating a plane wave traveling in a dielectric with an index equal to the cladding index (see section 1.2.2). As a result, this mode propagates for a much longer distance than the negative index mode, and it will generally dominate propagation in the waveguide further than  $\sim 100$  nm away from sources.

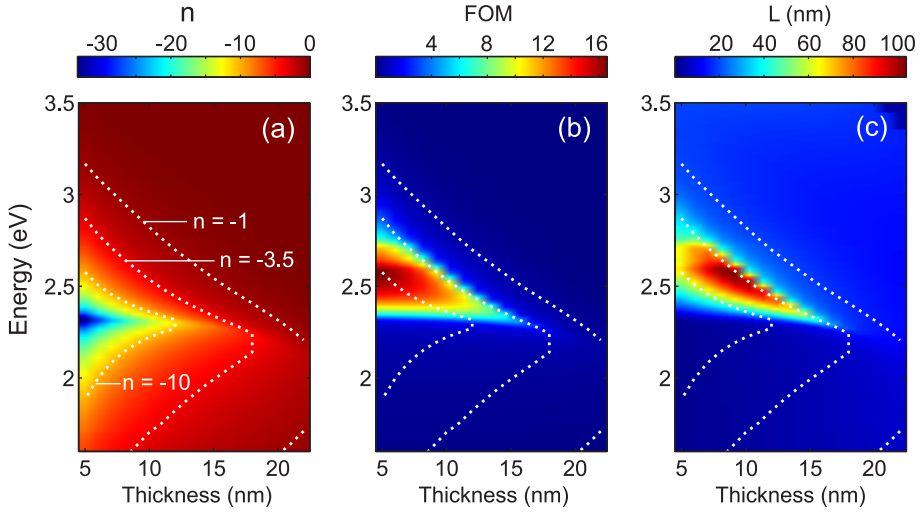


**Figure 3.8:** Refractive index (a), FOM (b), and propagation length (c) of the negative index mode in a air/GaP/Ag HIM waveguide, for varying GaP thickness and photon energy.

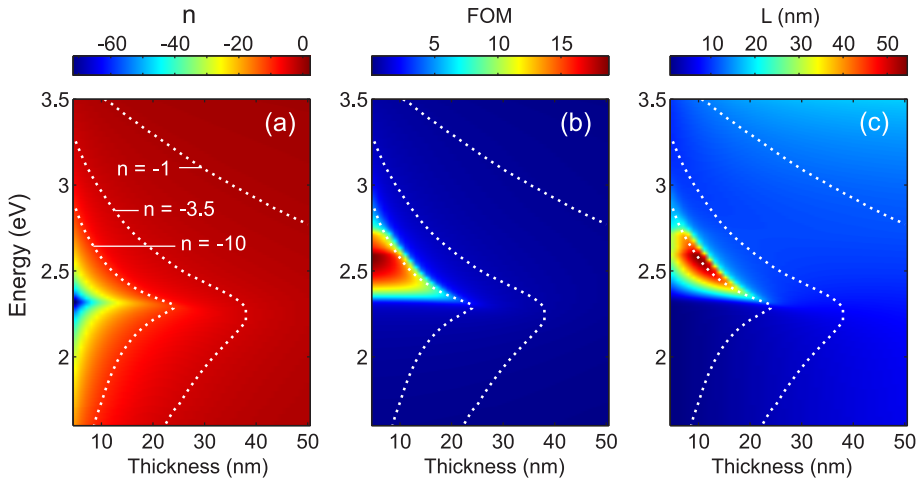


**Figure 3.9:** Refractive index (a), FOM (b), and propagation length (c) of the negative index mode in a GaP/Ag/GaP IMI waveguide, for varying Ag thickness and photon energy.

### 3.5 Conclusions

This chapter has explored the range of negative indices accessible in planar plasmonic geometries. Among planar plasmonic waveguides, MIM, IIM, and IMI-based structures all exhibit modes with negative indices between the bulk and surface plasmon resonances. Such negative index modes arise from an enhanced field penetration in the metal that gives rise to oppositely-oriented mode energy and phase velocities. Interestingly, these negative index modes can be characterized by high figures of merit despite high field confinement in the metal.

For MIM waveguides, the negative index mode is the only propagating (i.e., high figure-of-merit) mode between the bulk and surface plasmon resonances. In contrast, IIM and IMI waveguides support propagation of multiple high figure-of-merit modes, which are characterized by both positive and negative indices above resonance. Heuristically, the ‘open’ nature of these waveguides makes excitation and detection of IIM and IMI negative index modes inherently difficult, particularly since the negative and positive index modes share the same field symmetry. Therefore, IIM and IMI waveguides may not be formally considered metamaterials with a unique index assignment at a given frequency. Moreover, they cannot be used to achieve low-magnitude negative indices, and the maximum achievable absolute propagation lengths are smaller than for the MIM geometry. However, they do provide an interesting platform for index tunability and multimode propagation, and their field symmetry makes them readily excitable by scattering or end-fire methods.

Unlike these ‘open’ geometries, MIM waveguides are effective metamaterials that can be characterized by a unique index at each wavelength. For wavelengths below the surface plasmon resonance, the propagating plasmon mode is characterized by a symmetric  $H_y$  field distribution and a positive index. Between the bulk and surface plasmon resonances, this symmetric mode becomes evanescent, rendering the  $H_y$ -antisymmetric plasmon mode the only propagating mode. Interestingly, this antisymmetric mode is characterized by antiparallel energy and phase velocities, and hence negative indices. Therefore, light will propagate through the MIM waveguide as if through a negative index material, with an index equal to the plasmon mode index.

Judicious choice of metal and dielectric can enable large negative indices with high figures of merit. A high-index dielectric is most favorable to reach maximal extinction lengths. For Ag/GaP geometries, negative indices can range from 0 down to  $n = -60$ , with figures of merit approaching 20. Moreover, negative indices in MIM-based metamaterials can be achieved over a wide range of wavelengths that are tunable throughout the entire visible spectrum. Note that efficient coupling and impedance matching into these waveguides requires excitation of an antisymmetric mode. Still, the broad index tunability of MIM waveguides, their high figures of merit, and their relative ease of fabrication may render MIM-based metamaterials an attractive alternative to resonator-based metamaterials. As in all metal-

based metamaterial designs, absorption losses severely limit the extinction length in these structures. However, the losses in the geometries considered here match those in state-of-the-art resonator-based metamaterials, and are unrivaled in the visible frequency regime. Combined with traditional metamaterials, MIM geometries may enable realization of practical negative index and transformation-based optical elements, both in two-dimensional on-chip geometries and as basic elements of three-dimensional metamaterials.

# 4

---

## Enhanced upconversion of infrared light with a tapered plasmonic waveguide

*Infrared surface plasmon polaritons (SPPs) are concentrated in a laterally tapered planar Ag waveguide. The near field of SPPs excited with 1490 nm light at a Ag-sapphire interface is probed using the photoluminescence of upconverted Er ions at 550 and 660 nm. SPP interference patterns are observed that exhibit clear evidence of SPP concentration toward the taper end. The concentration leads to an enhancement of the upconversion luminescence intensity from Er energy levels that are populated by multiphoton processes.*

### 4.1 Introduction

The local enhancement of electromagnetic fields by the excitation of surface plasmon polaritons allows for the enhancement of nonlinear optical effects [8, 10]. On the one hand, the evanescent character of SPPs leads to high field confinements in the direction normal to the metal surface, which can enhance nonlinear processes near the surface [107]. On the other hand, the large wavevectors associated with these waves offer the possibility of confining SPPs also laterally to length scales smaller than the wavelength of light in the bounding dielectric. In view of large field concentrations, the conversion of light to SPPs, their subsequent guiding, and finally their concentration are of fundamental interest. The concentration of propagating SPPs is in competition with losses due to absorption and scattering, which

limit the typical propagation lengths of the SPP modes to several tens of micrometers. Several plasmonic waveguiding structures that provide lateral confinement have been demonstrated [56, 83, 108–110]. Finite-width metal stripe waveguides have been studied most thoroughly [111–115].

Focusing of SPPs has been demonstrated by metallodielectric lenses [116] and corrugations in the metal surface [117–120]. The first indication for SPP concentration in a triangularly shaped termination of a stripe waveguide has been shown by Weeber et al. [112] for SPP modes at the air side of a Au waveguide. In a nonplanar geometry, very large field concentrations and asymptotic slowing down of SPPs have recently been predicted to occur at the tip of conical metal waveguides [43]. This has close links to the field enhancements and subwavelength confinement near the tip of gold- or silver-coated fiber tips used in tip-enhanced near-field microscopy, which are also attributed to the generation of SPPs [121–123].

In this chapter, we investigate the enhancement of nonlinear effects due to SPP field concentration in laterally tapered planar Ag waveguides by studying optically active erbium ions as a nonlinear model system. These ions can absorb 1.5  $\mu\text{m}$  light to their first excited state, followed by nonlinear cooperative upconversion and excited-state absorption to populate higher energy levels that emit at 550 and 660 nm [124, 125]. The Er ions are implanted in sapphire at close proximity to a silver film. Infrared SPPs are launched along the Ag-sapphire interface by illuminating a subwavelength hole array in the film with a focused beam of 1490 nm laser light. By imaging the upconversion photoluminescence from the Er ions in a confocal microscope, the SPP propagation is visualized, and any upconversion enhancement can be spatially resolved. This luminescence microscopy technique [80, 126] allows probing of the field intensity of the purely bound SPP mode propagating along the Ag-sapphire interface, which cannot be readily observed using other methods such as photon scanning tunneling microscopy or leakage radiation microscopy. We observe interference mode patterns on the tapers that clearly show SPP concentration and measure a 4–5 fold enhancement of the 550 nm upconversion photoluminescence intensity near the tip of the waveguide. This work goes beyond experiments in which upconversion enhancement is achieved by field concentration in Kretschmann-Raether geometry [107] by also demonstrating the in-plane focusing of SPPs and the associated locally enhanced upconversion luminescence.

## 4.2 Methods

### 4.2.1 Er upconversion luminescence

A 400  $\mu\text{m}$  thick single-crystal sapphire substrate (refractive index 1.74) is implanted with 200 keV  $\text{Er}^+$  ions at a fluence of  $7 \times 10^{15} \text{ cm}^{-2}$  through a 10 nm thick Ge conducting layer, which is subsequently removed. This results in a Gaussian Er depth distribution with a peak Er concentration of 2 at.% at a distance of 35 nm to the sapphire surface, as simulated with the Monte Carlo program SRIM [127]. The

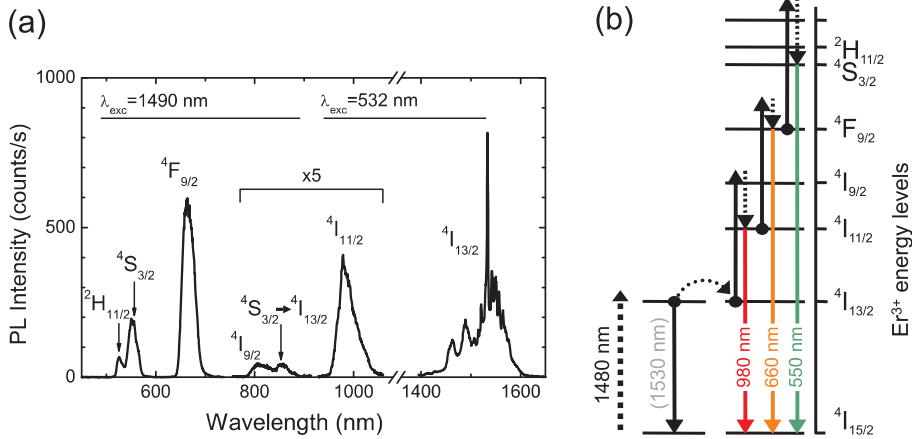


**Figure 4.1:** (a) Er photoluminescence spectrum showing emission from different Er levels. For  $\lambda_{em} < 900$  nm, the pump wavelength was 1490 nm, whereas for  $\lambda_{em} > 900$  nm, 532 nm excitation light was used. The luminescence signal in the region 750–1100 nm is five times enlarged. (b)  $\text{Er}^{3+}$  energy level scheme, depicting the cooperative upconversion mechanism that populates higher-order energy levels through energy transfer between two ions excited with 1490 nm light. A multistep upconversion process is shown to reach the levels emitting at 660 and 550 nm.

standard deviation in the Gaussian depth distribution is  $\sigma = 12$  nm. The sample is annealed in vacuum at 900 °C for one hour to remove implantation related defects and activate the Er ions [128].

A typical spectrum of the Er photoluminescence from the sample is shown in Figure 4.1(a). The visible part of this emission spectrum ( $\lambda_{em} < 900$  nm) is obtained by excitation with 1490 nm laser light from a 45 mW InGaAsP diode laser. The infrared part ( $\lambda_{em} > 900$  nm) is recorded with 532 nm excitation light from a 20 mW frequency-doubled Nd:YAG laser. The visible and infrared emission is dispersed by grating spectrographs onto a Si CCD detector and an InGaAs photodiode array detector, respectively. The spectrum is not corrected for variations in pump intensity and collection efficiency of the setup.

Comparing the measured spectrum to the level diagram of  $\text{Er}^{3+}$  depicted in Figure 4.1(b), we see that all excited-state-to-ground-state transitions are observed. All emission that is recorded with the 1490 nm pump is attributed to an upconversion process. The pump light excites Er ions to the first excited state, from which multiple upconversion processes can occur to populate higher Er levels [124, 125]. Two neighboring Er ions that are both excited can exchange energy in a dipole-dipole interaction to promote one to the  $^4\text{I}_{9/2}$  level. The excited Er ion then quickly relaxes to the second excited state ( $^4\text{I}_{11/2}$ ), which can decay either nonradiatively or through the emission of a 980 nm photon (see Fig. 4.1(b)). This process, based on

Förster transfer between two excited Er ions, is called cooperative upconversion. A competing process is excited state absorption, in which a second pump photon is directly absorbed by an Er ion residing in the first excited state. Excited state absorption is especially strong for large incident fluxes. At small pump powers, both processes will result in a quadratic dependence of the 980 nm upconversion photoluminescence on the excitation power. However, at higher excitation powers the pump power dependence can deviate from this quadratic dependence due to saturation of the Er levels [129]. Er ions excited to the  $^4I_{11/2}$  level can also undergo second- and third-order upconversion steps with Er ions in the first or higher excited states to populate even higher energy levels [124] leading to the observed emission from the  $^4F_{9/2}$ ,  $^4S_{3/2}$ , and  $^2H_{11/2}$  manifolds. It is the emission from the  $^4F_{9/2}$  and  $^4S_{3/2}$  levels at wavelengths of 660 and 550 nm, respectively, which is used to probe the infrared SPP pump field.

#### 4.2.2 Fabrication of Ag microstructures

Kretschmann–Raether coupling cannot be used to excite SPPs at the substrate side of a metal film. Instead, a subwavelength hole array is illuminated to achieve the necessary momentum matching of an incident 1490 nm light beam to SPPs. Such a geometry has been used before to excite SPPs at the air side of a metal film [130, 131]. The excited SPPs are subsequently coupled into a laterally tapered waveguide structured in the Ag film. A schematic of the measurement geometry is shown in Fig. 4.2.

Taper and hole array microstructures are fabricated in a  $140 \pm 5$  nm thick Ag film on the Er-implanted sapphire substrate by electron beam lithography in a bilayer

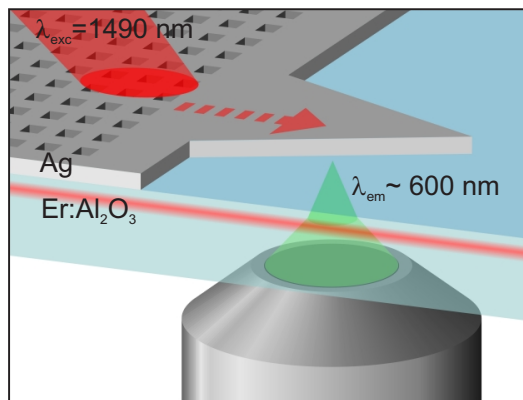


**Figure 4.2:** Schematic representation of the measurement principle. SPPs are excited at the Ag-sapphire interface by illuminating a hole array with light with a free-space wavelength of 1490 nm, and Er upconversion luminescence at visible frequencies is imaged with a confocal microscope.



PMMA resist followed by liftoff. The Ag is evaporated through resistive heating, and the use of an adhesive layer is avoided, as this layer would be detrimental to SPP excitation and propagation along the Ag-sapphire interface. In order to improve direct adhesion of the metal to the substrate, the sample is cleaned with an oxygen plasma directly before the Ag deposition. An optical microscopy image of the structure is shown in Fig. 4.3(a). The hole array, with a pitch of  $1.46\ \mu\text{m}$  and a hole diameter of roughly  $0.6\ \mu\text{m}$ , extends to the left of the dotted line. At a distance of  $7\ \mu\text{m}$  from the array, a laterally tapered waveguide of triangular shape is structured in the metal film, with a base width of  $12\ \mu\text{m}$  and a length of  $36\ \mu\text{m}$ .

### 4.2.3 Optical measurements

The  $1490\ \text{nm}$  excitation light is incident from the air side of the film under an angle of  $47^\circ$  with respect to the surface normal to achieve first-order diffractive coupling to SPPs at the Ag-sapphire interface, which propagate in the direction indicated by the arrow in Figure 4.3(a). From the angular dependence of the coupling, the excitation of SPPs at this interface can be confirmed. The p-polarized laser light is focused by a fiber focuser ( $\text{NA}=0.1$ ) to a  $10\ \mu\text{m}$  wide spot near the edge of the array, as depicted in Figure 4.2. Er luminescence is collected through the substrate by a  $20\times$  objective ( $\text{NA}=0.75$ ) in a scanning confocal microscope. The collected light passes through a polarizer to avoid distortions due to the birefringence of the sapphire substrate and is transported through a collection fiber to a spectrograph and a Si CCD detector.

The visible upconversion emission is used to determine the two-dimensional distribution of the infrared SPP intensities in the hole array/taper structure. We have shown previously that the bound SPP modes propagating at the high index side of a Ag film can be imaged by detecting the Er photoluminescence emission from the first excited-state at a wavelength of  $1530\ \text{nm}$  [80]. Here, the resolution of this imaging technique is significantly enhanced by detecting the radiation from higher energy levels of Er ions [132]. In this way, the SPPs excited with  $1490\ \text{nm}$  light can be probed with wavelengths as short as  $550$  and  $660\ \text{nm}$ .

## 4.3 Results and discussion

Parts (b) and (c) of Fig. 4.3 show upconversion images taken at  $645\text{--}690\ \text{nm}$  ( ${}^4\text{F}_{9/2} \rightarrow {}^4\text{I}_{15/2}$  transition) and  $520\text{--}570\ \text{nm}$  ( ${}^4\text{S}_{3/2}, {}^2\text{H}_{11/2} \rightarrow {}^4\text{I}_{15/2}$  transitions), respectively. At the left side of the images, Er emission in the excitation spot on the hole array is visible; a SPP beam with a width of  $\sim 10\ \mu\text{m}$  propagates out of this spot across the unstructured Ag before entering the tapered part of the film. Along the taper, a pronounced interference pattern is observed, and the intensity of the upconversion luminescence gradually increases as the taper tip is approached. The relative increase is stronger for the  $550\ \text{nm}$  emission than for the  $660\ \text{nm}$  emission. Note that the intensity in either image is scaled to the maximum intensity in the image,

which occurs near the tip of the waveguide in both cases. Along the complete length of the taper, the luminescence intensity is enhanced quite homogeneously near the edge of the waveguide. Outside the taper, the Er luminescence is observed to fade so quickly that a decay length cannot be determined quantitatively given the measurement resolution.

By comparing parts (b) and (c) of Figure 4.3, it can be seen that the positions of the nodes and antinodes in the interference pattern are identical for both emission wavelength ranges. This demonstrates clearly that 1490 nm SPP modes can be precisely imaged using upconversion luminescence in the visible. It proves that the interference pattern is caused by interference of the infrared pump light and that variations due to a possible dependence of the radiative decay rate on the distance from the taper edge are not responsible for this effect.

The 2.1  $\mu\text{m}$  separation between the interference fringes that are aligned parallel to the taper edges corresponds to that predicted to arise from the reflections of SPP waves at the edges of the waveguide, considering SPPs excited with 1490 nm light along the Ag-sapphire interface, which are incident at the taper side at a  $81^\circ$  angle. The good visibility of the interference fringes indicates that the reflectivity of the edges is quite large, in accordance with the notion of total internal reflection at the edges. Indeed, the critical angle for such reflections is  $\sim 80^\circ$ , as estimated from the index contrast between the effective refractive index inside the taper (given by the SPP dispersion relation of the mode at the substrate side of the film) and the refractive index of the sapphire substrate outside the taper [133].

We note that it is a priori difficult to make quantitative comparisons between the emission collected from Er ions close to the metal film and that from ions outside the taper. Taking into account local density of states effects [134], the radiative decay rate near the metal would be reduced and additional nonradiative channels would be introduced. However, redirection of the emitted light due to the metal increases the collected intensity by at most a factor two. Taking both counteracting effects into account, the maximum possible net increase of collected emission intensity due to the presence of the metal is a factor two. Therefore, we can conclude from the fact that the Er luminescence vanishes quickly outside the waveguide that at the edge of the Ag film SPPs are either efficiently reflected or scattered out in directions away from the Er doped region near the sapphire surface.

Because of reflections of the Gaussian SPP input beam, clear nodes and antinodes would be expected also along the edges of the waveguide. The fact that the Er upconversion luminescence intensity is quite homogeneous along these edges suggests that edge modes could possibly play a role in this structure [113, 114]. The focus of the SPP field remains confined to the Ag taper. This behavior is in contrast with what is observed for SPPs propagating at the air side of a Au film on glass [112, 135]. The fact that we find no evidence for leakage across the taper edge may be due to the larger angle of incidence used here, as well as the difference in character between the modes at different sides of the metal film [31, 115]. The contribution of the different plasmonic modes in the waveguides to the focusing will be discussed in detail in Chapters 5 and 6.

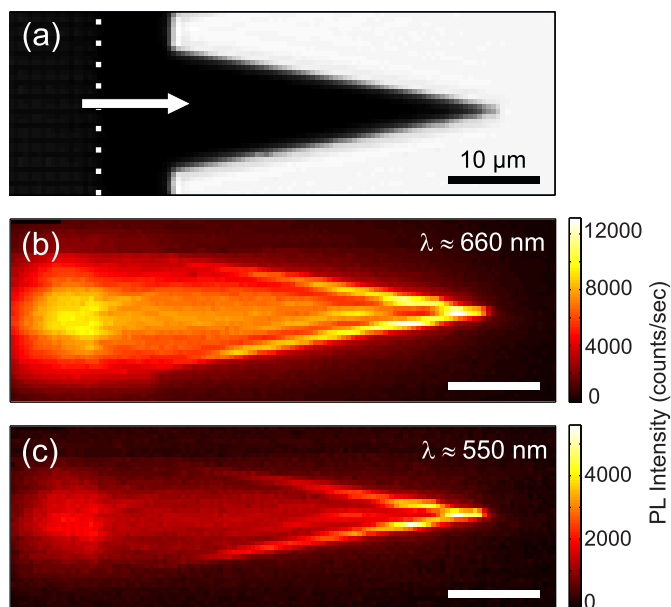


**Figure 4.3:** (a) Optical microscopy image of the studied structure, obtained by detecting transmitted 520–570 nm light from a halogen lamp in the confocal microscope. The hole array extends to the left of the dotted line. The dashed circle indicates the position of the excitation spot, and the arrow shows the direction of SPP propagation. (b) and (c) Spatially resolved photoluminescence maps of Er upconversion emission in the wavelength ranges of 645–690 nm and 520–570 nm, respectively. Both color scales are normalized to the maximum intensity in the field of view. The scale bars are 10  $\mu\text{m}$ .

Figure 4.4 shows intensity cross sections of Figure 4.3(b) and (c) taken along the center of the waveguide, normalized to the respective signal intensities measured at the unstructured metal film just outside the excitation spot. At the tip of the waveguide, a 4–5 fold enhancement of the 550 nm emission and a 1.7 fold enhancement of the 660 nm emission are observed, as compared to the intensity under the smooth film. This clearly demonstrates the effect of SPP concentration in a tapered metal film and the enhancement of the nonlinear upconversion of Er ions due to this concentration.

The difference between the two enhancement factors is attributed to the fact that the pump power dependencies of the emission at these two wavelengths are different; the  $^4\text{S}_{3/2}$  and  $^2\text{H}_{11/2}$  levels are populated through a higher-order upconversion process than the  $^4\text{F}_{9/2}$  level. Detailed pump-power dependent emission measurements are required to determine the relative contributions of cooperative upconversion and excited-state absorption for these transitions [125, 129]. We note that if the upconversion mechanism is known, a relative measurement of the dif-

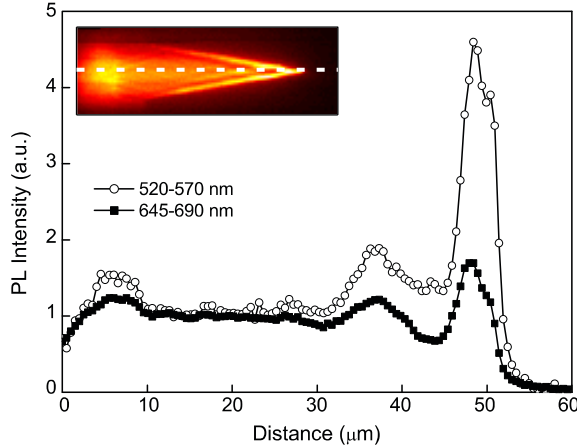


**Figure 4.4:** Cross sections of the luminescence microscopy images Fig. 4.3(b) (closed squares) and Fig. 4.3(c) (open circles) along the symmetry axis of the tapered waveguide (indicated by the dashed line in the inset), normalized to the luminescence intensities just outside the hole array.

ferent upconversion emission intensities is sufficient to determine the absolute SPP field intensity at the location of the Er ions. Because the 550 nm emission will scale with the fourth power of the excitation intensity at most [129], we can estimate a lower limit to the SPP intensity enhancement with respect to the SPP intensity at the start of the taper of roughly 1.5. This demonstrates that the SPP concentration compensates for the losses that occur during propagation along the taper due to absorption and scattering. Further optimization of the taper geometry should lead to even higher field concentrations in foci significantly beyond the diffraction limit.

## 4.4 Conclusions

In conclusion, we have visualized the excitation, propagation, and concentration of surface plasmon polaritons in laterally tapered silver waveguides. The use of erbium upconversion luminescence provides a unique tool to image the field distributions of infrared SPPs with visible light. Interference effects due to SPP reflection inside the waveguide are observed, and the Er upconversion luminescence is significantly enhanced due to increased field intensities near the end of the waveguide. The work presented in this chapter demonstrates the enhancement of nonlinear effects due to SPP field concentration in tapered plasmonic waveguides. It paves the way for the focusing of light to subwavelength length scales, which will be further investigated in the following chapters.

# 5

---

## Nanofocusing in laterally tapered plasmonic waveguides

*The focusing of surface plasmon polaritons (SPPs) excited with 1.5  $\mu\text{m}$  light in a tapered Au waveguide on a planar dielectric substrate is investigated by experiments and simulations. We find that nanofocusing can be obtained when the asymmetric bound mode at the substrate side of the metal film is excited. The propagation and concentration of this mode to the tip is demonstrated. No sign of a cutoff waveguide width is observed as the SPPs propagate along the tapered waveguide. Simulations show that such concentrating behavior is not possible for excitation of the mode at the low-index side of the film. The mode that enables the focusing exhibits a strong resemblance to the asymmetric mode responsible for focusing in conical waveguides.*

### 5.1 Introduction

The delivery of light to ultrasmall length scales is an issue of crucial importance in nanophotonics. Because surface plasmon polariton waves supported by metal/dielectric interfaces can exhibit in-plane wavevectors larger than that of light with the same frequency, SPPs are suitable to achieve focusing to length scales smaller than the diffraction limit of light in the surrounding dielectric. Achieving focusing of SPPs to truly nanoscale dimensions will, for most frequencies,

require wavevectors that are much larger than those for SPPs on an extended flat metal/dielectric interface. Several complex waveguiding geometries do exhibit larger wavevectors: the azimuthally symmetric mode supported by a narrow metal cylinder [136], the mode in a thin metal slab embedded between two dielectrics that has an asymmetric transverse electric field across the film [31], and the mode propagating in a thin dielectric slab between two metal half-spaces [34]. By gradually reducing the thickness of these geometries along the direction of propagation, the SPP modes they support are predicted to become more strongly confined and concentrated to very small dimensions [43, 137, 138]. Demonstrating this effect requires the challenging fabrication of very sharp conical metal tips [121, 122, 139–141], metallic wedges, or nanoscale gaps [142, 143]. Moreover, the requirement of asymmetric transverse modal fields in the first two geometries makes excitation of the required SPP modes not straightforward.

In the previous chapter, the concentration of SPPs in a laterally tapered metal stripe waveguide on a dielectric substrate was demonstrated. Here, we show that it is possible to achieve nanofocusing of SPPs at the very tip of such a waveguide, both in experiment and simulations. The purely bound SPP mode at the high-index side of the tapered waveguide is excited with light with a wavelength of  $1.48\ \mu\text{m}$  in air. In this respect, the experiment differs significantly from that by Weeber et al. [112], who excite SPPs at the air side of a similar structure. As we will show in this chapter this is an essential difference with regard to whether nanofocusing can be achieved efficiently. We observe the focusing of SPPs in the tapered waveguide by detecting upconversion luminescence from erbium ions implanted in the substrate (see Chapter 4). A detailed study of the upconversion luminescence intensity distribution shows that SPPs are guided and concentrated along the taper all the way to its tip. No sign of a cutoff width is observed for the mode excited at the metal/substrate interface. These results suggest the excitation of a SPP mode that remains closely bound to the metal and has an increasing wavevector along the taper. It allows the desired focusing at the taper tip.

To explain the experimental findings we perform finite-difference time-domain (FDTD) calculations of the electromagnetic field in this structure. We find that strong field confinement and concentration at the taper tip is indeed possible when the purely bound SPP mode propagating at the substrate side of the metal film is excited. This focusing is absent for the leaky SPP mode that propagates predominantly at the air side of the metal, which is the mode that is usually studied in near-field experiments [112, 118, 135]. Based on the FDTD simulations we explain the different behavior of these modes by symmetry arguments. These results provide insight in the mechanism of guiding and nanofocusing in complex SPP tapering geometries and show how such nanofocusing can be achieved using a structured metal film on a planar substrate.

## 5.2 Methods

The experimental techniques used in these experiments closely follow those described in section 4.2. We will review the main points of sample fabrication and microscopy here, and indicate the differences.

### 5.2.1 Sample fabrication

To image the SPPs excited at the substrate side of the metal film, erbium ions implanted at a mean depth of 35 nm beneath the surface of the sapphire substrate are used as a probe of the SPP near field. Because energy levels of  $\text{Er}^{3+}$  that emit visible light can be populated under  $1.48 \mu\text{m}$  excitation through a nonlinear up-conversion process, the infrared SPP field can be imaged using visible wavelengths. The upconversion processes that are responsible for the Er levels emitting at 660 and 550 nm were discussed in section 4.2.1.

The experiments in this chapter are performed with a patterned Au film on the sapphire substrate, which is fabricated in an electron beam lithography process using a negative electron beam resist. The substrate is first coated with a layered resist stack consisting of 300 nm photoresist (S1813), 20 nm Ge and 110 nm negative electron beam resist (Ma-N 2401). Taper and hole array structures are patterned in the electron beam resist layer with electron beam lithography, and this pattern is transferred to the layers underneath by reactive ion etching. A 100 nm thick Au film is then evaporated directly on the substrate through resistive heating. Finally, the remaining photoresist is stripped in a liftoff process. A SEM micrograph of the tip of a typical taper fabricated this way is shown in Fig. 5.1. The apex diameter of the taper tip is found to be  $65 \pm 5 \text{ nm}$ .

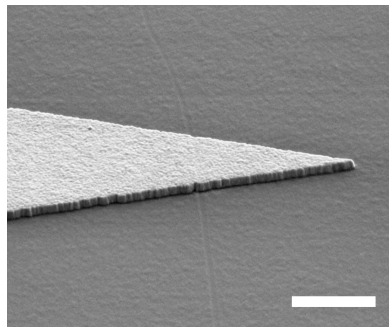


**Figure 5.1:** SEM micrograph of the end of a fabricated, tapered Au waveguide on an Er-implanted sapphire substrate. The scale bar is  $1 \mu\text{m}$ .

### 5.2.2 Optical measurements

A fiber-pigtailed 1.48  $\mu\text{m}$  diode pump laser (Fitel) is used as excitation source. The excitation beam is focused to a 10  $\mu\text{m}$  wide spot near the edge of a subwavelength hole array in the Au film to launch SPPs at the Au/sapphire interface. The SPPs propagate into a triangularly shaped tapered waveguide, starting at a distance of 6  $\mu\text{m}$  from the edge of the excitation array and having a base width of 12  $\mu\text{m}$  and a length of 60  $\mu\text{m}$  (taper angle 11.4°).

Two-dimensional maps of the SPP field intensity under the taper are obtained by detecting the luminescence of the Er ions implanted close to the Au/substrate interface in a scanning confocal microscope. The experiment is performed in two configurations.

In the geometry of Fig. 5.2(a), the sample is illuminated from the air side of the film under normal incidence through a microscope objective (NA= 0.12). In order to excite SPPs on the substrate side of the film, the pitch of the hole array is 0.8  $\mu\text{m}$ . The upconversion luminescence is collected through the substrate by a 50 $\times$  microscope objective (Nikon L Plan EPI CR, NA= 0.7). A rotated identical sapphire substrate is used below the implanted one to correct for the birefringence of sapphire, and the microscope objective is corrected to reduce the effect of spherical aberration induced by imaging through the two substrates.

In the configuration of Fig. 5.2(b), the sample is illuminated through the substrate under an angle of 47° with respect to the surface normal using a fiber focuser (NA= 0.1). Also in this configuration SPPs are excited on the substrate side of the film through the hole array that has a pitch of 1.46  $\mu\text{m}$ . A 100 $\times$  objective (Zeiss Epiplan-Neofluar, NA= 0.9) is used for imaging from the air side of the film. In both geometries the sample, together with the excitation source, is scanned using a piezo-electrically driven stage while the collection optics is kept fixed.

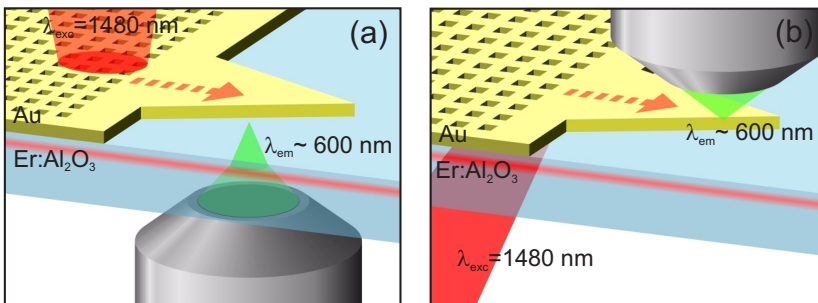


**Figure 5.2:** Schematic of the experimental geometry in the case of upconversion luminescence detection through the substrate (a), or from the air side of the sample (b). In both cases the SPPs are excited with infrared light at the Au/Al<sub>2</sub>O<sub>3</sub> interface in the direction of the arrow. The red line schematically indicates the Er depth profile.



Recorded upconversion luminescence spectra are integrated from 510 to 570 nm and from 640 to 700 nm to obtain images of the upconversion luminescence from the  $^4S_{3/2}/^2H_{11/2}$  and  $^4F_{9/2}$   $Er^{3+}$  levels, respectively.

### 5.3 Results and discussion

Figure 5.3(a) shows a two-dimensional image of the 550 nm upconversion luminescence intensity, obtained as described above with an excitation power of 20 mW at 1.48  $\mu m$ . The luminescence is collected through the substrate, i.e., from the side of the Au film where the SPPs are excited and the Er ions are located. In the left of the image, indicated by the arrow, the excitation spot on the hole array can be recognized. An excited SPP beam is visible that exits the excitation array to the right and is coupled into the tapered waveguide, which starts at  $x = 16 \mu m$ . Along the taper an interference pattern is observed and the upconversion luminescence intensity gradually increases as the beam propagates further into the taper. The interference pattern can be ascribed to the reflection of the infrared SPP beam at the sides of the tapered waveguide (see Chapter 4), which causes the optical energy to be concentrated as the waveguide width keeps decreasing. From  $x = 60 \mu m$  onwards toward the apex, only a single maximum is observed across the waveguide.

Shown in Figs. 5.3(b) and 5.3(c) are images of the last 12  $\mu m$  of the taper, obtained by detecting luminescence from the 550 nm and 660 nm Er levels, respectively. To indicate the position of the taper tip in these figures, Fig. 5.3(d) shows an image of the same scan area obtained by collecting normal-incident reflected light at a wavelength of 550 nm. A clear difference is noticeable between the images of the luminescence taken with 550 and 660 nm detection wavelengths. Whereas the intensity of the 660 nm upconversion luminescence is rather constant along the last 12  $\mu m$  of the tapered waveguide, the 550 nm luminescence intensity shows a marked increase towards the tip. The spot of maximum intensity is achieved within the last 2  $\mu m$  of the taper, where the lateral width of the waveguide is less than 400 nm. The 550 nm luminescence intensity in this spot is more than 10 times larger than at the start of the tapered waveguide. The differences between Figs. 5.3(b) and (c) can be explained through the different pump power dependencies of the nonlinear excitation of these two Er levels. While three infrared pump photons are needed to excite one ion to the  $^4F_{9/2}$  state emitting at 660 nm, four are needed to populate the  $^4S_{3/2}$  manifold emitting at 550 nm. The emission at 550 nm therefore exhibits a stronger dependence on the local SPP field intensity than the 660 nm luminescence.

Given this argument, it may seem surprising that the intensity of the 550 nm luminescence collected at  $x = 76 \mu m$  (position B) is two times higher than that at  $x = 67 \mu m$  (position A), while the 660 nm luminescence at position B is actually slightly smaller than at position A. We attribute this to an effect related to the spatial resolution of the detection, which is  $\sim 800$  nm. Suppose that the SPP field is concentrated at position B to a spot smaller than the focal area, and less so at position

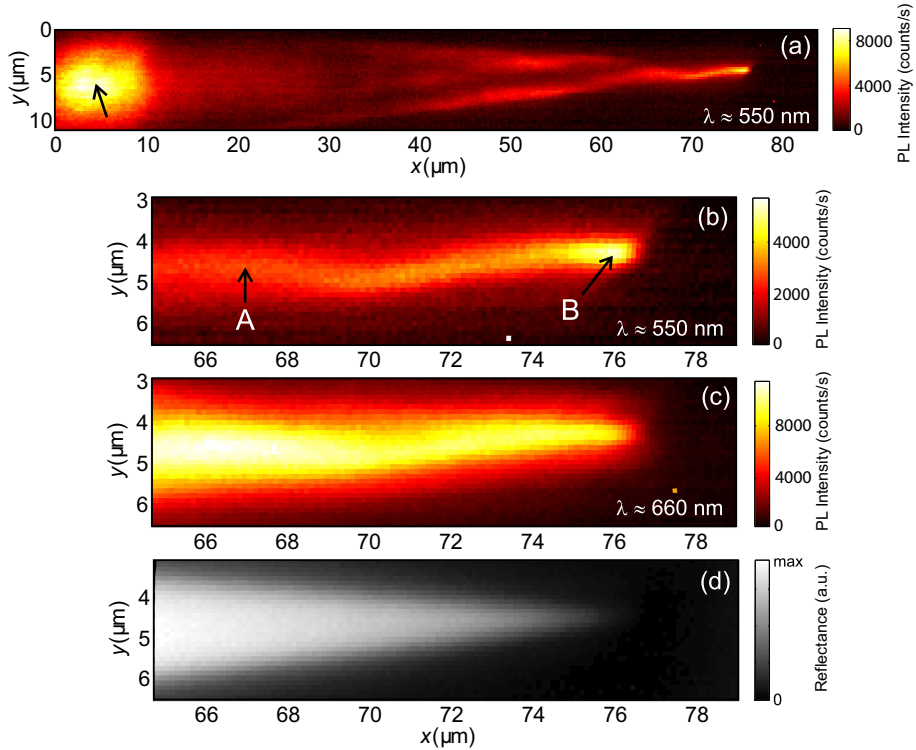


**Figure 5.3:** (a) Upconversion luminescence image from the hole array (left side) and 60  $\mu\text{m}$  long tapered waveguide (right side) sections, taken at 550 nm. The excitation spot is marked by the arrow on the left side of the image. (b) and (c) Detailed maps of the upconversion intensity near the tip of the waveguide, taken at 550 nm and 660 nm, respectively. A 1.48  $\mu\text{m}$  pump at a power of 20 mW was used. The arrows indicate the positions at which power dependency curves were obtained. (d) Optical microscopy image of the same region as (b) and (c), obtained by detecting reflected light from a halogen lamp at a wavelength of 550 nm.

A. In that case, it is possible that the averaged 660 nm upconversion luminescence intensity in the focal area is equal at both positions, while the averaged 550 nm intensity at position B is larger than that in A, as this level is populated by a higher-order nonlinear process.

### 5.3.1 Power dependence

The previous considerations suggest the importance of investigating the power dependence of the upconversion luminescence intensity at different positions along the waveguide. Figure 5.4 shows the upconversion luminescence at 550 nm and 660 nm measured at positions A and B indicated in Fig. 5.3(b), as a function of

the excitation laser power. The local pump intensity that is responsible for the generation of upconversion luminescence scales linearly with the excitation laser power, and it can be different at both positions for a particular excitation power. The data is plotted on a double-logarithmic scale. The numbers in the figure indicate the slopes of linear fits to the logarithm of the data with luminescence intensity between 100 and 1000 counts/s.

We first note that the slopes of the power dependence curves in Fig. 5.4 differ from the values expected in the limit of infinitely small pump power. These are 3 and 4 for the levels emitting at 660 nm and 550 nm, respectively. Even at moderate SPP excitation intensities, saturation of the various Er levels can reduce the slope significantly [125, 129]. If we assume 100% coupling efficiency of the incident light to SPPs propagating out of the excitation array, we can estimate an upper limit of the local SPP intensity just outside the array at the depth of the Er ions to be  $0.6 \text{ MW/cm}^2$  for the 20 mW incident power. For such excitation power densities and the Er concentration used here, large saturation effects are indeed expected [125].

Comparing the slopes at different positions, it is found that for both detection wavelengths the slope at position B is significantly less than the slope at position A. This implies that at the tip of the waveguide (position B) the Er energy levels are more strongly saturated. Hence the SPP field intensity in that position is larger. At relatively low excitation laser powers, we can see from Fig. 5.4 that the detected upconversion intensity at the tip exceeds that at position A also for the 660 nm luminescence, since the effect of saturation is smaller in that regime.

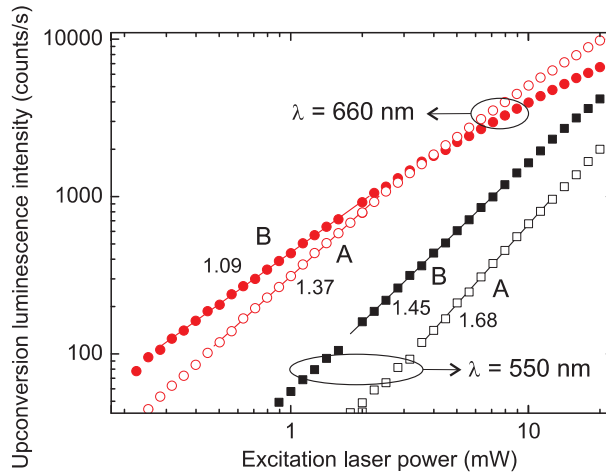


**Figure 5.4:** Excitation laser power dependence ( $\lambda = 1.48 \mu\text{m}$ ) of the upconversion luminescence at 550 and 660 nm collected at positions A and B (indicated with arrows in Fig. 5.3(b)). The lines are linear fits to the data for luminescence intensities between 100 and 1000 counts/s, and the slopes of these fits are indicated. The error in the fit is of order 0.01.

Even when considering pump conditions at positions A and B that result in an equal detected upconversion luminescence intensity (see Fig. 5.4), the difference in the slope of the curves at these excitation powers indicates that there is a clearly different amount of saturation at both positions. This observation strongly suggests that the local excitation field is indeed not homogeneously distributed within the focal area: at the tip (position B) the excitation field is concentrated to dimensions smaller than the microscope resolution. When averaging the upconversion luminescence over the focal area, this results in approximately equal detected intensities for the 660 nm luminescence in Fig. 5.3(c), even though the maximum SPP intensity at the tip is actually larger than that at position A. This SPP concentration is revealed through the observed increase in saturation at the tip.

As mentioned before, the level emitting at 550 nm is populated through a higher-order nonlinear process, so the increased SPP intensity at the tip (position B) with respect to position A can be apparent from both the enhanced upconversion intensity and the increased saturation at the tip. Still, for both wavelengths focal averaging limits the detection of the maximum luminescence intensity at the tip. With these considerations, both the observed difference between the intensity maps taken at different wavelengths as well as the behavior of the pump power dependencies at positions A and B can be explained in terms of an enhanced SPP field at the tip.

We note that towards the taper end, the radiative decay rate of the Er energy levels could change as a result of a change in the local optical density of states. The observed enhanced upconversion near the tip could be ascribed to an enhanced radiative decay rate; however, this is inconsistent with the larger degree of saturation near the tip. Although an effect of the taper on the emission rates cannot be excluded, it cannot be the dominant mechanism behind the observed luminescence enhancement near the tip.

### 5.3.2 Absence of cutoff

The broad lateral intensity variations along the length of the taper in Fig. 5.3(a) are explained by interference due to reflection of SPP waves at the metal taper edge (see Chapter 4). In addition to this effect, we conclude from these experiments that the SPP fields are further concentrated along the last stretch of the tapered waveguide, to the position of maximum intensity observed in Fig. 5.3(b).

The precise determination of the location of maximum SPP intensity with respect to the taper apex is limited by the spatial resolution of the microscope. To investigate this further, Fig. 5.5 shows upconversion luminescence images collected from the air side of the film for 550 nm and 660 nm (see Fig. 5.2(b) for the experimental configuration). In this case, the SPPs on the metal-substrate interface are excited by illuminating the hole array through the substrate under a properly chosen angle. This geometry allows the use of an objective with a larger numerical aperture for collecting the luminescence, which results in a higher spatial resolution compared to Fig. 5.3. The position of the edge of the taper, derived from

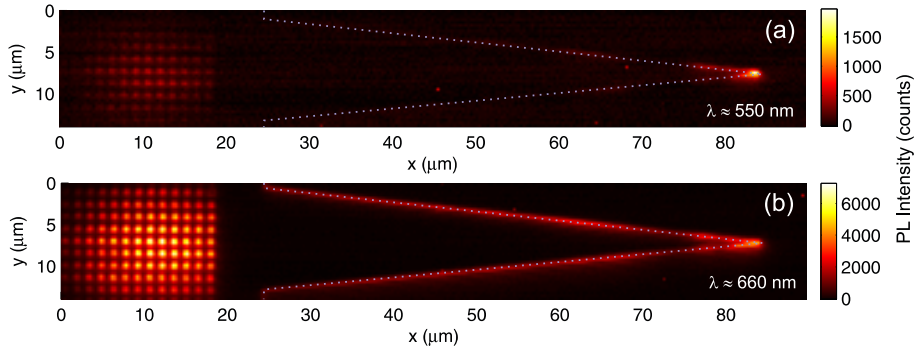


**Figure 5.5:** Upconversion luminescence images taken from the air side of the film at (a) 550 nm and (b) 660 nm. The edge of the taper is indicated by the dotted line. Upconversion luminescence is observed from the edges of the taper, and the maximum intensity is detected at the taper tip.

electron microscopy data, is drawn as a dotted line. Although the sample is now imaged from the side of the Au film opposite to the Er-doped substrate, clear Er upconversion luminescence is detected both through the holes and at the edges of the waveguide. A maximum is observed at the taper tip for both wavelengths. The detected 550 nm luminescence intensity at the tip is much larger than the intensity along the edges of the rest of the waveguide. The luminescence at the edges is hard to discern in the 550 nm luminescence intensity image as the color scale is scaled to the intensity at the tip. As in the previous experimental geometry, the luminescence increase at the tip is stronger for the 550 nm luminescence than for the 660 nm luminescence. Although the role of diffraction of the luminescence at the metal edges makes a quantitative interpretation of these images difficult, we note that the maxima are observed at a distance less than  $1.0 \mu\text{m}$  from the tip, corresponding to a waveguide width smaller than 200 nm.

In the experiments presented in Figs. 5.3 and 5.5 no indication is found that the mode propagating along the tapered waveguide experiences cutoff for a particular waveguide width. Such a cutoff width was predicted to exist for the SPP modes supported by a stripe waveguide on a dielectric substrate, both for the leaky modes at the air side of the metal film and for the bound modes at the substrate side [115]. In that work, a cutoff stripe width of  $\sim 500$  nm was calculated for the bound mode for a free-space wavelength of 800 nm. The cutoff results from a decreased wavevector, and hence reduced mode confinement in narrower waveguides. As a result, this mode could not exhibit focusing along a tapered waveguide. The fact that in the experiment reported here no cutoff behavior is observed down to a width smaller than 400 nm, for a wavelength much larger than that used in reference [115], suggests that another mode may be involved in the focusing that does not experience cutoff and that becomes more strongly confined to the waveguide as the width decreases.

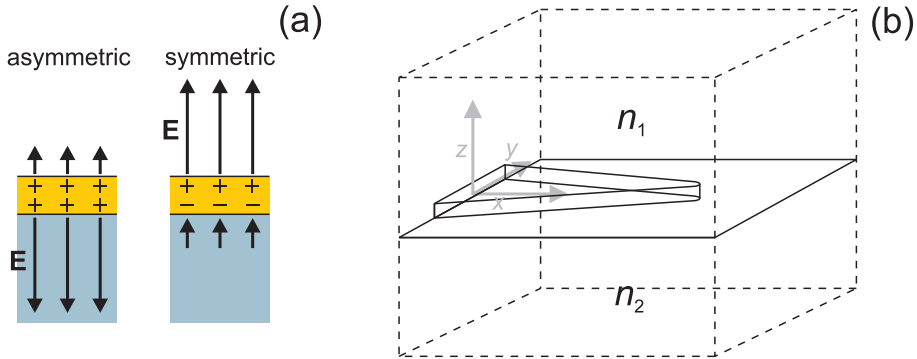


**Figure 5.6:** (a) Sketch of the electric field of the two SPP modes in an infinitely extended metal film, showing the symmetry of the transverse electric field and the surface charge. The direction of propagation is normal to the image plane. (b) Schematic of the geometry used in the FDTD calculations. The Au taper has a length of  $7.8 \mu\text{m}$  and an apex diameter of  $60 \text{ nm}$ . The refractive index of the substrate is  $n_2$ , and that of the surrounding medium is  $n_1$ .

## 5.4 Modeling

To investigate the absence of cutoff and the observed concentration up to very narrow waveguide widths we perform three-dimensional simulations of the electromagnetic fields in the tapered waveguide structure. A finite-difference time-domain (FDTD) algorithm [76] is used to calculate the time-averaged field intensity in the structure upon excitation of a SPP mode at the substrate side of the film. Additionally, a comparison is made with excitation of the SPP mode at the low-index side of the waveguide.

Modes localized at different sides of a metal film embedded in an asymmetric dielectric environment generally have different properties, as discussed in section 1.2.2 [31, 113, 115]. As sketched in Fig. 5.6(a), the SPP mode that has most of its field energy localized in the high-index substrate is called asymmetric since its transverse electric field has an opposing sign at either side of the metal film. The sign of the surface charge at both metal/dielectric interfaces is equal for this mode. In contrast, the mode propagating predominantly at the low-index side of the film has electric fields with equal sign at both sides of the film, and is therefore called symmetric. Accordingly, the surface charge at both interfaces associated with this mode has an opposite sign.

### 5.4.1 Simulation methods

The simulation geometry is displayed schematically in Fig. 5.6(b). All structural parameters are taken the same as in the experiment. The tip of the taper is rounded in the  $xy$  plane with an apex diameter of  $60 \text{ nm}$ , consistent with the experimentally

investigated apex. Only propagation on the last  $7.8 \mu\text{m}$  of the tapered waveguide is calculated to reduce the computational effort. This does not allow resolving the large scale interference pattern caused by reflection at the waveguide edges that was observed in Fig. 5.3(a), but it provides insight in the behavior of SPPs in the region of interest, corresponding to Figs. 5.3(b-c). Perfectly matched layer simulation boundaries are used around the structure to absorb all radiated power as well as SPPs reflected in the negative  $x$  direction. Electric field symmetry is assumed with respect to the  $y = 0$  plane. The Au permittivity is modeled by a Drude model including damping, of which the parameters are obtained by fitting the optical constants given by Johnson and Christy [26] around a wavelength of  $1.48 \mu\text{m}$ . The discretization step inside the metal is varied from  $4.5 \text{ nm}$  at the start of the taper to  $3 \text{ nm}$  in the vicinity of the apex. The excitation source is a  $25 \text{ fs}$  pulse with a center frequency corresponding to a free-space wavelength of  $1.48 \mu\text{m}$ . It is injected in the positive  $x$  direction at  $x = 0$  and has a transverse ( $yz$ ) field profile identical to a SPP mode profile of a waveguide with a width of  $1.56 \mu\text{m}$ . This SPP mode profile is calculated by a finite-difference frequency domain mode solver, described in reference [144], which uses the same spatial discretization as the FDTD simulation. Steady-state time-averaged field intensity profiles corresponding to a free-space wavelength of  $1.48 \mu\text{m}$  are obtained by Fourier transforming the fields obtained from the FDTD simulation.

Figure 5.7(a) shows the electric field intensity profile of the purely bound SPP mode that is excited at the start of the tapered waveguide. The strongest component of the electric field is directed normal to the film ( $E_z$ ) [113]; its real part is plotted in Fig. 5.7(b). From the opposing signs of  $E_z$  at both sides of the metal film it can be seen that the transverse electric field is asymmetric across the film. As mentioned before, this is characteristic for a mode localized at the substrate side

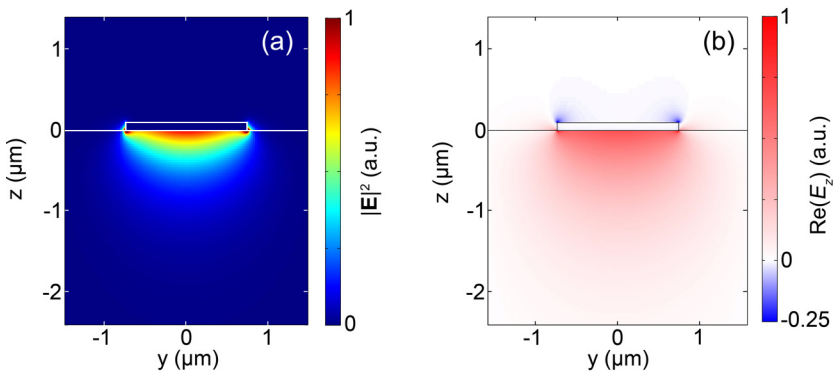


**Figure 5.7:** Mode profile of the asymmetric bound mode used as excitation source at  $x = 0$  in the FDTD simulation. Shown are the electric field intensity (a) and the real part of the electric field component in the  $z$  direction (b).

of the film [31, 113]. The calculated mode profile does not possess any field nodes along the width of the structure, and thus the induced surface charge has equal sign along the complete circumference of the waveguide. Although the mode possesses strong fields at the metal corners [113], a large fraction of its energy is contained in a single broad intensity maximum under the waveguide. It is therefore likely to be efficiently excited in our experiment.

### 5.4.2 Simulation results: Three-dimensional nanofocusing

The result of the FDTD simulation using the profile of Fig. 5.7(a) as input is shown in Fig. 5.8. Figure 5.8(a) shows the time-averaged electric field intensity in the plane  $z = -35$  nm, which is the depth at which the Er ions are located in the experiment. Three observations can be made. First, the field is strongly concentrated at the taper tip, to a spot much smaller than the wavelength of light in the substrate. The full width at half maximum of this spot in the  $y$  direction is 92 nm, which is limited by the 60 nm apex diameter. Second, no sign of a cutoff width is observed. Third, a pronounced interference pattern can be seen that extends to the end of the taper

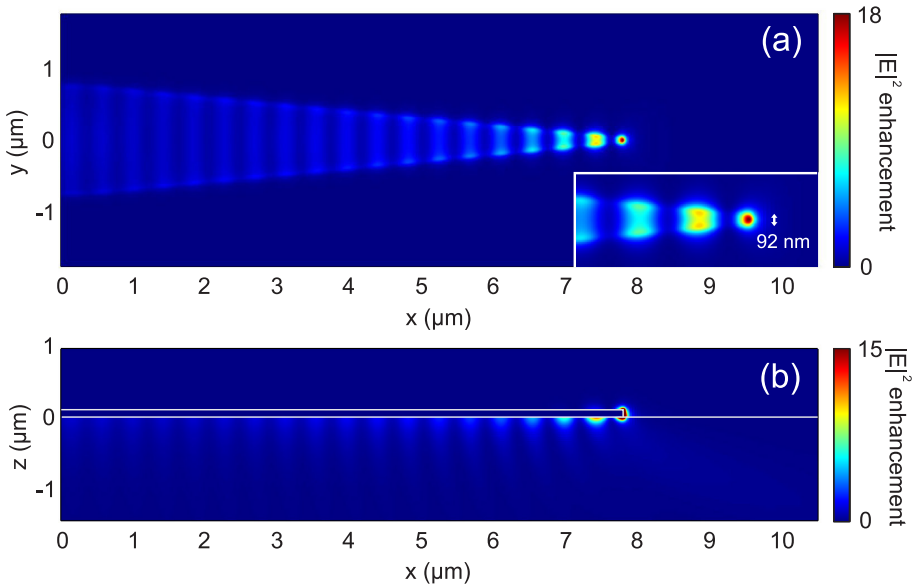


**Figure 5.8:** Electric field intensity in the planes  $z = -35$  nm (a), and  $y = 0$  (b). The scale is normalized to the average intensity at the start of the tapered waveguide. Both color scales are saturated to improve the visibility away from the tip. The intensity enhancement at  $z = -10$  nm below the tip apex is 100. The inset of (a) shows a detail of the electric field intensity in the plane  $z = -35$  nm at the tip. The intensity distribution at the tip has a full width at half maximum of 92 nm.



and has a periodicity of half the SPP wavelength. This suggests that the SPP wave propagating in the taper is reflected from the extremity of the tip. It resembles observations on SPPs propagating along a thin metal nanowire, which also show strong reflections from the nanowire ends [56].

Figure 5.8(b) shows a cross cut of the electric field intensity  $|\mathbf{E}|^2$  in the structure along the  $y = 0$  plane. At the tip at a depth of 10 nm below the film, the electric field intensity is enhanced by more than a factor 100 with respect to the start of the tapered waveguide (not visible in the scale bar due to saturation in the color scale). This enhancement is limited by the finite sharpness of the tip.

From Fig. 5.8(b) it is also clear that the SPP field becomes much more confined in the transverse ( $z$ ) direction as the taper tip is approached. In Fig. 5.9(a) the electric field intensity is plotted as a function of  $z$  for the start and the end of the taper. At the end of the taper the SPP intensity decays in a few tens of nm from the metal/substrate interface; more than an order of magnitude faster than at the start. Clearly, the field is truly concentrated to nanoscale transverse dimensions, remaining tightly confined to the metal surface.

It can be seen from Fig. 5.9(a) that for very narrow widths a significant intensity builds up at the air side of the metal film. This is further illustrated in Fig. 5.9(b), which shows a cross-section of the field intensity at the taper tip in the plane  $x = 7.77 \mu\text{m}$ , where the Au taper width is only 60 nm. The field is predominantly localized at the metal corners, but no nodes are observed in the field around the tapered waveguide. This indicates that also in this plane the surface charge has identical sign around the waveguide, and that the transverse electric field across the waveguide must thus be asymmetric. This symmetry strongly resembles that of the azimuthally symmetric mode supported by a metal cylinder embedded in a

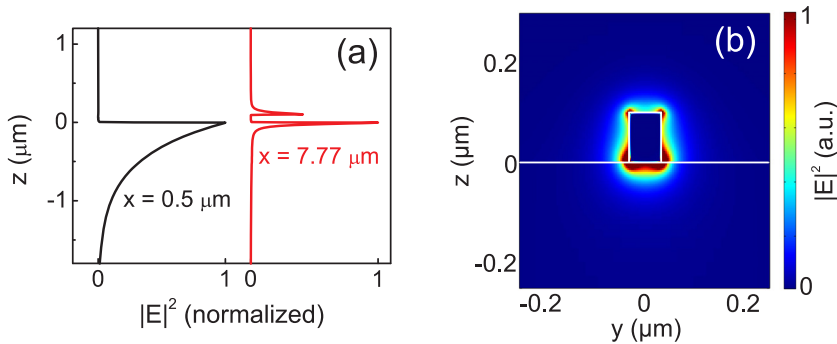


**Figure 5.9:** (a) Normalized vertical cross sections of Fig. 5.8(b) at the start ( $x = 0.5 \mu\text{m}$ , black) and the end ( $x = 7.77 \mu\text{m}$ , red) of the taper, showing the increase of vertical confinement towards the taper tip. (b) Cross section of the electric field intensity near the tip of the tapered waveguide, at  $x = 7.77 \mu\text{m}$ . The field is predominantly localized at the metal corners. No field nodes are present along the metal surface.

homogeneous dielectric background, which is predicted to allow nanofocusing in a conical waveguide [43]. Our results show that similar nanofocusing is possible in all-planar geometries. The analogy between modes propagating in metal cylinders and in laterally tapered waveguides will be discussed in detail in Chapter 6.

### 5.4.3 Comparison between excitation at the substrate or air sides of the metal film

Finally, we investigate if nanoscale focusing in planar waveguide tapers could also be possible when leaky symmetric SPP modes localized at the low-index side of the film are excited, and compare it to the behavior of bound SPPs at the high-index side of the film. This is relevant since SPPs at the low-index side of the film have been extensively studied in stripe waveguides, because they can be probed at high resolution using near-field microscopy [112, 118, 135]. To make a fair comparison, the effective guiding index of the two types of modes should be as close as possible in order not to affect cutoff conditions solely because of a difference in SPP wavevector. To study symmetric modes we therefore consider a structure in which the refractive index above the metal film is  $n_1 = 1.74$  (equal to that of the substrate for the asymmetric mode calculations). The refractive index of the substrate is increased such that the ratio  $n_1/n_2$  is the same as before ( $n_2 = 1.74^2$ ). Because the mode solver we used does not solve for leaky modes, we now use an array of ten coherent oscillating dipoles oriented along the  $z$  direction as excitation source in the FDTD calculation. The dipoles are positioned at a line parallel to the  $y$  direction, at a distance of 10 nm from the film, either in the high-index material to excite asymmetric modes (at  $x = 0$ ,  $z = 10$  nm) or in the low-index material to excite symmetric modes ( $x = 0$ ,  $z = 110$  nm). Figure 5.10 shows the electric field intensity in the plane  $y = 0$  for both cases. In Fig. 5.10(a), dipole excitation was used at the high-index side of the film; as expected, the result is very similar to that in Fig. 5.8(b), indicating that a mode is excited with the ability to cause nanofocusing. Figure 5.10(b) shows the result for excitation at the low-index side of the film. Now the behavior is completely different. Surface-bound waves are observed, but no concentration effect is visible at the taper tip. No reflection of SPPs from the tip is observed. This behavior is in agreement with earlier work that predicted that as the waveguide width is decreased, the mode effective index of the symmetric leaky mode will decrease and transverse confinement will be reduced [115]. As the mode gets less confined in the  $y$  direction, more energy is lost to radiation into the high-index dielectric substrate, and losses will increase. After a certain cutoff width, only radiation modes contribute to the local field [135], which cannot cause focusing to nanoscale dimensions.

As can be seen from these simulations, the excitation of a SPP mode that is guided and concentrated to arbitrarily small widths is only possible with the asymmetric bound mode of the stripe waveguide, and hardly with a symmetric leaky mode. This is due to the fact that only the former possesses the correct symmetry to cause nanofocusing. The fact that the predicted intensity enhancement and

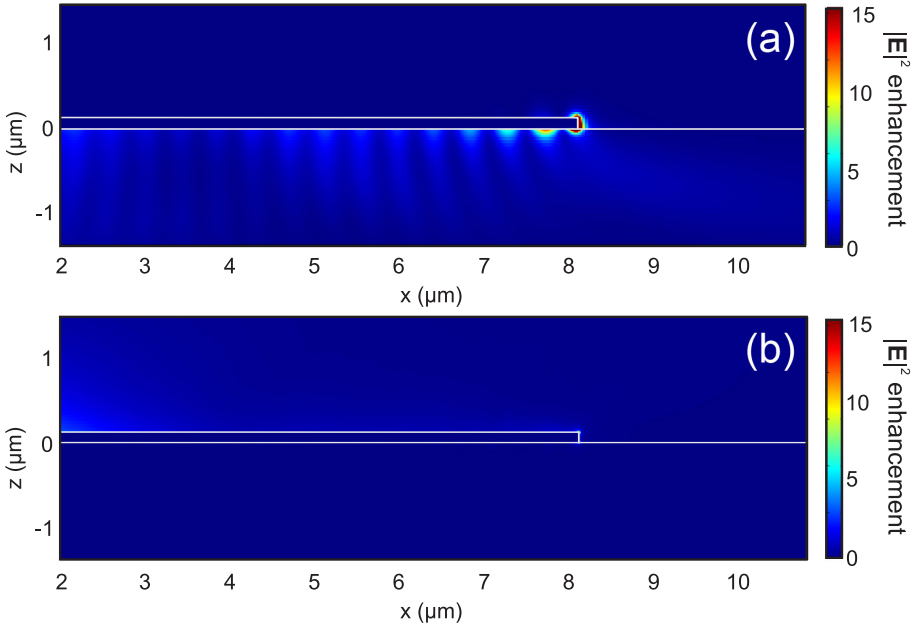


**Figure 5.10:** Electric field intensity in the  $y = 0$  plane for the asymmetric bound mode at the high-index side of the film (a), and the symmetric leaky mode at the low-index side of the film (b). The color scale is saturated in (a), and the same for both figures.

standing wave pattern are not fully reproduced in the detected upconversion luminescence is attributed to a combination of focal averaging and saturation of the excited Er levels, possibly in conjunction with losses due to surface and sidewall roughness [56]. We conclude that nanoscale focusing can be obtained at the taper tip to dimensions and intensities that are only limited by the sharpness of the taper apex.

## 5.5 Conclusions

We have shown experimentally that guiding and focusing of SPPs is possible in laterally tapered Au waveguides on a planar dielectric substrate when the proper initial SPP mode is excited. For the asymmetric bound mode propagating at the substrate side of the film, excited with  $1.48 \mu\text{m}$  light, experiments show concentration occurring beyond a waveguide width smaller than  $400 \text{ nm}$ . No sign of a cutoff width is observed along the taper. By comparing the spatially-resolved upconversion intensities and power dependencies of emission from different Er levels, we conclude that SPP focusing is the dominant mechanism producing the spot of maximum

intensity at the taper tip. FDTD simulations corroborate these results and show that focusing down to truly nanoscale volumes is possible in this geometry. The nanofocusing is attributed to a guided SPP mode that has an asymmetric electric field distribution across the tapered waveguide. For symmetry reasons, efficient nanofocusing cannot be achieved with symmetric leaky SPP modes propagating at the low-index side of the film. Varying parameters such as film thickness, tapering angle, excitation frequency and tip sharpness is expected to allow optimization of the possible field enhancements and focusing efficiency.

# 6

---

## Nanowire plasmon excitation by adiabatic mode transformation

*We show with both experiment and calculation that highly confined surface plasmon polaritons can be efficiently excited on metallic nanowires through the process of mode transformation. One specific SPP mode in a metallic waveguide is identified, that adiabatically transforms to the confined nanowire mode as the waveguide width is reduced. Phase- and polarization-sensitive near-field investigation reveals the characteristic antisymmetric polarization nature of the excited nanowire mode and explains the coupling mechanism.*

### 6.1 Introduction

The combined nature of surface plasmon polaritons as part matter excitation and part light field enables a large control of electromagnetic fields at subwavelength length scales. Metal surfaces support evanescent waves for all frequencies smaller than the surface plasmon resonance frequency. Whereas in all-dielectric photonic structures the wavelength in the dielectric sets a lower bound to the size to which light can be confined, properly shaped metallic structures can confine light fields to arbitrarily small length scales. The potential of highly confined SPPs includes subwavelength guiding [56, 65, 83, 110, 145–149], efficient single-molecule sensing [150], enhanced nonlinear effects [10, 123, 151], and the miniaturization of photonic circuits [18, 65, 83]. Moreover, the small mode sizes of nanoscopic plasmon

waveguides lead to a strong interaction with individual quantum emitters, which may be useful in quantum information [14, 15, 152].

On a metallic cylinder a waveguided mode with azimuthal field symmetry, i.e., having ‘radial’ polarization, exists for any cylinder radius. At THz frequencies and below, these so-called Sommerfeld waves are in general only weakly guided [153, 154]. In the optical and near-infrared regime however, the analogous SPP wave propagating along a metal nanowire is predicted to become strongly confined to the wire when its radius is reduced to tens of nanometers [43, 57, 147, 155, 156]. The combination of the subwavelength mode profile and the ‘radial’ symmetry of the nanowire mode causes the field overlap integral of this mode with a linearly polarized light wave to be very small. This makes it difficult to couple the nanowire mode efficiently to or from a macroscopic wave, such as a beam incident from the far field or a low-loss guided mode in a typical wavelength-sized waveguide.

In this chapter, we identify a unique SPP mode propagating on a metallic stripe of  $\mu\text{m}$ -scale width, which continuously evolves to the nanowire mode as the width of the stripe is decreased. When this mode is excited in a stripe that is tapered down to the desired nanowire size, the wave propagating along the taper can remain in the corresponding eigenmode, thereby being adiabatically converted [157, 158] to the nanowire mode. We experimentally demonstrate that such a structure can thus serve as the required coupling element to efficiently excite nanowire SPPs. The transformation and subsequent propagation of SPPs on nanowires as small as 60 nm is investigated by near-field microscopy. By combining phase- and polarization-sensitivity, we experimentally reveal the special polarization nature of the excited nanowire mode, underpin the efficiency of the adiabatic transformation process and determine the dispersion and losses of the nanowire mode.

## 6.2 Surface plasmon polariton mode transformation

To understand the evolution of waves propagating along tapered waveguides, it is useful to consider the modes guided by infinitely long waveguides for varying waveguide sizes. The SPP modes propagating along metal stripe waveguides are intimately related to those of cylindrical waveguides, for which analytical solutions can be obtained. In this section, we first revisit those modes to elucidate the connection between rectangular and cylindrical geometries and discuss the influence of shape and dielectric environment on the eigenmodes. We then focus our attention on the transformation of modes in stripe waveguides on a dielectric substrate.

### 6.2.1 Surface plasmon polaritons on a metal cylinder

The modes guided by a metal cylinder of radius  $a$  with dielectric constant  $\epsilon_1$  aligned along  $\hat{z}$  and embedded in a homogeneous dielectric  $\epsilon_2$ , as first described by Sommerfeld [153], can be found by solving the dispersion relation [136, 156, 159]

$$k_0^2 \left( \frac{J'_m(u)}{uJ_m(u)} - \frac{H_m^{(2)'}(v)}{vH_m^{(2)}(v)} \right) \left( \frac{\epsilon_1 J'_m(u)}{uJ_m(u)} - \frac{\epsilon_2 H_m^{(2)'}(v)}{vH_m^{(2)}(v)} \right) - m^2 k_z^2 \left( \frac{1}{v^2} - \frac{1}{u^2} \right)^2 = 0, \quad (6.1)$$

where

$$u = \gamma_1 a, \quad v = \gamma_2 a, \quad \gamma_i^2 = \epsilon_i k_0^2 - k_z^2, \quad (6.2)$$

and  $k_0$  is the free-space wavevector. The Bessel function of the first kind  $J_m(u)$  and Hankel function of the second kind  $H_m^{(2)}(v)$  are chosen such that the field is well behaved at the cylinder axis and decays to zero at infinite distance from the cylinder. The prime above a cylinder function denotes differentiation with respect to the function argument. The azimuthal symmetry of the modes is determined by the nonnegative integer  $m$ . This dispersion relation can be derived analogous to the treatment of multilayer slab waveguides in section 1.2.1 by employing cylindrical coordinates.

In Fig. 6.1(a), we plot the normalized wavevector  $\text{Re}\{k_{\parallel}\}/k_0$  of the bound modes guided by a gold cylinder embedded in a homogeneous medium with refractive index  $n_{\text{glass}} = 1.50$  as a function of cylinder radius. Here,  $k_{\parallel}$  is the SPP wavevector component along the waveguide, and  $k_0 = \omega/c$  is the free-space wavevector. The free-space wavelength is 1550 nm, and the optical constants were obtained from ellipsometry on the sample studied in the experiments in this chapter. The lowest order ( $m = 0$ ) mode (plotted for a radius of 2.5  $\mu\text{m}$  in the inset) is azimuthally symmetric and exhibits a diverging wavevector as the radius decreases to zero, characteristic for highly confined plasmonic modes.

If the waveguide size of dielectric or photonic crystal waveguides is decreased, the wavevector will either decrease until guided propagation stops at the critical waveguide cutoff size, or it will asymptotically approach the wavevector in the surrounding medium, in conjunction with a continuously increasing extent of the evanescent field outside the waveguide. The latter is also the case for the  $m = 1$  mode in this homogeneous dielectric environment. It is guided for arbitrarily small radii, albeit with a wavevector that tends to the wavevector in the dielectric surrounding. Correspondingly, the confinement for this mode is very weak for small wire radii. All higher order modes exhibit cutoff at some radius. In contrast, the  $m = 0$  mode is guided on cylinders with very small radius while becoming strongly confined when the radius decreases. It is therefore recognized as the nanowire mode.

## 6.2.2 Computation method for complex waveguiding geometries

Other waveguide geometries, such as stripe waveguides, cannot be treated by purely analytical means. In the following, we obtain the bound and leaky modes of infinitely long waveguides with rectangular cross sections using a finite-element method solver [160]. The optical constants and metal thickness were directly obtained from ellipsometry on the sample used in the experiments in this chapter.

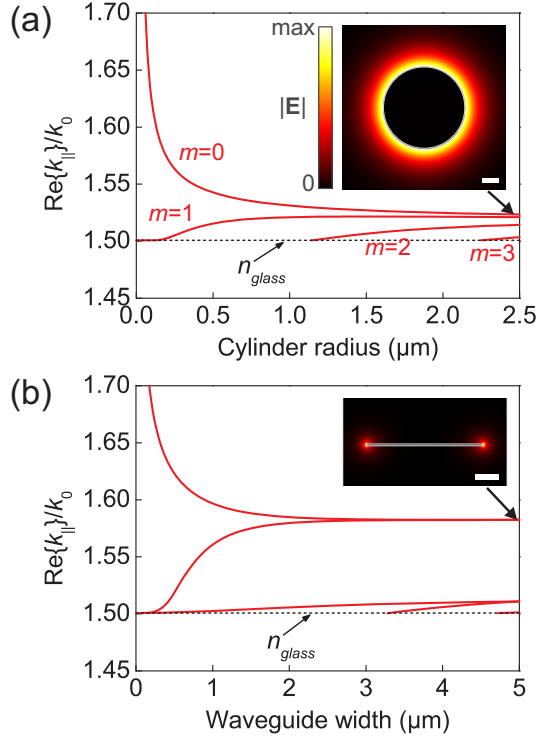


**Figure 6.1:** Normalized wavevector of the modes guided by a Au cylinder (a) or stripe waveguide (b) embedded in glass. The insets show profiles of the electric field amplitude of the lowest order modes. Scale bars are 1  $\mu\text{m}$ .

The spatial element size varies from 0.1 nm at the corners of the waveguide to 100 nm far from the guide. Perfectly matched layer (PML) simulation boundaries are located many micrometers from the guide. Throughout the calculations, convergence of  $|k_{\parallel}|/k_0$  to  $10^{-5}$  is maintained.

### 6.2.3 SPP modes in stripe waveguides in a homogeneous dielectric environment

Physical behavior similar to that for the modes on cylindrical waveguides is found for the SPP modes of a 77 nm thick rectangular stripe in a homogeneous dielectric, plotted in Fig. 6.1(b) [161, 162]. The lowest order mode (the mode with the largest wavevector) again corresponds to the nanowire mode for small waveguide widths, with a large wavevector and subwavelength confinement. In this case, two modes become low-loss, weakly confined waves (comparable to the  $m = 1$  mode in the cylinder) as the width is reduced [162, 163].



The rectangular waveguide shape has two main effects on the waveguide modes when compared to the cylindrical case. First, the strongly anisotropic waveguide cross section lifts the degeneracy of some modes guided by the cylinder, for instance that of the weakly guided  $m = 1$  mode. Second, the fields of some modes tend to be concentrated at the sharp waveguide edges. This is for example clear for the lowest order mode, which is guided predominantly by the waveguide edges (see inset of Fig. 6.1(b)). For that reason, it also has a rather large wavevector for large widths. This mode profile (with a transverse electric field that is purely anti-symmetric across the metal film) makes it difficult to excite this mode with a broad incident beam.

### 6.2.4 SPP modes in stripe waveguides on a dielectric substrate

Figure 6.2(a) presents the calculated width dependence of the normalized wavevector of the modes guided by a 77 nm thick straight Au stripe on glass for various wavelengths. For large widths the asymmetry of the dielectric environment has a strong effect on eigenmodes of the waveguide, separating modes that are localized

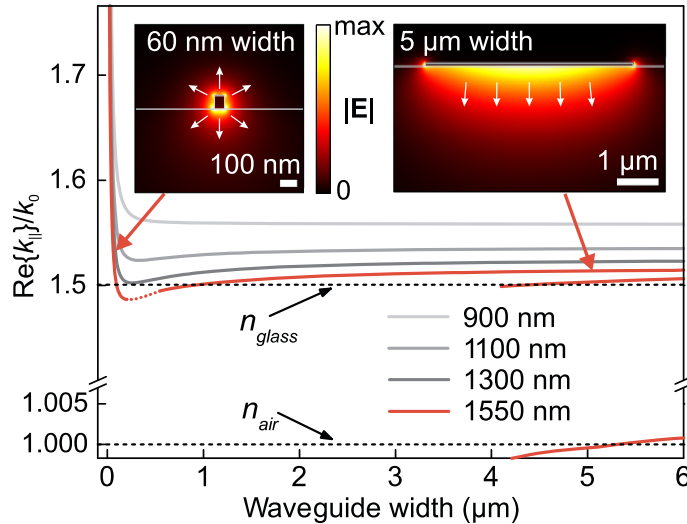


**Figure 6.2:** Normalized wavevector of the SPP modes guided by a Au waveguide on glass as a function of waveguide width. Due to a nonzero reflectivity of the PML boundaries at very shallow incident angles, the determination of the fundamental mode is not possible for a free-space wavelength of 1550 nm between 200 and 550 nm widths. A cubic spline interpolation in this range is indicated by a dotted line. For shorter wavelengths, only the fundamental mode is indicated. Plotted also are the cross sections of the electric field amplitude of the fundamental mode for 60 nm and 5  $\mu\text{m}$  widths at a free-space wavelength of 1550 nm. The arrows depict the direction of the transverse electric field schematically.

predominantly in air (with  $\text{Re}\{k_{\parallel}\}/k_0 \approx 1$ ) or in glass ( $\text{Re}\{k_{\parallel}\}/k_0 \approx 1.5$ ) [112, 115]. When the width is reduced only one mode persists. It exhibits a diverging wavevector and it is confined in a subwavelength area around the nanowire for small widths. It can be recognized as the nanowire mode, the rectangular equivalent of the  $m = 0$  Sommerfeld wave in a metal cylinder in a homogeneous environment. Like that wave, the transverse electric field at opposite sides of the waveguide has an opposite sign. This polarization nature, from here on called ‘antisymmetric’, is related to surface charges having equal sign around the circumference of the nanowire. As a result, the field interferes constructively inside the metal, giving rise to large induced charges and a pronounced longitudinal electric field component.

For longer wavelengths, the wavevector is first slightly reduced when the waveguide narrows, as the fraction of the modal field guided in air increases through the mode transformation. Importantly, for large widths the field of the mode of interest (which has the lowest energy) is predominantly localized at the substrate side of the guide. This mode is responsible for the focusing of SPPs on the substrate side of a laterally tapered metal film described in Chapter 5. Air-guided modes, which have previously been used to excite waveguides of subwavelength width [118, 164], are unsuitable for adiabatic coupling to the nanowire mode. This is clear in Fig. 6.2(a) from the fact that the normalized wavevector of these modes crosses the substrate light line as the width of the metal stripe is decreased.

### 6.2.5 The symmetry of the dielectric surrounding

The dielectric symmetry is essential for the excitation of the nanowire mode. In the system described in this work, the symmetry is broken with respect to that of a homogeneous dielectric environment. The asymmetric environment is responsible for the broad, Gaussian-like mode profile and approximately linear polarization at large stripe widths, which enables a more straightforward excitation of the required mode that is to be transformed. In contrast, the corresponding mode on a stripe embedded in a homogeneous dielectric environment would be localized at the waveguide edges while having a purely antisymmetric field distribution, as described in section 6.2.3.

To study the influence of the dielectric surrounding on SPP focusing in a laterally tapered stripe waveguide, we return to the experiments described in Chapter 5. We vary the contrast between the dielectric constants of substrate and superstrate by repeating the measurement presented in Fig. 5.3 while the sample is covered with immersion oil ( $n = 1.515$ ). In that way, the ratio between the refractive indices of substrate and superstrate is reduced from 1.74 to 1.15. The resulting upconversion luminescence micrograph at 550 nm is shown in Fig. 6.3(b). It shows two striking differences compared to the microscope image obtained with the sample covered in air (Fig. 6.3(a)). First, the interference pattern inside the triangular waveguide has changed, introducing pronounced intensity maxima at the waveguide edges. Second, no emission is observed from the taper tip, where for the sample in air we observe a maximum intensity. We conclude that decreasing the

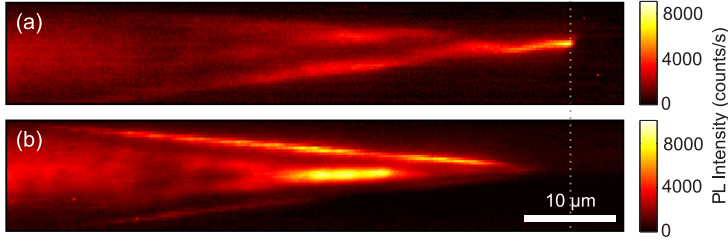


**Figure 6.3:** Upconversion microscopy images taken at 550 nm with different refractive indices of the superstrate:  $n = 1$  (a) and  $n = 1.515$  (b). In both cases SPPs are excited at the interface between the Au film and the sapphire substrate, which has a refractive index of 1.74. The dotted line is a guide to the eye, to show that when the sample is covered in immersion oil (b) no focusing is observed at the taper tip, whereas a maximum upconversion intensity is observed at the tip when the superstrate is air (a).

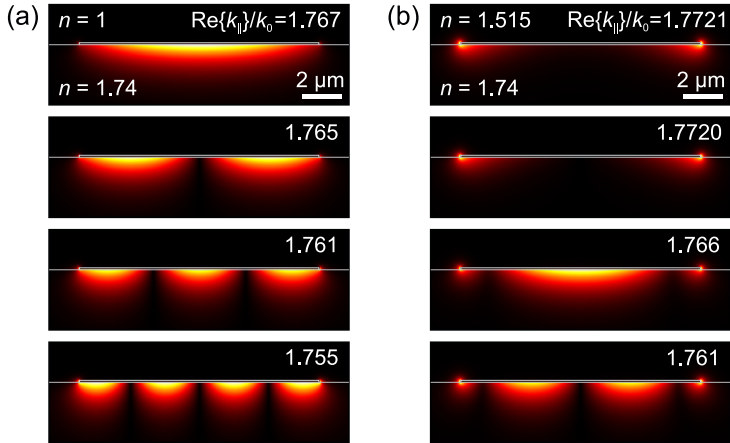


**Figure 6.4:** Mode profiles of  $|E|$  of the four lowest order bound modes guided by a  $12 \mu\text{m}$  wide and  $100 \text{ nm}$  thick Au waveguide on a sapphire substrate ( $n = 1.74$ ). The refractive index of the superstrate is changed from  $n = 1$  (a) to  $n = 1.515$  (b).

contrast between the dielectric constants of the two surrounding dielectrics has a large effect on the SPP focusing, strongly suppressing the field concentration at the taper tip.

Both effects can be explained in terms of the mode profiles of SPP modes propagating in the waveguide. Figure 6.4 shows the mode profiles of the four lowest order bound modes on a Au stripe waveguide on sapphire covered in air (Fig. 6.4(a)) or immersion oil (Fig. 6.4(b)). The waveguide width is  $12 \mu\text{m}$ , equal to the width of the taper entrance in the experiment in Fig. 6.3. All modes calculated with a high-index superstrate have intensity maxima at the waveguide edges, which are

absent on the waveguide covered in air. This difference can be interpreted as the result of a varying phase change upon reflection of SPP waves at a metal edge when the refractive index of the superstrate is varied. Most importantly, the lowest order mode (with the largest wavevector) is indeed localized predominantly at the waveguide edges when the index contrast between substrate and superstrate is reduced. This means that it will not be excited efficiently by the Gaussian SPP beam that is incident on the waveguide in the experiment. Instead, the third order mode ( $\text{Re}\{k_{\parallel}\}/k_0 = 1.766$ ) does have a much larger overlap with the incident SPPs, and this mode is therefore expected to be excited. This mode exhibits cutoff at some waveguide width. Since the lowest order mode (with  $\text{Re}\{k_{\parallel}\}/k_0 = 1.7721$ ) is the only one that can be guided without cutoff to the taper tip, no focusing is observed in Fig. 6.3(b).

## 6.3 Methods

In the experiments presented in this chapter the desired mode on the substrate side of a  $77 \pm 3$  nm thick Au film on BK7 glass ( $n_{\text{glass}} = 1.50$  at 1550 nm) is excited at the entrance of a 5  $\mu\text{m}$  wide waveguide using a hole array made in the Au film with a 1  $\mu\text{m}$  pitch. The excitation source is a continuous-wave tunable laser with a wavelength ranging from 1450 to 1570 nm (varied in 2 nm steps). The nanostructured Au film is fabricated as described in section 5.2.1. An optical microscope image of one of the structures is shown in Fig. 6.5. The width of the waveguide decreases over a length of 20  $\mu\text{m}$  after which the waveguide connects to a nanowire. The widths of different nanowires are determined from SEM micrographs.

### 6.3.1 Phase- and polarization-sensitive near-field microscopy

The evanescent SPP field is probed above the sample with a phase-sensitive near-field microscope which yields both the local field amplitude  $|A|$  and the phase  $\phi$  [165]. The complex signal  $A = |A|e^{i\phi}$  is a projection of the vectorial near field on the polarization state in the reference beam [166]. A detailed description of the near-field microscope can be found in ref. [167]. We discuss the main mechanisms leading to image formation in the microscope here, paying particular attention to the contribution of different components of the near field to the obtained microscope images.

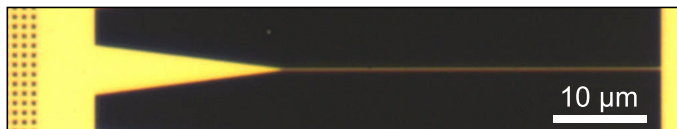


**Figure 6.5:** Optical microscope image of the investigated structure.

The evanescent field is collected by an Al-coated tapered fiber probe with an aperture diameter of  $\sim 220$  nm. The probe is scanned above the sample at a height of  $\sim 20$  nm, which is maintained by a shear-force feedback mechanism. The sample and near-field probe are incorporated in one branch of a Mach-Zehnder interferometer (see Fig. 6.6). The light in the probe fiber interferes with a frequency-shifted reference beam. The time-dependent interference signal is detected and analyzed with a lock-in amplifier [165].

The polarization in the reference branch is controlled. A spatial distribution of the measured complex signal  $A = |A|e^{i\phi}$  for any desired polarization angle  $\theta$  of the reference branch can be constructed by superimposing two images taken at orthogonal polarizations  $\hat{\mathbf{u}}$  and  $\hat{\mathbf{v}}$  in the detection fiber:

$$A(\theta) = A_u \cos(\theta - \theta_u) + e^{i\Delta\phi} A_v \sin(\theta - \theta_u), \quad (6.3)$$

where  $\Delta\phi$  is a phase offset between image  $A_u$  and  $A_v$ , which is determined by comparing the image constructed with (6.3) to images measured at several polarization angles  $\theta$ .

To understand image formation in this microscope, it is important to consider the role of the near-field probe. For a tip position  $\mathbf{r}_{\text{tip}}$  the field components of the nanowire mode at position  $\mathbf{r}$  are projected onto orthogonal fiber polarization directions  $\hat{\mathbf{u}}$  and  $\hat{\mathbf{v}}$  as

$$A_u = E_x * T_{xu} + E_y * T_{yu} + E_z * T_{zu} \quad (6.4)$$

$$A_v = E_x * T_{xv} + E_y * T_{yv} + E_z * T_{zv}, \quad (6.5)$$

where  $T_{xu}(\mathbf{r} - \mathbf{r}_{\text{tip}})$  is the complex transfer function [168, 169] that projects the component  $E_x$  on fiber polarization  $\hat{\mathbf{u}}$ . It is a function of position with respect to the center of the tip. The transfer functions will obey characteristic spatial symmetries. The *symmetry* of the transfer function that maps a certain field component

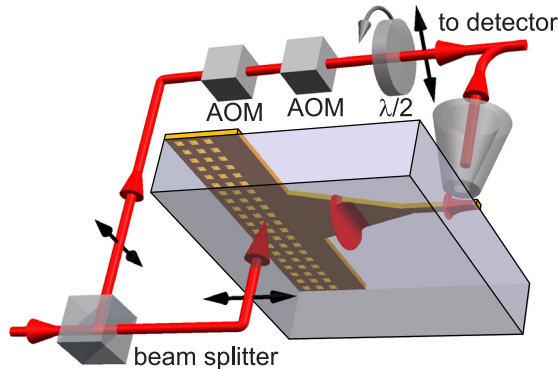


**Figure 6.6:** Schematic of the heterodyne near-field setup.

onto a particular fiber polarization is easily found by considering the reciprocal case of illumination through the tip: it is equal to the *symmetry* of the component that would be present when a fiber mode of that particular polarization is incident through the tip. Let's consider the particular choice of  $\hat{\mathbf{u}}$  and  $\hat{\mathbf{v}}$  corresponding to near-field polarizations  $\hat{\mathbf{x}}$  and  $\hat{\mathbf{y}}$ , for which  $T_{xu}$  and  $T_{yv}$  are maximal. For a perfectly cylindrically symmetric probe and fiber, this means that  $\hat{\mathbf{u}} = \hat{\mathbf{x}}$  and  $\hat{\mathbf{v}} = \hat{\mathbf{y}}$ , but in the actual experiment, bending of the fiber will have caused a rotation of these directions. As we will show in section 6.4.2, it is nonetheless possible to find these  $\hat{\mathbf{u}}$  and  $\hat{\mathbf{v}}$  from near-field measurements that can be used as polarization calibration. By considering the reciprocal case as mentioned above, we find that the functions  $T_{xu}$ ,  $T_{yv}$  and  $T_{zu}$  should all be symmetric with respect to the  $xz$  plane. For similar reasons  $T_{zv}$ ,  $T_{xv}$  and  $T_{yu}$  should be antisymmetric, and the latter two functions are expected to have particularly small magnitude.

## 6.4 Results and discussion

### 6.4.1 Coupling to nanowire SPPs

Figure 6.7(a) shows a map of the measured near-field amplitude  $|A|$  obtained by scanning the probe over the sample. In the left part of the image, the hole array with which the SPPs are excited is visible. In the tapered section the presence of SPPs propagating at the Au/glass interface is only evidenced by a field amplitude along the edge of the waveguide, as for these widths almost all of the energy of the SPP mode is located below the Au. At the end of the taper, the SPPs couple to a 150 nm wide nanowire. Near the end of the taper a clear intensity increase is observed as the guided wave becomes more strongly concentrated and the fraction of the modal field in air increases at the same time. The absence of phase or wavelength changes

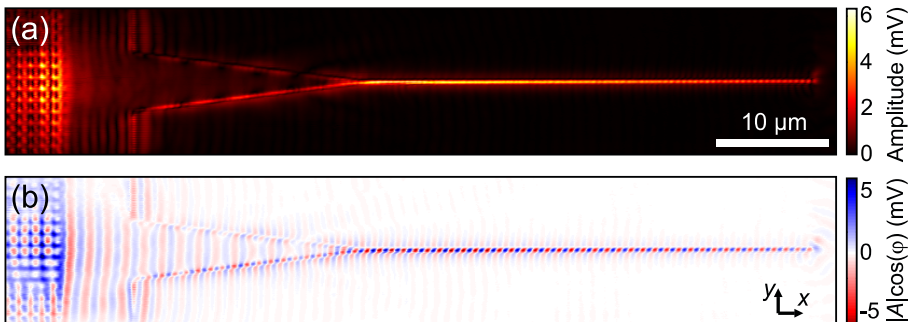


**Figure 6.7:** Near-field imaging of SPP excitation and propagation on a nanowire. (a) Collected near-field SPP amplitude and (b) distribution of  $|A| \cos \phi$ . SPPs excited on the Au/glass surface in the left are converted to a mode guided along a 150 nm wide nanowire. The excitation wavelength is 1550 nm.

along the edges of the taper in the distribution of  $|A|\cos\phi$  depicted in Fig. 6.7(b) shows that indeed the SPPs guided along the substrate side of the film smoothly convert to the nanowire SPP. The SPP wave is guided along the 40  $\mu\text{m}$  long wire until the wire terminates in a continuous Au film. The full width at half maximum of the intensity in the guided beam is 300 nm, which constitutes only an upper limit to the mode size as the probe diameter was 220 nm. The transverse size of the guided mode is therefore considerably smaller than the 1550 nm free-space wavelength (smaller than  $\sim\lambda/5$ ), experimentally proving that this structure can lead to nanofocusing of SPPs [43] and subsequent subwavelength guiding.

### 6.4.2 Polarization nature of the nanowire mode

To investigate the nature of the excited nanowire mode we vary the polarization of the reference beam, effectively selecting a polarization in the signal branch. Because the components of the optical near field couple to orthogonal polarizations in the probe fiber in different ways as described in section 6.3.1, this technique yields information about the vectorial character of the near field. Orthogonal polarization angles need to be found for which in-plane electric near-field components along either  $x$  or  $y$  contribute predominantly to the detected signal.

To calibrate these polarization angles, we consider the end of the nanowire waveguide, which terminates in a continuous Au film (see inset in Fig. 6.8(a)). At this abrupt termination, the nanowire mode scatters into SPPs propagating on both interfaces of the Au film. The SPPs at the Au/air interface are detected by the near-field probe. The nanowire acts as a subwavelength source of SPPs, launching them in all directions. Since SPPs on a flat interface are purely TM waves, the electric field of the SPPs launched along the  $x$  axis (aligned to the nanowire) at substan-

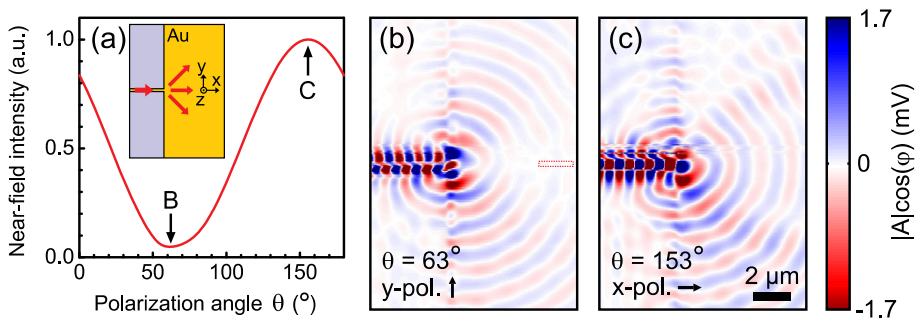


**Figure 6.8:** (a) Near-field SPP intensity on a smooth gold film as a function of the polarization angle of the reference beam. The intensity is monitored at a distance of 4  $\mu\text{m}$  from the end of a nanowire that launches SPPs in all directions onto the film. (b) and (c) Measured distributions of  $|A|\cos\phi$  for the polarization angles that cause minimum (b) and maximum (c) intensity in Fig. (a). Figure (b) therefore corresponds to  $y$  polarization, and Fig. (c) to  $x$  polarization.

tial distance from the source has only  $E_z$  and  $E_x$  components. Since the transfer functions  $T_{zV}$  and  $T_{xV}$  are both antisymmetric with respect to the  $x$  axis, and the distribution of  $E_y$  itself is also antisymmetric, it follows from (6.5) that the detected signal  $A_V$  must be antisymmetric with respect to the  $x$  axis when  $\hat{\mathbf{v}}$  corresponds to  $\hat{\mathbf{y}}$ . Hence, the intensity on the  $x$  axis should be zero for that polarization angle  $\hat{\mathbf{v}}$ . To find this angle, the polarization in the reference branch  $\theta$  is varied while monitoring the near-field intensity on the  $x$  axis at a distance of  $4 \mu\text{m}$  from the end of the nanowire (in the area denoted by the red dashed box in Fig. 6.8(b)). Indeed, a pronounced minimum and maximum are observed in Fig. 6.8(a) at two orthogonal angles, corresponding to the  $y$  and  $x$  polarizations, respectively. The corresponding near-field distributions, displayed in Figs. 6.8(b) and (c), are largely antisymmetric and symmetric, as expected. For  $y$  polarization, SPPs propagating along  $\hat{\mathbf{y}}$  are detected, whereas  $x$  polarization selects SPPs launched along the  $x$ -axis.

Figures 6.9(a) and (b) show spatial profiles of  $|A|\cos\phi$  measured on a small section of the nanowire for these two polarization angles. The measured signal distribution obtained with the polarization corresponding to the  $x$  direction (longitudinal to the wire) is highly symmetric with respect to the center of the wire, whereas the  $y$  polarization (transverse to the wire) is largely antisymmetric.

The observed symmetries are intimately related to the symmetry of the nanowire mode. The calculated electric field components of the mode are depicted in Figs. 6.9(c-e), for the height contour that the near-field probe follows. The measured pattern for  $x$  polarization (Fig.6.9(a)) closely resembles that of the calculated longitudinal field  $E_x$ . The close resemblance indicates that  $E_x$  provides the dominant contribution to the symmetric image, rather than the out-of-plane component  $E_z$ , which is also symmetric but with flat wavefronts unlike both  $E_x$  and

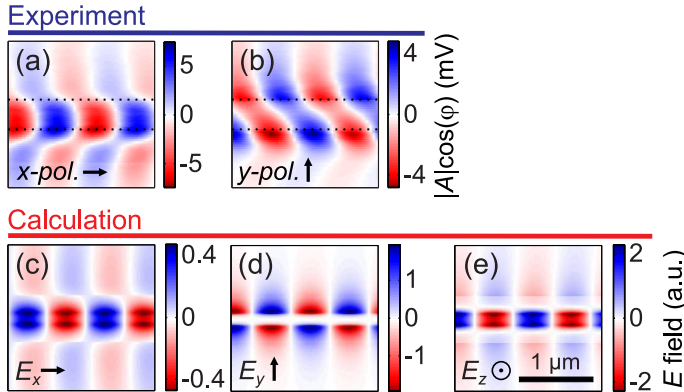


**Figure 6.9:** (a, b) Measured  $|A|\cos\phi$  on a small section of the nanowire for  $x$  and  $y$  polarizations. The dotted lines indicate the height step that the near-field probe makes due to the presence of the nanowire. (c-e) Calculated field components  $E_x$ ,  $E_y$  and  $E_z$  at a height of 20 nm above the sample.



the measured pattern. The measured amplitude of the longitudinal  $x$  polarization is comparable to that of the measured antisymmetric transverse  $y$  polarization (compare the amplitudes in Figs. 6.9(a) and (b)). The presence of a significant longitudinal field demonstrates the pronounced deviation of the highly confined nanowire mode from a transverse wave. It is immediately connected to the strong transverse confinement of the nanowire mode since  $\partial E_y/\partial y + \partial E_z/\partial z = -ik_x E_x$ , following from Coulomb's law. The observed antisymmetric distribution for  $y$  polarization (Fig. 6.9(b)) is related to the  $E_y$  field component. It proves that the excited nanowire mode is antisymmetric, like a Sommerfeld wave.

Finally, we note that provided a single mode is propagating along the wire (whatever its nature), the symmetry of the system guarantees the possibility to find two orthogonal polarizations for which the distribution of  $|A|\cos\phi$  is in principle either *entirely* symmetric or *entirely* antisymmetric with respect to the center of the nanowire. Since the nanowire geometry is symmetric with respect to the  $xz$ -plane, the field components of the waveguided eigenmodes normal or parallel to this plane are necessarily also either symmetric or antisymmetric. From the mode calculations (Figs. 6.9(c-e)) we know that the nanowire mode has symmetric  $E_x$  and  $E_z$ , and antisymmetric  $E_y$ . Since  $T_{xu}$  and  $T_{zu}$  are symmetric and  $T_{yu}$  is antisymmetric for polarization  $\hat{\mathbf{u}}$  for which  $T_{xu}$  is maximal, we see from (6.4) that  $A_u$  is entirely symmetric. Similarly,  $A_v$  is necessarily antisymmetric. A similar argument could be made for modes of opposite symmetry.

### 6.4.3 Wavevector, group velocity, and extinction of SPPs on nanowires

From the phase evolution of the mode, its wavevector is determined. Figure 6.10(a) shows measured dispersion curves for nanowire widths of 60, 85 and 150 nm, obtained by varying the excitation laser wavelength between 1450 and 1570 nm in 2 nm steps. As expected (see Fig. 6.2), for a given frequency the largest wavevector is observed for modes on the narrowest nanowire. The wavevector is in all cases close to that of light in the substrate, even though a significant fraction of the optical energy is guided in air. The plasmonic nature of the mode is clearly recognizable by the significantly reduced group velocity  $d\omega/dk$ , which is determined to be  $0.83 c/n_{\text{glass}}$  for the 60 nm wide nanowire from a linear fit to the data. The measured normalized wavevector and propagation lengths ( $L = \frac{1}{2}\text{Im}\{k_{\parallel}\}^{-1}$ , obtained from exponential fits to the near-field maps) are compared to theory for a free-space wavelength of 1550 nm in Fig. 6.10(b). For the two smallest widths, excellent agreement is found between measurements and calculations, which contain no adjustable parameters. The origin of the deviation for the 150 nm wide waveguide is as yet unknown; it indicates that the leakage into the substrate (which occurs for  $\text{Re}\{k_{\parallel}\}/k_0 < n_{\text{glass}}$ ) is larger than calculated. The excellent agreement between the measured and calculated propagation lengths for small widths indicates that Ohmic dissipation is the dominant loss mechanism, since the calculations neglect scattering losses.

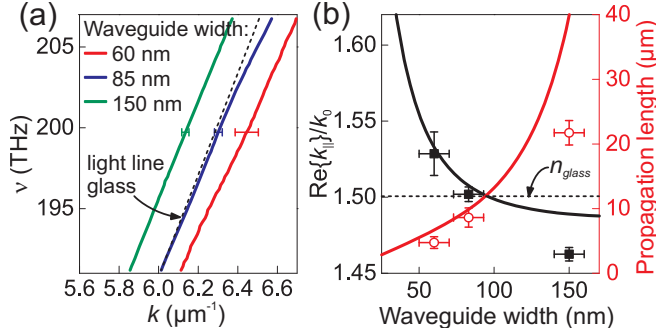


**Figure 6.10:** (a) Measured dispersion curves for three Au nanowire widths. The dashed line denotes the dispersion of light in the substrate. The error bars represent the experimental uncertainty. (b) Measured wavevector and propagation length as a function of waveguide width (symbols), compared to calculations (curves) for a free-space wavelength of 1550 nm.

#### 6.4.4 Coupling efficiency

To demonstrate that the adiabatic mode transformation causes an efficient transition to the nanowire, we consider a structure consisting of two tapers connected by a  $2\ \mu\text{m}$  long nanowire. Figure 6.11(a) is a SEM micrograph of the fabricated geometry. SPPs incident from the left are converted from a waveguide width of  $2\ \mu\text{m}$  to a  $90\ \text{nm}$  wide nanowire. In the output taper on the right, the transmitted SPPs are converted back to a  $2\ \mu\text{m}$  width. Figure 6.11(b) shows the near-field amplitude of waves that propagate from left to right, obtained from the experimental data using a Fourier analysis [170]. By comparing the amplitudes at the edges of the taper at  $4\ \mu\text{m}$  distance to either side of the nanowire, we determine the total intensity transmission to be  $20 \pm 6\%$ . From the Fourier analysis a  $2 \pm 1\%$  backreflection loss is found. Correcting for the known propagation loss of the  $2\ \mu\text{m}$  long nanowire (Fig. 6.10(b)), the combined coupling and decoupling efficiency of both tapers is calculated to be  $I_{\text{in}} e^{-\alpha l} / I_{\text{out}} = 24 \pm 7\%$ , with  $l$  the nanowire length. This corresponds to an average loss of  $\sim 50\%$  per coupler. The loss includes dissipation in the tapers, scattering to free-space radiation and leakage of the mode into the substrate when  $\text{Re}\{k_{\parallel}\} / k_0 < n_{\text{glass}}$ . Many parameters can be identified to improve the efficiency: the use of Ag rather than Au will reduce Ohmic damping, leakage radiation can be eliminated by increasing the refractive index of the substrate or reducing the film thickness, and an optimal tapering profile can further optimize adiabaticity and taper length. The optimum efficiency will be obtained by balancing Ohmic and scattering losses. A rough estimate of a lower bound to the maximum possible efficiency of  $\sim 70\%$  is obtained by assuming that the dissipative loss in the complete length of the taper is equal to that in the nanowire. This is however a conservative estimate, since the absorption in most of the taper is much lower than in the narrow nanowire.

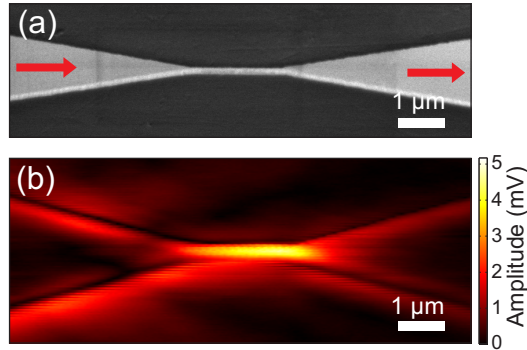


**Figure 6.11:** (a) SEM micrograph of a 2  $\mu\text{m}$  long nanowire connected by tapered waveguide sections for input and output coupling. (b) Near-field amplitude of forward propagating waves in the structure at  $\lambda = 1550$  nm. The intensity transmission of the complete structure is  $20 \pm 6\%$ .

### 6.4.5 Calculated efficiency: comparison to conical geometry

Even though the behavior of the lowest order mode in both cylindrical and stripe waveguides is qualitatively similar, the question remains what the influence of waveguide shape is on the degree of adiabaticity that can be obtained in a tapered geometry, and hence on the efficiency of coupling to the nanowire mode. This can only really be determined theoretically in three-dimensional full-field simulations that take into account tapering shape and scattering to free-space radiation. To provide a first rough estimate of the coupling efficiency difference between a tapered stripe waveguide and a conical geometry [43], we compare them with finite-difference time-domain (FDTD) simulations [76]. The geometries are sketched in Fig. 6.12. In both simulations, the proper waveguide mode is launched at the start of the waveguide. A nanowire is connected at the end of the 5  $\mu\text{m}$  long taper. To estimate the coupling efficiency, the Poynting flux through a  $600 \times 600$  nm<sup>2</sup> area around the nanowire at a distance of 1  $\mu\text{m}$  from the start of the nanowire is compared to the power in the incident mode. The width and diameter of the stripe and cylinder are both 2  $\mu\text{m}$  at the start of the taper. A Drude model is locally fitted to the measured dielectric constants at the operating free-space wavelength of 1550 nm to model the optical properties of the metal. Perfectly matched layer boundary conditions are used to absorb outgoing radiation. The spatial discretization is 3 nm close to the metal interfaces and  $\sim 20$  nm at the simulation boundaries. In the case of the stripe geometry, the Au film thickness is 77 nm and the width of the nanowire is 90 nm, which is exactly one of the investigated geometries. The substrate is glass. In the case of the conical geometry, the nanowire connected to the cone has a diameter of 80 nm. In this case, the structure is fully embedded in glass.

The simulated coupling efficiency as defined above was 58% for *both* geome-

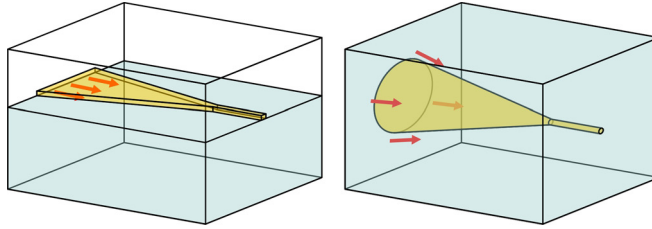


**Figure 6.12:** Geometries compared in the simulations.

tries. We note that this degree of correspondence must be partially serendipitous, considering the arbitrariness of some of the choices made in the modeled geometries. Nonetheless, the close agreement shows that the coupling efficiency can be substantial for both cylindrical and rectangular waveguides, and that in both cases a large degree of adiabaticity can be reached. Moreover, it corresponds well to the measured efficiency of  $\sim 50\%$ . Optimization of the tapering profile is necessary to determine the limits to the coupling efficiency.

#### 6.4.6 Exciting SPPs at the air side of the Au film

Finally, we return to the geometry used in the experiments, but now exciting the SPP mode at the air side of the film in the simulation. Because this mode is in cutoff for a width of  $2\ \mu\text{m}$ , it is instead launched at the start of a longer taper which has the same taper angle as before. The Poynting flux through the  $600 \times 600\ \text{nm}^2$  area around the nanowire is only  $0.8\%$  of the flux at the position where the taper width equals  $2\ \mu\text{m}$ . This is much smaller than the efficiency found when the correct mode at the substrate side is excited. Moreover, the power flowing through the  $600 \times 600\ \text{nm}^2$  area around the nanowire in the case of excitation at the air side cannot be fully ascribed to the nanowire mode. Inspection of the field around the nanowire reveals that most of the field is not strongly confined and that the polarization nature is not antisymmetric. This shows that the coupling to the desired nanowire mode is in fact even smaller than  $0.8\%$ .

## 6.5 Conclusions

In conclusion, we have shown the excitation of highly confined nanowire SPPs through the principle of adiabatic mode transformation. We have presented new calculations that identify a specific mode that can transform to a subwavelength-scale nanowire mode bearing strong resemblance to a Sommerfeld wave, while being easily excitable in a wide metallic waveguide. Phase- and polarization-sensitive near-field microscopy revealed the characteristic antisymmetric polarization nature of the excited nanowire mode, and showed that it gradually and efficiently

evolves from the fundamental SPP mode propagating at the substrate side of a metal stripe waveguide. These results demonstrate a practical implementation of the nanoscale miniaturization of light on a chip and provide the necessary tools to interface the macroscopic world with individual nano-objects.



# 7

---

## Plasmonic nanofocusing in a dielectric wedge

*We show that surface plasmon polaritons can be concentrated to subwavelength dimensions in a nanoscale dielectric wedge on a metal substrate. As the SPPs propagate on a Ag substrate covered with a thin Si film, they become highly confined inside the Si layer when the Si thickness is slowly increased. An adiabatic model is applied to explain the concentration mechanism, and compared to full-field electrodynamic simulations. A maximum magnetic field intensity enhancement by a factor 180 is predicted, at a frequency close to the surface plasmon resonance frequency of a Ag/Si interface. The focusing occurs in a subwavelength line on a smooth part of the wedge. Unlike alternative plasmonic nanofocusing strategies, this method does not require the nanoscale shaping of a metal surface.*

### 7.1 Introduction

Surface plasmon polaritons (SPPs) propagating along the interface between a metal and a dielectric have been suggested as means to control light at subwavelength scales [16]. Because the SPP wavevector is larger than that of light in the bounding dielectric, SPPs can be focused more strongly than light in the plane in which they propagate. Moreover, an increase of the wavevector leads to a decrease of the evanescent extent of the SPP wave normal to the metal surface, as the wavevector component in that direction ( $k_z$ ) is connected to the wavevector  $k_x$  along the direction of propagation  $\hat{\mathbf{x}}$  through  $k_z^2 = \epsilon_d k_0^2 - k_x^2$ , where  $\epsilon_d$  is the relative permittivity

of the dielectric. However, on a smooth metal surface the wavevector  $k_x$  is only significantly larger than the wavevector of light in the bounding dielectric when the refractive index of the dielectric is high, the losses of the metal are low, and the optical frequency is close to the surface plasmon resonance frequency  $\omega_{\text{sp}} = \omega_{\text{p}}/\sqrt{1 + \epsilon_{\text{d}}}$ .

In principle, one could think of manipulating SPPs excited at the interface of a metal with a high-index dielectric near the surface plasmon resonance frequency to focus light on small length scales. However, under those conditions the imaginary part  $k''_x$  of the wavevector  $k_x = k'_x + ik''_x$  becomes large, limiting propagation to impractically short lengths. Most designs that aim to achieve plasmonic nanofocusing, both theoretically proposed [43, 137, 171] and experimentally demonstrated (Chapters 5 and 6 and refs. [141–143]), therefore rely on a geometry that differs from a flat metal surface. In general, a SPP mode on a metallic waveguide of which the geometry is gradually modified can adiabatically transform while it propagates along the waveguide. If the waveguide supports a mode that becomes more strongly confined and that does not exhibit cutoff when the waveguide size is decreased, this mode can be used to achieve nanofocusing. Geometries that support such modes are metal cones [43, 155, 172–174], wedges [137, 175, 176], and tapered gaps [138, 171, 177]. Nanofocusing is achieved at a sharp extremity of such a waveguide. The size of the extremity determines the size to which light can be ultimately concentrated. The focusing is therefore limited by the fabrication quality of the nanoscale metal surfaces.

In this chapter, we apply the concept of a gradual transformation of a SPP mode in a design in which only the dielectric environment outside a metal surface is varied along the waveguide. SPPs propagating on a smooth metal substrate covered with a thin dielectric film become strongly confined when the dielectric film thickness increases [102]. We show in simulations that SPPs concentrate in a sub-wavelength focus at a specific position on a dielectric wedge on a Ag substrate when they propagate away from the end of the wedge. In contrast to alternative designs, the nanofocusing in this structure is not localized at a sharp extremity. The properties of the constitutive materials play an important role in the focusing, as it occurs most strongly at the surface plasmon resonance frequency  $\omega_{\text{sp}}$ . We explain the effect in terms of the modes of the waveguide, and show that intensity enhancements up to a factor 180 can be reached. The factors limiting the focusing are discussed.

## 7.2 SPPs on a metal surface covered with a thin dielectric film

The system considered in this chapter is a dielectric wedge on a Ag substrate, that is invariant in the  $y$  direction and has a thickness  $d(x)$  that increases along the  $x$  direction. We consider propagation of TM waves in the  $x$  direction. We treat the wedge as a tapered waveguide that varies slowly along  $x$ , such that at each position



$x$  the transverse  $z$  dependence of the field can be described by the field of a mode propagating in an infinitely long waveguide with constant thickness  $d(x)$ .

Figure 7.1 shows the  $H_y$  field profiles of SPP modes guided by a Ag surface covered with a thin Si film of varying thickness, for a free-space wavelength of 628 nm. The optical constants of the Ag are taken from ref. [26], and the refractive index of the Si film is taken as  $n = 3.85$ . First dispersion and absorption in Si are neglected as they are much smaller than in the metal to focus our attention on plasmonic effects only. The modes are calculated as described in section 1.2.1. The frequency is taken to be real, and we solve for complex eigenvalues  $k_x$  describing phase velocity and damping of the SPP modes guided along the waveguide.

As Fig. 7.1 shows, a SPP wave that is only moderately confined at a Ag/air interface becomes strongly confined inside the dielectric as  $d$  is increased to  $\sim 20$  nm. The confinement can be explained by considering the dispersion curves of SPPs for varying Si thickness, displayed in Fig. 7.2. The blue and black curves represent the SPP dispersion at a single Ag/air or Ag/Si interface, respectively. Clearly, the higher permittivity of Si shifts the surface plasmon resonance frequency  $\omega_{\text{sp}}$  (which we define as the frequency for which  $k'_x$  is maximal) to a smaller frequency (514 THz), and in principle allows very large wavevectors to be reached near that frequency. The presence of material losses limits the maximum value of  $k'_x$ , and causes the losses  $k''_x$  to be high for frequencies close to  $\omega_{\text{sp}}$ .

The dispersion curves of SPPs on a very thin ( $< 20$  nm) Si film follow those of SPPs on a Ag/air interface closely for most frequencies. As the film thickness increases, the effective surface plasmon resonance can be observed to shift to lower frequencies as the film thickness increases, approaching the value of  $\omega_{\text{sp}}$  for a single Ag/Si interface. We note that for these small thicknesses SPPs with large wavevec-

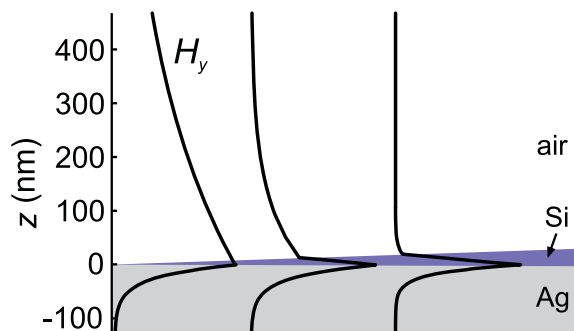


**Figure 7.1:** SPPs on a metal surface covered with a dielectric film, for varying film thickness. The calculated  $H_y$  mode profiles of SPPs in an infinitely long waveguide consisting of a thin Si film on a Ag substrate are plotted for different Si thicknesses for a free-space wavelength of 628 nm. The Si thickness for the three plotted modes is 0, 15, and 20 nm, from left to right. This illustrates that the SPP mode can transform such that its field becomes fully confined within the Si film as the Si thickness is slowly increased.

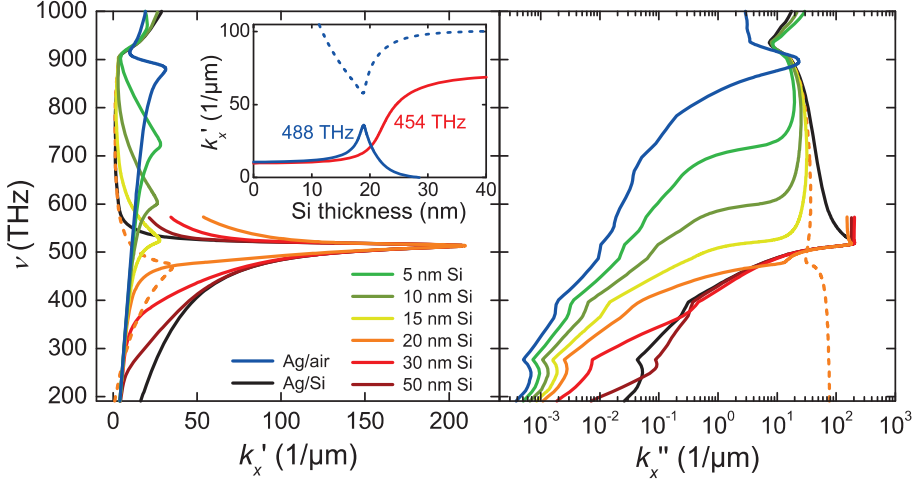


**Figure 7.2:** Dispersion curves of SPPs on a thin Si film on Ag, for different Si thicknesses. The real ( $k'_x$ ) and imaginary ( $k''_x$ ) part of  $k_x$  are displayed in the left and right graphs, respectively. The blue and black curves show the dispersion curves for single Ag/air and Ag/Si interfaces, respectively. For finite Si thickness, the modes can show a hybrid behavior, resembling SPPs at a Ag/air interface for low frequencies while tending towards the dispersion of SPPs at a Ag/Si interface close to  $\omega_{\text{sp}}$ . For clarity, the dispersion curves for Si thicknesses larger than 20 nm are not plotted for frequencies above 575 THz, where losses are extremely large. The dashed curve shows the dispersion of a second mode for 20 nm, which can play a role in the mode transformation for relatively large frequencies. The inset shows the evolution of  $k'_x$  as a function of Si thickness for two frequencies. For 488 THz, the mode that exhibits the largest wavevectors, which cannot be reached adiabatically, is shown as a dashed curve.

tors also exist (see section 3.3.2 and refs. [53, 178]). These modes have a negative index and were discussed in Chapter 3. For larger Si thicknesses, the dispersion curves approach that of Ag/air SPPs only for small frequencies. Closer to  $\omega_{\text{sp}}$ , the SPP wavevector is similar to that on a Ag/Si interface. The mode makes a transition from being guided predominantly in air to being confined within the Si film as the frequency increases [54].

Similar behavior will occur when the frequency is kept fixed and the dielectric thickness is continuously increased [102]. This is plotted in the inset of Fig. 7.2. For a frequency of 454 THz (somewhat smaller than  $\omega_{\text{sp}}$ )  $k_x$  changes around a critical thickness of 20 nm from the value for a Ag/air interface to the value for a Ag/Si interface. As a result a SPP mode on a Si wedge on Ag propagating along the direction of increasing Si thickness transforms to a SPP mode that is highly confined in the Si film. Because the losses increase in conjunction with this transformation, the SPPs will not propagate far once they are fully confined in the Si film. The propagation length  $L_{\text{SPP}}$  reduces to  $\sim 200$  nm. Nonetheless, the compression could

cause a significant field enhancement in a subwavelength volume.

It is at first sight logical to assume that the desired effect would be maximal for frequencies near  $\omega_{\text{sp}}$ , since the largest wavevectors can be reached there (see Fig. 7.2). In the presence of metal absorption the situation is however somewhat more complex, as other modes can come into play. An example of the dispersion curve of such a mode is plotted for a Si thickness of 20 nm as the dashed line in Fig. 7.2. Although this mode has such high losses that it is in fact an overdamped (evanescent) wave in the  $x$  direction [102], it plays an important role in the transformation process for frequencies close to or larger than  $\omega_{\text{sp}}$ . As can be seen in the inset of Fig. 7.2, for a frequency of 488 THz  $k'_x$  first reaches a maximum as the thickness increases, after which it diminishes again. This behavior is due to coupling between this mode and another mode, which is shown as the dashed curve in the inset of Fig. 7.2. At the critical thickness, the modes couple, resulting in an anti-crossing of their wavevectors as a function of thickness. Above the critical thickness of  $\sim 20$  nm, the losses increase dramatically, corresponding to propagation length  $L_{\text{SPP}} = 20$  nm [102]. The coupling between the modes makes it impossible for SPPs on the wedge to transform to the mode with the highest possible value of  $k'_x$  — which is  $\sim 200 \mu\text{m}^{-1}$  at  $\omega_{\text{sp}}$ . Nonetheless, we will show that the modes that do get excited can still be responsible for significant field enhancements, provided the thickness is varied slowly enough.

The mode conversion process is only fully adiabatic when  $d$  varies slowly enough for a SPP mode to remain in the corresponding eigenmode while it propagates along the tapered waveguide. Because the eigenvalue  $k_x$  can be seen to change rather rapidly with thickness in the inset of Fig. 7.2, it is likely that adiabaticity can only be reached for shallow taper angles.

### 7.3 The geometrical optics approximation

In the geometrical optics approximation (GOA) — the optical equivalent of the WKB approximation in quantum mechanics — the individual field components  $\Psi$  of a wave propagating in the  $x$  direction and invariant in the  $y$  direction are assumed to vary as [179]

$$\Psi(x, z, t) = \psi(x, z) \exp(i k_0 \varphi(x) - i \omega t) \quad (7.1)$$

where  $\psi(x, z)$  is a function that varies slowly in  $x$ , and we have assumed translation invariance along the  $y$  direction. The scalar function  $\varphi(x)$  is called the *eikonal*, and satisfies

$$\frac{d\varphi}{dx} = n(x), \quad (7.2)$$

where  $n(x)$  is the local index of refraction. When we interpret the propagation of SPPs along a tapered waveguide with thickness  $d(x)$  in terms of this formalism,  $n(x)$  is equal to  $k_x/k_0$  as calculated for an infinitely long waveguide with constant thickness  $d$ . The function  $\psi(x, z) = A(x)f(x, z)$  contains both the mode profile  $f(x, z)$ , i.e., the  $z$  dependence of the field component  $\Psi$  of the mode calculated for

thickness  $d(x)$ , and the mode amplitude  $A(x)$  along the slowly varying waveguide. The energy flux of the mode along the waveguide diminishes only through the calculated mode absorption, as can be found by making use of (7.1) and (7.2) [43, 171]:

$$\frac{d}{dx} \left( \int \operatorname{Re} \{ \langle S_x \rangle \} dz \right) = -2k'_x \int \operatorname{Re} \{ \langle S_x \rangle \} dz \quad (7.3)$$

Here  $\operatorname{Re} \{ \langle S_x \rangle \} = -\frac{1}{2} E_z H_y^*$  is the  $x$  component of the time-averaged Poynting vector. Hence, in the absence of absorption the energy flux of the mode integrated over the full mode profile remains constant, illustrating that the geometrical optics approximation neglects scattering to other modes completely and is therefore fully adiabatic by definition. Equation (7.3) can now be solved to obtain  $A(x)$ , up to a scaling factor which determines the total power at the start of the waveguide. With that, the field strength along the taper in the geometrical optics approximation is known for any taper profile  $d(x)$ .

Figure 7.3(a) shows the calculated intensities  $|\mathbf{H}|^2$  and  $|\mathbf{E}|^2$  along wedges with two different opening angles  $\theta$ . The intensities are evaluated inside the Si film at the Ag/Si interface, and they are normalized to the intensities at the start of the taper (where  $d = 0$ ) in air at the Ag/air interface. The frequency is 480 THz ( $\lambda_0 = 625$  nm). Pronounced maxima are observed at specific positions along the wedge. For both wedges these positions correspond to a local Si thickness of 19 nm. As shown in Fig. 7.3(b), the phase velocity  $v_p$  approaches a minimum value at that position, after which it remains constant at the value for SPPs at a Ag/Si interface. The group velocity, defined as  $v_g = d\omega/dk'$ , reaches a value as small as  $0.003 \times c$  because the slope of the dispersion curves reduces significantly (see Fig. 7.2) [54, 102].

After the maximum intensity is reached, the field quickly diminishes because the SPPs are absorbed. Absorption thus also limits the maximum field enhancement that can be obtained. Nevertheless the created field enhancement is significant: intensity enhancements of  $|\mathbf{H}|^2$  by a factor 350 are calculated for a taper angle of  $1.43^\circ$ . The enhancement of  $|\mathbf{E}|^2$  is five times smaller, which is due to the fact that the requirement of continuity of normal  $\mathbf{D}$  fields at the Si/air interface strongly reduces the magnitude of  $\mathbf{E}$  inside the Si wedge.

The question remains whether the geometrical optics approximation presented here is accurate. It is only strictly valid in the limit when [43, 171]

$$\left| \frac{d(k_x)^{-1}}{dx} \right| \ll 1. \quad (7.4)$$

The left hand side of this equation acquires a maximum value of 0.4 for  $\theta = 1.43^\circ$  at the critical thickness. It is therefore important to perform full-field simulations that take into account scattering into reflection and free-space modes caused by the loss of translational invariance.

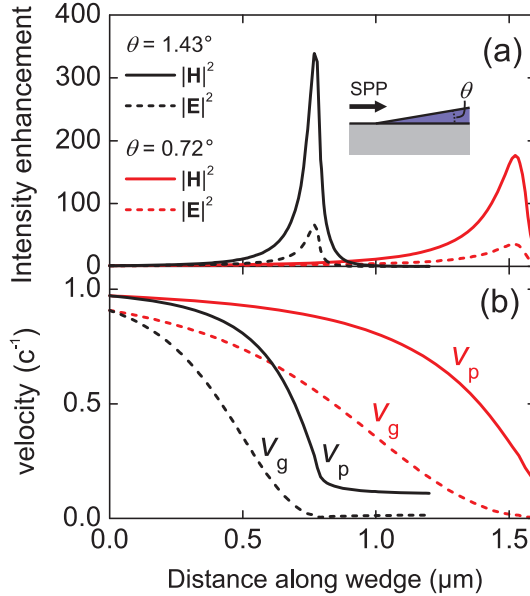


**Figure 7.3:** (a) Magnetic and electric field intensity enhancements at the Ag/Si interface along Si wedges on Ag, calculated in the geometrical optics approximation. Two different taper angles  $\theta$  are considered, and the frequency is 480 THz. The intensities are normalized to the intensity in air at the Ag/air interface at the start of the wedge. (b) Phase and group velocities of the SPPs propagating along the wedges, relative to the speed of light in air.

## 7.4 Comparing the geometrical optics approximation to full-field simulations: limits to adiabaticity

We perform two-dimensional finite-difference time-domain (FDTD) simulations to quantify the field enhancement [76]. At one of the simulation boundaries a SPP mode on a Ag/air interface is launched with a fixed frequency. A different simulation is performed for every frequency. At each frequency, a Drude model is locally fitted to the Ag optical constants given by ref. [26]. The mesh size near the Ag interface is 1 nm, and perfectly matched layers are used as simulation boundaries. The complex fields are recorded at a time of 300 fs, at which time the simulation has reached steady state.

The SPPs propagate onto the metal surface with a Si wedge ( $n = 3.85$ ). Figure 7.4(a) shows the intensity enhancement of  $|H|^2$  in Si at the Ag/Si interface normalized to the value of  $|H|^2$  in air at the start of the waveguide, for both the geometrical optics approximation and the FDTD simulations. The excitation frequency is 520 THz ( $\lambda_0 = 577$  nm). Both the position and the shape of the intensity distributions obtained from the FDTD simulation agree well with the GOA results.

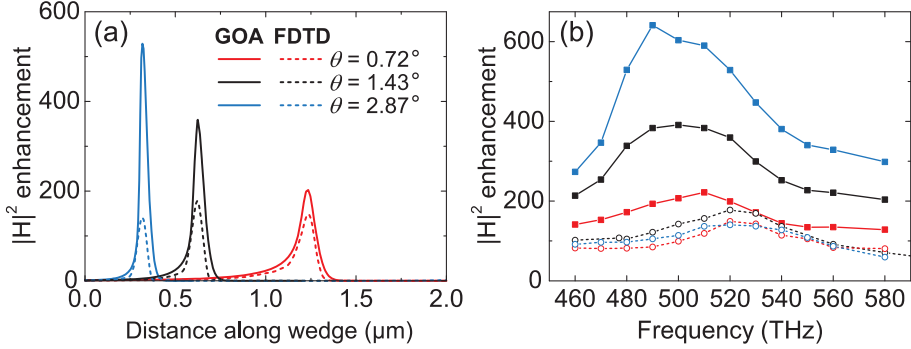


**Figure 7.4:** Comparison of the  $|\mathbf{H}|^2$  intensity enhancements obtained in the GOA (full curves) and in FDTD simulations (dashed curves). (a) Spatial dependence of the magnetic field intensity enhancement along wedges of three different angles, at a frequency of 520 THz. (b) Spectral dependence of the maximum magnetic field intensity enhancement on the wedges, for the same angles as in (a).

The agreement indicates that the explanation of the concentration effect observed in the full-field simulations in terms of a mode transformation in the wedge, as described in the GOA, is valid.

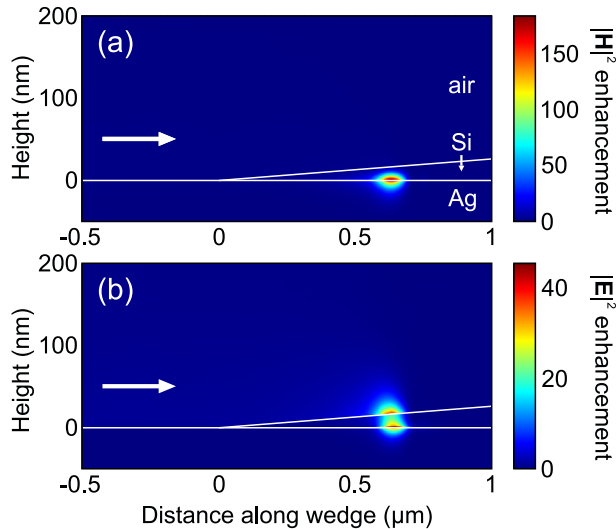
As expected, the magnitude of the field enhancement in the FDTD simulations is in general smaller than in the GOA, since the latter neglects scattering to all other modes, either reflected or free-space. As can be seen in Fig. 7.4(a), for the smallest taper angle of  $0.72^\circ$  the maximum enhancement of  $|\mathbf{H}|^2$  in the FDTD simulations is 0.75 times the maximum enhancement in the GOA. For larger angles, the deviation is larger, illustrating that adiabaticity breaks down above a taper angle of the order of  $\sim 1^\circ$ . Even though the process is not fully adiabatic, the focusing mechanism still yields a strong field enhancement. A maximum  $|\mathbf{H}|^2$  enhancement by a factor 180 is observed for the taper angle of  $1.43^\circ$ . For the largest angles, the deviation from the GOA is larger at the right side of the curves, i.e., the field obtained in FDTD starts to diminish after reaching a maximum at a slightly smaller distance along the taper than predicted by the GOA. This shows that the breakdown of adiabaticity is most severe very close to the critical thickness.

Figure 7.4(b) shows the spectral dependence of the maximum enhancement for the three different taper angles, both for the GOA and FDTD methods. Maximum field enhancement is seen to occur at somewhat larger frequencies (520 THz) in the FDTD simulations than in the GOA ( $\sim 500$  THz). The fact that this frequency is close to  $\omega_{\text{sp}}$ , which is 514 THz for a Ag/Si interface, shows that the focusing effect relies strongly on the material properties of bulk Si and Ag, which determine the plasmon resonance frequency  $\omega_{\text{sp}}$ .

### 7.4.1 Subwavelength confinement

To estimate the spatial confinement of the concentrated optical energy in the wedge, we plot the field intensity enhancements of  $|\mathbf{H}|^2$  and  $|\mathbf{E}|^2$  simulated with FDTD at 520 THz ( $\lambda_0 = 577$  nm) in Fig. 7.5. The maximum of  $|\mathbf{H}|^2$  indeed occurs at the Ag/Si interface, at a very specific position along the wedge. The magnetic intensity is almost fully contained within the Si film at that position, decaying in the  $z$  direction to a fraction of  $1/e$  of the maximum value at a distance of 10 nm. In the direction along the surface, the full width at half maximum is 73 nm. This distance is approximately half the wavelength of light in bulk Si, which is 150 nm at this frequency. It demonstrates that the field concentration occurs within a subwavelength length scale in the longitudinal dimension as well.

The enhancement of the electric field intensity is displayed in Fig. 7.5(b). A maximum intensity enhancement of  $|\mathbf{E}|^2$  by a factor 45 is observed. As noted before, the electric field enhancement is rather small compared to the magnetic field enhancement due to the fact that the condition of continuity of the normal  $\mathbf{D}$  field component at the Si/air interface must be satisfied. In fact, the electric field in the air just outside the wedge is seen to be quite strongly enhanced as well, with approximately the same magnitude as the maximum at the Ag/Si interface. The full width at half maximum in the  $x$  direction (along the wedge) of the region of enhanced field intensity at the air/Si interface is 75 nm, comparable to the longitu-



**Figure 7.5:** Two-dimensional maps of the magnetic (a) and electric (b) field intensity enhancement in a Si wedge on glass with a taper angle of  $1.43^\circ$ , at a frequency of 520 THz ( $\lambda_0 = 577$  nm). SPPs are incident from the left, propagating in the direction of the arrow.

dinal confinement at the Ag/Si interface.

So far, the focusing effect investigated in this chapter was demonstrated with a Si wedge on a Ag substrate, under the assumption that absorption and dispersion in Si could be neglected. To verify the validity of this assumption, we have performed FDTD simulations including dispersion and absorption of the Si as well. In those simulations, the field intensity enhancement amounts to  $\sim 70\%$  of the value obtained in the absence of absorption and dispersion for the  $1.43^\circ$  taper angle. The small deviation between the enhancements obtained with and without absorption in Si indicates that the most important factor limiting the maximum field enhancement is in fact absorption in the metal.

We note that the concentration effect should also occur when other materials are used. The concentration will be achieved for frequencies near the surface plasmon resonance frequency for that particular metal/dielectric combination. A metal with a higher absorption, such as Au or Al, will likely result in a decrease of the field enhancement. A decrease is also expected when the wedge material is replaced by a dielectric with a smaller refractive index, since this would allow less confinement. On the other hand, it could be true that with a lower-index dielectric it is easier to reach adiabatic performance, as the wavevector does not change as dramatically.

The fabrication of ultrathin tapered dielectric films is certainly challenging, but a large range of techniques exist that are especially well suited to shape dielectrics and semiconductors to realize these kinds of structures in practice. By structuring the dielectric in the  $y$  direction as well, the SPPs could be focused in that direction too, yielding even higher field enhancements in subwavelength volumes.

## 7.5 Conclusions

We have demonstrated the subwavelength concentration of light in a dielectric wedge on a metal substrate in full-field simulations. The magnetic field intensity of SPPs propagating along a Si wedge on a Ag substrate in the direction of increasing Si thickness is enhanced by a factor 180 at a well-defined position on the wedge. The mechanism responsible for the concentration effect is the gradual transformation of the SPP mode propagating on a Ag surface covered with a thin Si film of which the thickness slowly increases. At a critical thickness of  $\sim 20$  nm, the SPPs slow down and become fully confined within the Si film, leading to a large buildup of optical energy. Maximum field enhancement is observed for relatively shallow taper angles of  $\sim 1^\circ$ , close to the surface plasmon resonance frequency of SPPs at a Ag/Si interface. The field enhancement in the wedge is maximal at the Ag/Si interface, but is still significant at the Si/air surface. It can therefore be of practical interest, for example if one intends to couple emitters dispersed on the surface to the concentrated optical fields. This work presents an alternative route to achieve plasmonic nanofocusing, without the need to fabricate very small metal features. It shows that it is possible to make use of a regime of SPP dispersion that is usually considered impractical because of the associated high losses.



---

## Field enhancement in metallic subwavelength aperture arrays probed by erbium upconversion luminescence

*Upconversion luminescence from erbium ions placed in the near field of subwavelength aperture arrays is used to investigate field enhancement of incident near-infrared light in such nanostructures. We study field enhancement due to the excitation of both propagating and localized surface plasmon resonances in arrays of square and annular apertures in a Au film. The conversion of 1480 nm excitation light to 980 nm emission is shown to be enhanced up to a factor 450 through a subwavelength hole array. It is shown that a Fano model can describe both far-field transmission and near-field intensity. The upconversion enhancement reveals the wavelength and linewidth of the surface plasmon modes that are responsible for extraordinary transmission in such arrays. Angle-dependent measurements on annular aperture arrays prove that the field enhancement due to localized resonances is independent of the incident angle.*

### 8.1 Introduction

There has been a large interest in subwavelength aperture arrays in metallic films ever since the first report of extraordinary transmission through such structures

[180]. Much effort has been dedicated to elucidating the fundamental principles that govern the far-field properties of aperture arrays [181, 182]. Additionally, the enhancement of the near field in aperture arrays due to the excitation of optical resonances has been recognized to yield many possible applications. Among those applications are efficient sensing [183, 184], strong control over light extraction [185, 186] and the enhancement of nonlinear effects [9, 10, 187, 188].

Broadly speaking, two types of resonances can be distinguished that are responsible for the main transmission peaks observed in far-field transmission spectra as well as for the accompanying enhancement of the near field. The first type relies on the resonant excitation of surface waves (surface plasmon polaritons (SPPs) for optical frequencies) propagating along the metal film surface. As the excitation is due to grating diffraction, this effect depends strongly on incident angle and wavelength. The responsible surface waves can be described as eigenmodes of the corrugated metal surface [189]. Secondly, properly shaped apertures can support localized plasmonic modes that can lead to very large transmission [68, 190].

In particular, arrays of annular apertures exhibit a strong transmission resonance [72, 191, 192]. This resonance is associated to the cutoff condition for the  $TE_{11}$  mode propagating inside individual apertures [71, 73–75]. A single aperture can be viewed as a truncated waveguide. Bounded by the air and substrate outside the metal film, it forms a low quality factor optical cavity. At cutoff, the wavevector of the  $TE_{11}$  mode propagating inside this waveguide approaches zero, which results in a cavity resonance that is independent of the metal film thickness. Because of the localized nature of the mode, this transmission resonance is independent of incident angle and polarization [193], which is a large benefit for many applications. Moreover, the resonance has a wide bandwidth.

In this chapter, we investigate field enhancement in aperture arrays supporting both types of resonances using the photoluminescence from emitters placed in the near field of the metallic nanostructures. The emitters are erbium ions located in the sapphire substrate at an average depth of 35 nm below the structured Au film. The Er ions can convert infrared radiation with a free-space wavelength of 1480 nm to emission at shorter wavelengths (most notably at 980 nm) through an upconversion process [124, 125]. The upconversion luminescence emitted into the far field is used as a direct probe of the local field intensity at the position of the Er ions. We find that the emitted upconversion luminescence from Er ions excited through hole arrays supporting propagating surface plasmon resonances can be enhanced up to a factor of 450. We investigate the influence of hole size and array periodicity on the field enhancement, and show the connection between far-field transmission and near-field intensity in a Fano model. Annular aperture arrays that exhibit localized plasmon resonances also lead to upconversion enhancements, albeit of smaller magnitude. We experimentally demonstrate that the field enhancement due to the excitation of such modes is independent of incident angle.

We note that enhancing the strength of the upconversion process with plasmonic nanostructures is a valuable goal in itself. Upconversion is of importance in lasers [194–196], display technology [197], and luminescent probes in microscopy

[198]. Moreover, it has been proposed as a possible route to enhance the efficiency of silicon solar cells. By converting part of the infrared solar radiation that is not captured by a silicon solar cell to radiation with shorter wavelengths, this part of the solar spectrum could be absorbed as well [199, 200]. However, all of these applications are hindered by the fact that the upconversion process is nonlinear in the excitation power and — in the case of rare earth ions — by the fact that typical absorption cross sections are small. Both facts limit the upconversion efficiency, especially at small pump powers. By making use of the enhanced fields of plasmonic resonances (which have large cross sections) as an intermediate step in the excitation of the emitters by incident light, their cross section can be effectively enhanced. This could lead to an increased upconversion efficiency [107, 200–202], from which all of the above applications might benefit.

## 8.2 Methods

The aperture arrays are fabricated in a 110 nm thick Au film on a sapphire substrate with the method described in section 5.2.1. The substrate (refractive index 1.74) is doped with  $\text{Er}^{3+}$  ions at an average depth of 35 nm below the surface, as described in section 4.2.1. The size of each aperture array is  $50 \times 50 \mu\text{m}^2$ . Many arrays are fabricated, of which the period as well as aperture size and shape are varied. Two general aperture shapes are considered: square and annular (also termed coaxial). Figure 8.1 shows SEM micrographs of details of both an array of square holes and an array of annular apertures. The annular apertures are designed to be square rather than circular, but these two types of hole shape are known to exhibit comparable behavior [203].

The measurement geometry is schematically depicted in Fig. 8.2. The arrays are illuminated from the air side of the Au film at normal incidence with a numerical aperture of 0.02, effectively illuminating individual arrays completely. The excitation source is a fiber-pigtailed 1480 nm CW diode pump laser (Fitel). To record broad-band transmission spectra, a fiber-coupled halogen lamp is used.

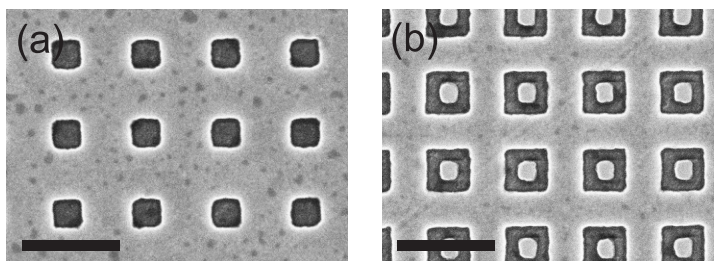


**Figure 8.1:** SEM micrographs of details of fabricated arrays of square (a) and annular (b) apertures. Scale bars are  $1 \mu\text{m}$ .

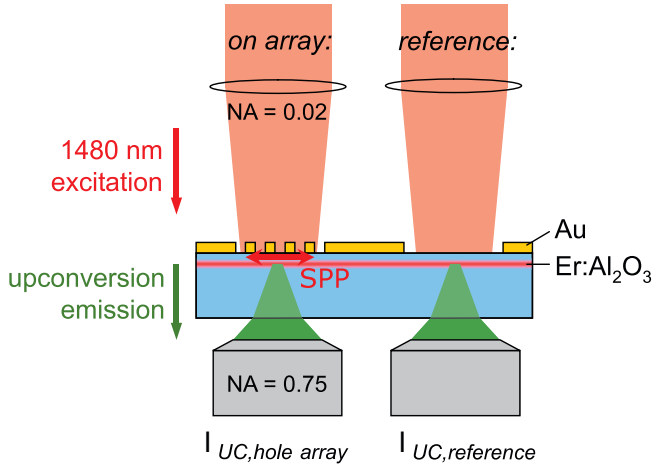


**Figure 8.2:** Schematic depiction of the measurement geometry. The sample is illuminated with 1480 nm pump light, and upconversion luminescence from Er ions implanted in the sapphire substrate is collected through the substrate.

Light from the sample is collected through the substrate using a microscope objective (NA=0.75), and focused on the entrance facet of a 100  $\mu\text{m}$  core diameter optical fiber. Because the magnification of the microscope is 12.5 $\times$ , only light originating from the center of the illumination spot is detected, and the illumination within this collection spot can therefore be considered as homogeneous. The collected Er upconversion emission or white light transmission is then led to a spectrograph and a Si CCD detector to record spectra for visible wavelengths, or to a spectrograph and an InGaAs photodiode array detector to record infrared transmission spectra.

For the angle-dependent measurements reported in section 8.5, the illumination optics are replaced by a microscope objective with an NA of 0.75. By limiting the width of the beam entering the back aperture of the objective, the illumination NA is effectively reduced to 0.1. The illumination angle is then controlled by displacing the beam that enters the objective with respect to the optical axis.

Upconversion emission from the Er ions is used as a probe of the local intensity of the 1480 nm excitation laser light. The upconversion mechanisms in Er ions were discussed in section 4.2.1. In this work we will focus on the emission from the  $^4I_{11/2}$  level at 980 nm (see the  $\text{Er}^{3+}$  level diagram in Fig. 4.1(b)). Because the emission wavelength is spectrally separated from the excitation wavelength, plasmon resonances will not simultaneously affect both excitation and emission channels. It is however impossible to exclude any effects on the upconversion emission due to the presence of the metal nanostructures, such as an altered branching ratio due to a changed local density of states at the emission wavelength [201] or emission into preferred directions due to grating diffraction. The effect of the latter is suppressed by collecting with a large numerical aperture. As we will show, it is possible to

ascribe all observations in this chapter to modifications of the Er excitation rate due to a variation in pump intensity in the near field of the aperture arrays.

The depth profile of Er ions is designed such that the ions do not directly quench to the Au film [134]. At a wavelength of 1480 nm, the intensity of SPPs on an uncorrugated Au/sapphire interface decays into the substrate to  $1/e$  of the maximum value within a distance of  $\sim 390$  nm. This means the intensity varies negligibly over the Er distribution. Nonetheless, near a corrugated film it is possible that the field varies within shorter length scales. We should consider the measured upconversion intensity therefore to be related to the field intensity averaged over the spatial distribution of the implanted Er ions.

### 8.3 Field enhancement in hole arrays

We first focus our attention to arrays of square-shaped holes. Figure 8.3 shows a white light transmission spectrum of an array with a periodicity of 810 nm and a hole diameter of 290 nm, normalized to the transmittance through the sample without the Au film. It shows three distinct transmission peaks for wavelengths longer than 800 nm. These maxima have been attributed to the excitation of surface plasmon polaritons that are excited when the condition

$$k_{\text{SPP}} = \left| \mathbf{k}_{0,\parallel} + \frac{2\pi i}{a} \hat{\mathbf{x}} + \frac{2\pi j}{a} \hat{\mathbf{y}} \right| \quad (8.1)$$

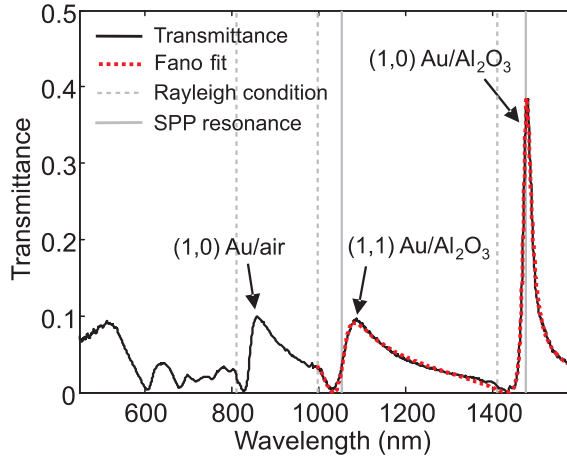


**Figure 8.3:** Transmission spectrum of a hole array in a Au film with a pitch of 810 nm. The red dotted curve is a fit of the Fano model described in section 8.4. The vertical gray lines indicate the resonance frequencies deduced from the Fano model, and the dashed gray lines depict the Rayleigh conditions for different diffraction orders.

is satisfied [180, 204, 205]. Here  $\mathbf{k}_{0,\parallel}$  is the in-plane component of the incident wavevector, respectively. The array pitch is given by  $a$ . The integers  $i$  and  $j$  together specify the diffraction order  $(i, j)$  that couples to SPPs with in-plane wavevector  $k_{\text{SPP}}$ . It is important to note that  $k_{\text{SPP}}$  is a priori unknown, since it is the wavevector of an eigenmode of the corrugated surface (i.e. a pole of the scattering matrix of the array), and it depends on the exact geometry of the structure [189]. The two peaks with longest wavelengths correspond to excitation of the surface plasmon mode at the metal/sapphire surface, and they are therefore expected to enhance the field at the position of the Er ions.

The resonance wavelengths can be precisely tuned by varying the array periodicity, as can be seen for the transmission peak associated to excitation of the surface wave at the  $\text{Al}_2\text{O}_3$  interface by the  $(\pm 1, 0)$  diffraction order in Fig. 8.4(a). The wavelength of the transmission maximum is a linear function of the periodicity to close approximation, since the SPP dispersion is nearly linear in this frequency regime. In the following experiment the periodicity is chosen such that the transmission peak coincides with the excitation wavelength of 1480 nm (see dashed line in Fig. 8.4(a)). This periodicity is 810 nm, as in Fig. 8.3. The upconversion photoluminescence spectrum as collected from that particular array is depicted by the red curve in Fig. 8.5, at an excitation power of  $200 \text{ W/cm}^2$ . Emission from four different Er manifolds that are all populated through upconversion processes is observed, at wavelengths of 550, 660, 810 and 980 nm. Also plotted is the luminescence spectrum obtained under equal experimental conditions in the absence of gold (through an aperture in the Au film of  $50 \times 50 \mu\text{m}^2$ ), multiplied by a factor 10. Clearly, the upconversion emission on the hole array is strongly enhanced with respect to that reference. In the following, we define the ‘upconversion enhancement’ caused by

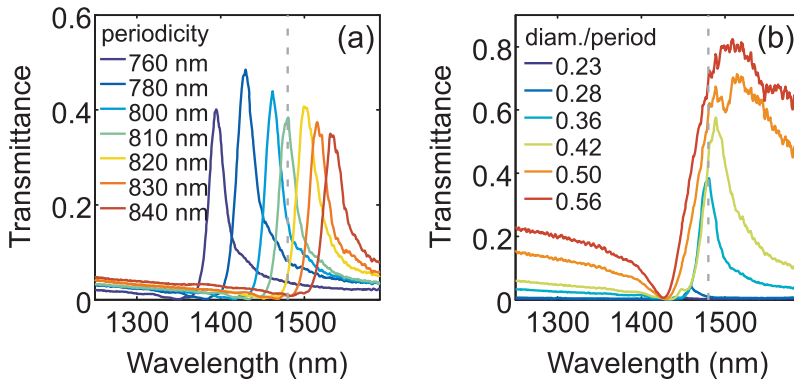


**Figure 8.4:** (a) Transmission spectra of a hole array in a Au film around the  $(\pm 1, 0)$  peak at the Au/ $\text{Al}_2\text{O}_3$  interface for various array periods. (b) Evolution of the same transmission peak with increasing hole size (indicated as diameter/period). The dashed gray lines depict the wavelength with which Er is excited.

an array as the ratio of the collected upconversion photoluminescence intensity on that array and the detected upconversion emission in a reference measurement in the absence of the Au film.

### 8.3.1 Quantifying field enhancement

We note that the measured upconversion enhancement does not directly reflect the average field enhancement at the position of the Er ions. The pump power dependence of the upconversion luminescence intensity is not a simple function such as a power law with a known exponent, which would make extraction of the pump power enhancement straightforward. The measured 980 nm upconversion emission as a function of 1480 nm pump power density is plotted on a double-logarithmic scale in the inset of Fig. 8.5, both on the array (red) and on the reference (black). For low pump powers, the upconversion luminescence can be seen to scale roughly quadratically with the excitation power as expected, but for larger pump powers saturation clearly occurs.

By comparing the two power dependency curves, we can deduce a better estimate of the pump power enhancement on the array. We extract the pump powers for which the collected upconversion luminescence intensities on the array and on the reference are equal. The ratio of these pump powers represents the average field intensity enhancement at the position of the Er ions, since it tells us how much the pump intensity on the array can be diminished with respect to that of the reference, to still result in the same amount of emission. We find a field intensity

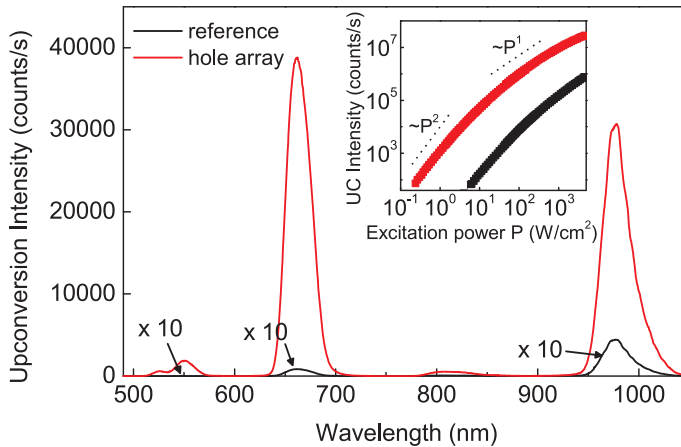


**Figure 8.5:** Er upconversion spectra obtained from a hole array with a pitch of 810 nm (red) and from a reference in the absence of the Au film (black) under 1480 nm pumping at  $200 \text{ W/cm}^2$ . Spectral resolution is  $\sim 20 \text{ nm}$ . The inset depicts the dependence of the 980 nm emission on 1480 nm pump power, measured on the array (red) and on the reference (black).

enhancement of a factor 40. For practical reasons we will use the aforementioned upconversion enhancement to compare the field enhancement on different arrays.

We note that the upconversion luminescence emitted at shorter wavelengths is even more strongly enhanced, as the corresponding Er levels are populated through higher order nonlinear upconversion processes. In the following, only the upconversion enhancement from the level emitting at a wavelength of 980 nm is considered.

### 8.3.2 Dependence of enhancement on structural parameters

We now systematically vary the periodicity and the hole diameter. Figure 8.6 shows the upconversion enhancement at an incident flux of  $2 \text{ W/cm}^2$  as a function of array periodicity and hole size (expressed as the hole diameter divided by the period). By varying the period in this range, both the  $(\pm 1,0)$  and the  $(\pm 1,\pm 1)$  transmission resonances corresponding to SPPs at the Au/sapphire interface can be tuned to the excitation wavelength, at periods of approximately 800 and 1150 nm, respectively (see arrows in Fig. 8.6).

For a given enhancement peak, a strong dependence of the upconversion luminescence on the aperture size can be seen in Fig. 8.6. For the resonance excited with a period of  $\sim 800 \text{ nm}$ , maximum field enhancement is observed for a hole size

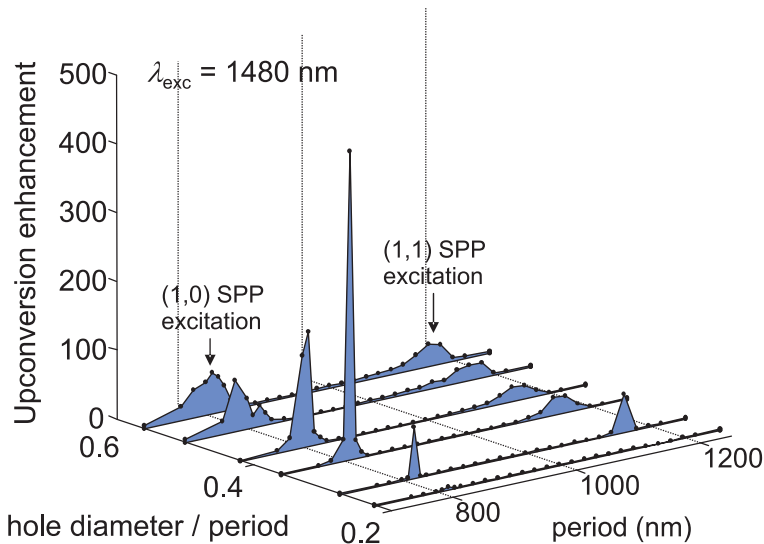


**Figure 8.6:** 980 nm upconversion enhancement (under 1480 nm pumping at  $2 \text{ W/cm}^2$ ) at an emission wavelength of 980 nm on hole arrays as a function of array period and hole size. Every point in the figure is derived from measurements such as in Fig. 8.5 on a corresponding array.



that is 0.36 times the period, giving rise to a 450-fold upconversion enhancement. For larger holes, the field enhancement gradually decreases.

Increasing the hole size will increase the evanescent tunneling of light through the holes as well as their scattering strength. Therefore the fraction of light coupled to SPPs will increase with increasing diameter. This becomes apparent as a monotonous increase of the far-field transmittance with increasing diameter [206], that is depicted in Fig. 8.4(b). The near-field enhancement represented by the data in Fig. 8.6 on the other hand reveals the existence of an optimum hole size. The stronger coupling between far-field radiation and SPPs for larger holes results in a widening and a redshift of the transmission peak. Both effects can be observed in the data in Fig. 8.6, as well as in the transmission spectra in Fig. 8.4(b). Unlike the far-field transmittance, the near-field enhancement does not only scale with the fraction of light coupled to SPPs, but also with the resonance linewidth. A larger quality factor of the SPP resonance results in a stronger build-up of optical energy close to the array. A trade-off therefore exists between quality factor and coupled fraction as the hole size is varied, resulting in an optimum hole size that yields maximum field enhancement.

Note that this optimum strongly depends on other parameters as well; most notably the film thickness and the illumination geometry. If the array would have been illuminated from the substrate side of the film, the exciting radiation would not have needed to tunnel through the apertures before exciting SPPs at the Au/sapphire interface, likely resulting in a stronger field enhancement at a smaller optimum hole size compared to the geometry studied here.

## 8.4 The Fano model: far field transmission and near field enhancement

We also investigate the relation between far-field transmittance and near-field enhancement by comparing their dependence on array periodicity. Figure 8.7 (red circles) shows the upconversion enhancement as a function of period for a hole diameter of 0.42 times the period from Fig. 8.6. Again, every data point represents a measurement on an array with a different periodicity. Also indicated is the transmittance at the excitation wavelength of 1480 nm on those same arrays. While both data sets show two maxima at similar periods (at 800 nm and  $\sim$ 1150 nm), striking differences between the shapes of the curves can be observed. The transmission peaks are wider, shifted to smaller pitches (corresponding to a spectral redshift), and pronouncedly more asymmetric than the peaks observed in the near-field enhancement probed by the upconversion emission.

These differences can be fully explained in terms of the Fano model [207]. The response of a subwavelength hole array can be described as that of multiple discrete states (the surface plasmon modes resonantly excited by various diffraction orders) coupled to a continuum (all far-field scattering states) [208, 209]. The array can scatter light to the far field either directly or by first exciting surface plasmons and

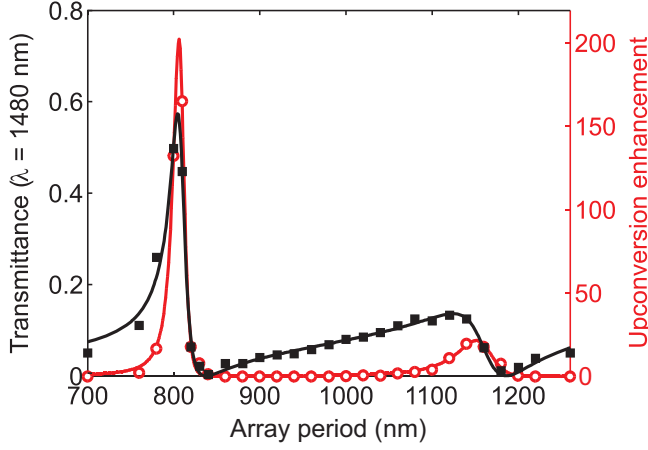


**Figure 8.7:** Comparison between the 980 nm upconversion enhancement (red) and the transmittance at 1480 nm (black) as a function of the hole array period (hole diameter/period = 0.42). Each data point is measured on a different array. The curves are fits of a Fano model to the data. The resonance wavelengths and widths derived from the Fano model fitted to the transmittance data are imposed on the Fano model that is fitted to the upconversion enhancement data. The Fano model correctly predicts both the position and linewidth of the surface plasmon resonances, which are revealed by the upconversion enhancement.

subsequently radiating to the far field. These non-resonant and resonant channels can interfere to produce asymmetric transmission spectra when both contributions are of approximately equal magnitude, as the resonant channel acquires an opposite phase as the frequency crosses the resonance [207]. The spectral shape, generalized to a system of multiple resonances with resonance frequencies  $\omega_r$  and linewidths  $\gamma_r$  is given by [72]

$$T(\omega) = T_a \frac{(1 + \sum_r q_r / \epsilon_r)^2}{1 + (\sum_r \epsilon_r^{-1})^2}, \quad \text{with} \quad \epsilon_r = \frac{\omega - \omega_r}{\gamma_r / 2}, \quad (8.2)$$

where  $T_a$  is a slowly varying background representing the non-resonant transmission channel and  $q_r$  is a shape parameter that is related to the strength and phase of the resonant channel with respect to the non-resonant contribution. To illustrate the potential of this model we return to the transmission spectrum of the hole array with a pitch of 810 nm shown in Fig. 8.3. We fit (8.2) to this spectrum for wavelengths larger than 1000 nm, allowing for two resonances. The non-resonant contribution  $T_a$  is assumed to scale as  $\lambda^{-4}$ , in accordance with the transmittance of a circular aperture of a perfectly conducting screen as given by Bethe [210]. The excellent fit of the Fano model (the red dashed line in Fig. 8.3) to the experimental transmission spectrum suggests that the most important physics of the system is indeed determined by the two surface wave resonances. The transmission peaks

are redshifted with respect to the fitted resonance frequencies, which are indicated by the grey lines. For comparison, the Rayleigh conditions, for which the right-hand side of (8.1) equals the wavevector of light in the bounding dielectrics, are indicated by the grey dashed lines.

As an aside, we note that the peak associated with  $(\pm 1, 0)$  diffraction to surface plasmons at the Au/air interface can also be fitted when a third resonance is introduced. However, in that case it becomes apparent that the assumption  $T_a \propto \lambda^{-4}$  overestimates the direct transmission through the apertures at small wavelengths. A better fit is obtained for  $T_a \propto \lambda^{-3}$ . An explanation for a deviation from Bethe's theory could be sought in the finite thickness of the metal film and metal absorption.

While the above analysis regards measurements of the far-field transmission, the Fano effect can play a role in the near-field as well, because the field of the resonantly excited surface plasmons can interfere with the incident field transmitted through the apertures. But because the surface plasmon field is strongly enhanced (by a factor related to the resonance linewidth), the shape parameter  $q$  will in general be much larger, making the resonant contribution dominant.

This is reflected in the differences between the transmittance and upconversion enhancement data sets for varying periodicity in Fig. 8.7. We first fit the Fano model (8.2) to the transmittance data in Fig. 8.7, where  $\omega$  is fixed by the laser wavelength and we assume that the resonance frequencies  $\omega_r$  are inversely proportional to the periodicity  $a$ :  $\omega_r = c_r a^{-1}$  (the SPP dispersion is nearly linear near 1480 nm). We again assume that the direct transmission through a single hole scales as  $(\lambda/R)^{-4}$ . The hole radius  $R$  scales linearly with the period  $a$ . Because the hole density decreases quadratically with increasing period and the wavelength  $\lambda$  is fixed, we now have to take  $T_a \propto a^2$ . An excellent fit to the transmittance data is obtained, depicted by the black curve in Fig. 8.7.

We then fit the upconversion enhancement data by taking the values for  $c_r$  and  $\gamma_r$  derived from the fit of the transmittance data, only fitting  $q_r$  and  $T_a$ . The fit resulting from this procedure is depicted as the red line in Fig. 8.7. In the analysis the measured power-dependence (see the inset of Fig. 8.5) has been taken into account to yield the upconversion enhancement from the field intensity enhancement given by the Fano model. A near-perfect fit to the data is obtained. The larger relative contribution of the resonant channel to the near field results in almost Lorentzian lineshapes of the resonances observed in the upconversion enhancement, centered around the resonant periodicity.

The transmission maxima are significantly shifted and broadened with respect to the actual surface wave resonance, as is most clear for the peak at a pitch of  $\sim 1150$  nm (for which the hole size and therefore the nonresonant contribution are largest). Similar shifts were reported for second harmonic generation in aperture arrays [9, 187, 188]. The Fano interpretation presented here yields a new and powerful explanation for those observations. These results show that the Fano model correctly predicts the wavelength and spectral width of the surface plasmon eigenmodes of the corrugated surface. The luminescence from emitters placed

in the near field of hole arrays can be used to experimentally reveal the surface modes that are responsible for the extraordinary transmission phenomenon [180, 189, 205].

## 8.5 Field enhancement in arrays of annular apertures

The field enhancement in arrays of round or square subwavelength holes depends strongly on the frequency and the angle of incidence, as it relies to a large degree on grating diffraction (see (8.1)). In contrast, field enhancement due to localized resonances such as those supported by annular apertures does not suffer from this limitation. The transmission spectra of arrays of annular apertures can exhibit features that are due to the excitation of both localized and propagating modes [72, 73].

Figure 8.8(a) shows the transmission spectra of annular aperture arrays in Au consisting of apertures of varying size. The array period is kept constant at 800 nm. We denote the length of the side of the Au island as  $D_1$  and the length of the side of the total aperture as  $D_2$  (see inset in Fig. 8.8(b)). Both  $D_1$  and  $D_2$  are continuously increased, starting from array A (dark blue) to array C (dark red). Due to fabrication intricacies, it was not possible to keep the ratio of  $D_1$  to  $D_2$  perfectly constant throughout the series. Therefore, we include SEM micrographs of three of the annular aperture shapes in the legend of Fig. 8.8.

The transmission spectrum of array A shows a strong resemblance to that of an array of square holes in the absence of the central Au island (black), displaying the diffractive resonances described in the previous sections. As the aperture

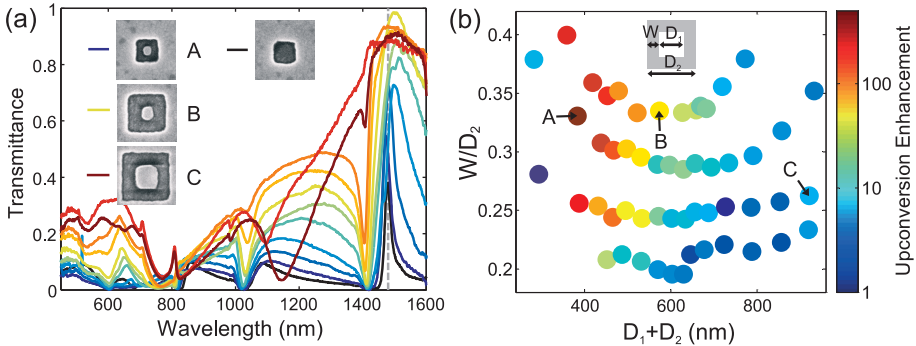


**Figure 8.8:** (a) Transmission spectra of annular aperture arrays for increasing aperture size (array period 800 nm). The black curve is the transmittance of an array of square holes with the same period. (b) 980 nm upconversion enhancement (1480 nm pump at  $2 \text{ W/cm}^2$ ) as a function of the main parameters describing the shape of the annular apertures: the sum of  $D_1$  and  $D_2$ , and the width of the air gap  $W$  expressed as a fraction of the total aperture size  $D_2$ .

size increases, the transmission peaks broaden and increase in magnitude, until for the largest apertures (array C) a single broad transmission peak dominates the spectrum for wavelengths larger than 1100 nm, which we attribute to a localized resonance. These aperture dimensions agree roughly to the cutoff condition of the  $TE_{11}$  mode in a perfectly conducting waveguide [74], which scales to first order with  $(D_1 + D_2)$ . Note that grating effects observed for the regular holes such as the minimum around 1400 nm are in this case largely suppressed.

In Fig. 8.8(b) we plot the measured upconversion enhancement on a collection of arrays with varying aperture dimensions. The horizontal axis specifies the sum of  $D_1$  and  $D_2$  of the annular apertures, and the vertical axis denotes the width of the air gap between the central Au island and the continuous Au film  $W$ , expressed as a fraction of the total aperture size  $D_2$ . The periodicity of all arrays is 800 nm, and the excitation power is  $2 \text{ W/cm}^2$ . The overall trend in Fig. 8.8(b) is that largest upconversion enhancements are observed for the smaller radii. Enhancements of over a factor 100 are observed for radii around 100 nm. The maximum upconversion enhancement factor is achieved on array A, which exhibits a transmission maximum related to the excitation of propagating surface plasmons that is resonant with the 1480 nm excitation wavelength. The magnitude of the enhancement is a factor 370, comparable to the maximum enhancement observed on arrays of square holes. Array C, which supports a localized resonance (see Fig. 8.8(a)), yields a lower enhancement factor of approximately 10. Nonetheless, the field enhancement in this structure is larger than in structures with slightly different gap widths or sizes, which we attribute to the enhanced spectral overlap of the corresponding localized resonance to the excitation wavelength for this aperture shape.

### 8.5.1 Angle dependence of field enhancement in annular apertures

Finally, we investigate the effect of the angle of incidence on the field enhancement due to either propagating or localized resonances. Figure 8.9 shows the measured upconversion enhancement on three different aperture arrays as a function of angle of incidence as described in section 8.2. The incident light is  $p$ -polarized. As expected, the upconversion enhancement on array A, which is associated to the excitation of propagating SPPs, shows a strong dependence on the incident angle, vanishing for angles larger than  $10^\circ$ . Note that the maximum enhancement at normal incidence is now reduced compared to that in Fig. 8.8(b) due to the use of a larger NA. The maximum enhancement on array B is observed for an incident angle of  $\sim 6^\circ$ . For this array, the resonance was not tuned exactly to the laser wavelength at normal incidence. Instead, (8.1) is satisfied at a slightly different angle. The upconversion enhancement diminishes less rapidly with increasing angle than for array A, since the resonance width is larger in this case. Nonetheless, still a clear angle-dependence is observed. Array C does not show an effect of the incident angle on the upconversion enhancement, which is  $\sim 10$  for the angular range studied here. This shows that the field enhancement due to localized plasmonic resonances in

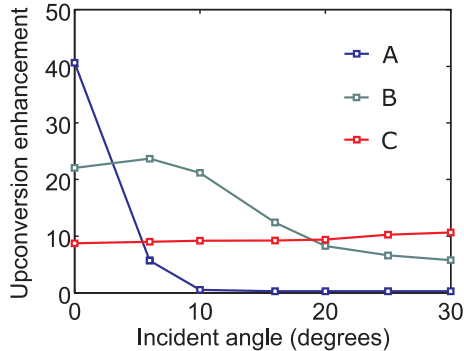


**Figure 8.9:** 980 nm upconversion enhancement as a function of incident angle for three different annular aperture arrays specified in Fig. 8.8 (1480 nm pump at  $16 \text{ W/cm}^2$ ). The field enhancement that is caused by a localized resonance (array C) is independent of the angle of incidence.

annular aperture arrays is indeed independent on the incident angle.

## 8.6 Conclusions

We have shown that Er upconversion luminescence can be used to probe the field enhancement in subwavelength aperture arrays. Field enhancement due to the excitation of both propagating and localized resonances in aperture arrays was studied. In hole arrays supporting propagating resonances, an enhancement of the 980 nm upconversion luminescence of Er ions under 1480 nm pumping by a factor 450 is demonstrated. This maximum upconversion enhancement is achieved for a hole size that balances SPP coupling efficiency and resonance linewidth. We note that the field enhancement can be further increased by changing the experimental geometry. The evanescent tunneling of the excitation light incident from the air side of the sample to excite SPPs at the substrate side of the sample (where the Er ions are located) limits the measured upconversion enhancement in the present geometry.

We have confirmed that the Fano model accurately predicts the frequencies and linewidths of the resonances that cause the extraordinary transmission phenomena. These properties are revealed by observing the Er upconversion enhancement. The relative strength of the resonant contribution to the near-field enhancement with respect to the non-resonant contribution is much larger than the ratio of both contributions in far-field transmission spectra. This results in much more symmetric lineshapes of the upconversion enhancement. The transmission peaks are significantly redshifted from the spectral position of maximal field enhancement.

The transmission spectra of annular aperture arrays can be tuned by varying the aperture size, from an array exhibiting propagating surface plasmon resonances to

one that supports localized plasmon resonance in the individual apertures. While the field enhancement is smaller in the latter case, we show experimentally that, unlike the field enhancement related to the excitation of propagating SPPs, this enhancement is independent of the angle of incidence.

This work reveals basic mechanisms governing near-field enhancement in metallic subwavelength aperture arrays, which is important for many practical applications of such nanostructures. In doing so, it sheds light on the mechanisms behind far-field extraordinary transmission properties as well.





---

## Enhanced spontaneous emission rate in annular plasmonic nanocavities

*The spontaneous emission rate of erbium ions is enhanced by coupling to localized plasmonic resonances in subwavelength annular apertures fabricated in a Au film. The  $\text{Er}^{3+}$  ions, embedded in  $\text{SiO}_2$ , are selectively located inside the apertures. The annular apertures act as nanocavities enhancing the local density of optical states at the Er emission wavelength of  $1.54 \mu\text{m}$  when the cavities are tuned to that wavelength. We show that this leads to an 8-fold increase of the photoluminescence intensity, in conjunction with a 2.4-fold enhancement of the spontaneous emission rate.*

### 9.1 Introduction

Control of spontaneous emission is of interest for many applications, including LEDs, sensors, quantum information processing and photovoltaics [12, 13]. By modifying the local electromagnetic environment of an optical emitter, the polarization and the directionality of its radiation as well as its overall decay rate can be modified. In recent years a number of different plasmonic geometries have been used to modify the spontaneous emission rate, including nanoparticles and nano-antennas [211–218].

Suitably shaped subwavelength apertures in a metal film can also support a localized plasmonic resonance. For example, annular apertures, composed of an

inner metal core, separated from the surrounding metal by a dielectric ring, can act as nanocavities with a modal field that is strongly confined to the aperture [71, 72, 191]. Even though the quality factor  $Q$  of these cavities is modest, the ultra small mode volume  $V$  can potentially lead to a significant Purcell enhancement of the spontaneous emission rate, which is given by [219]

$$F = \frac{3\lambda_0^3 Q}{4\pi^2 V}. \quad (9.1)$$

Because of the relatively low  $Q$ , any Purcell enhancement induced by the localized plasmon resonances would be observed over a large bandwidth. It is well known that annular apertures couple strongly to far-field radiation, since they can assist large transmission of light through a metal film [71, 72, 191]. This makes these structures promising candidates for enhancing the radiative emission rate. Previous studies of fluorescence from circular subwavelength apertures have demonstrated the modification of spontaneous emission in various ways [185, 220–222], but these did not exploit localized resonances in the apertures.

In this chapter, we demonstrate the enhancement of the radiative emission rate of optically active erbium ions positioned inside annular apertures in a gold film. We observe an increase in both PL intensity and decay rate as we tune the aperture's resonance wavelength to the Er transition wavelength. For the apertures with a resonance closest to the Er transition wavelength the total decay rate is increased by a factor 2.4 with respect to Er in a reference area, i.e., a part of the sample without patterning or Au.

## 9.2 Methods

### 9.2.1 Sample fabrication

To obtain maximum spatial overlap of the Er ions with the nanocavity mode field the ions have to be positioned inside the annular apertures. A schematic of the fabricated structures is shown in Fig. 9.1. A fused silica (Heraeus Suprasil 300) substrate is first doped with erbium by 150 keV  $\text{Er}^+$  ion implantation at normal incidence using a fluence of  $3.0 \times 10^{14} \text{ cm}^{-2}$ . This results in a distribution of Er ions at a mean depth of 82 nm with a standard deviation of 18 nm, as calculated with the Monte Carlo program SRIM [127]. The peak Er concentration is 0.29 at. %. We then remove the top 30 nm of silica with reactive ion etching in order to reduce the mean depth of the Er ions to 50 nm. Next, the substrate is covered with a resist stack of 500 nm PMMA, 20 nm Ge and 90 nm negative electron beam resist (Ma-N 2401) in which we pattern hexagonal arrays of annular structures by electron beam lithography. Square regions near these arrays are also exposed to provide reference areas. After developing the patterned layer, reactive ion etching through the resist layers and through 100 nm of silica is used to leave 100 nm thick Er-doped silica rings on the substrate. A 100 nm thick layer of gold is evaporated on the sample and

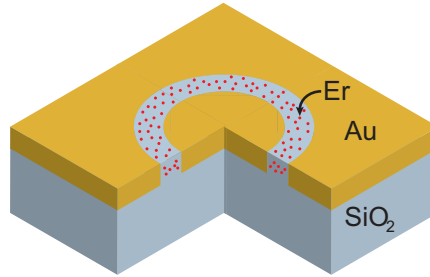


**Figure 9.1:** Schematic of a single Er-doped  $\text{SiO}_2$  annular aperture in a Au film on  $\text{SiO}_2$ .

the excess gold and resist is removed using lift-off. This results in annular apertures in a Au film on  $\text{SiO}_2$ , filled with Er-doped  $\text{SiO}_2$ . The apertures are arranged in  $50 \times 50 \mu\text{m}^2$  hexagonally ordered arrays. A top-view SEM image of part of such an array is depicted in Fig. 9.2(a). A small air gap is observed between the  $\text{SiO}_2$  rings and Au surrounding.

### 9.2.2 Optical measurements

Optical transmission spectra of the arrays are obtained by illuminating the sample from the air side with an NA of 0.02 and collecting the transmitted light through a 0.75 NA objective. The light is passed through a spectrometer and detected with either a silicon CCD for visible wavelengths or an InGaAs diode array for infrared light. Reflection spectra are recorded using a 0.65 NA reflective objective and a Biorad FTS6000 Fourier transform spectrometer with an InAs photodiode.

To measure the photoluminescence (PL) of the erbium ions the sample is il-

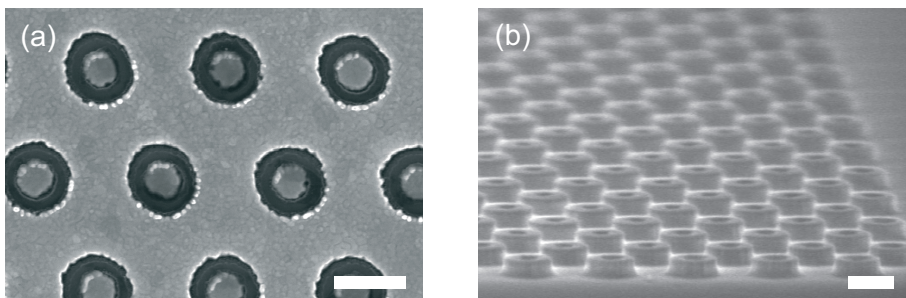


**Figure 9.2:** (a) SEM image of a fabricated hexagonal array of annular apertures in a Au film. (b) SEM image of Er-doped rings of  $\text{SiO}_2$ , not coated with Au. Scale bars are 500 nm.

luminated with light from an argon ion laser operating at 488 nm incident under a  $20^\circ$  angle to the sample surface from the air side of the metal film. The light is focused to an elliptically shaped Gaussian spot with a full width at half maximum of  $34 \mu\text{m}$  along one direction and  $85 \mu\text{m}$  along the other, as measured using a razor blade. The peak power density is  $275 \text{ W/cm}^2$  for intensity measurements and  $680 \text{ W/cm}^2$  for time-resolved measurements. We collect the luminescence with a 0.45 NA objective at the air side of the sample. PL intensity is measured with a spectrometer with an InGaAs diode array detector while measurements of the decay rate are performed with a North Coast EO-817s Ge photodiode detector with a response time of  $30 \mu\text{s}$ . The laser is modulated at 7 Hz with an acousto-optic modulator for decay rate measurements.

### 9.2.3 Tuning the localized resonance

The resonance wavelength of the annular aperture nanocavities can be tuned by varying the aperture size and shape. The localized resonance that is considered here can be related to cutoff of the  $\text{TE}_{11}$  mode of a coaxial waveguide with an equivalent cross section [71, 72], as discussed in section 1.3. The cutoff wavelength for the  $\text{TE}_{11}$  mode in an annular waveguide in a perfect electric conductor is approximated by  $\lambda = n(R_o + R_i)\pi$  [71, 72], where  $R_o$ ,  $R_i$  and  $n$  are the outer and inner radius of the aperture and the refractive index of the medium in the apertures, respectively. Here, we control the resonance wavelength by varying the average radius  $R = (R_o + R_i)/2$  from 193 to 303 nm. The width,  $R_o - R_i$ , of the annular apertures is kept constant at 100 nm to maintain a constant average separation between Er ions and the metal surface, and therefore a constant rate of direct quenching to the metal of excited Er [134]. Concurrent with the increase in  $R$  the periodicity is increased from 903 to 1086 nm such that the average areal density of Er ions is the same in all arrays, which simplifies the comparison of PL intensities.

## 9.3 Results

Transmission and reflection spectra of the arrays with varying  $R$  are shown in Fig. 9.3. A large transmittance peak is seen in conjunction with a dip in reflectance, associated with the localized resonance. As expected, the resonance wavelength shifts to larger wavelengths when  $R$  is increased. It varies from  $\sim 1.6 \mu\text{m}$  for the smallest radius to about  $2.4 \mu\text{m}$  for the largest radius. In Fig. 9.4(a) we plot the transmittance at  $1.54 \mu\text{m}$  for the different cavities as a function of the average radius  $R$ : it reduces from 0.84 to 0.08. As all transmission at this wavelength is mediated by the localized resonance, the transmittance can be used as a measure of the strength of the resonant mode at a given frequency. The decreasing transmittance for increasing  $R$  therefore implies that the local density of states at the Er transition wavelength will decrease as the radius is increased.

A typical PL spectrum of the  $\text{Er}^{3+} {}^4\text{I}_{13/2} \rightarrow {}^4\text{I}_{15/2}$  transition at  $1.54 \mu\text{m}$  is shown

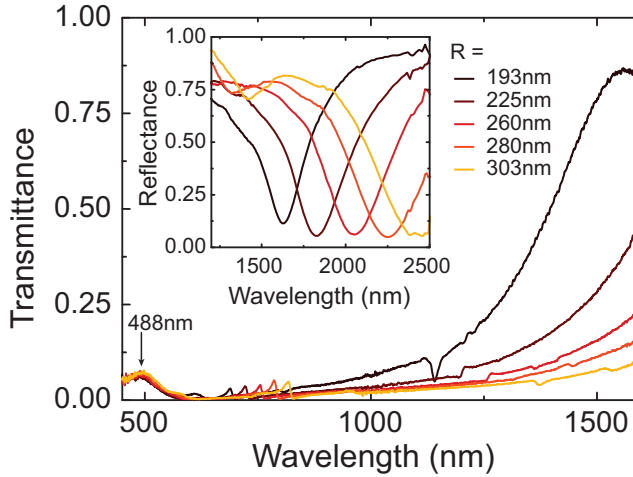


**Figure 9.3:** Transmission and reflection (inset) spectra for the annular aperture arrays. The arrays show large transmission at the resonance wavelength. By increasing the average radius of the annular apertures this resonance wavelength is shifted. The pump wavelength (488 nm) in PL experiments is indicated by an arrow.

in Fig. 9.5(a). We compare the integrated PL intensity in Au annular nanocavities to that in similar arrays of silica rings that are not covered in Au, as depicted in Fig. 9.2(b). In Fig. 9.4(b) we plot the PL enhancement, taken as the ratio of the PL intensity from the Au nanocavities to that from the silica rings without Au for rings with different  $R$ . We observe an enhancement up to a factor 8 for the annular apertures with a resonance near the erbium emission wavelength, i.e., for the apertures with  $R = 193$  nm. As we increase  $R$  the resonance wavelength increases, shifting away from the Er emission wavelength (see Fig. 9.4(a)), and the PL enhancement decreases, demonstrating a strong correlation between the PL enhancement and the cavity resonance condition.

To investigate the origin of the observed trend in the PL enhancement for decreasing  $R$ , we performed time-resolved measurements of the PL decay. For the apertures with a resonance near  $1.6 \mu\text{m}$  ( $R = 193$  nm) and the ones with a resonance the furthest away from the erbium emission wavelength ( $R = 303$  nm) the decay curves are plotted in Fig. 9.5(b). Single-exponential functions are fitted to the curves to obtain a first-order estimate of the decay rate of Er in the various nanocavities. The fitted decay rates for all arrays are plotted in Fig. 9.4(c). We find that the total decay rate for the resonant array with  $R = 193$  nm ( $\Gamma = 311 \text{ s}^{-1}$ ,  $\tau = 3.2$  ms) is 1.5 times as large as that for apertures with  $R = 303$  nm ( $\Gamma = 207 \text{ s}^{-1}$ ,  $\tau = 4.8$  ms). The decay rate for Er in the reference area is  $\Gamma = 132 \text{ s}^{-1}$  ( $\tau = 7.6$  ms), shown as the dashed line in Fig. 9.4(c). Accordingly, the total decay rate of Er for

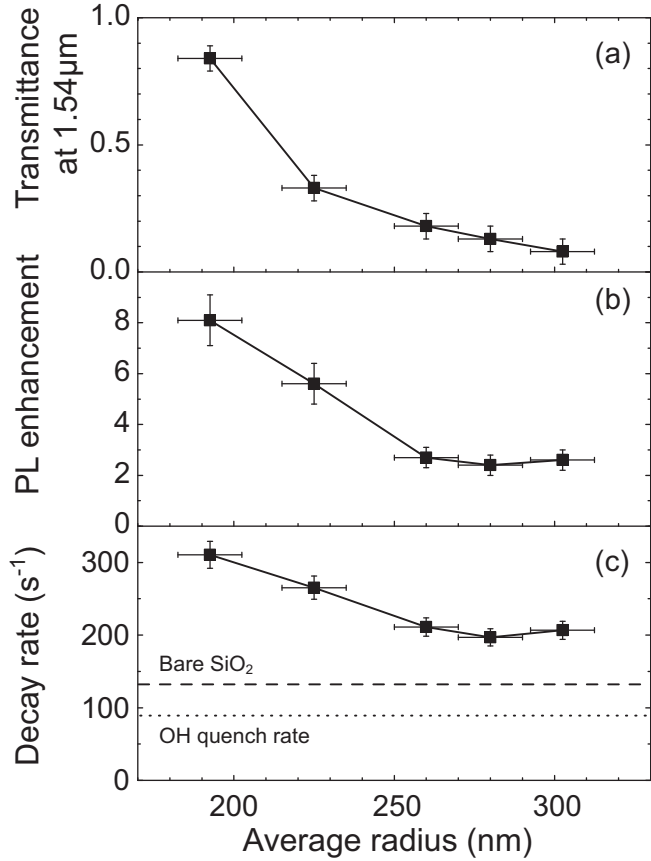


**Figure 9.4:** Optical properties of Er-doped annular apertures as a function of average aperture radius  $R$ . (a) Transmittance at 1.54  $\mu\text{m}$ ; (b) PL enhancement compared to similar arrays of silica rings not covered in Au; (c) Er decay rate at 1.54  $\mu\text{m}$ . The decay rate of Er in a reference area is indicated by a dashed line and the additional rate due to OH quenching by the dotted line.

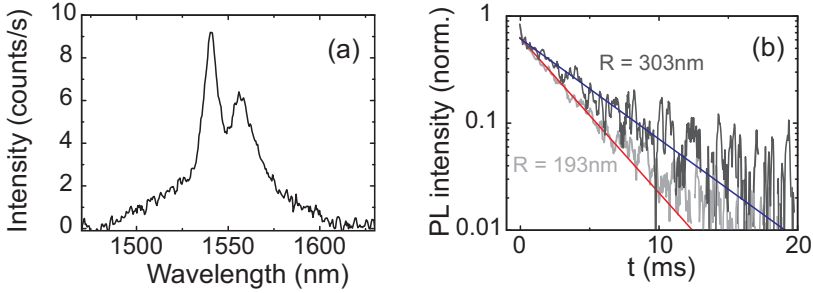


**Figure 9.5:** (a) Erbium luminescence spectrum taken on a planar SiO<sub>2</sub> film ( $\lambda_{\text{pump}} = 488$  nm) and (b) decay curves for two different annular aperture arrays with a resonance near the erbium emission wavelength ( $R = 193$  nm) and with a resonance the furthest away from  $1.5 \mu\text{m}$  ( $R = 303$  nm).

the resonant apertures is increased by a factor 2.4 as compared to that of Er in the reference area.

## 9.4 Discussion

The corresponding trends in PL intensity and decay rate with varying  $R$  are a strong indication that the observed increase of the PL intensity as the resonance is tuned to the Er transition is related to an increase of the radiative decay rate. As the PL experiments were performed in the linear pumping regime, the increase in PL enhancement from 2.5 for apertures with large radii to 8.1 for the apertures with  $R = 193$  nm indicates that the luminescence quantum efficiency is increased by a factor 3 as we tune the resonance wavelength to the Er emission wavelength. We exclude a difference in pump rate for the various aperture arrays as an alternative cause for the trend observed in the PL intensity. The pump wavelength is much smaller than the resonance wavelength and we observe no change in the transmission near 488 nm for the various aperture arrays (see arrow in Fig. 9.3). It is nonetheless possible that the pump intensity is enhanced for all structures compared to the pump rate in the reference area without Au. Because the magnitude of this effect is unknown, it is not straightforward to quantitatively compare the decay rate enhancement and the PL enhancement.

We can however estimate an upper bound to the enhancement of the radiative rate when the structure is tuned to resonance. The total decay rate  $\Gamma$  is composed of radiative and non-radiative components. There are two sources for non-radiative decay: quenching by OH impurities in the glass [223], which is independent of the dielectric environment [224], and absorption by the Au. The OH quench rate, derived from a comparison of the measured decay rate of Er in the reference area, the known radiative decay rate in bulk SiO<sub>2</sub> ( $54 \text{ s}^{-1}$ ) [225], and the known relative

local density of states at the depth of the Er ions in the reference area [226], amounts to  $\Gamma_{\text{OH}} = 89 \text{ s}^{-1}$  (dotted line in Fig. 9.4(c)). Correcting for the LDOS-independent OH quenching, the remaining decay rate, i.e.,  $\Gamma - \Gamma_{\text{OH}}$ , for the apertures resonant near the Er transition wavelength is increased by a factor 4.1 as compared to the radiative decay rate in bulk  $\text{SiO}_2$ . Taking into account the refractive index of  $\text{SiO}_2$ , the remaining decay rate is thus enhanced by a factor 6 with respect to the decay rate in vacuum. This number constitutes an upper limit to the enhancement of the radiative rate, if the absorption by Au is negligible compared to the power radiated to the far field by the aperture mode.

The quality factor derived from the reflectance data is  $Q = 5.2$  for the array with  $R = 193 \text{ nm}$ . To make a first estimate of the expected Purcell factor  $F$  we take the mode volume equal to the geometrical volume ( $1.3 \times 10^{-2} \mu\text{m}^3$ ), and find  $F = 135$  for these annular apertures. The experimentally derived rate enhancement of a factor 6 is much smaller than the estimate of the Purcell factor. The difference suggests that the coupling of Er to the nanocavity mode is less than optimal. It could be partly due to a possible spatial mismatch between the Er distribution and the  $\text{TE}_{11}$  mode profile, and to a distribution in orientation of the Er emission dipole. Moreover, the effective mode volume could differ significantly from the geometrical volume [82, 227].

More insight in the coupling between emitters and the nanocavity mode could be gained in further experiments, by considering the ensemble distribution of decay rates, the spatial overlap between the cavity mode profile and the Er distribution and the variation in coupling ratio to modes other than the  $\text{TE}_{11}$  mode, for off-resonant arrays.

## 9.5 Conclusions

In summary, we have shown that the spontaneous emission decay rate of  $\text{Er}^{3+}$  ions at  $1.54 \mu\text{m}$  is controlled using annular apertures fabricated in a Au film. An increased decay rate and PL intensity are observed for apertures filled with Er-doped  $\text{SiO}_2$  in a Au film when the localized plasmon resonance of the apertures is tuned to the Er emission wavelength. A 2.4-fold decay rate enhancement and a 8-fold intensity enhancement are observed. The various decay processes and their effects on the decay rate and PL intensity were discussed.



# 10

---

## Applications and outlook

*Based on surface plasmon nanofocusing, localized surface plasmon resonances, and dispersion control, we propose several applications and research directions that can arise from the work described in this thesis. We discuss strategies for interfacing optics and electronics on the nanoscale, the efficient concentration of light for photovoltaics, controllable field enhancement for sensing and spectroscopy, and a possible route towards a lens based on negative refraction.*

The field of plasmonics owes much of the interest it currently attracts to the fact that it combines fundamental science with the prospect of technological applications. This chapter aims to identify some directions in which the concepts developed in this thesis can be applied. The examples given are by no means exhaustive, nor are they complete device proposals. Many require more fundamental questions to be answered first. We provide a quantitative analysis of some of the proposals to recognize challenges and opportunities that can be expected along the road.

### **10.1 Integrated photonics**

#### **10.1.1 Coupling light to the nanoscale**

Photonic waveguides can serve multiple purposes on computer chips. On the one hand, they can function as off-chip or on-chip interconnects because of their large

bandwidth and low power consumption [2]. On the other hand, they are the signal carriers in integrated photonic circuits. For both applications, arranging the waveguides as densely as possible is an important goal.

Because of the losses that are inherent to highly confined SPPs, they are not suitable as millimeter-scale interconnects [228]. On a smaller scale, they could provide useful functionality. Subwavelength confinement allows the use of photodetectors of smaller size than usual, improving noise, latency, and power dissipation [7]. As such, even off-chip interconnects that are interfaced to electronics at the edge of a chip can benefit from a subwavelength concentration of light, if the light in a waveguide can be efficiently concentrated to the size of a nanoscale photodetector. In photonic circuits, a strong field enhancement can enhance nonlinear processes, facilitating optical switching at smaller powers [11, 229–231]. Elements are needed that can couple light efficiently between highly confined modes and low-loss guided waves with moderate confinement [110].

The taper design presented in Chapters 5 and 6 provides a coupling element to convert a broad low-loss SPP beam to a nanoscale size. To use this design to focus light that is propagating in a dielectric waveguide or in free space, the light first needs to be coupled to SPPs at the high-index side of a metal stripe. Figure 10.1 depicts three compact implementations of structures that perform both light-SPP coupling and subsequent SPP nanofocusing.

In Fig. 10.1(a), a grating coupler is used to couple light that is incident at some angle from free space or from an optical fiber, similar to the experiments in Chapters 4–6. The grating coupling efficiency is expected to be largest when the size of individual diffracting elements (e.g., nanoscale holes in the film) is such that the SPP propagation length on the grating is of the same order as the beam waist. For normal incidence, the grating period should be equal to the SPP wavelength  $\lambda_{\text{SPP}}$  on the grating. A reflector element (depicted in Fig. 10.1(a) as a Bragg grating with period  $\lambda_{\text{SPP}}/2$ ) could in that case be used to direct SPPs towards the tapered waveguide. Since the SPP propagation length on a smooth film is much larger than a typical beam or fiber core size at telecommunication wavelengths, the task of optimiz-

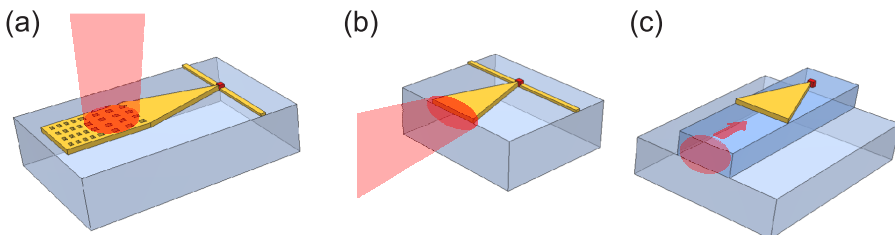


**Figure 10.1:** Three designs to interface light to a nanoscale photodetector (red) for photonic integration on a chip, employing nanofocusing of SPPs. The conversion of light to SPPs is performed by grating coupling (a), endfire coupling (b), or mode matching in a dielectric waveguide (c).

ing the coupling efficiency is expected to be similar to that in dielectric waveguides, in which near-unity coupling efficiency has been demonstrated [232]. However, if the light is incident from the low-index side of the metal film, the need to transmit energy through the film will possibly limit the efficiency (see section 8.3.2).

Because the mode profile at the start of a tapered waveguide is broad, it will have a relatively large mode overlap with a Gaussian beam in free-space or with the TM-polarized fundamental mode in a dielectric waveguide or fiber. The cross section of the beam should be elliptical to obtain maximum mode overlap with the mode profile depicted in Fig. 6.2. It may then be possible to achieve significant coupling in an end-fire arrangement, as sketched in Fig. 10.1(b). Similarly, the design shown in Fig. 10.1(c) could be used to focus a TM-polarized mode in a dielectric waveguide, since that mode will have significant mode overlap with the SPP mode guided by a metal-covered waveguide. It may therefore transfer a large fraction of its energy to the SPP mode in the metal-covered waveguide at the interface between the covered and non-covered parts of the waveguide, especially if no other guided modes exist in the metal-covered section. By tapering the metal film on the waveguide, the excited SPPs are expected to subsequently concentrate in a subwavelength spot on the waveguide.

In Fig. 10.1, the tapered waveguides are interfaced to a nanoscale photodetector at the taper tip, to offer high speed and large bandwidth. This is just one of the possible uses of nanoscale concentration. It is worth mentioning the possibility to perform heat-assisted magnetic recording by locally heating a ferromagnetic medium above its Curie point to reduce the coercivity. The optical energy used to heat single magnetic domains must be delivered to a subwavelength spot efficiently. This has been demonstrated using a resonant plasmonic element at the end of a solid immersion lens integrated in a magnetic recording head [233]. The geometry sketched in Fig. 10.1(a) could provide the same functionality using adiabatic mode transformation, in a design that can be fabricated in a straightforward lithographic process.

### 10.1.2 Nanowire directional couplers

As we have seen in Chapter 6, the tapers can also be used to efficiently launch SPPs in metal nanowires, which could provide a platform for nanoscale photonic circuits. In such a circuit, one needs elements to split, combine, and preferably even actively switch signals between different waveguides. In dielectric waveguides, these functions are often performed by directional couplers [230, 234].

Here we consider codirectional coupling between two nanowires. The eigenmodes supported by the combination of two parallel waveguides are even and odd superpositions (supermodes) of the modes of the individual wires for large separations. With increasing interaction between the waveguides, the splitting in frequency and wavevector of the supermodes also increases. This means that if only one of the two waveguides is excited (i.e., resulting in a coherent superposition of the even and odd modes), interference of the two modes will cause spatial mode

beating, effectively transferring the optical energy back and forth between the waveguides with a period  $2\pi/|\text{Re}\{\beta_e - \beta_o\}|$ , where  $\beta_e$  and  $\beta_o$  are the wavevectors of the even and odd supermodes, respectively.

Figure 10.2(a) depicts a directional coupler with two nanowires on a glass substrate ( $n_{\text{glass}} = 1.5$ ). The nanowires can effectively couple over a finite length, along which the nanowires approach each other to a distance  $a$ . Care must be taken to make gradual transitions to and from the coupling region, to ensure that the mode transformations occur adiabatically.

We define the length over which the energy transfers from one nanowire to the other as the coupling length  $L_c = \pi/|\text{Re}\{\beta_e - \beta_o\}|$ . To reduce the size of the coupler,  $L_c$  should be as small as possible. In SPP waveguides, other length scales that play a role are the propagation lengths  $L_{\text{SPP}}$  of the even and odd modes. Ideally, the coupling length should be much smaller than either propagation length. Additionally, the propagation length of both modes should be approximately equal to ensure an optimal contrast between the intensity in the two output waveguides.

Figure 10.2(b) shows the propagation lengths of the supermodes and the coupling length for infinitely long coupled Ag nanowires as a function of  $a$ . The calculations are performed as described in section 6.2.2. The width of the wires is 100 nm, and their height is 60 nm. The free-space wavelength is 1550 nm. The blue and red full curves depict the propagation length  $L_{\text{SPP}}$  of the even and odd mode, respectively. They asymptotically approach  $L_{\text{SPP}}$  for a single nanowire for large  $a$ . The coupling length  $L_c$  is plotted as the black line. The effective mode index  $n_{\text{eff}} = \beta/k_0$  is plotted as dashed curves for both modes. As is evident from

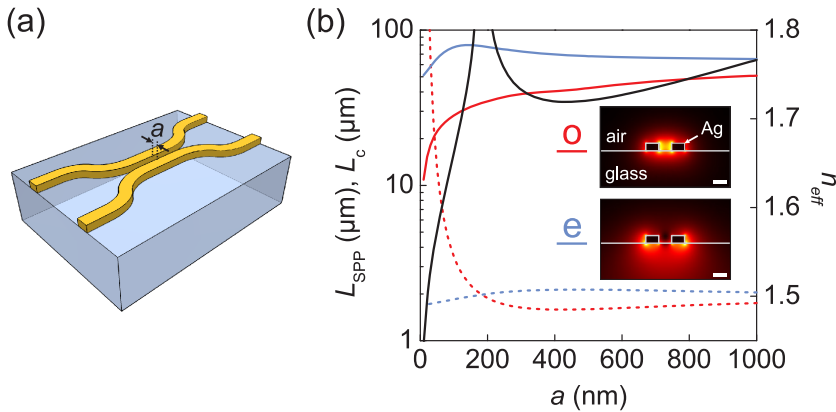


**Figure 10.2:** (a) A codirectional coupler for nanowires on a dielectric substrate. (b) Coupling length  $L_c$  (black curve) and mode propagation lengths  $L_{\text{SPP}}$  (blue and red full curves) of the even and odd modes supported by two Ag nanowires on glass separated by a distance  $a$ . The dashed curves show the effective mode indices  $n_{\text{eff}}$ . The free-space wavelength is 1550 nm. The insets depict the distribution of  $|\mathbf{E}|$  for both modes for  $a = 100$  nm. Scale bars are 100 nm.

this graph,  $L_c$  is smaller than both propagation lengths only for separations below  $\sim 100$  nm. For Au, we note that this occurs at a distance as small as  $\sim 20$  nm due an enhanced absorption as compared to Ag. Figure 10.2(b) also shows that the maximum possible contrast between the output guides is limited because the propagation lengths of both modes are different.

The large coupling length for  $a > 100$  nm and the fact that the propagation lengths of even and odd modes are different can be explained upon inspection of the mode profiles, shown in the inset in Fig. 10.2(b) for  $a = 100$  nm. The odd mode (o), which has surface charges of opposing sign on the two nanowires, has its electric field concentrated within the air gap between the wires. The resulting increase in confinement upon decreasing  $a$  has an increasing effect on the wavevector. However, the fact that a larger fraction of the field becomes localized in the air between the nanowires instead of in the higher-index glass has a decreasing effect on the wavevector. These counteracting effects, apparent from the behavior of the effective mode index  $n_{\text{eff}}$  plotted in Fig. 10.2(b), are similar to those observed for narrowing stripe waveguides on glass in section 6.2.4. The opposite effects occur for the even mode, which becomes less confined as the gap narrows. The net result is that both wavevectors change little from the value of a single waveguide and that therefore the coupling length remains large for most  $a$ , until confinement ultimately dominates for the odd mode for  $a < 100$  nm. But because the odd mode has the strongest confinement, its propagation length is shorter than that of the even mode by a factor 1.5 to 5 for separations between 500 and 10 nm.

The effects of the redistribution of mode energy in different dielectric media upon coupling are expected to be opposite with respect to the previous geometry if the medium in the gap between the nanowires has a higher refractive index than the surrounding. Increasing the index in the gap should enhance the coupling strength. We demonstrate this behavior for two nanowires on opposite sides of a 100 nm thick  $\text{Si}_3\text{N}_4$  membrane ( $n = 2$ ) surrounded by air (see Fig. 10.3(a)). The nanowires are 150 nm wide and 100 nm thick. We choose this geometry because it can be readily fabricated. Alternatively, one could consider filling the gap between the nanowires in Fig. 10.2(a) with a dielectric.

The propagation lengths and coupling length for the geometry of Fig. 10.3(a) are plotted in Fig. 10.3(b). This time, the wavevectors separate already at a much larger  $a$ , which is now defined as the horizontal separation between the centers of the nanowires. The coupling length becomes shorter than the propagation lengths for  $a < 1000$  nm, and the propagation lengths of the even and odd modes are practically identical down to  $a \approx 400$  nm.

To demonstrate the performance of such a directional coupler, we performed FDTD calculations of the geometry sketched in Fig. 10.3(a), with the same nanowire dimensions as used in Fig. 10.3(b). The mesh size was 5 nm, and perfectly matched layer (PML) boundary conditions were used at  $3 \mu\text{m}$  from the waveguides to absorb outgoing SPPs and radiation. Figure 10.4 shows the intensity of the vertical component of the electric field,  $|E_z|^2$ , in a plane through the center of the  $\text{Si}_3\text{N}_4$  slab. The nanowire mode is excited in the nanowire at the top left of the image, where

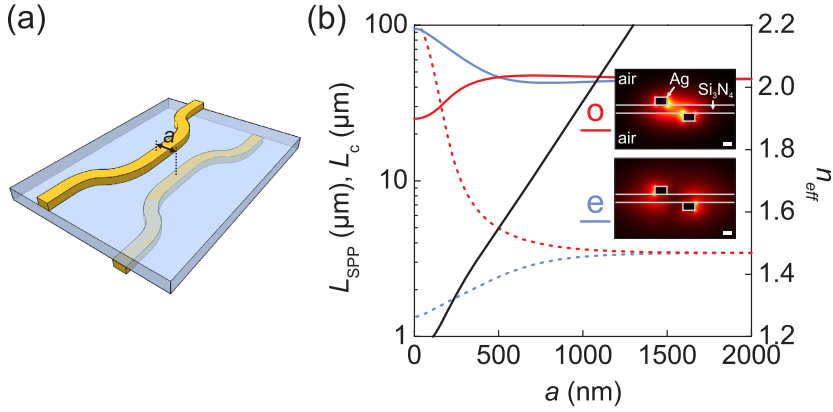


**Figure 10.3:** (a) A nanowire coupler for nanowires on opposite sides of a dielectric slab, to enhance the coupling strength. (b)  $L_c$  (black curve) and  $L_{SPP}$  (blue and red full curves) of the even and odd modes in the coupled Ag nanowires at a free-space wavelength of 1550 nm. The  $\text{Si}_3\text{N}_4$  slab is 100 nm thick. The dashed curves show the effective mode indices  $n_{\text{eff}}$ . The insets depict the distribution of  $|\mathbf{E}|$  for both modes for  $a = 350$  nm.

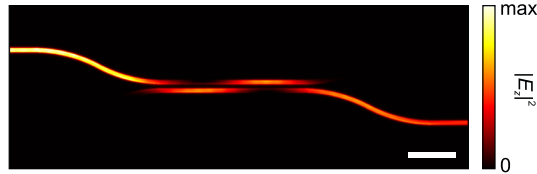


**Figure 10.4:** Field intensity  $|E_z|^2$  for the directional coupler depicted in Fig. 10.3(a), calculated with the FDTD method in the  $xy$  plane in the center of the  $\text{Si}_3\text{N}_4$  slab. The minimum waveguide separation is  $a = 350$  nm, and the free-space wavelength is 1550 nm. SPPs are launched in the nanowire shown in the top left. The intensity in the bottom output nanowire on the right is 100 times larger than that in the top output nanowire. The scale bar is 2  $\mu\text{m}$ .

the nanowire separation is 3.1  $\mu\text{m}$ . The minimum wire separation  $a$  in a plane parallel to the slab is 350 nm, occurring over a length of 5.9  $\mu\text{m}$ . A clear beating is observed along the coupling region, with most of the energy finally transferring to the nanowire on the opposite side of the membrane. The intensity contrast between the two nanowires on the right is larger than 100 for this particular coupler length, demonstrating that such a structure allows effective coupling between SPPs on nanowires in a relatively compact structure.

## 10.2 Photovoltaics

Concentration of sunlight in solar cells can serve three purposes [4]. First, material cost can be reduced because the same amount of light can be absorbed in a smaller active material volume. Second, an increase of the light intensity and reduction of the cell size will increase the ratio of photocurrent to reverse saturation current. This increased ratio enhances the open circuit voltage and can therefore increase the cell's conversion efficiency. Third, reducing the cell thickness necessary to absorb all incident light could allow the use of materials that are otherwise impractical, for example because of their small charge carrier mobility.

As we have seen throughout this thesis, surface plasmons can be used to concentrate light to small volumes. SPP field enhancement has been proposed as a possible method to enhance light absorption in photovoltaic applications [200, 235–240]. Such an approach differs fundamentally from an alternative application of surface plasmons in solar cells based on scattering of metal nanoparticles [241]. In the latter case, plasmons serve as ‘intermediate’ excitations, to scatter incident light to photonic modes in the solar cell.

In this section, we discuss the applicability of plasmonic field enhancement for photovoltaic purposes and provide an approach to convert broadband free-space radiation to SPPs. We do not consider the implications of such strategies on electrical device performance here, and limit the discussion to fundamental aspects of light absorption using plasmonic structures.

### 10.2.1 Light absorption in plasmonic solar cells

In a solar cell that makes use of plasmonic field concentration to reduce the active volume, sunlight first needs to be converted to SPPs, which should subsequently be absorbed by the active material. When SPPs are excited, a part of the optical energy will necessarily be lost to Ohmic dissipation. To determine whether plasmonic field concentration can be applied to make efficient solar cells, it is therefore important to compare the fraction of light in the excited surface plasmon mode that is usefully absorbed in the active material to the Ohmic losses in the metal. Although these quantities depend on the precise geometry, it is useful to first consider SPPs at the interface of a metal with dielectric constant  $\epsilon_m$  and an absorbing dielectric with dielectric constant  $\epsilon_d$ . The fraction  $\eta$  of power absorbed in the dielectric with respect to the total absorbed power is given by

$$\eta = \frac{\int_d \text{Im}\{\epsilon_d\} |\mathbf{E}(z)|^2 dz}{\int_d \text{Im}\{\epsilon_d\} |\mathbf{E}(z)|^2 dz + \int_m \text{Im}\{\epsilon_m\} |\mathbf{E}(z)|^2 dz} \quad (10.1)$$

where  $\int_d$  and  $\int_m$  represent integration over the dielectric and metal half-spaces, respectively. The value of  $\eta$  provides an upper limit to the efficiency with which SPPs can be usefully absorbed.

The thickness of a solar cell intended to absorb SPPs would need to be of the order of the  $1/e$  intensity decay length  $L_z$  into the dielectric. Figure 10.5(a) shows

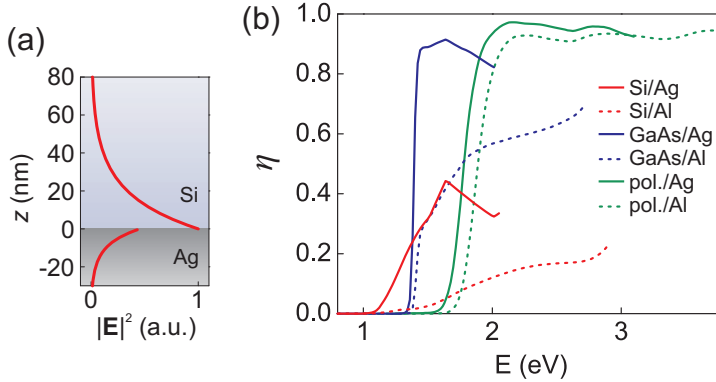


**Figure 10.5:** (a) Electric field intensity profile of a SPP mode at a Ag/Si interface at a free-space wavelength of 785 nm. (b) Fraction of power absorbed in the active medium as a function of photon energy for SPP modes on different metal/semiconductor interfaces. The metals are Ag (solid curves) and Al (dashed curves). The semiconductors are crystalline Si, GaAs, and a polymer blend (pol.) of PF10TBT:[C60]PCBM [242]. The curves are drawn for energies up to the surface plasmon resonance frequency.

the  $z$  dependence of the electric field intensity of SPPs on a Ag/Si interface at a free-space wavelength of 785 nm. Because of the high permittivity of Si,  $L_z$  is only 20 nm. The SPP field is confined within a very thin layer of Si. Only a small volume of semiconductor material is thus needed to absorb the SPP field usefully.

In Fig. 10.5(b), we compare the fraction of power absorbed in the dielectric for combinations of the metals Ag [26] and Al [104] with three different dielectrics: the indirect-bandgap semiconductor Si, the direct-bandgap material GaAs, and a typical high-performance polymer mixture used in organic solar cells (a 1:4 blend of PF10TBT:[C60]PCBM) [242]. The curves are only plotted for photon energies below the surface plasmon resonance energy. Figure 10.5(b) shows that  $\eta$  is larger for Ag than for Al which is due to the fact that  $\text{Im}\{\epsilon_m\}$  is smaller for Ag. The spectral range over which SPPs exist is larger for Al, since Al has a larger plasma frequency than Ag. For this reason, the widely abundant material Al is not necessarily a worse candidate than Ag for plasmonic solar cells, even though its absorption is higher. As can be seen from the figure, the choice of active material is important as well. The absorption of crystalline Si is too small to obtain values of  $\eta$  above  $\sim 0.4$ , even with Ag as the metal. Both the direct-bandgap semiconductor GaAs and the highly absorptive polymer blend perform better. The fraction absorbed by GaAs is larger than 0.8 for photon energies exceeding the GaAs bandgap if Ag is used, and approximately 0.6 in combination with Al between 1.8 and 2.8 eV. The polymer performs the best, with  $\eta$  above 0.9 irrespective of the choice of metal. This is at first sight surprising, since  $\text{Im}\{\epsilon_d\}$  is smaller for the polymer than for GaAs. However, since  $\text{Re}\{\epsilon_d\}$  of the polymer is  $\sim 3\text{--}4$  and that of GaAs ranges between 12 and 23, the



fraction of the intensity  $|\mathbf{E}|^2$  in the dielectric is larger for the lower-index polymer. As a result, the polymer absorbs a larger fraction of the SPP energy. We note that for all frequencies at which the polymer absorbs, the extent of the field intensity into the dielectric  $L_z$  remains smaller than 100 nm. It may therefore be possible to construct solar cells with optically thin active polymer layers, which would be limited by charge carrier collection for larger thicknesses.

Interestingly, the value of  $\eta$  does not decrease for frequencies close to the surface plasmon resonance frequency, where the field strength in the metal approaches that in the dielectric and the losses are largest. This is due to the fact that as the frequency increases,  $\text{Im}\{\epsilon_d\}$  increases and  $\text{Im}\{\epsilon_m\}$  decreases, counterbalancing the effect of plasmonic confinement on  $\eta$ .

We conclude that absorption losses in the metal do not necessarily preclude their use in an efficient plasmonic solar cell, provided that the active material has a large enough absorption coefficient. The maximum possible efficiency with which SPPs can be usefully absorbed increases when the refractive index of the active material is small. The use of SPP field enhancement in photovoltaics is especially promising for materials that have a high absorption coefficient and for which charge carrier mobility precludes the use of optically thick layers in conventional solar cell designs.

So far we have not addressed the question of how the SPPs should be excited efficiently, preferably over the full bandwidth of the solar spectrum and for a wide range of angles. Some proposals have been put forward that rely on scattering, but these often exploit resonances with finite bandwidth [200, 239].

### 10.2.2 Adiabatic concentration of light from free-space

Here we investigate the possibility of using adiabatic mode transformation to convert plane waves incident from free-space to highly confined SPPs. The structure that we consider is shown in Fig. 10.6(a), which is a one-dimensional array of funnels with metal side walls, ending in small MIM waveguides with a dielectric core thickness  $d$ . It is closely related to tapered MIM waveguides [138, 142, 171, 177]. A single funnel bears strong resemblance to a horn antenna at microwave frequencies [243], and can be considered as an element that matches the impedance of the waveguide to that of free space. A process to fabricate such structures could possibly involve anisotropic etching of the inverse structure in a semiconductor such as Si, before transferring the structure to a metal film. In the calculations presented here, the dielectric in both the funnels and the waveguides is air. We note that further studies need to be performed to investigate the best way to incorporate active materials.

The mode transformation process can be easily understood by considering the structure as a periodic array of vertical aligned waveguides of which the geometry varies gradually with height. At the top, it resembles an array of weakly coupled IMI waveguides. If these are illuminated with a plane wave polarized normal to the metal/air interfaces, the weakly confined symmetric mode will be excited in

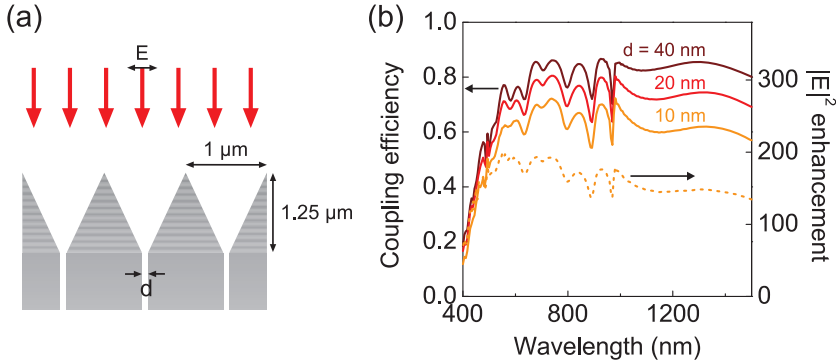


**Figure 10.6:** (a) A geometry that allows the adiabatic conversion of TM-polarized plane waves from free space to MIM waveguides, consisting of a periodic array of funnels with metal sidewalls. (b) Coupling efficiency (solid curves) of light to the MIM waveguide as a function of the free-space wavelength, for three different waveguide thicknesses, obtained from FDTD simulations. The metal is Ag. The dashed curve shows the enhancement of  $|E|^2$  inside the 10 nm thick waveguide.

the IMI waveguides. For the infinitesimally small metal thickness at the top of the structure, this mode is identical to a plane wave. If the angle of incidence is normal, all waveguides will be excited in phase, so the field inside a single funnel resembles that of a symmetric MIM mode. Because the thickness of the insulator reduces along the direction of propagation, this mode will become more strongly confined, ultimately concentrating the energy into the MIM waveguide at the end of the funnel.

Figure 10.6(b) shows the fraction of incident power that is coupled into the MIM waveguide, obtained from FDTD simulations of the structure. The width of the funnels is  $1\ \mu\text{m}$ , and their height is  $1.25\ \mu\text{m}$ . The metal is Ag, which is modeled by a Drude-Lorentz model fitted to the optical constants in ref. [26] to allow broadband simulations. The mesh size is  $0.5\ \text{nm}$ . Bloch boundary conditions are used to simulate an infinite array while facilitating various incident angles, and PMLs absorb light exiting at the top and bottom boundaries.

In Fig. 10.6(b), the structure is illuminated with a TM-polarized plane wave at normal incidence, for various thicknesses  $d$  of the MIM waveguide at the end of the funnel. The coupling efficiency is evaluated by integrating the Poynting flux in the MIM waveguides at a depth of  $200\ \text{nm}$  below the bottom of the funnels. For wavelengths larger than  $\sim 550\ \text{nm}$ , the coupling efficiency to a  $40\ \text{nm}$  thick waveguide stays rather constant, around a value of  $80\%$ . It reduces for smaller thicknesses, but even for a waveguide thickness of  $10\ \text{nm}$  the efficiency is consistently larger than  $60\%$ . The resulting field intensity enhancement inside a  $10\ \text{nm}$  thick waveguide approaches a factor  $200$  at a wavelength of  $550\ \text{nm}$ . For shorter wavelengths, the coupling efficiency decreases due to absorption in the funnel and due to a mode mismatch between the incident plane waves and the fundamental

SPP mode just below the top of the waveguides. In the top section of the funnel, the excited SPP mode is converted from a plane wave to SPPs propagating on the metal surfaces. This conversion has more dramatic effects on the mode profile for short wavelengths, since the SPP field is more strongly confined than the width of the air gap between the surfaces. The rapidly changing mode profile of the fundamental mode in the funnel limits adiabaticity. Nonetheless, the bandwidth over which field enhancement occurs is large compared to other plasmonic systems.

The coupling efficiency for funnels made using Ag is compared to different metals in Fig. 10.7(a). The waveguide width is 40 nm. For Au, absorption limits the efficiency below 650 nm, but the efficiency approaches that for Ag for larger wavelengths. Even for Al, which has considerably larger losses than Ag or Au, the coupling efficiency is larger than  $\sim 40\%$  throughout the full spectrum, reaching more than 70% in the near-infrared. These results suggest that the losses are limited by diffraction, which is further corroborated by comparing these results with the efficiency obtained with a perfect electric conductor (PEC), also plotted in Fig. 10.7(a). Interestingly, the coupling efficiency for PEC funnels is smaller than that of Ag above a wavelength of 650 nm. The reason for this difference is not completely clear. We note that the field enhancement and bandwidth can be further improved by optimization of the length and shape of the taper.

Finally, we consider the influence of the angle of incidence  $\theta$  with respect to the normal. Figure 10.7(b) shows the coupling efficiency into an array of funnels with 40 nm thick Ag waveguides as a function of the frequency and the in-plane wavevector  $k_{\parallel} = k_0 \sin\theta$  of the incident light. The straight line denotes the light line ( $\omega = ck_0$ ). We see that for the smallest frequencies, efficient coupling occurs over a wide range of angles. The range of angles for which the efficiency is large decreases for increasing frequency because the overlap integral of the incident light

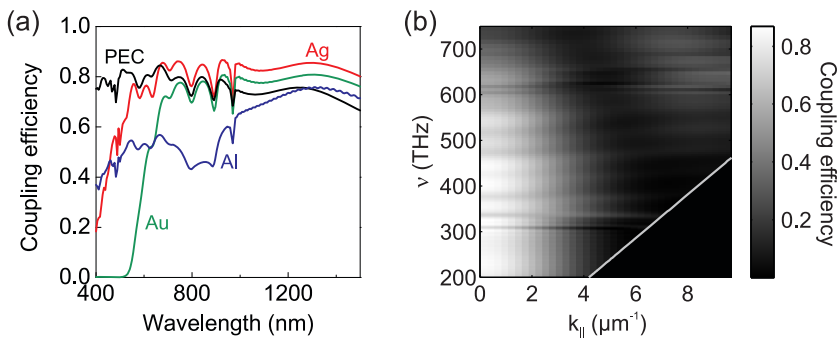


**Figure 10.7:** (a) Dependence of the coupling efficiency in the array of funnels on the choice of metal. The waveguide width is 40 nm. Ag, Au, Al, and a perfect electric conductor (PEC) are compared. (b) The coupling efficiency for various angles, plotted as a function of frequency and in-plane wavevector  $k_{\parallel}$ . The gray line denotes the light line.

with the lowest order symmetric mode of the MIM waveguide reduces for larger  $k_{||} = \omega \sin\theta/c$ . For example, the angle at which the efficiency is 40% is  $15^\circ$  for a wavelength of 550 nm. The acceptance angle for nanoconcentration can be increased by reducing the opening width of the waveguide, at the expense of reduced field enhancement in the individual waveguides.

To summarize, we have demonstrated in this section a structure that allows efficient concentration of light incident from free-space to nanoscale MIM waveguides. Since it is related to adiabatic mode transformation and not to plasmonic resonances, the effect has a large bandwidth and occurs for a relatively large range of incident angles. Even though this structure cannot be directly implemented in conventional solar cell designs, it may inspire new ideas to achieve light collection for photovoltaics or spectroscopy. The two-dimensional structure presented here is only effective for TM-polarized light. By also tapering the waveguide in the third dimension to some extent, further concentration can be achieved. In more complex arrangements of tapered waveguides based on this concept, it might be possible to concentrate light of both polarizations.

### 10.2.3 Upconversion for photovoltaics

One of the proposed routes towards third generation high-efficiency solar cells involves the conversion of infrared photons that cannot be absorbed in a silicon solar cell to photons with an energy higher than the Si bandgap energy [199]. Various rare-earth ions exhibit such upconversion processes, which can be rather efficient under laser illumination in the proper host material [124]. The parity-forbidden character of the intra- $4f$  transitions in rare earth ions causes their excited states to have long lifetimes, which enables upconversion through interactions between excited ions. At low pump powers, the efficiency of the nonlinear upconversion processes in rare earth ions is hindered by their small absorption cross sections, which are typically of the order of  $10^{-21}$ – $10^{-20}$   $\text{cm}^2$ . Because of concentration quenching, the maximum doping concentration of rare earth ions is limited to  $\sim 10^{22}$   $\text{cm}^{-3}$ .

In  $\text{Er}^{3+}$  ions, the  $^4I_{11/2}$  level can be populated through upconversion under 1500 nm illumination. From the  $^4I_{11/2}$  level photons can be emitted with a wavelength of 980 nm, ideal for absorption in Si (see Fig. 10.8). The AM1.5 solar spectrum contains a power flux density of 2.4  $\text{mW}/\text{cm}^2$  in the spectral region that overlaps with the  $\text{Er}^{3+}$  absorption spectrum between 1480 and 1580 nm. In a recent experimental study on Er upconversion in a low-phonon-energy host ( $\text{NaYF}_4$ ), Shalav and co-workers concluded that sunlight would have to be concentrated by a factor 40000 to reach an average conversion efficiency of 3% between 1480 and 1580 nm [244].

We have demonstrated the enhancement of upconversion in  $\text{Er}^{3+}$  ions using field concentration in tapered plasmonic waveguides in Chapter 4 and in subwavelength aperture arrays in Chapter 8. In principle, such structures could be incorporated in the metal back reflector of a solar cell to reach up to  $\sim 10^3$  intensity enhancements. However, additional or alternative methods are needed to obtain

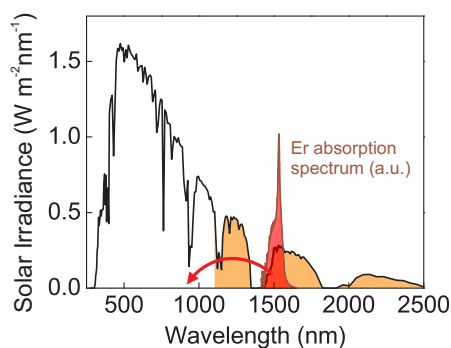


**Figure 10.8:** Infrared upconversion for Si solar cells. The shaded part of the solar spectrum is not directly absorbed by Si. Er ions can convert part of that radiation at  $\sim 1500$  nm to shorter wavelengths. The Er absorption spectrum was taken from ref. [245].

the necessary concentration factor of  $\sim 10^5$ . Such concentration has only been predicted in plasmonic systems that allow extreme confinement, such as nanoparticles separated by nanometer-sized gaps. In that case, the field in the metal becomes comparable to the field in the dielectric gap. Since  $\text{Im}\{\epsilon_d\}$  of a dielectric with a high Er dotation is  $\sim 3$  orders of magnitude smaller than that of Ag or Au at  $1.5 \mu\text{m}$ , the useful absorption and therefore the efficiency of upconversion by Er ions positioned in the dielectric gap would be negligible. Moreover, the high local density of states in such a structure would depopulate the first excited state quickly, further weakening upconversion.

Upconversion processes have also been observed in fluorescent molecules [246] and quantum dots [247]. If those effects can be extended to energies below  $1.1$  eV, such systems could be useful in photovoltaics. Since upconversion in molecules and quantum dots is nonlinear, it can be strengthened by field concentration. Because the cross sections of molecules and quantum dots are larger than those of rare-earth ions, the efficiency of upconversion in molecules or quantum dots can benefit from plasmonic field concentration such as that described in this thesis.

## 10.3 Sensing and spectroscopy

### 10.3.1 Localized surface plasmon resonance sensing

Measuring the spectral or angular variation of the surface plasmon resonance (SPR) in a prism-based attenuated total reflection setup is a powerful method to detect small changes of the refractive index of a dielectric, allowing the label-free sensing of small concentrations of molecules. Localized surface plasmon resonances (LSPR) are also widely used for that purpose [5, 6]. Even though the plasmon resonance linewidth of the metal nanoparticles that are most typically used for LSPR

sensing is broader than that in SPR, the two methods offer comparable sensitivity to molecule adsorption. Because the LSPR field is closely confined to the metal surface, even the small refractive index change due to adsorption of molecules can cause a measurable shift of the resonance wavelength [5]. Measuring single particle resonances allows the detection of  $\sim 10^2$ – $10^4$  molecules [248].

The localized resonances in annular apertures studied in Chapters 8 and 9 have potential use in LSPR sensing. Sensing a refractive index change due to molecules adsorbed in subwavelength hole arrays has been demonstrated [249] and it has been shown that changing the hole shape can enhance the sensitivity [250, 251]. We propose to use the localized resonance of annular apertures in a transmission geometry. The high transmission of such apertures makes single-aperture sensing with low background straightforward, without the need of dark-field illumination [248]. As can be seen from Fig. 1.7, the field is largest near the inner metal surface. Molecules adsorbed on this surface are expected to cause the resonance to redshift. Calculations similar to those in section 1.3 have shown that by reducing the size of the gap between the inner and outer metal surfaces the reflectivity of the  $TE_{11}$  mode in the aperture at the top and bottom interfaces can be increased. As a result, the plasmon resonance linewidth can be decreased which increases the possible sensitivity.

The localized nature of the resonance offers a high spatial resolution. This, in combination with single aperture detection, allows imaging of the resonance shift to map out the spatial distribution of molecule adsorption with diffraction-limited resolution. Such spatially-resolved label-free sensing could find potential use in microfluidic networks, which can be fabricated on top of an annular aperture array [250]. Specific binding can then be imaged in parallel bioassays by recording spectra of transmitted light in a microscope.

### 10.3.2 Enhanced spectroscopy

Another powerful application of localized plasmonic resonances is the enhancement of Raman scattering in surface-enhanced Raman spectroscopy (SERS) [5, 6] to reveal chemical fingerprints of molecules with sensitivity up to the single-molecule level [150]. Since the Raman signal scales with the square of the electric field intensity, it can benefit enormously from plasmonic field enhancement.

The calculated field intensity enhancement at the metal surface of annular apertures reaches values of a few hundred (see Fig. 1.7). With a further reduction of the aperture size, electromagnetic SERS enhancements larger than  $10^6$  should be easily attainable. This enhancement is smaller than the field enhancement that can occur at hotspots between nanoparticle dimers. However, in contrast to those hotspots, the position of the field enhancement in annular apertures is well-defined, and the enhancement is independent of incident angle and polarization. Annular apertures therefore hold the promise of providing reproducible enhancement factors for easy comparison. The fact that measurements can be performed in transmission may be an advantage in miniaturized devices [183].

The enhanced excitation and radiative emission rate in annular apertures could also enhance fluorescence spectroscopy. Unlike SERS, fluorescence cannot make use of high fields in hotspots directly on a metal surface, since fluorescence of molecules in contact with the surface is quenched. Subwavelength apertures are ideal for fluorescence spectroscopy of small numbers of molecules as they provide a rather homogeneous field enhancement in a small volume [222, 252]. As we have shown in Chapters 8 and 9, both the excitation rate and the radiative rate of emitters placed inside annular apertures can be further increased by exploiting localized resonances. They are therefore promising candidates to increase the sensitivity of fluorescence spectroscopy.

The most widely used plasmonic system for SERS are single or aggregated metal nanoparticles. The field close to the particle is directly proportional to the illumination field at the position of the particle. If that driving field can be increased beyond the magnitude obtainable in a diffraction-limited focus, SERS enhancement can improve. For this purpose, we propose to position nanoparticles at the end of tapered waveguides. A possible geometry is depicted in Fig. 10.9, where the metallic funnel structure considered in section 10.2.2 is coated with a nanometer-scale dielectric film. Particles are dispersed in the bottom of the grooves by self-assembly [253]. When the structure is illuminated with a beam that is polarized normal to the metal ridges, the field is concentrated in the bottom of the groove, leading to a larger field enhancement than when the particle would be illuminated directly. Considering the efficiency of the concentration demonstrated in section 10.2.2, intensity enhancements of a factor 10 should be easily reached, which would lead to a 100-fold increase in the SERS signal. Moreover, the fact that the particles are separated from the metal substrate by a thin dielectric will cause concentration of energy in reproducible hotspots between the particle and the metal substrate, further increasing the SERS enhancement. The magnitude of the

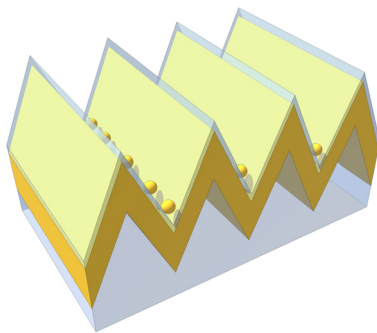


**Figure 10.9:** Geometry for a SERS substrate combining nanofocusing and localized resonances of metal nanoparticles. The incident field concentrates in the grooves, driving the resonance of the nanoparticles at the bottom of the grooves with large amplitude.

hotspots can be controlled by the thickness of the dielectric film. The deposition of SiO<sub>2</sub> films of a few nanometers thick has been demonstrated [64]. By combining adiabatic nanoconcentration with localized resonances, molecules adsorbed in the cusps between the particles and the dielectric film are thus expected to exhibit strong and controllable SERS enhancement.

## 10.4 Towards a three-dimensional left-handed material at visible frequencies

In Chapter 3, we showed that SPP waveguides can exhibit negative effective refractive indices, enabling two-dimensional negative refraction at visible frequencies with relatively low loss. It has been proposed that such a waveguide could be used to construct a negative-index lens [51], transferring an image from one side to the other side in a slab waveguide of finite length. The imaging is however purely two-dimensional, limiting its applicability.

Here we explore the possibility to construct a material composed of multiple SPP waveguides that can show negative refraction in the third dimension as well. We look at a stack of MIM slab waveguides, such as depicted in Fig. 10.10(a). To study refraction of waves at the boundary of a homogeneous medium with such a layered material, it is useful to interpret the material as a periodic array of coupled waveguides. One can then use coupled mode theory to describe wave propagation in the material [234].

We consider only incident waves polarized normal to the waveguide interfaces, as the SPP modes in the structure are TM polarized. Refraction in the  $xy$  plane will be governed by the effective mode index of a single waveguide. We focus our attention to refraction in the  $xz$  plane, which is determined by waveguide coupling. The field in the  $j^{\text{th}}$  slab waveguide can be described by a wave amplitude  $a_j$  given by

$$a_j(x, z, t) = A_j(x) e^{i\beta x - i\omega t}, \quad (10.2)$$

where  $A_j(x)$  is a slowly varying amplitude and  $\beta$  is the wavevector of the SPP mode in a single slab waveguide.

Taking only coupling between nearest-neighbor waveguides into account, the amplitudes in adjacent waveguides are related through [254]

$$\frac{\partial a_j}{\partial x} = i\beta a_j + i\kappa (a_{j-1} + a_{j+1}), \quad (10.3)$$

where  $\kappa$  is a coupling constant. The solution of (10.3) is obtained by taking  $a_j = C e^{ik_x x + ik_z d j}$  as a trial solution, where  $d$  is the center-to-center distance between adjacent waveguides and  $C$  a constant. This yields

$$k_x = \beta + 2\kappa \cos(k_z d). \quad (10.4)$$



The coupling constant between two adjacent waveguides (denoted by subscripts (1,2)) can be approximated by [234]

$$\kappa = \omega \epsilon_0 \frac{\int_{d,1} (\epsilon_d - \epsilon_m) \mathbf{E}_1^\dagger \cdot \mathbf{E}_2 dz}{\int_{-\infty}^{\infty} \hat{\mathbf{z}} \cdot (\mathbf{E}_1^\dagger \times \mathbf{H}_1 + \mathbf{E}_1 \times \mathbf{H}_1^\dagger) dz}. \quad (10.5)$$

The integration in the numerator of (10.5) is performed over the dielectric region of waveguide 1 only, since the mode in waveguide 2 is perturbed by the presence of waveguide 1 only in the region where the dielectric constant differs from the dielectric constant of the metal waveguide cladding. The field  $\mathbf{E}_2$  is the field of waveguide 2 at the position of waveguide 1, i.e., the modal field evaluated at a height  $(z - d)$ . The dagger indicates the adjoint field, obtained by substituting  $-\beta$  for  $\beta$  and  $-\omega$  for  $\omega$ . The use of the adjoint field instead of the complex conjugate allows the dielectric constants to be complex [22, 234]. The mode solutions can be found with the method described in section 1.2.1.

We first look at a stack of MIM waveguides illuminated with a frequency below  $\omega_{\text{sp}}$ , i.e., in the regime of positive effective mode index (see Fig. 3.2(a)). The symmetric SPP mode profile in a single waveguide is sketched in Fig. 10.10(b). Due to the fact that the metal permittivity is negative, the coupling constant  $\kappa$  becomes smaller than zero. Now that the relation between  $k_z$  and  $k_x$  is qualitatively known, we can determine the refraction behavior by considering isofrequency contours of the waves in the two media [255]. These are sketched in the first Brillouin zone in Fig. 10.10(c), assuming that  $\text{Re}\{|k|\} \gg \text{Im}\{|k|\}$  so that the wavevectors can be considered to be real. Only waves that have a positive Poynting vector component in the  $x$  direction are shown, since we consider light that is incident from  $x < 0$ . The possible wavevectors of light in air are indicated by the blue circle. The red curve denotes the possible wavevectors in the waveguide array, given by (10.4). Momentum matching at the  $yz$  interface (indicated by the dashed line) determines the wavevector of the refracted wave from that of the incident wave. The direction of the Poynting vector is given by the normal to the isofrequency contour. As can be seen from this analysis, an array of MIM waveguides exhibits negative refraction in the  $xz$  plane due to the hyperbolic shape of the dispersion curve [98]. It is not a true left-handed medium, however, since  $(\mathbf{k} \cdot \mathbf{S}) > 0$ , and hence phase and energy do not flow in opposite directions [256]. The refraction in the  $xy$  plane is always positive for this geometry [257]. The arrows in Fig. 10.10(a) depict the refraction directions in both dimensions.

Above the surface plasmon resonance frequency, the antisymmetric mode in the MIM waveguides (shown in Fig. 10.10(e)) does exhibit negative refraction in the  $xy$  plane, as described in section 3.4.1. Evaluation of (10.5) reveals that  $\kappa$  is positive, in contrast to the symmetric positive index mode below  $\omega_{\text{sp}}$ . Together with the negative value of  $\beta$ , the positive  $\kappa$  causes refraction in the  $xz$  plane to be positive, as explained in the wavevector diagram in Fig. 10.10(f). The fact that  $\kappa$  is positive even though  $\epsilon_m < 0$  is related to the antisymmetric field distribution of the mode.

To obtain negative refraction in both the  $xy$  and the  $xz$  planes, we need to

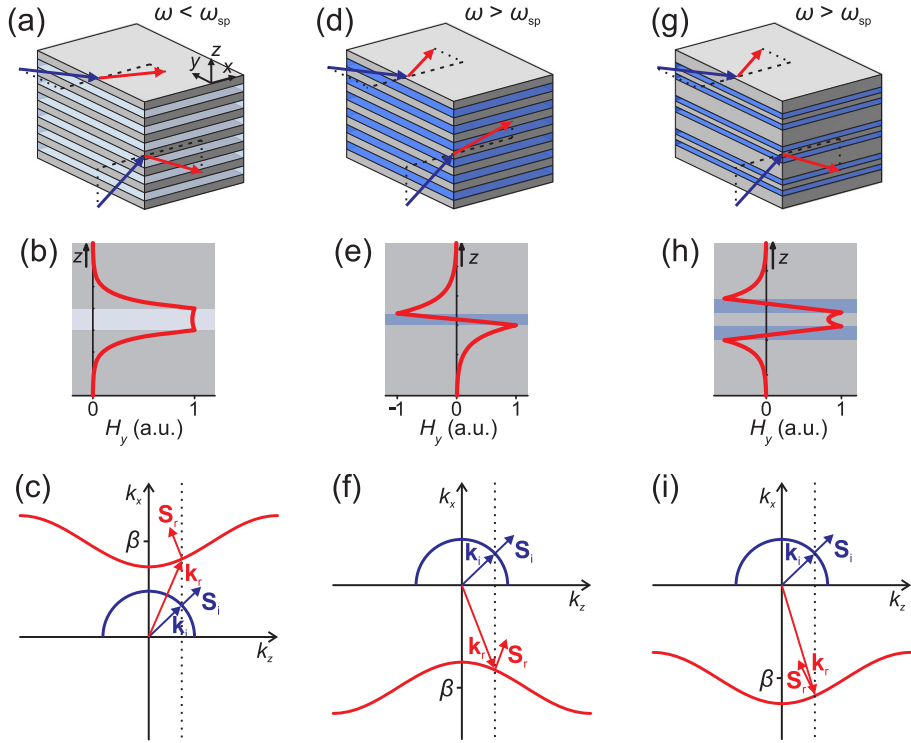


**Figure 10.10:** Refraction of light into arrays of coupled MIM waveguides. (a) For  $\omega < \omega_{sp}$ , refraction is positive in the  $xy$  plane and negative in the  $xz$  plane. (b)  $H_y$  field of the symmetric mode in an individual MIM waveguide. The mode profile is calculated for a free-space wavelength of 1000 nm. The 50 nm thick dielectric core has  $\epsilon_d = 2$  and the metal cladding is Ag. (c) Relation between  $k_z$  and  $k_x$  in air (blue) and in the waveguide array (red). Refraction in the  $xz$  plane is negative, and the array behaves like a right-handed medium. (d) For  $\omega_{sp} < \omega < \omega_p$ , refraction is negative in the  $xy$  plane but positive in the  $xz$  plane. (e)  $H_y$  field of the antisymmetric mode in an individual MIM waveguide. The free-space wavelength is 420 nm. The 20 nm thick dielectric core has  $\epsilon_d = 12$  and the metal cladding is Ag. (f) Refraction in the  $xz$  plane is positive, even though the array behaves like a left-handed medium since  $(\mathbf{k} \cdot \mathbf{S}) < 0$ . (g) In an array of strongly coupled pairs of MIM waveguides, refraction is negative in both  $xy$  and  $xz$  planes for  $\omega_{sp} < \omega < \omega_p$ . (h)  $H_y$  field of the symmetric mode supported by a pair of coupled MIM waveguides. The free-space wavelength is 420 nm. The dielectric layers are 20 nm thick and have  $\epsilon_d = 12$ . The metal is Ag, and the thickness of the middle Ag layer is also 20 nm. (i) Refraction in the  $xz$  plane is negative, and the array behaves like a left-handed medium.

search for a mode that has both a negative value of  $\beta$  and a negative coupling constant  $\kappa$ . This can be realized in a strongly coupled pair of MIM waveguides, shown in Fig. 10.10(h). The eigenmodes of one such pair resemble odd or even superpositions of the two antisymmetric modes in a single MIM waveguide. The odd superposition, plotted in Fig. 10.10(h), exhibits the lowest losses. Because its mode profile is symmetric, the coupling constant  $\kappa$  between weakly coupled adjacent pairs of waveguides is negative, as can be confirmed by evaluating (10.5) for this geometry. As a result, in an array of such pairs of MIM waveguides as depicted in Fig. 10.10(g) negative refraction occurs both in the  $xy$  plane and in the  $xz$  plane for wavevectors  $k_z < \pi/d$ . Moreover,  $(\mathbf{k} \cdot \mathbf{S}) < 0$ , so the waveguide array behaves like a left-handed medium. An additional advantage of exploiting the symmetric mode in the coupled pair of waveguides is that it has a nonvanishing overlap with a plane wave propagating in the  $x$  direction. It can therefore also be excited at normal incidence.

We have outlined a route towards optical negative refraction in a left-handed medium for a wide range of angles, which is a prerequisite for constructing a negative-index lens. The design only transmits TM-polarized waves, so a lens would only work for object fields in which that polarization dominates. More complex structures based on coupled MIM waveguides should be considered to transfer all polarizations [52, 258]. Further investigation is needed to optimize the coupling strength for angle-independent negative refraction, to prove the existence of surface waves that can assist in subwavelength focusing, and to determine the extent to which material losses would deteriorate the performance of a near-field lens composed of the negative index metamaterial proposed here.



# A

## Waveguide modes in multilayer geometries: TE polarization

In section 1.2.1 we derived the wavevectors and fields of TM-polarized waveguide modes sustained by a multilayer slab waveguide. Here we provide the solutions for TE polarization. The derivation is analogous to that described in section 1.2.1.

In TE polarization, the electric field in layer  $i$  is

$$\mathbf{E}_i(x, z, t) = E_{yi}(z) e^{ik_x x - i\omega t} \hat{y}. \quad (\text{A.1})$$

The  $z$  dependence of the field is given by

$$E_{yi}(z) = \begin{cases} E_{y0} e^{-ik_{z1} z}, & i = 1, \\ \left( Q_{i,11}^{\text{TE}} - ik_{z1} Q_{i,12}^{\text{TE}} \right) E_{y0} \cos(k_{zi}(z - z_i)) + \cdots & 1 < i < n, \\ \quad + \left( Q_{i,21}^{\text{TE}} - ik_{z1} Q_{i,22}^{\text{TE}} \right) \frac{E_{y0}}{k_{zi}} \sin(k_{zi}(z - z_i)), & \\ \left( Q_{n,11}^{\text{TE}} - ik_{z1} Q_{n,12}^{\text{TE}} \right) E_{y0} e^{ik_{zn}(z - z_n)}, & i = n. \end{cases} \quad (\text{A.2})$$

Here,  $Q_{i,pq}^{\text{TE}}$  is the  $(p, q)$  matrix element of  $\mathbf{Q}_i^{\text{TE}}$  given by

$$\mathbf{Q}_i^{\text{TE}} = \mathbf{M}_{i-1}^{\text{TE}} \mathbf{M}_{i-2}^{\text{TE}} \cdots \mathbf{M}_2^{\text{TE}}, \quad (\text{A.3})$$

$$\mathbf{M}_i^{\text{TE}} = \begin{bmatrix} \cos(k_{zi} d_i) & \frac{1}{k_{zi}} \sin(k_{zi} d_i) \\ -k_{zi} \sin(k_{zi} d_i) & \cos(k_{zi} d_i) \end{bmatrix}. \quad (\text{A.4})$$

The magnetic field can be obtained from the electric field by Faraday's law:

$$\mathbf{H}_i(x, z, t) = \left( \frac{i}{\mu_0 \omega} \frac{d}{dz} E_{yi}(z) \hat{x} + \frac{k_x}{\mu_0 \omega} E_{yi}(z) \hat{z} \right) e^{ik_x x - i\omega t}. \quad (\text{A.5})$$

The dispersion relation that must be solved to yield the eigenvalues  $k_x$  is

$$Q_{n,11}^{\text{TE}} - ik_{z1}Q_{n,12}^{\text{TE}} + \frac{i}{k_{zn}}Q_{n,21}^{\text{TE}} + \frac{k_{z1}}{k_{zn}}Q_{n,22}^{\text{TE}} = 0. \quad (\text{A.6})$$

---

## References

- [1] G. P. Agrawal, *Fiber-optic communication systems*, Wiley, New York, 2002.
- [2] D. A. B. Miller, *Device requirements for optical interconnects to silicon chips*, Proc. IEEE **97**, 1166 (2009).
- [3] E. Ozbay, *Plasmonics: Merging photonics and electronics at nanoscale dimensions*, Science **311**, 189 (2006).
- [4] H. J. Queisser, *Photovoltaic conversion at reduced dimensions*, Physica E: Low-dimensional Systems and Nanostructures **14**, 1 (2002).
- [5] K. A. Willets and R. P. Van Duyne, *Localized surface plasmon resonance spectroscopy and sensing*, Annu. Rev. Phys. Chem. **58**, 267 (2007).
- [6] M. E. Stewart, C. R. Anderton, L. B. Thompson, J. Maria, S. K. Gray, J. A. Rogers, and R. G. Nuzzo, *Nanostructured plasmonic sensors*, Chem. Rev. **108**, 494 (2008).
- [7] L. Tang, S. E. Kocabas, S. Latif, A. K. Okyay, D.-S. Ly-Gagnon, K. C. Saraswat, and D. A. B. Miller, *Nanometre-scale germanium photodetector enhanced by a near-infrared dipole antenna*, Nature Photon. **2**, 226 (2008).
- [8] F. T. Chang, R., *Surface enhanced Raman scattering*, Plenum, New York, 1981.
- [9] M. Airola, Y. Liu, and S. Blair, *Second-harmonic generation from an array of sub-wavelength metal apertures*, J. Opt. A: Pure Appl. Opt. **7**, S118 (2005).
- [10] J. A. H. van Nieuwstadt, M. Sandtke, R. H. Harmsen, F. B. Segerink, J. C. Prangma, S. Enoch, and L. Kuipers, *Strong modification of the nonlinear optical response of metallic subwavelength hole arrays*, Phys. Rev. Lett. **97**, 146102 (2006).
- [11] M. Soljačić and J. D. Joannopoulos, *Enhancement of nonlinear effects using photonic crystals*, Nature Mater. **3**, 211 (2004).
- [12] C. Weisbuch and N. A. J. Rarity, editors, *Microcavities and Photonic Bandgaps: Physics and Applications*, Kluwer, Dordrecht, 1996.
- [13] P. Bharadwaj, B. Deutsch, and L. Novotny, *Optical antennas*, Adv. Opt. Photon. **1**, 438 (2009).
- [14] D. E. Chang, A. S. Sørensen, P. R. Hemmer, and M. D. Lukin, *Quantum optics with surface plasmons*, Phys. Rev. Lett. **97**, 053002 (2006).

- [15] D. E. Chang, A. S. Sorensen, E. A. Demler, and M. D. Lukin, *A single-photon transistor using nanoscale surface plasmons*, Nature Phys. **3**, 807 (2007).
- [16] W. L. Barnes, A. Dereux, and T. W. Ebbesen, *Surface plasmon subwavelength optics*, Nature **424**, 824 (2003).
- [17] S. Lal, S. Link, and N. J. Halas, *Nano-optics from sensing to waveguiding*, Nature Photon. **1**, 641 (2007).
- [18] T. W. Ebbesen, C. Genet, and S. I. Bozhevolnyi, *Surface plasmon circuitry*, Phys. Today **61**, 44 (2008).
- [19] A. Polman, *Plasmonics applied*, Science **322**, 868 (2008).
- [20] E. Abbe, *Beiträge zur Theorie des Mikroskops und der mikroskopischen Wahrnehmung*, Archiv f. Mikroskop. Anat. **9**, 413 (1873).
- [21] V. V. Shevchenko, *Continuous transitions in open waveguides*, Golem Press, Boulder, Colorado, 1971.
- [22] R. F. Oulton, D. F. P. Pile, Y. Liu, and X. Zhang, *Scattering of surface plasmon polaritons at abrupt surface interfaces: Implications for nanoscale cavities*, Phys. Rev. B **76**, 035408 (2007).
- [23] R. Petit, editor, *Electromagnetic theory of gratings*, Springer-Verlag, Berlin, 1980.
- [24] H. Raether, *Surface plasmons on smooth and rough surfaces and on gratings*, Springer-Verlag, Berlin Heidelberg, 1988.
- [25] A. Archambault, T. V. Teperik, F. Marquier, and J. J. Greffet, *Surface plasmon Fourier optics*, Phys. Rev. B **79**, 195414 (2009).
- [26] P. B. Johnson and R. W. Christy, *Optical constants of the noble metals*, Phys. Rev. B **6**, 4370 (1972).
- [27] C. Kittel, *Introduction to solid state physics*, Wiley, New York, 1996.
- [28] A. Lagendijk and van B. A. van Tiggelen, *Resonant multiple scattering of light*, Physics Reports **270**, 143 (1996).
- [29] L. Novotny and B. Hecht, *Principles of nano-optics*, Cambridge University Press, Cambridge, 2006.
- [30] S. A. Maier and H. A. Atwater, *Plasmonics: Localization and guiding of electromagnetic energy in metal/dielectric structures*, J. Appl. Phys. **98**, 011101 (2005).
- [31] J. J. Burke, G. I. Stegeman, and T. Tamir, *Surface-polariton-like waves guided by thin, lossy metal films*, Phys. Rev. B **33**, 5186 (1986).
- [32] J. Hu and C. R. Menyuk, *Understanding leaky modes: slab waveguide revisited*, Adv. Opt. Photon. **1**, 58 (2009).
- [33] L. Ahlfors, *Complex Analysis*, McGraw-Hill, 1979.
- [34] E. N. Economou, *Surface plasmons in thin films*, Phys. Rev. **182**, 539 (1969).
- [35] R. Zia, M. D. Selker, P. B. Catrysse, and M. L. Brongersma, *Geometries and materials for subwavelength surface plasmon modes*, J. Opt. Soc. Am. A **21**, 2442 (2004).
- [36] J. A. Dionne, L. A. Sweatlock, H. A. Atwater, and A. Polman, *Plasmon slot waveguides: Towards chip-scale propagation with subwavelength-scale localization*, Phys. Rev. B **73**, 035407 (2006).
- [37] D. Sarid, *Long-range surface-plasma waves on very thin metal films*, Phys. Rev. Lett. **47**, 1927 (1981).
- [38] T. Nikolajsen, K. Leosson, I. Salakhutdinov, and S. Bozhevolnyi, *Polymer-based surface-plasmon-polariton stripe waveguides at telecommunication wavelengths*, Appl. Phys. Lett. **82**, 668 (2003).
- [39] L. Wendler and R. Haupt, *Long-range surface plasmon-polaritons in asymmetric layer structures*, J. Appl. Phys. **59**, 3289 (1986).



- [40] T. J. Cui and J. A. Kong, *Time-domain electromagnetic energy in a frequency-dispersive left-handed medium*, Phys. Rev. B **70**, 205106 (2004).
- [41] P. Berini, *Figures of merit for surface plasmon waveguides*, Opt. Express **14**, 13030 (2006).
- [42] R. F. Oulton, G. Bartal, D. F. P. Pile, and X. Zhang, *Confinement and propagation characteristics of subwavelength plasmonic modes*, New J. Phys. **10**, 105018 (2008).
- [43] M. I. Stockman, *Nanofocusing of optical energy in tapered plasmonic waveguides*, Phys. Rev. Lett. **93**, 137404 (2004).
- [44] V. G. Veselago, *The electrodynamics of substances with simultaneously negative values of  $\epsilon$  and  $\mu$* , Sov. Phys. Uspekhi **10**, 509 (1968).
- [45] J. B. Pendry, *Negative refraction makes a perfect lens*, Phys. Rev. Lett. **85**, 3966 (2000).
- [46] D. R. Smith, J. B. Pendry, and M. C. K. Wiltshire, *Metamaterials and negative refractive index*, Science **305**, 788 (2004).
- [47] V. M. Shalaev, *Optical negative-index metamaterials*, Nature Photon. **1**, 41 (2007).
- [48] C. M. Soukoulis, S. Linden, and M. Wegener, *Negative refractive index at optical wavelengths*, Science **315**, 47 (2007).
- [49] R. Merlin, *Metamaterials and the Landau-Lifshitz permeability argument: Large permittivity begets high-frequency magnetism*, Proc. Nat. Acad. Sc. **106**, 1693 (2009).
- [50] A. Alù, A. Salandrino, and N. Engheta, *Negative effective permeability and left-handed materials at optical frequencies*, Opt. Express **14**, 1557 (2006).
- [51] H. Shin and S. Fan, *All-angle negative refraction for surface plasmon waves using a metal-dielectric-metal structure*, Phys. Rev. Lett. **96**, 073907 (2006).
- [52] G. Shvets, *Photonic approach to making a material with a negative index of refraction*, Phys. Rev. B **67**, 035109 (2003).
- [53] M. I. Stockman, *Criterion for negative refraction with low optical losses from a fundamental principle of causality*, Phys. Rev. Lett. **98**, 177404 (2007).
- [54] A. Karalis, E. Lidorikis, M. Ibanescu, J. D. Joannopoulos, and M. Soljačić, *Surface-plasmon-assisted guiding of broadband slow and subwavelength light in air*, Phys. Rev. Lett. **95**, 063901 (2005).
- [55] J. A. Dionne, E. Verhagen, A. Polman, and H. A. Atwater, *Are negative index materials achievable with surface plasmon waveguides? A case study of three plasmonic geometries*, Opt. Express **16**, 19001 (2008).
- [56] H. Ditlbacher, A. Hohenau, D. Wagner, U. Kreibig, M. Rogers, F. Hofer, F. R. Aussenegg, and J. R. Krenn, *Silver nanowires as surface plasmon resonators*, Phys. Rev. Lett. **95**, 257403 (2005).
- [57] L. Novotny, *Effective wavelength scaling for optical antennas*, Phys. Rev. Lett. **98**, 266802 (2007).
- [58] J. Dorfmueller, R. Vogelgesang, R. T. Weitz, C. Rockstuhl, C. Etrich, T. Pertsch, F. Lederer, and K. Kern, *Fabry-Pérot resonances in one-dimensional plasmonic nanostructures*, Nano Lett. **9**, 2372 (2009).
- [59] J. A. Porto, F. J. Garca-Vidal, and J. B. Pendry, *Transmission resonances on metallic gratings with very narrow slits*, Phys. Rev. Lett. **83**, 2845 (1999).
- [60] H. E. Went, A. P. Hibbins, J. R. Sambles, C. R. Lawrence, and A. P. Crick, *Selective transmission through very deep zero-order metallic gratings at microwave frequencies*, Appl. Phys. Lett. **77**, 2789 (2000).
- [61] A. Barbara, P. Quémerais, E. Bustarret, and T. Lopez-Rios, *Optical transmission through subwavelength metallic gratings*, Phys. Rev. B **66**, 161403 (2002).
- [62] R. de Waele, S. P. Burgos, A. Polman, and H. A. Atwater, *Plasmon dispersion in coaxial*

- waveguides from single-cavity optical transmission measurements*, Nano Lett. **9**, 2832 (2009).
- [63] J. Beermann, S. M. Novikov, T. Søndergaard, A. Boltasseva, and S. I. Bozhevolnyi, *Two-photon mapping of localized field enhancements in thin nanostrip antennas*, Opt. Express **16**, 17302 (2008).
- [64] H. T. Miyazaki and Y. Kurokawa, *Squeezing visible light waves into a 3-nm-thick and 55-nm-long plasmon cavity*, Phys. Rev. Lett. **96**, 097401 (2006).
- [65] J. A. Dionne, H. J. Lezec, and H. A. Atwater, *Highly confined photon transport in subwavelength metallic slot waveguides*, Nano Lett. **6**, 1928 (2006).
- [66] A. Degiron, H. Lezec, N. Yamamoto, and T. Ebbesen, *Optical transmission properties of a single subwavelength aperture in a real metal*, Opt. Commun. **239**, 61 (2004).
- [67] J. Prikulis, P. Hanarp, L. Olofsson, D. Sutherland, and M. Käll, *Optical spectroscopy of nanometric holes in thin gold films*, Nano Lett. **4**, 1003 (2004).
- [68] F. J. García-Vidal, E. Moreno, J. A. Porto, and L. Martín-Moreno, *Transmission of light through a single rectangular hole*, Phys. Rev. Lett. **95**, 103901 (2005).
- [69] A. Degiron and T. W. Ebbesen, *The role of localized surface plasmon modes in the enhanced transmission of periodic subwavelength apertures*, J. Opt. A: Pure Appl. Opt. **7**, S90 (2005).
- [70] Z. Ruan and M. Qiu, *Enhanced transmission through periodic arrays of subwavelength holes: The role of localized waveguide resonances*, Phys. Rev. Lett. **96**, 233901 (2006).
- [71] F. Baida, D. Van Labeke, G. Granet, A. Moreau, and A. Belkhir, *Origin of the super-enhanced light transmission through a 2-D metallic annular aperture array: a study of photonic bands*, Appl. Phys. B: Lasers Opt. **79**, 1 (2004).
- [72] W. Fan, S. Zhang, B. Minhas, K. J. Malloy, and S. R. J. Brueck, *Enhanced infrared transmission through subwavelength coaxial metallic arrays*, Phys. Rev. Lett. **94**, 033902 (2005).
- [73] S. M. Orbons and A. Roberts, *Resonance and extraordinary transmission in annular aperture arrays*, Opt. Express **14**, 12623 (2006).
- [74] F. I. Baida, A. Belkhir, D. Van Labeke, and O. Lamrous, *Subwavelength metallic coaxial waveguides in the optical range: Role of the plasmonic modes*, Phys. Rev. B **74**, 205419 (2006).
- [75] M. I. Haftel, C. Schlockermann, and G. Blumberg, *Enhanced transmission with coaxial nanoapertures: Role of cylindrical surface plasmons*, Phys. Rev. B **74**, 235405 (2006).
- [76] Lumerical FDTD Solutions.
- [77] P. Dawson, F. de Fornel, and J-P. Goudonnet, *Imaging of surface plasmon propagation and edge interaction using a photon scanning tunneling microscope*, Phys. Rev. Lett. **72**, 2927 (1994).
- [78] B. Hecht, H. Bielefeldt, L. Novotny, Y. Inouye, and D. W. Pohl, *Local excitation, scattering, and interference of surface plasmons*, Phys. Rev. Lett. **77**, 1889 (1996).
- [79] H. Dittlbacher, J. R. Krenn, N. Felidj, B. Lamprecht, G. Schider, M. Salerno, A. Leitner, and F. R. Aussenegg, *Fluorescence imaging of surface plasmon fields*, Appl. Phys. Lett. **80**, 404 (2002).
- [80] E. Verhagen, A. L. Tchebotareva, and A. Polman, *Erbium luminescence imaging of infrared surface plasmon polaritons*, Appl. Phys. Lett. **88**, 121121 (2006).
- [81] P. Neutens, P. Van Dorpe, I. De Vlaminck, L. Lagae, and G. Borghs, *Electrical detection of confined gap plasmons in metal-insulator-metal waveguides*, Nature Photon. **3**, 283 (2009).
- [82] S. Maier, *Effective mode volume of nanoscale plasmon cavities*, Opt. Quantum

- Electron. **38**, 257 (2006).
- [83] S. I. Bozhevolnyi, V. S. Volkov, E. Devaux, J.-Y. Laluet, and T. W. Ebbesen, *Channel plasmon subwavelength waveguide components including interferometers and ring resonators*, Nature **440**, 508 (2006).
- [84] D. F. P. Pile, T. Ogawa, D. K. Gramotnev, Y. Matsuzaki, K. C. Vernon, K. Yamaguchi, T. Okamoto, M. Haraguchi, and M. Fukui, *Two-dimensionally localized modes of a nanoscale gap plasmon waveguide*, Appl. Phys. Lett. **87**, 261114 (2005).
- [85] J. A. Veerman, A. M. Otter, L. Kuipers, and N. F. van Hulst, *High definition aperture probes for near-field optical microscopy fabricated by focused ion beam milling*, Appl. Phys. Lett. **72**, 3115 (1998).
- [86] C. Sönnichsen, A. C. Duch, G. Steininger, M. Koch, G. von Plessen, and J. Feldmann, *Launching surface plasmons into nanoholes in metal films*, Appl. Phys. Lett. **76**, 140 (2000).
- [87] E.-S. Kwak, J. Henzie, S.-H. Chang, S. K. Gray, G. C. Schatz, and T. W. Odom, *Surface plasmon standing waves in large-area subwavelength hole arrays*, Nano Lett. **5**, 1963 (2005).
- [88] J. B. Pendry, D. Schurig, and D. R. Smith, *Controlling electromagnetic fields*, Science **312**, 1780 (2006).
- [89] D. Schurig, J. B. Pendry, and D. R. Smith, *Transformation-designed optical elements*, Opt. Express **15**, 14772 (2007).
- [90] N. Fang, H. Lee, C. Sun, and X. Zhang, *Sub-diffraction-limited optical imaging with a silver superlens*, Science **308**, 534 (2005).
- [91] T. Taubner, D. Korobkin, Y. Urzhumov, G. Shvets, and R. Hillenbrand, *Near-field microscopy through a SiC superlens*, Science **313**, 1595 (2006).
- [92] Z. Jacob, L. V. Alekseyev, and E. Narimanov, *Optical Hyperlens: Far-field imaging beyond the diffraction limit*, Opt. Express **14**, 8247 (2006).
- [93] N. Engheta, *Circuits with light at nanoscales: Optical nanocircuits inspired by metamaterials*, Science **317**, 1698 (2007).
- [94] D. Schurig, J. J. Mock, B. J. Justice, S. A. Cummer, J. B. Pendry, A. F. Starr, and D. R. Smith, *Metamaterial electromagnetic cloak at microwave frequencies*, Science **314**, 977 (2006).
- [95] A. Alù and N. Engheta, *Achieving transparency with plasmonic and metamaterial coatings*, Phys. Rev. E **72**, 016623 (2005).
- [96] R. A. Shelby, D. R. Smith, and S. Schultz, *Experimental verification of a negative index of refraction*, Science **292**, 77 (2001).
- [97] J. Valentine, S. Zhang, T. Zentgraf, E. Ulin-Avila, D. A. Genov, G. Bartal, and X. Zhang, *Three-dimensional optical metamaterial with a negative refractive index*, Nature **455**, 376 (2008).
- [98] X. Fan, G. P. Wang, J. C. W. Lee, and C. T. Chan, *All-angle broadband negative refraction of metal waveguide arrays in the visible range: theoretical analysis and numerical demonstration*, Phys. Rev. Lett. **97**, 073901 (2006).
- [99] H. J. Lezec, J. A. Dionne, and H. A. Atwater, *Negative refraction at visible frequencies*, Science **316**, 430 (2007).
- [100] I. I. Smolyaninov, Y.-J. Hung, and C. C. Davis, *Magnifying superlens in the visible frequency range*, Science **315**, 1699 (2007).
- [101] A. S. Barker and R. Loudon, *Response functions in the theory of raman scattering by vibrational and polariton modes in dielectric crystals*, Rev. Mod. Phys. **44**, 18 (1972).
- [102] M. I. Stockman, *Slow propagation, anomalous absorption, and total external reflection of surface plasmon polaritons in nanolayer systems*, Nano Lett. **6**, 2604 (2006).

- [103] R. Ruppin, *Electromagnetic energy density in a dispersive and absorptive material*, Phys. Lett. A **299**, 309 (2002).
- [104] E. Palik, editor, *Handbook of optical constants of solids*, Academic Press, Inc., New York, New York, 1985.
- [105] S. A. Ramakrishna, J. B. Pendry, D. Schurig, D. R. Smith, and S. Schultz, *The asymmetric lossy near-perfect lens*, J. Mod. Opt. **49**, 1747 (2002).
- [106] G. Dolling, C. Enkrich, M. Wegener, C. M. Soukoulis, and S. Linden, *Low-loss negative-index metamaterial at telecommunication wavelengths*, Opt. Lett. **31**, 1800 (2006).
- [107] S. Balushev, F. Yu, T. Miteva, S. Ahl, A. Yasuda, G. Nelles, W. Knoll, and G. Wegner, *Metal-enhanced up-conversion fluorescence: Effective triplet-triplet annihilation near silver surface*, Nano Lett. **5**, 2482 (2005).
- [108] S. I. Bozhevolnyi, J. Erland, K. Leosson, P. M. W. Skovgaard, and J. M. Hvam, *Waveguiding in surface plasmon polariton band gap structures*, Phys. Rev. Lett. **86**, 3008 (2001).
- [109] B. Steinberger, A. Hohenau, H. Ditlbacher, A. L. Stepanov, A. Drezet, F. R. Aussenegg, A. Leitner, and J. R. Krenn, *Dielectric stripes on gold as surface plasmon waveguides*, Appl. Phys. Lett. **88**, 094104 (2006).
- [110] L. Chen, J. Shakya, and M. Lipson, *Subwavelength confinement in an integrated metal slot waveguide on silicon*, Opt. Lett. **31**, 2133 (2006).
- [111] B. Lamprecht, J. R. Krenn, G. Schider, H. Ditlbacher, M. Salerno, N. Felidj, A. Leitner, and F. R. Aussenegg, *Surface plasmon propagation in microscale metal stripes*, Appl. Phys. Lett. **79**, 51 (2001).
- [112] J.-C. Weeber, J. R. Krenn, A. Dereux, B. Lamprecht, Y. Lacroute, and J. P. Goudonnet, *Near-field observation of surface plasmon polariton propagation on thin metal stripes*, Phys. Rev. B **64**, 045411 (2001).
- [113] P. Berini, *Plasmon-polariton waves guided by thin lossy metal films of finite width: Bound modes of asymmetric structures*, Phys. Rev. B **63**, 125417 (2001).
- [114] J.-C. Weeber, Y. Lacroute, and A. Dereux, *Optical near-field distributions of surface plasmon waveguide modes*, Phys. Rev. B **68**, 115401 (2003).
- [115] R. Zia, M. D. Selker, and M. L. Brongersma, *Leaky and bound modes of surface plasmon waveguides*, Phys. Rev. B **71**, 165431 (2005).
- [116] A. Hohenau, J. R. Krenn, A. L. Stepanov, A. Drezet, H. Ditlbacher, B. Steinberger, A. Leitner, and F. R. Aussenegg, *Dielectric optical elements for surface plasmons*, Opt. Lett. **30**, 893 (2005).
- [117] A. Drezet, A. L. Stepanov, H. Ditlbacher, A. Hohenau, B. Steinberger, F. R. Aussenegg, A. Leitner, and J. R. Krenn, *Surface plasmon propagation in an elliptical corral*, Appl. Phys. Lett. **86**, 074104 (2005).
- [118] L. Yin, V. K. Vlasko-Vlasov, J. Pearson, J. M. Hiller, J. Hua, U. Welp, D. E. Brown, and C. W. Kimball, *Subwavelength focusing and guiding of surface plasmons*, Nano Lett. **5**, 1399 (2005).
- [119] Z. Liu, J. M. Steele, W. Srituravanich, Y. Pikus, C. Sun, and X. Zhang, *Focusing surface plasmons with a plasmonic lens*, Nano Lett. **5**, 1726 (2005).
- [120] H. L. Offerhaus, B. van den Bergen, M. Escalante, F. B. Segerink, J. P. Korterik, and N. F. van Hulst, *Creating focused plasmons by noncollinear phasematching on functional gratings*, Nano Lett. **5**, 2144 (2005).
- [121] J. Koglin, U. C. Fischer, and H. Fuchs, *Material contrast in scanning near-field optical microscopy at 1&10 nm resolution*, Phys. Rev. B **55**, 7977 (1997).
- [122] N. Janunts, K. Baghdasaryan, K. Nerkararyan, and B. Hecht, *Excitation and superfo-*

- cusings of surface plasmon polaritons on a silver-coated optical fiber tip*, Opt. Commun. **253**, 118 (2005).
- [123] A. Bouhelier, M. Beversluis, A. Hartschuh, and L. Novotny, *Near-field second-harmonic generation induced by local field enhancement*, Phys. Rev. Lett. **90**, 013903 (2003).
- [124] F. Auzel, *Upconversion and anti-Stokes processes with f and d ions in solids*, Chem. Rev. **104**, 139 (2004).
- [125] G. N. van den Hoven, E. Snoeks, A. Polman, C. van Dam, J. W. M. van Uffelen, and M. K. Smit, *Upconversion in Er-implanted  $Al_2O_3$  waveguides*, J. Appl. Phys. **79**, 1258 (1996).
- [126] G. N. van den Hoven, A. Polman, C. van Dam, J. W. M. van Uffelen, and M. K. Smit, *Direct imaging of optical interference in erbium-doped  $Al_2O_3$  waveguides*, Opt. Lett. **21**, 576 (1996).
- [127] URL: [www.srim.org](http://www.srim.org).
- [128] G. N. van den Hoven, E. Snoeks, A. Polman, J. W. M. van Uffelen, Y. S. Oei, and M. K. Smit, *Photoluminescence characterization of Er-implanted  $Al_2O_3$  films*, Appl. Phys. Lett. **62**, 3065 (1993).
- [129] M. Pollnau, D. R. Gamelin, S. R. Lüthi, H. U. Güdel, and M. P. Hehlen, *Power dependence of upconversion luminescence in lanthanide and transition-metal-ion systems*, Phys. Rev. B **61**, 3337 (2000).
- [130] D. S. Kim, S. C. Hohng, V. Malyarchuk, Y. C. Yoon, Y. H. Ahn, K. J. Yee, J. W. Park, J. Kim, Q. H. Park, and C. Lienau, *Microscopic origin of surface-plasmon radiation in plasmonic band-gap nanostructures*, Phys. Rev. Lett. **91**, 143901 (2003).
- [131] E. Devaux, T. W. Ebbesen, J.-C. Weeber, and A. Dereux, *Launching and decoupling surface plasmons via micro-gratings*, Appl. Phys. Lett. **83**, 4936 (2003).
- [132] A. Fragola, L. Aigouy, Y. D. Wilde, and M. Mortier, *Upconversion fluorescence imaging of erbium-doped fluoride glass particles by apertureless SNOM*, J. Microsc. **210**, 198 (2003).
- [133] R. Zia, A. Chandran, and M. L. Brongersma, *Dielectric waveguide model for guided surface polaritons*, Opt. Lett. **30**, 1473 (2005).
- [134] J. Kalkman, L. Kuipers, A. Polman, and H. Gersen, *Coupling of Er ions to surface plasmons on Ag*, Appl. Phys. Lett. **86**, 041113 (2005).
- [135] R. Zia, J. A. Schuller, and M. L. Brongersma, *Near-field characterization of guided polariton propagation and cutoff in surface plasmon waveguides*, Phys. Rev. B **74**, 165415 (2006).
- [136] C. A. Pfeiffer, E. N. Economou, and K. L. Ngai, *Surface polaritons in a circularly cylindrical interface: Surface plasmons*, Phys. Rev. B **10**, 3038 (1974).
- [137] D. Gramotnev and K. Vernon, *Adiabatic nano-focusing of plasmons by sharp metallic wedges*, Appl. Phys. B: Lasers Opt. **86**, 7 (2007).
- [138] D. K. Gramotnev, D. F. P. Pile, M. W. Vogel, and X. Zhang, *Local electric field enhancement during nanofocusing of plasmons by a tapered gap*, Phys. Rev. B **75**, 035431 (2007).
- [139] F. Keilmann, *Surface-polariton propagation for scanning near-field optical microscopy application*, J. Microsc. **194**, 567 (1999).
- [140] A. Bouhelier, J. Renger, M. R. Beversluis, and L. Novotny, *Plasmon-coupled tip-enhanced near-field optical microscopy*, J. Microsc. **210**, 220 (2003).
- [141] C. Ropers, C. C. Neacsu, T. Elsaesser, M. Albrecht, M. B. Raschke, and C. Lienau, *Grating-coupling of surface plasmons onto metallic tips: A nanoconfined light source*, Nano Lett. **7**, 2784 (2007).
- [142] H. Choi, D. F. Pile, S. Nam, G. Bartal, and X. Zhang, *Compressing surface plasmons for*

- nano-scale optical focusing*, Opt. Express **17**, 7519 (2009).
- [143] V. S. Volkov, S. I. Bozhevolnyi, S. G. Rodrigo, L. Martín-Moreno, F. J. García-Vidal, E. Devaux, and T. W. Ebbesen, *Nanofocusing with channel plasmon polaritons*, Nano Lett. **9**, 1278 (2009).
- [144] Z. Zhu and T. Brown, *Full-vectorial finite-difference analysis of microstructured optical fibers*, Opt. Express **10**, 853 (2002).
- [145] M. Quinten, A. Leitner, J. R. Krenn, and F. R. Aussenegg, *Electromagnetic energy transport via linear chains of silver nanoparticles*, Opt. Lett. **23**, 1331 (1998).
- [146] S. A. Maier, P. G. Kik, H. A. Atwater, S. Meltzer, E. Harel, B. E. Koel, and A. A. Requicha, *Local detection of electromagnetic energy transport below the diffraction limit in metal nanoparticle plasmon waveguides*, Nature Mater. **2**, 229 (2003).
- [147] J. Takahara, S. Yamagishi, H. Taki, A. Morimoto, and T. Kobayashi, *Guiding of a one-dimensional optical beam with nanometer diameter*, Opt. Lett. **22**, 475 (1997).
- [148] R. M. Dickson and L. A. Lyon, *Unidirectional plasmon propagation in metallic nanowires*, J. Phys. Chem. B **104**, 6095 (2000).
- [149] M. W. Knight, N. K. Grady, R. Bardhan, F. Hao, P. Nordlander, and N. J. Halas, *Nanoparticle-mediated coupling of light into a nanowire*, Nano Lett. **7**, 2346 (2007).
- [150] S. Nie and S. R. Emory, *Probing single molecules and single nanoparticles by surface-enhanced Raman scattering*, Science **275**, 1102 (1997).
- [151] S. Kim, J. Jin, Y.-J. Kim, I.-Y. Park, Y. Kim, and S.-W. Kim, *High-harmonic generation by resonant plasmon field enhancement*, Nature **453**, 757 (2008).
- [152] A. V. Akimov, A. Mukherjee, C. L. Yu, D. E. Chang, A. S. Zibrov, P. R. Hemmer, H. Park, and M. D. Lukin, *Generation of single optical plasmons in metallic nanowires coupled to quantum dots*, Nature **450**, 402 (2007).
- [153] A. Sommerfeld, *Ueber die Fortpflanzung elektrodynamischer Wellen längs eines Drahtes*, Ann. der Physik und Chemie **67**, 233 (1899).
- [154] K. Wang and D. M. Mittleman, *Metal wires for terahertz wave guiding*, Nature **432**, 376 (2004).
- [155] A. J. Babadjanyan, N. L. Margaryan, and K. V. Nerkararyan, *Superfocusing of surface polaritons in the conical structure*, J. Appl. Phys. **87**, 3785 (2000).
- [156] U. Schröter and A. Dereux, *Surface plasmon polaritons on metal cylinders with dielectric core*, Phys. Rev. B **64**, 125420 (2001).
- [157] M. Born and V. Fock, *Beweis des Adiabatenatzes*, Z. Phys. **51**, 165 (1928).
- [158] J. E. Avron and A. Elgart, *Adiabatic theorem without a gap condition*, Comm. Math. Phys. **203**, 445 (1999).
- [159] J. A. Stratton, *Electromagnetic Theory*, McGraw-Hill, 1941.
- [160] COMSOL Multiphysics.
- [161] P. Berini, *Plasmon-polariton waves guided by thin lossy metal films of finite width: Bound modes of symmetric structures*, Phys. Rev. B **61**, 10484 (2000).
- [162] J. Jung, T. Søndergaard, and S. I. Bozhevolnyi, *Theoretical analysis of square surface plasmon-polariton waveguides for long-range polarization-independent waveguiding*, Phys. Rev. B **76**, 035434 (2007).
- [163] K. Leosson, T. Nikolajsen, A. Boltasseva, and S. I. Bozhevolnyi, *Long-range surface plasmon polariton nanowire waveguides for device applications*, Opt. Express **14**, 314 (2006).
- [164] J. R. Krenn, B. Lamprecht, H. Ditlbacher, G. Schider, M. Salerno, A. Leitner, and F. R. Aussenegg, *Non-diffraction-limited light transport by gold nanowires*, Europhys. Lett. **60**, 663 (2002).

- [165] M. L. M. Balistreri, J. P. Korterik, L. Kuipers, and N. F. van Hulst, *Local observations of phase singularities in optical fields in waveguide structures*, Phys. Rev. Lett. **85**, 294 (2000).
- [166] M. Burreli, R. J. P. Engelen, A. Opheij, D. van Oosten, D. Mori, T. Baba, and L. Kuipers, *Observation of polarization singularities at the nanoscale*, Phys. Rev. Lett. **102**, 033902 (2009).
- [167] M. Sandtke, R. J. P. Engelen, H. Schoenmaker, I. Attema, H. Dekker, I. Cerjak, J. P. Korterik, F. B. Segerink, and L. Kuipers, *Novel instrument for surface plasmon polariton tracking in space and time*, Rev. Sci. Instrum. **79**, 013704 (2008).
- [168] J.-J. Greffet and R. Carminati, *Image formation in near-field optics*, Prog. Surf. Sci. **56**, 133 (1997).
- [169] S. I. Bozhevolnyi, B. Vohnsen, and E. A. Bozhevolnaya, *Transfer functions in collection scanning near-field optical microscopy*, Opt. Commun. **172**, 171 (1999).
- [170] R. J. P. Engelen, Y. Sugimoto, H. Gersen, N. Ikeda, K. Asakawa, and L. K. Kuipers, *Ultrafast evolution of photonic eigenstates in k-space*, Nature Phys. **3**, 401 (2007).
- [171] D. K. Gramotnev, *Adiabatic nanofocusing of plasmons by sharp metallic grooves: Geometrical optics approach*, J. Appl. Phys. **98**, 104302 (2005).
- [172] R. Ruppini, *Effect of non-locality on nanofocusing of surface plasmon field intensity in a conical tip*, Phys. Lett. A **340**, 299 (2005).
- [173] N. Issa and R. Guckenberger, *Optical nanofocusing on tapered metallic waveguides*, Plasmonics **2**, 31 (2007).
- [174] D. K. Gramotnev, M. W. Vogel, and M. I. Stockman, *Optimized nonadiabatic nanofocusing of plasmons by tapered metal rods*, J. Appl. Phys. **104**, 034311 (2008).
- [175] M. Durach, A. Rusina, M. I. Stockman, and K. Nelson, *Toward full spatiotemporal control on the nanoscale*, Nano Lett. **7**, 3145 (2007).
- [176] K. C. Vernon, D. K. Gramotnev, and D. F. P. Pile, *Adiabatic nanofocusing of plasmons by a sharp metal wedge on a dielectric substrate*, J. Appl. Phys. **101**, 104312 (2007).
- [177] D. F. P. Pile and D. K. Gramotnev, *Adiabatic and nonadiabatic nanofocusing of plasmons by tapered gap plasmon waveguides*, Appl. Phys. Lett. **89**, 041111 (2006).
- [178] G. Webb-Wood and P. G. Kik, *Simultaneous excitation of fast and slow surface plasmon polaritons in a high dielectric contrast system*, Appl. Phys. Lett. **92**, 133101 (2008).
- [179] M. A. Born and E. Wolf, *Principles of optics*, Pergamon Press, London New York Paris Los Angeles, 1959.
- [180] T. W. Ebbesen, H. J. Lezec, H. F. Ghaemi, T. Thio, and P. A. Wolff, *Extraordinary optical transmission through sub-wavelength hole arrays*, Nature **391**, 667 (1998).
- [181] C. Genet and T. W. Ebbesen, *Light in tiny holes*, Nature **445**, 39 (2007).
- [182] F. J. García de Abajo, *Colloquium: Light scattering by particle and hole arrays*, Rev. Mod. Phys. **79**, 1267 (2007).
- [183] A. G. Brolo, E. Arctander, R. Gordon, B. Leathem, and K. L. Kavanagh, *Nanohole-enhanced Raman scattering*, Nano Lett. **4**, 2015 (2004).
- [184] M. Tanaka, F. Miyamaru, M. Hangyo, T. Tanaka, M. Akazawa, and E. Sano, *Effect of a thin dielectric layer on terahertz transmission characteristics for metal hole arrays*, Opt. Lett. **30**, 1210 (2005).
- [185] Y. Liu and S. Blair, *Fluorescence enhancement from an array of subwavelength metal apertures*, Opt. Lett. **28**, 507 (2003).
- [186] A. G. Brolo, S. C. Kwok, M. D. Cooper, M. G. Moffitt, C.-W. Wang, R. Gordon, J. Riordon, and K. L. Kavanagh, *Surface plasmon-quantum dot coupling from arrays of nanoholes*, J. Phys. Chem. B **110**, 8307 (2006).

- [187] W. Fan, S. Zhang, N.-C. Panoui, A. Abdenour, S. Krishna, R. M. Osgood, K. J. Malloy, and S. R. J. Brueck, *Second harmonic generation from a nanopatterned isotropic nonlinear material*, Nano Lett. **6**, 1027 (2006).
- [188] W. Fan, S. Zhang, K. J. Malloy, S. R. J. Brueck, N. C. Panoui, and R. M. Osgood, *Second harmonic generation from patterned GaAs inside a subwavelength metallic hole array*, Opt. Express **14**, 9570 (2006).
- [189] P. Lalanne, J. C. Rodier, and J. P. Hugonin, *Surface plasmons of metallic surfaces perforated by nanohole arrays*, J. Opt. A: Pure Appl. Opt. **7**, 422 (2005).
- [190] K. J. Klein Koerkamp, S. Enoch, F. B. Segerink, N. F. van Hulst, and L. Kuipers, *Strong influence of hole shape on extraordinary transmission through periodic arrays of subwavelength holes*, Phys. Rev. Lett. **92**, 183901 (2004).
- [191] F. I. Baida and D. Van Labeke, *Light transmission by subwavelength annular aperture arrays in metallic films*, Opt. Commun. **209**, 17 (2002).
- [192] F. I. Baida and D. Van Labeke, *Three-dimensional structures for enhanced transmission through a metallic film: Annular aperture arrays*, Phys. Rev. B **67**, 155314 (2003).
- [193] D. Van Labeke, D. Gérard, B. Guizal, F. I. Baida, and L. Li, *An angle-independent Frequency Selective Surface in the optical range*, Opt. Express **14**, 11945 (2006).
- [194] W. von Klitzing, E. Jahier, R. Long, F. Lissillour, V. Lefevre-Seguín, J. Hare, J.-M. Raimond, and S. Haroche, *Very low threshold green lasing in microspheres by up-conversion of IR photons*, J. Opt. B: Quantum Semiclassical Opt. **2**, 204 (2000).
- [195] E. Heumann, S. Bär, K. Rademaker, G. Huber, S. Butterworth, A. Diening, and W. Seelert, *Semiconductor-laser-pumped high-power upconversion laser*, Appl. Phys. Lett. **88**, 061108 (2006).
- [196] T. Lu, L. Yang, R. V. A. van Loon, A. Polman, and K. J. Vahala, *On-chip green silica upconversion microlaser*, Opt. Lett. **34**, 482 (2009).
- [197] E. Downing, L. Hesselink, J. Ralston, and R. Macfarlane, *A three-color, solid-state, three-dimensional display*, Science **273**, 1185 (1996).
- [198] S. F. Lim, R. Riehn, W. S. Ryu, N. Khanarian, C.-K. Tung, D. Tank, and R. H. Austin, *In vivo and scanning electron microscopy imaging of upconverting nanophosphors in Caenorhabditis elegans*, Nano Lett. **6**, 169 (2006).
- [199] T. Trupke, M. A. Green, and P. Würfel, *Improving solar cell efficiencies by up-conversion of sub-band-gap light*, J. Appl. Phys. **92**, 4117 (2002).
- [200] F. Hallermann, C. Rockstuhl, S. Fahr, G. Seifert, S. Wackerow, H. Graener, G. v. Plessen, and F. Lederer, *On the use of localized plasmon polaritons in solar cells*, Phys. Status Solidi A **205**, 2844 (2008).
- [201] T. Aisaka, M. Fujii, and S. Hayashi, *Enhancement of upconversion luminescence of Er doped Al<sub>2</sub>O<sub>3</sub> films by Ag island films*, Appl. Phys. Lett. **92**, 132105 (2008).
- [202] V. K. Rai, L. de S. Menezes, C. B. de Araújo, L. R. P. Kassab, D. M. da Silva, and R. A. Kobayashi, *Surface-plasmon-enhanced frequency upconversion in Pr<sup>3+</sup> doped tellurium-oxide glasses containing silver nanoparticles*, J. Appl. Phys. **103**, 093526 (2008).
- [203] A. Moreau, G. Granet, F. Baida, and D. V. Labeke, *Light transmission by subwavelength square coaxial aperture arrays in metallic films*, Opt. Express **11**, 1131 (2003).
- [204] H. F. Ghaemi, T. Thio, D. E. Grupp, T. W. Ebbesen, and H. J. Lezec, *Surface plasmons enhance optical transmission through subwavelength holes*, Phys. Rev. B **58**, 6779 (1998).
- [205] W. L. Barnes, W. A. Murray, J. Dintinger, E. Devaux, and T. W. Ebbesen, *Surface plasmon polaritons and their role in the enhanced transmission of light through periodic arrays*



- of subwavelength holes in a metal film*, Phys. Rev. Lett. **92**, 107401 (2004).
- [206] K. L. van der Molen, F. B. Segerink, N. F. van Hulst, and L. Kuipers, *Influence of hole size on the extraordinary transmission through subwavelength hole arrays*, Appl. Phys. Lett. **85**, 4316 (2004).
- [207] U. Fano, *Effects of configuration interaction on intensities and phase shifts*, Phys. Rev. **124**, 1866 (1961).
- [208] M. Sarrazin, J.-P. Vigneron, and J.-M. Vigoureux, *Role of Wood anomalies in optical properties of thin metallic films with a bidimensional array of subwavelength holes*, Phys. Rev. B **67**, 085415 (2003).
- [209] C. Genet, M. P. van Exter, and J. P. Woerdman, *Fano-type interpretation of red shifts and red tails in hole array transmission spectra*, Opt. Commun. **225**, 331 (2003).
- [210] H. A. Bethe, *Theory of diffraction by small holes*, Phys. Rev. **66**, 163 (1944).
- [211] J. N. Farahani, D. W. Pohl, H.-J. Eisler, and B. Hecht, *Single quantum dot coupled to a scanning optical antenna: A tunable superemitter*, Phys. Rev. Lett. **95**, 017402 (2005).
- [212] I. Gryczynski, J. Malicka, E. Holder, N. DiCesare, and J. R. Lakowicz, *Effects of metallic silver particles on the emission properties of  $[Ru(bpy)_3]^{2+}$* , Chem. Phys. Lett. **372**, 409 (2003).
- [213] H. Mertens, J. S. Biteen, H. A. Atwater, and A. Polman, *Polarization-selective plasmon-enhanced silicon quantum-dot luminescence*, Nano Lett. **6**, 2622 (2006).
- [214] H. Mertens and A. Polman, *Plasmon-enhanced erbium luminescence*, Appl. Phys. Lett. **89**, 211107 (2006).
- [215] S. Kühn, U. Håkanson, L. Rogobete, and V. Sandoghdar, *Enhancement of single-molecule fluorescence using a gold nanoparticle as an optical nanoantenna*, Phys. Rev. Lett. **97**, 017402 (2006).
- [216] F. Tam, G. P. Goodrich, B. R. Johnson, and N. J. Halas, *Plasmonic enhancement of molecular fluorescence*, Nano Lett. **7**, 496 (2007).
- [217] O. L. Muskens, V. Giannini, J. A. Sanchez-Gil, and J. Gomez Rivas, *Strong enhancement of the radiative decay rate of emitters by single plasmonic nanoantennas*, Nano Lett. **7**, 2871 (2007).
- [218] R. M. Bakker, V. P. Drachev, Z. Liu, H.-K. Yuan, R. H. Pedersen, A. Boltasseva, J. Chen, J. Irudayaraj, A. V. Kildishev, and V. M. Shalaev, *Nanoantenna array-induced fluorescence enhancement and reduced lifetimes*, New J. Phys. **10**, 125022 (2008).
- [219] E. M. Purcell, *Spontaneous emission probabilities at radio frequencies*, Phys. Rev. **69**, 681 (1946).
- [220] S. H. Garrett, L. H. Smith, and W. L. Barnes, *Fluorescence in the presence of metallic hole arrays*, J. Mod. Opt. **52**, 1105 (2005).
- [221] A. G. Brolo, S. C. Kwok, M. G. Moffitt, R. Gordon, J. Riordon, and K. L. Kavanagh, *Enhanced fluorescence from arrays of nanoholes in a gold film*, J. Am. Chem. Soc. **127**, 14936 (2005).
- [222] J. Wenger, D. Gérard, J. Dintinger, O. Mahboub, N. Bonod, E. Popov, T. W. Ebbesen, and H. Rigneault, *Emission and excitation contributions to enhanced single molecule fluorescence by gold nanometric apertures*, Opt. Express **16**, 3008 (2008).
- [223] A. Polman, *Erbium implanted thin film photonic materials*, J. Appl. Phys. **82**, 1 (1997).
- [224] M. J. A. de Dood, J. Knoester, and A. Polman, *Förster transfer and the local optical density of states in erbium-doped silica*, Phys. Rev. B **71**, 115102 (2005).
- [225] M. J. A. de Dood, L. H. Slooff, A. Polman, A. Moroz, and A. van Blaaderen, *Local optical density of states in  $SiO_2$  spherical microcavities: Theory and experiment*, Phys. Rev. A **64**, 033807 (2001).

- [226] E. Snoeks, A. Lagendijk, and A. Polman, *Measuring and modifying the spontaneous emission rate of erbium near an interface*, Phys. Rev. Lett. **74**, 2459 (1995).
- [227] Y. C. Jun, R. D. Kekatpure, J. S. White, and M. L. Brongersma, *Nonresonant enhancement of spontaneous emission in metal-dielectric-metal plasmon waveguide structures*, Phys. Rev. B **78**, 153111 (2008).
- [228] R. S. Tucker, *Energy consumption in digital optical ICs with plasmon waveguide interconnects*, IEEE Photon. Technol. Lett. **19**, 2036 (2007).
- [229] V. R. Almeida, C. A. Barrios, R. R. Panepucci, and M. Lipson, *All-optical control of light on a silicon chip*, Nature **431**, 1081 (2004).
- [230] T. Kampfrath, D. M. Beggs, T. P. White, M. Burrelli, D. van Oosten, T. F. Krauss, and L. Kuipers, *Ultrafast rerouting of light via slow modes in a nanophotonic directional coupler*, Appl. Phys. Lett. **94**, 241119 (2009).
- [231] K. F. MacDonald, Z. L. Samson, M. I. Stockman, and N. I. Zheludev, *Ultrafast active plasmonics*, Nature Photon. **3**, 55 (2009).
- [232] D. Taillaert, P. Bienstman, and R. Baets, *Compact efficient broadband grating coupler for silicon-on-insulator waveguides*, Opt. Lett. **29**, 2749 (2004).
- [233] W. A. Challener, C. Peng, A. V. Itagi, D. Karns, W. Peng, Y. Peng, X. Yang, X. Zhu, N. J. Gokemeijer, Y.-T. Hsia, G. Ju, R. E. Rottmayer, M. A. Seigler, and E. C. Gage, *Heat-assisted magnetic recording by a near-field transducer with efficient optical energy transfer*, Nature Photon. **3**, 220 (2009).
- [234] D. Marcuse, *Light transmission optics*, Van Nostrand Reinhold, New York, 1982.
- [235] S. Hayashi, K. Kozaru, and K. Yamamoto, *Enhancement of photoelectric conversion efficiency by surface plasmon excitation: A test with an organic solar cell*, Solid State Commun. **79**, 763 (1991).
- [236] O. Stenzel, A. Stendal, K. Voigtsberger, and C. von Borczyskowski, *Enhancement of the photovoltaic conversion efficiency of copper phthalocyanine thin film devices by incorporation of metal clusters*, Sol. Energy Mat. Sol. Cells **37**, 337 (1995).
- [237] M. Westphalen, U. Kreibig, J. Rostalski, H. Lüth, and D. Meissner, *Metal cluster enhanced organic solar cells*, Sol. Energy Mat. Sol. Cells **61**, 97 (2000).
- [238] A. J. Morfa, K. L. Rowlen, T. H. Reilly, III, M. J. Romero, and J. van de Lagemaat, *Plasmon-enhanced solar energy conversion in organic bulk heterojunction photovoltaics*, Appl. Phys. Lett. **92**, 013504 (2008).
- [239] V. E. Ferry, L. A. Sweatlock, D. Pacifici, and H. A. Atwater, *Plasmonic nanostructure design for efficient light coupling into solar cells*, Nano Lett. **8**, 4391 (2008).
- [240] C. Hägglund and B. Kasemo, *Nanoparticle plasmonics for 2D-photovoltaics: mechanisms, optimization, and limits*, Opt. Express **17**, 11944 (2009).
- [241] K. R. Catchpole and A. Polman, *Plasmonic solar cells*, Opt. Express **16**, 21793 (2008).
- [242] L. H. Slooff, S. C. Veenstra, J. M. Kroon, D. J. D. Moet, J. Sweelssen, and M. M. Koetse, *Determining the internal quantum efficiency of highly efficient polymer solar cells through optical modeling*, Appl. Phys. Lett. **90**, 143506 (2007).
- [243] C. A. Balanis, *Antenna theory*, Wiley, Hoboken, NJ, 2005.
- [244] A. Shalav, *Rare-earth doped up-converting phosphors for an enhanced silicon solar cell response*, PhD thesis, University of New South Wales, 2006.
- [245] H. Mertens, A. Polman, I. M. P. Aarts, W. M. M. Kessels, and M. C. M. van de Sanden, *Absence of the enhanced intra-4f transition cross section at 1.5  $\mu\text{m}$  of  $\text{Er}^{3+}$  in Si-rich  $\text{SiO}_2$* , Appl. Phys. Lett. **86**, 241109 (2005).
- [246] S. Balushev, T. Miteva, V. Yakutkin, G. Nelles, A. Yasuda, and G. Wegner, *Up-conversion fluorescence: Noncoherent excitation by sunlight*, Phys. Rev. Lett. **97**, 143903 (2006).

- 
- [247] C. Kammerer, G. Cassabois, C. Voisin, C. Delalande, P. Roussignol, and J. M. Gérard, *Photoluminescence up-conversion in single self-assembled InAs/GaAs quantum dots*, Phys. Rev. Lett. **87**, 207401 (2001).
- [248] A. D. McFarland and R. P. Van Duyne, *Single Silver Nanoparticles as Real-Time Optical Sensors with Zeptomole Sensitivity*, Nano Lett. **3**, 1057 (2003).
- [249] A. G. Brolo, R. Gordon, B. Leathem, and K. L. Kavanagh, *Surface plasmon sensor based on the enhanced light transmission through arrays of nanoholes in gold films*, Langmuir **20**, 4813 (2004).
- [250] M. E. Stewart, N. H. Mack, V. Malyarchuk, J. A. N. T. Soares, T.-W. Lee, S. K. Gray, R. G. Nuzzo, and J. A. Rogers, *Quantitative multispectral biosensing and 1D imaging using quasi-3D plasmonic crystals*, Proc. Nat. Acad. Sc. **103**, 17143 (2006).
- [251] A. Lesuffleur, H. Im, N. C. Lindquist, and S.-H. Oh, *Periodic nanohole arrays with shape-enhanced plasmon resonance as real-time biosensors*, Appl. Phys. Lett. **90**, 243110 (2007).
- [252] H. Rigneault, J. Capoulade, J. Dintinger, J. Wenger, N. Bonod, E. Popov, T. W. Ebbesen, and P.-F. Lenne, *Enhancement of single-molecule fluorescence detection in subwavelength apertures*, Phys. Rev. Lett. **95**, 117401 (2005).
- [253] J. A. Liddle, Y. Cui, and P. Alivisatos, *Lithographically directed self-assembly of nanostructures*, J. Vac. Sci. Technol. B **22**, 3409 (2004).
- [254] H. S. Eisenberg, Y. Silberberg, R. Morandotti, and J. S. Aitchison, *Diffraction management*, Phys. Rev. Lett. **85**, 1863 (2000).
- [255] P. S. J. Russel, T. A. Birks, and F. D. Lloyd-Lucas, *Confined electrons and photons*, chapter Photonic Bloch waves and photonic band gaps, pages 585–633, Plenum, New York, 1995.
- [256] S. Foteinopoulou and C. M. Soukoulis, *Negative refraction and left-handed behavior in two-dimensional photonic crystals*, Phys. Rev. B **67**, 235107 (2003).
- [257] V. A. Podolskiy and E. E. Narimanov, *Comment on “All-angle broadband negative refraction of metal waveguide arrays in the visible range: Theoretical analysis and numerical demonstration”*, Phys. Rev. Lett. **98**, 179401 (2007).
- [258] R. de Waele, *Controlling light with resonant plasmonic nanostructures*, PhD thesis, Utrecht University, 2009.



---

## Summary

The interaction of light with metals extends far beyond the reflection of light by a mirror. A metal surface supports surface plasmon polaritons (SPPs), which are electromagnetic waves that are strongly coupled to oscillations of the free electrons in the metal and that propagate along the surface. The ability to control the shape of metallic surfaces with nanofabrication technology allows us to manipulate the flow of SPPs. The resulting control over electromagnetic fields opens up a rich world of opportunities in science and technology, ranging from lighting and photovoltaics to photonic circuits and quantum optics. Many of those opportunities emanate from the fact that SPPs can be confined to smaller length scales than those attainable with the diffraction limit of light in free space.

In this thesis, we explore new ways to tailor the properties of SPPs such that they enable the confinement of light at nanoscale dimensions. To this end, we use a variety of metallodielectric geometries that can serve as waveguides for SPPs. We show how the propagation characteristics in such waveguides can be controlled, and we concentrate light in subwavelength volumes by tapering and truncating the waveguides.

We probe the evanescent fields of SPPs by two methods. On the one hand, SPPs are detected or excited in a near-field microscope through a very small aperture in a metal-coated probe that is brought in close proximity to the metal surface on which the SPPs propagate. On the other hand, we exploit the interaction of the SPP fields with emitters by collecting the photoluminescence emission from rare-earth ions that are located near the metal nanostructures.

In Chapter 2, we use a near-field microscope to image the fields of SPPs that are squeezed into a 50 nm thick dielectric layer between two Ag surfaces. We show that the wavelength of SPPs in such a metal slot waveguide is significantly shortened

with respect to that of light in the dielectric. Chapter 3 focuses on specific waveguided SPP modes that can exhibit the peculiar characteristic that phase velocity is directed opposite to the direction of energy propagation. This phenomenon enables negative refraction of light into the waveguide at optical frequencies, steering light in a different direction than usually possible. We provide a quantitative theoretical comparison of the aforementioned slot waveguide and of other geometries that support modes with a negative refractive index.

Chapter 4 introduces a tapered waveguide design to focus SPPs. We show that the concentration of infrared SPPs in a laterally tapered Ag stripe waveguide enhances the conversion of infrared to visible light in Er ions that are implanted in the substrate close to the waveguide, when SPPs are excited at the substrate side of the metal film at the start of the waveguide. In Chapter 5 it is revealed that SPPs propagate all the way to the end of a tapered waveguide, which has a diameter of only  $\sim 65$  nm, without being hindered by the small size of the waveguide. Calculations confirm this experimental observation, and show that the observed focusing effect can only occur when SPPs are excited at the start of the waveguide at the interface between the metal stripe and the high-index substrate.

The focusing in tapered waveguides is explained in terms of an adiabatic transformation of a mode guided by the waveguides in Chapter 6. We illustrate the correspondence of the excited mode with the fundamental mode that can be guided by a metal cylinder of arbitrarily small diameter. Inspired by this analogy, we use tapered waveguides to efficiently excite SPPs on metal nanowires with diameters as small as 60 nm that extend from the end of the tapers. The mode transformation in the tapers and subsequent propagation on the nanowires are investigated in a phase- and polarization-sensitive near-field microscope. This allows the retrieval of the propagation speed and polarization nature of the excited mode on the nanowires, and proves that the structures achieve subwavelength concentration of light. We experimentally demonstrate that the efficiency with which a taper couples light to a nanowire can be as high as  $\sim 50\%$ .

In Chapter 7, we discuss the possibility to concentrate SPPs by structuring a thin dielectric film on top of a metal surface instead of by structuring the metal itself. We show that SPPs that propagate onto a Si wedge on Ag in the direction of increasing wedge thickness come to a halt at a specific thickness, concentrating energy in a subwavelength focus. The effect is explained in terms of SPP mode transformation, and can lead to an intensity enhancement by a factor 180.

In Chapter 8, we investigate field enhancement at a wavelength of  $1.5 \mu\text{m}$  in arrays of subwavelength apertures in a metal film. To do so, we study the enhanced excitation of Er ions positioned close to the metal film by collecting emission that is converted by the ions to wavelengths shorter than the infrared pump wavelength. The structural parameters that govern the properties of the aperture arrays are varied. Field enhancement due to two different types of SPP resonances is considered. On the one hand, propagating SPPs are excited on the surface of the metal film. We show that the array period for which resonant field enhancement occurs is slightly different from that at which a transmission resonance is observed, due

to interference of the light wave coupled to the resonant mode with the directly transmitted wave. On the other hand, localized SPPs are excited inside annular apertures. We demonstrate that due to the localized nature of those resonances, the field enhancement occurs for a wide range of incident angles.

Not only the excitation rate, but also the emission rate of emitters can be enhanced by localized SPP resonances. Chapter 9 describes the enhancement of the radiative emission rate of Er ions placed inside annular apertures. An increase of both the photoluminescence intensity and the photoluminescence decay rate is observed when the aperture resonance is tuned to the Er emission wavelength at 1.5  $\mu\text{m}$ .

We discuss some possible applications and future research directions based on SPP field concentration and dispersion control in Chapter 10. Metal tapers and nanowires can be used as components in photonic circuits and to interface photonics and electronics on a chip. We discuss the applicability of light concentration using SPPs for photovoltaic energy conversion. We propose to exploit localized resonances in annular apertures and adiabatic nanofocusing for molecular sensing and enhanced spectroscopy. Finally, we provide a route to establish three-dimensional negative refraction in stacked geometries of plasmonic waveguides.





---

## Samenvatting

Een metaaloppervlak kan licht geleiden in de vorm van oppervlakteplasmonpolaritonen. Deze elektromagnetische golven, in het kort 'plasmonen', planten zich voort langs het oppervlak en zijn gekoppeld aan trillingen van de geleidingselektronen in het metaal. Door het metaaloppervlak op nanometerschaal een bepaalde vorm te geven kan de voortplanting van plasmonen gemanipuleerd worden, waardoor controle over elektromagnetische velden op zeer kleine schaal verkregen wordt. Dit biedt een groot aantal wetenschappelijke en technologische mogelijkheden, in toepassingsgebieden variërend van verlichting en zonnecellen tot fotonische circuits en quantumoptica. Veel van die toepassingen zijn direct gerelateerd aan het feit dat plasmonen opgesloten kunnen worden op lengteschalen die kleiner zijn dan die waarop licht in de vrije ruimte geconcentreerd kan worden.

Dit proefschrift demonstreert nieuwe manieren om de eigenschappen van plasmonen zodanig te manipuleren dat ze de opsluiting van licht op nanometerschaal mogelijk maken. Voor dit doel worden verschillende metallodiëlektrische geometrieën gebruikt die kunnen dienen als golfgeleiders voor plasmonen. We laten zien hoe de voortplanting in de golfgeleiders kan worden beïnvloed, en hoe licht opgesloten kan worden in zeer kleine volumes door de golfgeleiders spits toe te laten lopen of door plasmonen in korte golfgeleiders te laten reflecteren.

We meten het evanescente veld van plasmonen op twee manieren. Ten eerste worden plasmonen gedetecteerd of geëxciteerd in een nabije-veld-microscoop door een zeer klein gaatje in de metalen buitenlaag van een sonde die dicht bij het metaaloppervlak wordt gebracht dat de plasmonen geleidt. Ten tweede gebruiken we het licht dat uitgezonden wordt door zeldzame-aard-ionen die zich dicht bij de metalen nanostructuren bevinden, om de interactie tussen plasmonen en deze emitters te detecteren.

In hoofdstuk 2 wordt een nabije-veld-microscoop gebruikt om de velden af te beelden van plasmonen die in een 50 nm dikke diëlektrische film tussen twee zilveroppervlakken geperst zijn. We laten zien dat de golflengte van de plasmonen in zo'n golfgeleider aanzienlijk korter is dan die van licht. Hoofdstuk 3 beschrijft specifieke typen plasmonen die de eigenschap hebben dat de voortplanting van de fase van de golf tegengesteld gericht is aan de richting waarin de golfenergie stroomt. Dit betekent dat de voortplanting van de plasmonen in de golfgeleiders beschreven kan worden met een negatieve brekingsindex. Door deze eigenschap kan licht negatieve breking vertonen in een golfgeleider. We vergelijken verschillende geometrieën die plasmonen met een negatieve brekingsindex kunnen geleiden.

Hoofdstuk 4 introduceert een spits toelopende metalen golfgeleider waarin plasmonen gefocuseerd kunnen worden. De golfgeleider bestaat uit een dunne metaallaag waarvan de breedte geleidelijk afneemt. De metaallaag bevindt zich op een transparant substraat. We demonstreren dat de concentratie van plasmonen in zo'n golfgeleider de conversie van infrarood naar zichtbaar licht versterkt. Die conversie vindt plaats in erbiumionen die geïmplanteerd zijn in het substraat, dicht bij het metaal. Hoofdstuk 5 laat zien dat plasmonen naar het 65 nm brede uiteinde van de spitse golfgeleider worden geleid, zonder gehinderd te worden door de beperkte breedte van de geleider. Berekeningen staven deze experimentele observatie, en laten zien dat de focussing alleen plaats kan vinden wanneer plasmonen worden geëxciteerd aan het begin van de golfgeleider aan het oppervlak tussen de metaallaag en het substraat.

De focussing van licht in spits toelopende golfgeleiders wordt in hoofdstuk 6 beschreven in termen van een adiabatische transformatie van een specifieke plasmoniegolf in de golfgeleider. We beschrijven de equivalentie van deze golf met de plasmoniegolf die door een dunne metalen cylinder geleid kan worden, de zogenaamde Sommerfeldgolf. Geïnspireerd door deze analogie gebruiken we spits toelopende golfgeleiders om efficiënt plasmonen te exciteren op metalen nanodraden van slechts 60 nm breed. De golftransformatie in de spitse golfgeleiders en de voortplanting van plasmonen op de nanodraden waarin de golfgeleiders uitmonden wordt onderzocht in een nabije-veld-microscoop die de fase en polarisatie van het nabije veld kan meten. Dit maakt het mogelijk de voortplantingssnelheid en de bijzondere polarisatie van de plasmonen op de nanodraden te meten. We laten zien dat de efficiëntie waarmee de plasmonen in de spitse golfgeleider naar de nanodraad koppelen ~50% bedraagt.

Hoofdstuk 7 beschouwt de mogelijkheid om plasmonen te concentreren door op een metaaloppervlak een dunne diëlektrische laag te structureren, in plaats van het metaal zelf. We laten zien dat plasmonen die zich op een silicium wig op zilver voortplanten tot stilstand komen bij een specifieke dikte van de wig. Daardoor wordt energie geconcentreerd in een zeer klein gebied. Het effect wordt verklaard in termen van een golftransformatie, en kan leiden tot een 180-voudige versterking van de intensiteit.

In hoofdstuk 8 onderzoeken we veldversterking bij een golflengte van 1.5  $\mu\text{m}$

in een periodiek rooster van kleine gaatjes in een metaallaag. Daarbij maken we gebruik van de versterkte excitatie van erbiumionen die zich dicht bij de metaallaag bevinden, door het licht te detecteren dat door de ionen is omgezet naar golflengtes die korter zijn dan de infrarode excitatiegolflengte. We beschouwen veldversterking door twee verschillende typen plasmonresonanties. In de eerste plaats worden propagerende plasmonen geëxciteerd op het oppervlak van de metaallaag. We laten zien dat de roosterperiode waarvoor maximale veldversterking plaatsvindt, verschilt van de periode waarvoor de transmissie door het rooster maximaal is. Dit wordt veroorzaakt door de interferentie van licht dat gekoppeld is aan de plasmonresonantie, met licht dat direct door de gaatjes doorgelaten wordt. In de tweede plaats worden plasmonen geëxciteerd in gaatjes met een coaxiale geometrie. We laten zien dat dankzij het gelokaliseerde karakter van die plasmonresonanties de veldversterking in coaxiale gaatjes optreedt voor een groot hoekbereik van het invallende excitatielicht.

Naast de waarschijnlijkheid waarmee emitters worden geëxciteerd kan ook de waarschijnlijkheid waarmee emitters hun licht uitzenden, worden vergroot door gelokaliseerde plasmonresonanties. Hoofdstuk 9 beschrijft de versterking van de emissiewaarschijnlijkheid van erbiumionen in coaxiale gaatjes. We observeren zowel een versterking van de uitgezonden lichtintensiteit als een verkorting van de gemiddelde tijd dat de erbiumionen in hun aangeslagen toestand verblijven, wanneer de plasmonresonantie overlapt met de emissiegolflengte van  $1.5 \mu\text{m}$ .

We beschrijven enkele toepassingen en mogelijke onderzoeksrichtingen die gebaseerd zijn op de concentratie van licht met behulp van plasmonen in hoofdstuk 10. Spits toelopende metalen golfgeleiders en nanodraden kunnen gebruikt worden als componenten in fotonische circuits en om fotonica en electronica op een chip te combineren. We beschouwen de mogelijkheid om de concentratie van licht met plasmonen te gebruiken in zonnecellen. Gelokaliseerde resonanties in coaxiale gaatjes en adiabatische nanofocussing kan worden gebruikt voor de detectie van moleculen en voor efficiënte spectroscopie. Tenslotte beschrijven we de mogelijkheid om drie-dimensionale negatieve breking te realiseren in gestapelde plasmongolfsgeleiders.



---

## List of publications

### This thesis is based on the following publications:

- *Near-field visualization of strongly confined surface plasmon polaritons in metal-insulator-metal waveguides*, E. Verhagen, J. A. Dionne, L. Kuipers, H. A. Atwater, and A. Polman, *Nano Lett.* **8**, 2925 (2008). **(Chapter 2)**
- *Are negative index materials achievable with surface plasmon waveguides? A case study of three plasmonic geometries*, J. A. Dionne, E. Verhagen, A. Polman, and H. A. Atwater, *Opt. Express* **16**, 21793 (2008); also highlighted in *Nature Mater.* **7**, 925 (2008). **(Chapter 3)**
- *Enhanced nonlinear optical effects with a tapered plasmonic waveguide*, E. Verhagen, L. Kuipers, and A. Polman, *Nano Lett.* **7**, 334 (2007). **(Chapter 4)**
- *Nanofocusing in laterally tapered plasmonic waveguides*, E. Verhagen, A. Polman, and L. Kuipers, *Opt. Express* **16**, 45 (2008). **(Chapter 5)**
- *Nanowire plasmon excitation by adiabatic mode transformation*, E. Verhagen, M. Spasenović, A. Polman, and L. Kuipers, *Phys. Rev. Lett.* **102**, 203904 (2009). **(Chapter 6)**
- *Plasmonic nanofocusing on a dielectric wedge*, E. Verhagen, L. Kuipers, and A. Polman, in preparation. **(Chapter 7)**
- *Field enhancement in metallic subwavelength aperture arrays probed by erbium upconversion luminescence*, E. Verhagen, L. Kuipers, and A. Polman, *Opt. Express* **17**, 14586 (2009). **(Chapter 8)**

- *Enhanced spontaneous emission rate in annular plasmonic nanocavities*, E. Kroekenstoel, E. Verhagen, R. J. Walters, L. Kuipers, and A. Polman, Appl. Phys. Lett. **95** (2009), in press. (**Chapter 9**)

### **Other publications by the author:**

- *Erbium luminescence imaging of infrared surface plasmon polaritons*, E. Verhagen, A. Tchebotareva, and A. Polman, Appl. Phys. Lett. **88**, 121121 (2006).
- *Direct imaging of propagation and damping of near-resonance surface plasmon polaritons using cathodoluminescence spectroscopy*, J. T. van Wijnngaarden, E. Verhagen, A. Polman, C. E. Ross, H. J. Lezec, and H. A. Atwater, Appl. Phys. Lett. **88**, 221111 (2006); also featured in Science **312**, 1719 (2006).
- *Measurement of modal symmetry in subwavelength plasmonic slot waveguides*, M. Spasenović, D. van Oosten, E. Verhagen, and L. Kuipers, Appl. Phys. Lett. **95** (2009), in press.
- *Electric and magnetic dipole coupling in near-infrared split ring metamaterial arrays*, I. Sersic, M. Frimmer, E. Verhagen, and A. F. Koenderink, Phys. Rev. Lett. **103** (2009), in press.

---

## Dankwoord

De laatste pagina's van een proefschrift worden vaak het best gelezen. En niet zonder reden. Hoe exact ook, wetenschap staat of valt bij contacten tussen mensen. In de loop van mijn promotieonderzoek heb ik direct samengewerkt met een aantal mensen die een vernoeming hier dubbel en dwars verdienen. Zij en vele anderen hebben me op allerlei vlakken veel geleerd, en bovenal voortdurend geïnspireerd.

Ik heb het bijzondere voorrecht gehad om de begeleiding van twee promotoren te genieten: Albert Polman en Kobus Kuipers. Albert, jouw enthousiasme voor het vak bracht me ooit naar AMOLF, en heeft samen met je voortvarende aanpak van nieuwe kansen altijd aanstekelijk gewerkt. Je alles-is-mogelijk-mentaliteit is een uitstekende aanvulling en inspiratiebron voor me geweest. Bedankt voor alle ruimte en mogelijkheden die je me hebt geboden, en voor de kans om ons werk overal te kunnen presenteren. Kobus, onze update-gesprekken waren altijd een enerverende belevenis, soms bijna verdrinkend in dispersiespaghetti maar vaak zinderend van ideeën en inzichten. Ik heb veel geleerd van je passie voor het aanpakken van schijnbaar onverklaarbare problemen en van onze gedeelde interesse voor de sociologische aspecten van wetenschap en het publicatieproces.

Of all my colleagues, the biggest “thanks” goes to the people with whom I have shared the ups and downs of obtaining, interpreting and publishing experimental results. Without the help of Marko Spasenović, the cover of this thesis and everything in Chapter 6 would not look like it does. I wish you everything you hope for in the future. It's been a great pleasure to work with someone who is as motivated, high-spirited and skilled as Jen Dionne, with whom I have collaborated on the work presented in Chapters 2 and 3. Ik heb enorm veel geleerd van het begeleiden van Erwin Kroekenstoel, wiens vasthoudendheid uiteindelijk heeft geleid tot de resultaten in Hoofdstuk 9.

In het enigszins vat krijgen op de fundamenten van optica en fotonica heb ik veel gehad aan Hans Mertens en Femius Koenderink. Ik heb een klein deel van hun kennis gretig geabsorbeerd gedurende mijn zoektocht naar interessante onderwerpen. I've had many interesting physics discussions as well as enjoyable hours off duty with co-boat-owners Ernst Jan Vesseur and Robb Walters. De discussies bij het whiteboard met René de Waele waren altijd weer een genot. I would like to thank all other members of the Photonic Materials group for the pleasant atmosphere: Jeroen Kalkman, Joan Penninkhof, Rob van Loon, Martin Kuttge, Sébastien Bidault, Kylie Catchpole, Marc Verschuuren, Maarten Hebbink, Vivian Ferry, Toon Coenen and Claire van Lare.

AMOLF is gezegend met uitstekende ondersteuning. Grote dank gaat in het bijzonder naar degenen die assisteren in de cleanroom en alle aanverwante apparatuur onderhouden: Chris Rétif, Hans Zeijlemaker en Johan Derks. Ik wil Hans en Johan ook specifiek bedanken voor de steun rond de verhuizing. Nick de Jong heeft een belangrijke bijdrage geleverd aan het fabricageproces dat ik veel heb gebruikt. Ook wil ik de tekenkamer en werkplaats bedanken voor hun grote vakmanschap.

Thanks to past and present members of the Nano Optics and Resonant Nanophotonics groups for advice and stimulating discussions during group meetings, and for conversations about near-field microscopy in particular. I am grateful to all members of the Center for Nanophotonics for the lively colloquia, which I think are an essential part of the education of all people involved. Ik wil Simon Huisman en Willem Vos bedanken voor het gebruik van hun opstelling voor de reflectiviteitsmetingen in Hoofdstuk 9. I would like to thank Harry Atwater for our fruitful collaboration and for the invigorating discussions on plasmonics and photovoltaics during his stays in Amsterdam and our visit to Pasadena. I thank the members of his group for the enjoyable company at many conferences.

Buiten AMOLF zijn er veel mensen die een geslaagde poging doen me af en toe te laten ontspannen. Om te beginnen wil ik alle mensen bedanken met wie ik de afgelopen jaren muziek heb gemaakt; het zijn er teveel om allemaal bij naam te noemen. Guus, ik hoop dat we regelmatig blijven cc'en, ook als onze koffieautomaten wat verder uit elkaar staan. Joep, Steven, Vicencio, Joost, Siddharth, Ivo, Arno en Meile, bedankt voor alle uitjes, vakanties en mooie avonden met de GVR. Jesse, we hebben veel te weinig tijd voor elkaar tegenwoordig, maar gelukkig altijd nog de rest van ons leven om te blijven proberen het in te halen.

Nany, Miguel, en Isabelle, bedankt voor de regelmatige bezoeken en ontbijtjes en met name voor jullie onvoorwaardelijke steun rond en sinds de geboorte van Inez. Lennart en Inge, het valt niet altijd mee om ideale (schoon)broers te zijn als je allemaal in de wetenschap zit, maar bedankt voor alle vrolijkheid en succes met jullie eigen promoties. Anneke en Arie, heel veel dank voor jullie voortdurende aanmoediging en steun op alle fronten.

En tenslotte, Kiki, bedankt voor je eindeloze geduld en alle liefde. Wat wij zijn wordt mooier met iedere nieuwe herinnering en elke nieuwe toekomst.



---

## About the author



Ewold Verhagen was born on October 28, 1980 in Leiderdorp, The Netherlands. After obtaining his high school diploma at the Stedelijk Gymnasium Leiden in 1999, he studied physics at Utrecht University. He performed a small research project on two-photon fluorescence microscopy in the Molecular Biophysics group led by prof. dr. Hans Gerritsen. He obtained his Master's degree in 2005 with a project performed in the Photonic Materials group at the FOM-Institute for Atomic and Molecular Physics (AMOLF) in Amsterdam supervised by prof. dr. Albert Polman. In September 2005 he started his PhD research at AMOLF under the supervision of prof. dr. Albert Polman and prof. dr. Kobus Kuipers. The results of that work are described in this thesis. In his spare time, he enjoys making music and playing with his daughter.



The work described in this thesis was performed at the  
FOM-Institute for Atomic and Molecular Physics, Science  
Park 104, 1098 XG Amsterdam, The Netherlands.

Affiliation:

Prof. Dr. A. Polman  
Center for Nanophotonics  
FOM-Institute AMOLF, Amsterdam, The Netherlands

Prof. Dr. L. Kuipers  
Center for Nanophotonics  
FOM-Institute AMOLF, Amsterdam, The Netherlands